

**STUDY OF FORMATION AND DYNAMICS OF
INTERNAL AND EXTERNAL TRANSPORT BARRIERS
BASED ON BIFURCATION CONCEPTS**

BY

BOONYARIT CHATTHONG

**A DISSERTATION SUBMITTED IN PARTIAL FULFILLMENT OF
THE REQUIREMENTS FOR THE DEGREE OF DOCTOR OF
PHILOSOPHY (TECHNOLOGY)
SIRINDHORN INTERNATIONAL INSTITUTE OF TECHNOLOGY
THAMMASAT UNIVERSITY
ACADEMIC YEAR 2015**

**STUDY OF FORMATION AND DYNAMICS OF
INTERNAL AND EXTERNAL TRANSPORT BARRIERS
BASED ON BIFURCATION CONCEPTS**

BY

BOONYARIT CHATTHONG

**A DISSERTATION SUBMITTED IN PARTIAL FULFILLMENT OF
THE REQUIREMENTS FOR THE DEGREE OF DOCTOR OF
PHILOSOPHY (TECHNOLOGY)
SIRINDHORN INTERNATIONAL INSTITUTE OF TECHNOLOGY
THAMMASAT UNIVERSITY
ACADEMIC YEAR 2015**



STUDY OF FORMATION AND DYNAMICS OF INTERNAL AND EXTERNAL
TRANSPORT BARRIERS BASED ON BIFURCATION CONCEPTS

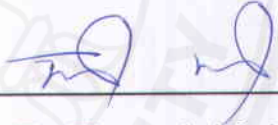
A Dissertation Presented

By
BOONYARIT CHATTHONG

Submitted to
Sirindhorn International Institute of Technology
Thammasat University
In partial fulfillment of the requirements for the degree of
DOCTOR OF PHILOSOPHY (TECHNOLOGY)

Approved as to style and content by

Advisor and Chairperson of Thesis Committee



(Assoc. Prof. Dr. Thawatchai Onjun, Ph.D.)

Co-Advisor



(Asst. Prof. Dr. Paiboon Sreearunothai, Ph.D.)

Committee Member and
Chairperson of Examination Committee




(Dr. Roppon Picha, Ph.D.)

Committee Member



(Assoc. Prof. Dr. Nirattaya Khamsemanan, Ph.D.)

Committee Member



(Prof. Dr. David Ruffolo, Ph.D.)

External Examiner: Prof. Dr. Tohru Mizuuchi, Ph.D.

AUGUST 2015

Abstract

STUDY OF FORMATION AND DYNAMICS OF INTERNAL AND EXTERNAL TRANSPORT BARRIERS BASED ON BIFURCATION CONCEPTS

by

BOONYARIT CHATTHONG

BS in Physics/Mathematics with distinction, University of Virginia, 2005

MS in Physics, Mahidol University, 2010

The formation and dynamics of both Edge Transport Barriers (ETB) and Internal Transport Barriers (ITB) are analyzed based on bifurcation concepts. In this thesis, one-field (thermal) and two-field (coupled thermal and particle) transport equations are solved analytically and numerically for the profiles of pressure and density gradients as functions of heat and particle fluxes, respectively. The transport effect includes a combination of neoclassical transport and anomalous transport. The transport suppression mechanisms based on flow shear and magnetic shear are assumed to be only in the anomalous channel. It is found that plasmas can exhibit bifurcation where a sudden jump in plasma gradients can be achieved at the transition point corresponding to the critical flux. Local stability analysis shows that the transition occurs at a threshold flux and exhibits hysteresis only if the ratio of anomalous to neoclassical transport exceeds a critical value. The depth of the hysteresis loop depends on both neoclassical and anomalous transport, as well as the suppression strength. Dynamically, it is found that an ETB expands inward, in which the radial growth of the pedestal initially appears to be super-diffusive but later slows down and stops. In addition, the time of barrier expansion is found to be much longer than the time plasma takes to evolve from L -mode to H -mode. Evidently, an ETB can form only when the local flux (heat/particle) surpasses the critical value. The ITB formation is possible only with a presence of reverse q profile. The location and width

of ITB are found to be correlated with the plasma current profile. Particularly, the top of ITB is found near the location of off-axis maximum current density and zero magnetic shear. Both ITB and ETB widths appear to be governed by the heat source, off-axis current drive position and transport strengths. In the second part of the thesis, a 1.5D BALDUR integrated predictive modeling code, with inclusion of toroidal velocity models, is used to simulate plasma profiles. The predictive toroidal velocity models are based on neoclassical toroidal viscosity (NTV) and toroidal current density effects. It is found that the predicted intrinsic rotation can result in the formation of an ITB, located mostly between $r/a = 0.6$ to 0.8 and having a strong impact on plasma performance. It is also found that plasma density and heating power affect minimally the toroidal rotation, whereas the increase of plasma effective charge can considerably reduce the toroidal velocity peaking. In the last part, the impacts of toroidal flow on the L - H transition phenomenon are investigated based on bifurcation concepts. It is found that inclusion of toroidal velocity can substantially increase the plasma pressure and density, mainly due to an increase of the pedestal width. In addition, the pedestal for pressure tends to form shortly before that of density. After the pedestal forms, it expands inwards super-diffusively in the initial state and sub-diffusively in the final state before reaching a steady state. The expansion speed is sensitive to the flow shear strength. The time required for the plasma to reach a steady state in H -mode is much longer than the transition time.

Keywords: Fusion reaction, Tokamak, ETB, ITB, Bifurcation

Acknowledgements

The success of this thesis is contributed greatly by my advisor, Ajarn Thawatchai Onjun. His ideas, suggestions and lessons as well as our discussions lead me to the right direction. I also would like to thank Yanick Sarazin and Frederick Imbeaux for their help and advice during my time at CEA, Cadarache. I am grateful for all the questions and comments from my thesis committee. These help me to improve myself.

I thank all the friends in PFRU lab, SIIT, for their help, suggestion and entertainment. It is good to relax and recharge yourself when work is overloaded. I also want to acknowledge Natee who found out an interesting result, which I continue on. Importantly, this thesis cannot be completed at all if I do not get motivation and support from my family. Thank you so much my lovely wife and my funny son, Anna and Anton. Thank you for understanding that sometimes I have to work hard. Thank you for always be there for me. I also want to thank my parents for being the great examples, without them I would not even continue my study and my life would be completely different.

Respectfully, I want to thank those whom I forget to mention names, every bit of their contribution to my success are always recognized and valued. At last, I want to express my gratitude toward the Royal Thai Scholarship for supporting my education all these years. This work was supported by the Commission on Higher Education (CHE) and the Thailand Research Fund (TRF) under Contract No.RSA5580041, Thailand Institute of Nuclear Technology and Bangchak Petroleum PCL (Low Carbon scholarship).

Mr. Boonyarit Chatthong

Accomplishments

Publications included in this thesis:

- **B. Chatthong** and T. Onjun. "Simulations of ITER with the Presence of ITB using NTV Intrinsic Toroidal Rotation Model", *Nuclear Fusion* **53** 1 (2013) 013007
- **B. Chatthong** and T. Onjun. "Comparison of H-mode plasma simulations using toroidal velocity models depending on plasma current density and ion temperature in presence of an ITB", *Songklanakarin J. Sci. Technol.*, **36**(3) (2014) 375-387
- **B. Chatthong** and T. Onjun. "Investigation of toroidal flow effects on L-H transition in tokamak plasma based on bifurcation model", *Journal of Physics: Conference Series*, **611**(1) (2015) 012003
- **B. Chatthong** and T. Onjun. "Locality Effects on Bifurcation Paradigm of L-H Transition", accepted for publication in Songklanakarin Journal of Science and Technology (2015)
- **B. Chatthong** and T. Onjun. "Analysis of Transport Barriers Formation and Properties in Tokamak Plasma using Bifurcation Concept", submitted to Nuclear Fusion
- **B. Chatthong** and T. Onjun. "Study of L-H Transition and Pedestal Width Based on 2 Fields Bifurcation and Fixed Point Concept", accepted for publication in Acta Polytechnica (2015)

Publications not included in this thesis:

- Y. Pianroj, S. Jumrat, **B. Chatthong** and T. Onjun. "A Full Radial Electric Field Calculation for Predicting Pedestal Formation in H-mode Tokamak Plasma by using BALDUR code", *Thammasat Int. J. Sc. Tech.*, **19**(2) (2014) 63-70
- P. Intharat, **B. Chatthong**, T. Onjun, N. Poolyarat, and R. Picha. "The investigation of L-H transition using MMM95 transport model", *Journal of Physics: Conference Series*, **611**(1) (2015) 012005

Conference:

- **T. Onjun, B. Chatthong, R. Picha, N. Poolyarat, and J. Prompting.** "Transport Barriers Formation and Properties Study Based on Bifurcation Concept", in 42nd EPS (European Physical Society) Conference on Plasma Physics (EPS2015), 22-26 June 2015, Lisbon, Portugal (2015) P2.177
- **T. Onjun, B. Chatthong, R. Picha and N. Poolyarat.** "Analysis of ITB and ETB Formations in Tokamak Plasma Using Bifurcation Concept", in 25th IAEA Fusion Energy Conference (FEC2014), 13-18 October 2014, Saint Petersburg, Russia (2014) TH/P6-8
- **B. Chatthong, R. Picha, N. Poolyarat, and T. Onjun.** "Investigation of Toroidal Flow Effects on *L-H* Transition in Tokamak Plasma Based on Bifurcation Model", in 1st International Science and Technology Conference (INST2014), 28-30 August 2014, Bangkok, Thailand (2014) PHY-0 038
- **J. Prompting, W. Kanjanaput, W. Buangam, B. Chatthong, R. Picha, N. Poolyarat, Y. Pianroj, and T. Onjun.** "Simulation of Plasma Performance of the Tokamak DEMO Nuclear Fusion Reactors Design", in 1st International Science and Technology Conference (INST2014), 28-30 August 2014, Bangkok, Thailand (2014) PHY-P 095
- **P. Intharat, B. Chatthong, T. Onjun, N. Poolyarat and R. Picha.** "Investigation of *L-H* Transition in Tokamak Plasma Using BALDUR Code", in 1st International Science and Technology Conference (INST2014), 28-30 August 2014, Bangkok, Thailand (2014) PHY-0 042
- **K. Wihakhaphirom, B. Chatthong, R. Picha, N. Poolyarat, and T. Onjun.** "Study of Pellet Injection Effects on Transport Barrier Formation and Pedestal Width Using Bifurcation Concept", in 1st International Science and Technology Conference (INST2014), 28-30 August 2014, Bangkok, Thailand (2014) PHY-P 037
- **B. Chatthong, K. Wihakhaphirom, R. Picha, N. Poolyarat, J. Prompting, and T. Onjun.** "Investigation of ETB Formation, Pedestal Width and Dynamics Based on Bifurcation Concept", in 41st EPS (European Physical Society) Conference on Plasma Physics (EPS2014), 23-27 June 2014, Berlin, Germany (2014) P4.065

- W. Kanjanaput, B. Kitpitak, **B. Chatthong**, J. Promping, N. Poolyarat, R. Picha, and T. Onjun. "The Behaviours of Plasma during Pellet Injection Using Sandpile Model", in 41st EPS (European Physical Society) Conference on Plasma Physics (EPS2014), 23-27 June 2014, Berlin, Germany (2014) P4.064
- W. Buangam, S. Dangkong, J. Promping, **B. Chatthong**, T. Onjun, N. Poolyarat, and R. Picha. "Behaviors of Impurity in ITER using BALDUR code", in 41st EPS (European Physical Society) Conference on Plasma Physics (EPS2014), 23-27 June 2014, Berlin, Germany (2014) P5.011
- **B. Chatthong**, R. Picha, N. Poolyarat, and T. Onjun. "Study of Bifurcation Based L-H Transition Using Fixed Points Stability Analysis", in 26th Symposium on Plasma Physics and Technology (SPPT2014), 16-19 June 2014, Czech Technical University in Prague, Prague, Czech Republic (2014)
- **B. Chatthong**, N. Poolyarat, R. Picha, and T. Onjun. "Bifurcation Behavior Analysis for Internal Transport Barrier Formation in Tokamak Plasma", in Siam Physics Congress (SPC2014), "High-Speed Physics", 26-29 March 2014, Nakhon Ratchasima, Thailand (2014)
- P. Intharat , **B. Chatthong**, N. Poolyarat, R. Picha, and T. Onjun. "Bifurcation Behavior Study of L-H Transition in Tokamak Plasmas using BALDUR Code", in Siam Physics Congress (SPC2014), "High-Speed Physics", 26-29 March 2014, Nakhon Ratchasima, Thailand (2014)
- **B. Chatthong**, T. Onjun, N. Poolyarat, and R. Picha. "Numerical Approach Based on Bifurcation Concept for Explanation of Intrinsic L-H-L Transitions Behaviors in Tokamak Plasmas", in the 18th International Annual Symposium on Computational Science and Engineering (ANSCSE18), 17 - 19 March 2014, Pattaya, Thailand (2014)
- P. Intharat , **B. Chatthong**, T. Onjun, N. Poolyarat, and R. Picha. "The Investigation of L-H Transition in Tokamak Plasmas using BALDUR Code", in the 18th International Annual Symposium on Computational Science and Engineering (ANSCSE18), 17 - 19 March 2014, Pattaya, Thailand (2014)
- Y. Pianroj, **B. Chatthong**, T. Onjun, W. Werapun, J. Promping, and R. Picha. "A Prediction of Pedestal Formation in H-Mode Tokamak Plasma by Using The Full Calculation of The Radial Electric Field in BALDUR Code", in the

4th TSME International Conference on Mechanical Engineering (TSME-ICoME2013), 16-18 October 2013, Pattaya, Chonburi, Thailand (2013)

- **B. Chatthong**, T. Onjun, R. Picha, and N. Poolyarat. "Study of L-H-L Transitions, Hysteresis and Effects of Pellet and Heat Injections Using Bifurcation Concept", in 3rd Asia Pacific Transport Working Group (APTWG) International Conference, 21-24 May 2013, Hyatt Regency Hotel, Jeju Island, South Korea (2013)
- **B. Chatthong** and **T. Onjun**. "Understanding of L-H Transitions in Tokamak Plasmas Using Bifurcation Concept", in Siam Physics Congress (SPC2013), "Thai Physics Society on the Road to ASEAN Community", 21-23 March 2013, Chiang Mai, Thailand (2013)
- **B. Chatthong**, Y. Yotharak, T. Onjun, R. Picha, and N. Poolyarat. "Analytical Study of L-H Transition and Transition Criteria Using Bifurcation Concept", in 2012 International Symposium on Technology for Sustainability (ISTS2012), 21-24 November 2012, Swissotel Le Concorde, Bangkok, Thailand (2012)
- **B. Chatthong**, Y. Yotharak, T. Onjun, R. Picha and N. Poolyarat. "The Bifurcation and Hysteresis of L-H Transition in Plasmas", in The 38th Congress on Science and Technology of Thailand (STT38), "Science for the Future of Mankind", 17-19 October 2012, Chiang Mai University, Chiang Mai, Thailand (2012)
- **B. Chatthong**, T. Onjun, R. Picha, and N. Poolyarat. "Study of L-H Transition in the Plasma Based on Bifurcation Concept", in IWPSA 2012 International Workshop on Plasma Science & Applications, 4-5 October 2012, Chulalongkorn University, Bangkok, Thailand (2012)
- **B. Chatthong**, T. Onjun, N. Poolyarat, and R. Picha. "Effects of Thermal and Particle Sources on L-H Transition and Plasma Profiles", in Siam Physics Congress (SPC2012), "Past, Present and Future of Physics", 9-12 May 2012, Ayutthaya, Thailand (2012)
- **B. Chatthong**, T. Onjun, R. Picha, and N. Poolyarat. "Impact of Toroidal Flow on ITB H-Mode Plasma Performance in Fusion Tokamak", in the 2nd TSME

International Conference on Mechanical Engineering (TSME-ICoME2011), 19-21 October 2011, Krabi, Thailand (2011) ETM15

- **B. Chatthong**, T. Onjun, Y. Sarazin, F. Imbeaux, A. Strugarek, R. Picha, and N. Poolyarat. "Study of Hysteresis for L-H Transition Using Coupled 2-Field Bifurcation Model", in 13th International workshop on *H*-mode physics and transport barriers, 10-12 October 2011, Oxford, UK (2011)
- **B. Chatthong**, T. Onjun, R. Picha, and N. Poolyarat. "Self-Consistent Simulations of ITER with NTV Toroidal Rotation Model in BALDUR Code", in 13th International workshop on *H*-mode physics and transport barriers, 10-12 October 2011, Oxford, UK (2011)
- **B. Chatthong**, T. Onjun, F. Imbeaux, Y. Sarazin, A. Strugarek, R. Picha and N. Poolyarat. "Study of Heat Flux Threshold and Perturbation Effect on Transport Barrier Formation Based on Bifurcation Model", in the 12th Conference on Nuclear Science and Technology (NST12), "Half Century and Upcoming Decades of Nuclear Thailand", 1-2 July 2011, Bangkok, Thailand (2011)
- **B. Chatthong**, Y. Sarazin, T. Onjun, N. Wongsrisujarit, F. Imbeaux, A. Strugarek, R. Picha, and N. Poolyarat "Numerical Study of L-H Transition Using Bifurcation Approach", in the 1st Asia Pacific Transport Working Group (APTWG) International Conference, 14-17 June 2011, Toki-City, Gifu, Japan (2011)
- **B. Chatthong**, Y. Sarazin, T. Onjun, N. Wongsrisujarit, F. Imbeaux, A. Strugarek, R. Picha, and N. Poolyarat "Analytical and Numerical Modelling of Transport Barrier Formation Using Bifurcation Concept", in European 38th EPS (European Physical Society) Conference on Plasma Physics (EPS2011), 27 June - 1 July 2011, Strasbourg, France (2011) P4.097
- **B. Chatthong**, T. Onjun, F. Imbeaux, J.F. Artaud, R. Picha, and N. Poolyarat "Study of ITB Plasmas using CRONOS Integrated Tokamak Predictive Modeling Codes", in the 15th International Annual Symposium on Computational Science and Engineering (ANSCSE15), 30 March - 1 April 2011, Bangkok University, Thailand (2011)

- **B. Chatthong**, T. Onjun, R. Picha, N. Poolyarat, F. Imbeaux, Y. Sarazin, and A. Strugarek "The Formation of Transport Barrier in Tokamak Plasmas", in Siam Physics Congress (SPC2011), "Physics for all, all for physics", 23-26 March 2011, Pattaya, Chon Buri, Thailand (2011)
- N. Poolyarat, Y. Pianroj, **B. Chatthong**, T. Onjun, and A. Fukuyama. "Core-Edge Simulations of H-Mode Tokamak Plasmas using BALDUR and TASK Codes", in 23rd IAEA Fusion Energy Conference (FEC2010), 11-16 October 2010, Daejeon, Republic of Korea (2010) THC/P4-23
- Y. Pianroj, **B. Chatthong**, T. Onjun, and N. Poolyarat. "Core-edge simulations of H-mode Tokamak plasma using BALDUR codes", in 1st International Youth Conference on Fusion Energy (IYC2010), 9-10 October 2010, Daejeon, Republic of Korea (2010) FEC2010-0079

Table of Contents

Chapter	Title	Page
	Signature Page	i
	Abstract	ii
	Acknowledgements	iv
	Accomplishments	v
	Table of Contents	xi
	List of Tables	xvi
	List of Figures	xvii
1	Introduction	1
	1.1 Fusion energy	1
	1.1.1 Plasma	2
	1.1.2 Fusion reactions	3
	1.1.3 Tokamaks	5
	1.1.4 Development of fusion research	9
	1.2 Motivation, research concept and outline of the thesis	10
	1.3 Objectives	13
	1.4 Scope of research	13
	1.5 Research procedure	13
2	Literature Review	15
	2.1 Transport barriers	15
	2.1.1 <i>L-H</i> transition and formation of ETB	16
	2.1.2 Formation of ITB	19
	2.1.3 Causes of transport barriers	20

2.1.3.1	Radial velocity shear	20
2.1.3.2	Magnetic shear	22
2.1.3.3	Safety factor	23
2.2	Bistable s -curve bifurcation model	24
2.3	Integrated predictive modeling code	26
2.3.1	Description of BALDUR	28
2.3.1.1	Boundary conditions	29
2.3.1.2	Initial conditions	29
2.3.1.3	Description of physics used in BALDUR	29
2.3.2	BALDUR transport modules	30
2.3.2.1	Mixed Bohm/gyro-Bohm module	30
(a)	Bohm term	31
(b)	Gyro-Bohm term	32
(c)	Mixed Bohm/Gyro-Bohm model	32
2.3.2.2	NCLASS module	33
2.3.2.3	Pedestal module	34
2.3.2.4	Toroidal velocity module	35
3	Locality Effects on Bifurcation Paradigm of L - H Transition	37
3.1	Introduction	37
3.2	Bifurcation concepts and transition points	38
3.3	Locality effects on L - H transition and hysteresis	42
3.3.1	Transition criteria	42
3.3.2	Backward transition and hysteresis properties	45
3.3.3	Stability diagram	48
3.4	Conclusion	49
4	Study of L - H Transition and Pedestal Width Based on 2 Fields	50
	Bifurcation and Fixed Point Concepts	
4.1	Introduction	50

4.2 Bifurcation model and fixed points analysis	50
4.3 Numerical results and discussions	54
4.3.1 Pedestal dynamics	55
4.3.2 Pedestal width	58
4.4 Conclusion	63
5 Analysis of Hysteresis Properties in Tokamak Plasma Based on Bifurcation Concepts	64
5.1 Introduction	64
5.2 Transport equations and bifurcation diagrams	65
5.3 Hysteresis depth analysis	69
5.3.1 Effects of thermal transports	69
5.3.2 Effects of particle transport	73
5.3.3 Effects of critical gradient thresholds	76
5.3.4 Effects of sources	79
5.4 Plasma gradients at the transitions	81
5.5 Conclusion	90
6 Analysis of Transport Barriers Formation and Properties in Tokamak Plasma Using Bifurcation Concept	91
6.1 Introduction	91
6.2 Modeling of plasma transport based on bifurcation concept	91
6.3 Plasma profiles and bifurcation behavior	93
6.4 Sensitivity analysis	98
6.4.1 Effects of heat and particle sources	98
6.4.2 Effects of transport strength	104
6.4.3 Effects of current drive location	109
6.5 Conclusion	110

7	Toroidal Rotation Effects on <i>L-H</i> Transition Based on Bifurcation Concept	112
7.1	Introduction	112
7.1.1	Simulation procedure	114
7.2	Simulations of ITER with the presence of ITB using NTV intrinsic toroidal rotation model	116
7.2.1	NTV toroidal rotation model	116
7.2.2	Results and discussion	117
7.2.2.1	Plasma profiles and ITER performance	118
7.2.2.2	ITB analysis	122
7.2.2.3	Sensitivity study	128
(a)	Line average density	128
(b)	Auxiliary power	130
(c)	Effective charge number	131
(d)	Strength of the toroidal rotation	132
7.2.3	Conclusion	133
7.3	Comparison of <i>H</i> -mode plasma simulations using toroidal velocity models depending on plasma current density and ion temperature in presence of an ITB	134
7.3.1	Models for predictive toroidal velocity	134
7.3.1.1	Current density dependent approach	134
7.3.1.2	Ion temperature dependent approach	135
7.3.2	Results and discussion	135
7.3.2.1	JET simulations	135
(a)	Comparison	136
(b)	Simulation profiles	138
(c)	ITB formation	143
7.3.2.2	ITER predictions	145
(a)	ITER performance and ITB effect	145
(b)	Test for plasma ignition	150

7.3.3 Conclusion	152
7.4 Investigation of toroidal flow effects on L - H transition in tokamak plasma based on bifurcation model	153
7.4.1 Bifurcation concept and toroidal velocity models	154
7.4.1.1 Two-field bifurcation model	154
7.4.1.2 Toroidal velocity models	155
7.4.2 Numerical results and discussions	156
7.4.2.1 Plasma response on profile and pedestal width	156
7.4.2.2 Pedestal dynamics	158
7.4.3 Conclusion	160
8 Summary and Recommendations	162
8.1 Summary	162
8.2 Recommendations for future work	163
References	163
Appendices	182
Appendix A: Abbreviations and notations	183
Biography	187

List of Tables

Tables	Page
1.1 Design ITER parameters and performance capabilities	8
1.2 Milestones in Fusion Research	10
5.1 Changes of pressure gradients and their ratios at $L-H$ transition and $H-L$ back transition as a function of model parameters illustrated as ratio to the lowest value	82
5.2 Changes of density gradients and their ratios at $L-H$ transition and $H-L$ back transition as a function of model parameters illustrated as ratio to the lowest value	83
6.1 Heating effects on plasma pressure and transport barriers	101
6.2 Effects of current density peaking location on plasma pressure and transport barriers	110
7.1 Standard type I ELMy H -Mode ITER design engineering parameters	117
7.2 Average values of central ion temperature, central electron density and alpha power for each simulation during stationary state	129
7.3 Summary of plasma parameters for 10 JET optimized shear discharges during their diagnostic time	136

List of Figures

Figures	Page
1.1 Schematic view of tokamak	5
1.2 Cross-section of tokamak plasma	7
2.1 Illustration of pressure, density and temperature profiles as a function of plasma minor radius, the shaded area indicates region of ETB	16
2.2 Illustration of current density and safety factor profiles for center peak (left) and off-center peak (right) currents	22
2.3 Illustration of bifurcation diagram	24
2.4 Schematic structure of integrated predictive modeling code	27
2.5 Plot of temperature profile near the edge of H -mode plasmas	33
3.1 Fixed points for each value of heat flux and their stabilities: solid dot for stable, open dot for unstable and semi-open dot for half-stable fixed points	40
3.2 Bifurcation diagram constructed from fixed points illustrating 2 stable branches and 1 unstable branch with $L-H$ and $H-L$ transitions	41
3.3 Bifurcation diagram at different values of critical gradient	45
3.4 Effects of critical pressure gradient on the pressure gradient (top left) and threshold flux (top right) at $L-H$ transition and effects of anomalous (bottom left) and neoclassical (bottom right) transport coefficients on the threshold limit of the critical pressure gradient	46
3.5 Hysteresis depth as a function of neoclassical transport	46
3.6 Hysteresis depth as a function of anomalous transport	47
3.7 Hysteresis depth as a function of m	48
3.8 Fixed points for each value of heat flux and its stability	49
4.1 Fixed points for each value of heat/particle flux and their stabilities: solid dot for stable, open dot for unstable, and semi-open dot for half-stable fixed points	52
4.2 Bifurcation diagram illustrating 2 stable branches and 1 unstable branch with $L-H$ and $H-L$ transitions	53
4.3 Bifurcation diagram of pressure field at different values of particle flux	54
4.4 Plasma density (top) and pressure (bottom) profiles as a function of	55

normalized minor radius at times 200 ms apart	
4.5 Pressure (top) and density (bottom) pedestal widths as a function of time for constant sources (horizontal line) scenario	57
4.6 Pressure (top) and density (bottom) pedestal widths as a function of time for heat ramping scenario	57
4.7 Pedestal width and central pressure and density at steady state as a function of heat source	58
4.8 Pedestal width and central pressure and density at steady state as a function of particle source	59
4.9 Pedestal width and central pressure and density at steady state as a function of thermal anomalous transport	60
4.10 Pedestal width and central pressure and density at steady state as a function of particle anomalous transport	61
4.11 Pedestal width and central pressure and density at steady state as a function of thermal neoclassical transport	62
4.12 Pedestal width and central pressure and density at steady state as a function of particle neoclassical transport	62
5.1 Bifurcation diagrams for pressure field (top) and density field (bottom) illustrating $L-H$ and $H-L$ back transitions	68
5.2 Hysteresis depth in pressure field as a function of thermal anomalous transport coefficient proportional constant	71
5.3 Hysteresis depth in density field as a function of thermal anomalous transport coefficient proportional constant	71
5.4 Hysteresis depth in pressure field as a function of thermal neoclassical transport coefficient	73
5.5 Hysteresis depth in density field as a function of thermal neoclassical transport coefficient	73
5.6 Hysteresis depth in pressure field as a function of particle anomalous transport coefficient proportional constant	74
5.7 Hysteresis depth in density field as a function of particle anomalous transport coefficient proportional constant	75
5.8 Hysteresis depth in pressure field as a function of particle neoclassical	76

transport coefficient	
5.9 Hysteresis depth in density field as a function of particle neoclassical transport coefficient	76
transport coefficient	
5.10 Hysteresis depth in pressure field as a function of critical pressure gradient	77
5.11 Hysteresis depth in density field as a function of critical pressure gradient	78
5.12 Hysteresis depth in pressure field as a function of critical density gradient	79
5.13 Hysteresis depth in density field as a function of critical density gradient	79
5.14 Hysteresis depth in pressure field as a function of particle flux	80
5.15 Hysteresis depth in density field as a function of heat flux	81
5.16 Pressure gradient changes at $L-H$ (left) and $H-L$ (right) transitions as a function of thermal anomalous transport coefficient proportional constant	83
5.17 Density gradient changes at $L-H$ (left) and $H-L$ (right) transitions as a function of thermal anomalous transport coefficient proportional constant	84
5.18 Pressure gradient changes at $L-H$ (left) and $H-L$ (right) transitions as a function of thermal neoclassical transport coefficient	84
5.19 Density gradient changes at $L-H$ (left) and $H-L$ (right) transitions as a function of thermal neoclassical transport coefficient	85
5.20 Pressure gradient changes at $L-H$ (left) and $H-L$ (right) transitions as a function of particle anomalous transport coefficient proportional constant	85
5.21 Density gradient changes at $L-H$ (left) and $H-L$ (right) transitions as a function of particle anomalous transport coefficient proportional constant	86
5.22 Pressure gradient changes at $L-H$ (left) and $H-L$ (right) transitions as a function of particle neoclassical transport coefficient	86
5.23 Density gradient changes at $L-H$ (left) and $H-L$ (right) transitions as a function of particle neoclassical transport coefficient	87
5.24 Pressure gradient changes at $L-H$ (left) and $H-L$ (right) transitions as a function of critical pressure gradient	87
5.25 Density gradient changes at $L-H$ (left) and $H-L$ (right) transitions as a function of critical pressure gradient	88
5.26 Pressure gradient changes at $L-H$ (left) and $H-L$ (right) transitions as a function of critical density gradient	88

5.27 Density gradient changes at $L-H$ (left) and $H-L$ (right) transitions as a function of critical density gradient	89
5.28 Pressure gradient changes at $L-H$ (left) and $H-L$ (right) transitions as a function of particle flux	89
5.29 Density gradient changes at $L-H$ (left) and $H-L$ (right) transitions as a function of heat flux	90
6.1 Plasma pressure (top left) and density (top right) as a function of normalized minor radius x/a for setup scenarios 1 (thick line) and 2 (thin line), and the results mapped onto heat flux versus pressure gradient (bottom left) and particle flux versus density gradient (bottom right)	94
6.2 Plasma pressure (top left) and density (top right) as a function of normalized minor radius x/a for setup scenarios 3 (thick line) and 4 (thin line), and the results mapped onto heat flux versus pressure gradient (bottom left) and particle flux versus density gradient (bottom right)	95
6.3 Plasma pressure (top left) and density (top right) as a function of normalized minor radius x/a for setup scenarios 5 (thick line) and 6 (thin line), and the results mapped onto heat flux versus pressure gradient (bottom left) and particle flux versus density gradient (bottom right)	96
6.4 Profiles of magnetic shear (top) and suppression function (bottom) as a function of normalized minor radius x/a for setup scenarios 1 to 6; the heat source profile is also shown as dashed line	97
6.5 Comparison of plasma pressure gradient as a function of normalized minor radius x/a for setup scenarios 1 and 2 (top left), 3 and 4 (top right), 5 and 6 (bottom left) and 3 and 5 (bottom right)	98
6.6 Central pressure (top) and density (bottom) contour field plots with x-axis as location of current density peaking and y-axis as heat/particle flux over critical threshold ratios	100
6.7 Pedestal width (top) and ITB width (bottom) as a function of heat flux	102
6.8 Bootstrap current fraction of total current as a function of heating at various location of driving current peaking (top) and pressure (bottom left) and density (bottom right) profiles as a function of normalized radius at different heating and driving current peaking at $x_0 = 0.2$	103

6.9 Pedestal width (top left), ITB width (top right) and central plasma values (middle left) as a function of thermal anomalous transport strength (diamond is for pressure and square is for density), heat flux versus pressure gradient (middle right) and radial profiles of pressure (bottom left) and density (bottom right) at different values of thermal anomalous transport 104

6.10 Pedestal width (top left), ITB width (top right) and central plasma values (middle left) as a function of particle anomalous transport strength (diamond is for pressure and square is for density), heat flux versus pressure gradient (middle right) and radial profiles of pressure (bottom left) and density (bottom right) at different values of particle anomalous transport 106

6.11 Pedestal width (top left), ITB width (top right) and central plasma values (middle left) as a function of thermal neoclassical transport strength (diamond is for pressure and square is for density), heat flux versus pressure gradient (middle right) and radial profiles of pressure (bottom left) and density (bottom right) at different values of thermal neoclassical transport 108

6.12 Pedestal width (top left), ITB width (top right) and central plasma values (middle left) as a function of particle neoclassical transport strength (diamond is for pressure and square is for density), heat flux versus pressure gradient (middle right) and radial profiles of pressure (bottom left) and density (bottom right) at different values of particle neoclassical transport 109

7.1 Profiles of ion (top left) and electron temperatures (top right), and ion (bottom left) and electron densities (bottom right) at stationary state ($t = 2,600$ s). Each line represents simulation results using empirical model (solid), model based on NTV (dash-dot), and no-value (dot) for toroidal rotation calculation 118

7.2 Toroidal velocity (solid) and the value of Heaviside step function (dash) profiles at 2600 s obtained from the simulation using NTV toroidal velocity model 120

7.3 Toroidal velocity (top left), flow shear (top right), and ion and electron thermal diffusivities (bottom) profiles at stationary state ($t = 2,600$ s) obtained from the simulation using NTV toroidal velocity model 121

7.4 Toroidal velocity (dash) and ion temperature (solid) profiles at stationary state; 2600 s (top) and 2,900 s (bottom) obtained from the simulation using NTV toroidal velocity model	123
7.5 Ion temperature gradient image plot, darker region implying higher gradient obtained from the simulation using NTV toroidal velocity model	124
7.6 Total current density (top left), bootstrap current density (top right), safety factor (bottom left) and magnetic shear (bottom right) profiles at stationary state ($t = 2,600$ s). Each line represents simulation results with empirical model (solid), model based on NTV (dash-dot), and no-value (dot) for toroidal rotation calculation	125
7.7 Ion temperature profiles as a function of normalized minor radius at various times illustrating the dynamic of ITB obtained from the simulation using NTV toroidal velocity model	126
7.8 Toroidal velocity and temperature gradients evolution profiles near location of ITB obtained from the simulation using NTV toroidal velocity model	127
7.9 Radial electric field, its components, and flow shear profile as a function of normalized minor radius from the simulation using NTV toroidal velocity model	127
7.10 Ion temperature (top left), ion density (top right), toroidal velocity (bottom left), and flow shear (bottom right) profiles at stationary state ($t = 2,600$ s) obtained from the simulation using NTV toroidal velocity model. Each line represents simulation results with different values of line average density	129
7.11 Ion temperature (top left), ion density (top right), toroidal velocity (bottom left), and flow shear (bottom right) profiles at stationary state ($t = 2,600$ s) obtained from the simulation using NTV toroidal velocity model. Each line represents simulation results with different values of auxiliary power	131

7.12 Ion temperature (top left), ion density (top right), toroidal velocity (bottom left), and flow shear (bottom right) profiles at stationary state ($t = 2,600$ s) obtained from the simulation using NTV toroidal velocity model. Each line represents simulation results with different values of effective charge number	132
7.13 Profile plot of toroidal velocity v_ϕ (solid) together with toroidal current density J_ϕ (dashed) as a function of r/a for JET 40847 discharge at the diagnostic time	134
7.14 Comparison of toroidal velocity v_ϕ between experimental values (dots) and simulation results using ion temperature T_i dependent (solid-triangle) and current density J_ϕ dependent (solid) models for JET discharges 40542 (top) and 40847 (bottom) during their diagnostic time	137
7.15 RMSE deviations of 10 JET discharges and their average for toroidal velocity v_ϕ using current density J_ϕ dependent (solid bars) and ion temperature T_i dependent (striped bars) models	138
7.16 JET 40847 (left) and 52009 (right) time-evolution profiles of ion temperature T_i (top), electron temperature T_e (middle), and electron density n_e (bottom): experimental data (dots) simulation results using current density J_ϕ dependent (dashed) and ion temperature dependent (solid) models at the center (dark) and edge (gray) of the plasma	140
7.17 RMS deviations of 10 JET discharges and their averages for ion temperature T_i , electron temperature T_e , and electron density n_e simulation results using current density J_ϕ dependent (dark) and ion temperature T_i dependent (gray) models	142
7.18 Contour plots of ion temperature gradient ∇T_i profile of JET discharges 4664 (left) and 53532 (right): experimental results (top) and simulation results using current density J_ϕ dependent (middle) and ion temperature T_i dependent (bottom) models	144

7.19 Comparison of ITER performance (for ion temperature T_i , electron temperature T_e , deuterium density n_D , tritium density n_T , beryllium density n_{Be} , and helium density n_{He}) between simulations with ITB (both current density and ion temperature dependent models) and without ITB effect during steady state ($t = 2700$ s)	145
7.20 Time-evolution plots of central ion temperature T_i (top), total fusion power output W_{tot} (middle), and alpha power P_α (bottom) for simulations with ITB (both current density J_ϕ and ion temperature T_i dependent models) and without ITB effect during steady state ($t = 2700$ s)	147
7.21 Contour plots of ion temperature gradient ∇T_i profile of ITER simulations: simulation results using current density J_ϕ dependent (top) and ion temperature T_i dependent (bottom) models	149
7.22 Toroidal velocity v_ϕ and flow shear ω_{ExB} profiles of simulations results for current density J_ϕ dependent (solid) and ion temperature T_i dependent (dashed) models during steady state ($t = 2700$ s)	150
7.23 Time-evolution plots of central ion temperature T_i (top), total fusion power output W_{tot} (middle), and alpha power P_α (bottom) for simulations with ITB (both current density J_ϕ and ion temperature T_i dependent models) and without ITB effect during steady state ($t = 2700$ s), auxiliary heating is turned off after 2000 s	151
7.24 ITER performance simulations (for ion temperature T_i , electron temperature T_e , deuterium density n_D , tritium density n_T , beryllium density n_{Be} , and helium density n_{He}) with ITB (both current density and ion temperature dependent models) and without ITB effect at time after auxiliary heating is turned off ($t = 2400$ s)	152
7.25 Plasma core profiles for pressure (top left) and density (top right), and plasma edge profiles for pressure (bottom left) and density (bottom right) at steady state. Each line represents simulation results without toroidal flow (thin solid), using model a (thin dashed), model b (thick solid), model c (thick dashed) and model d (dotted)	157

7.26 Profiles of radial electric field (solid), pressure gradient term (dashed) 158
and toroidal rotation term (dotted) at steady state for simulations using model
a(top left), b (top right), c (bottom left) and d (bottom right)

7.27 Time evolution of pedestal width of pressure (top) and density (bottom) 160
channels



Chapter 1

Introduction

1.1 Fusion energy

It is clear that global energy demand has increased every year. This is largely due to an increase of the world population and the advancement of technology and industry. In 2006, the United Nations has released data showing that the world population has been continuously increasing every year. For example, in 1950, it was just over 2 billion people. The projection models predict that the world population could be up to 12 billion people in 2050 [1]. Currently, the main energy sources for supporting human's lives and their activities are fossil fuels, like oil, natural gas and coal [2]. Regrettably, these sources will not last forever. Based on the present consumption rate, the available reserves of oil, coal and natural gas will only last for about 30 years, 200 years and 60 years, respectively [3]. Additionally, burning fossil fuels pollutes our environment because of carbon dioxide released during burning process, which leads to global warming [4]. Therefore, the scientific community has aimed their research on the hunt for new kinds of alternative energy sources, in which nuclear fusion energy is one of the possible solutions.

There are several advantages of fusion energy over other kinds of alternative energy source. Firstly, the energy per mass yielded for fusion reaction is much higher than other energy types that human can harvest including nuclear fission energy. This fusion reaction is likely to be based on deuterium-tritium (DT) reaction and the reasons will be explained shortly. Deuterium, a heavier isotope of hydrogen, can be found in sea water. It can be separated from hydrogen by the use of electrolysis process. Tritium can be produced via reactions with lithium as one of the sources. Approximately, one kilogram of deuterium can generate 3×10^5 GJ of energy and one kilogram of lithium can produce 10^{15} GJ of electricity. These numbers are immense comparing to the present day consumption rate of 3×10^{11} GJ per year [5]. Secondly, the nuclear fusion fuels will last over lifetime of human because the sources are abundant on Earth. There is roughly 10^{15} tons of deuterium available in the ocean and lithium is widely available. The broad availability of fusion fuels means that every

country with access to sea water can use it. Lastly, fusion production is rather environmental friendly because it does not produce global warming gas like carbon dioxide or other toxic gases. Furthermore, unlike fission production, radioactive waste from fusion is not a long-term problem. Tritium is radioactive but its half-life is only of 12 years. The structure of a fusion reactor can also become radioactive by neutron activation process because of the neutron bombardment. After the end of reactor's lifetime it needs to be shielded for about 100 years. As oppose to nuclear fission reactor, there is no real burden problem for future generation. Lastly, fusion reaction is inherently safe because it is not a chain reaction and its core volume contains about atmospheric pressure so there will not be enough stored energy to cause any damage in case of accidents.

To produce and sustain nuclear fusion reaction, high temperature and long enough energy confinement is needed. The temperature required for fusing two nuclei is very high (about millions of degree Celsius) that the state of matters becomes plasma.

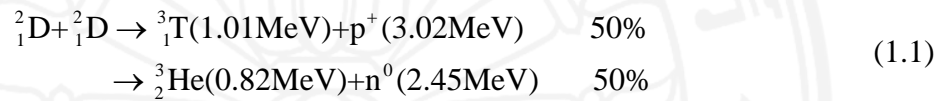
1.1.1 Plasma

When a gas is heated to sufficiently high temperature, all electrons are fully ionized and the gas breaks up into a mixture of negatively charged electrons and positively charged ions. A material in this state is called plasma. Plasma has many properties of a normal gas, for example it can be described by particle density and temperature as macro-characteristics. Nevertheless, plasma has two important characteristic properties. First, electric charge densities of electrons and protons are so large that a separation of them would lead to a very large restoring force. Hence, the global ion and electron charge densities in plasma tend to be equal. Second, it has the ability to carry a current as a result of a relative drift between the ions and electrons. System with plasma is very complicated because it is like a gas with charge. Physically, charged particles are known to be able to travel freely parallel to magnetic field. On the other hand, they circles around the magnetic field in perpendicular direction. The combination of the two motions results in Larmor orbits, which is a helical path around the field line. Plasma can be confined by introducing magnetic

field. It is possible to arrange the magnetic field configuration to contain plasma particles in a system.

1.1.2 Fusion reactions

Fusion reaction is a process in which two light atoms combine to form heavier atom. Typically, the total input mass is more than total output mass and the difference turns into energy according to Einstein's mass-energy equivalence. In order to merge atomic nuclei together one needs strong enough attracting force or high enough energy to overcome electrostatic repulsive force (Coulomb's potential). Two nuclei can fuse to produce nuclear fusion reaction. Equations (1.1) - (1.3) show examples of fusion reactions [5]:

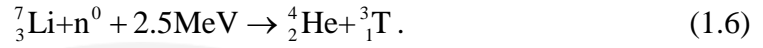
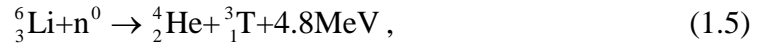


Because the total mass of the sources is larger than that of the products, the difference in mass is turned into energy by Einstein's mass-energy equivalence:

$$\Delta E = \Delta mc^2, \quad (1.4)$$

where ΔE is the energy generated, Δm is the difference in mass, and c is the speed of light. There are many fusion reactions known to exist but for the purpose of this research, two reactions are focused on: deuterium-deuterium (DD) and deuterium-tritium reactions. The reason is because some conditions are required for fusion reactions to be viable, for example the reactions must be exothermic and the sources must be low charged nuclei to avoid strong Coulomb potential. The two reactions are showed in equations (1.1) and (1.2). DT reaction produces helium ion (α particle) and neutron with total energy of 17.6 MeV per reaction. Whereas, DD reaction can produce two different results with equal probability, one is helium-3 and neutron with total energy of 3.27 MeV per reaction and another one is tritium and proton with total energy of 4.03 MeV per reaction [6]. The additional benefit of using deuterium and tritium as fusion sources is their abundance on Earth. Deuterium can be mined from sea water using electrolysis method. They are left from cosmological processes since

the creation of the Earth. There is roughly 1 deuterium in every 7000 hydrogen atoms in water. Tritium is produced by bombarding lithium with neutron [5],



There is enough resource of lithium and deuterium to supply human's need for a thousand of years.

The energy gained from fusion reactions is in form of kinetic energy of product particles. There are three main types of fusion confinement: gravitational confinement fusion, inertial confinement fusion (ICF) and magnetic confinement fusion (MCF). Gravitation confinement system is naturally occurring in the sun. The sun has a large amount of mass so its gravitational force surpasses coulomb potential repulsion and is able to fuse two nuclei together. Unfortunately, there is not enough mass on Earth to generate this kind of confinement. Thus, fusion on Earth must rely on other two types of confinement, inertial (laser-based) and magnetic confinements. To achieve fusion reactions on Earth, one requires the temperature in the order of a few hundred millions degree Celsius (100-200 keV), which is even hotter than the sun itself. At this extreme high temperature, gas becomes completely ionized and all ions and electrons are separated from each other. This state of matter is called a plasma.

ICF relies on high power laser beams shooting on a small target to produce fusion reaction in a blink of time. It occurs so fast that the fuel's inertia prevents it from escaping before fusing. There are some drawbacks on using ICF as possible energy generating choice, for example it is inherently pulsed so steady-state operational capability is doubtful. Moreover the capsule must be made with high precision to achieve good sphericity. The arrival timing of laser beams is also very crucial. To prevent the Rayleigh-Taylor instability, the capsule needs to be heated with uniformity of better than 1% which requires many simultaneous laser beams. In Lawrence Livermore National Laboratory, California, the National Ignition Facility (NIF) has been installed with 192 laser beams for total energy of 1.8 million joules to achieve the required uniformity [7-9].

MCF controls the hot plasma particles by utilizing magnetic field. Since the temperature suitable for fusion reaction is very high, at that state the gas is completely

ionized and becomes a plasma. The positively charged ions and negatively charged electrons can be trapped using magnetic field. MCF uses this concept to trap the plasma fuels to generate fusion energy. The trapped particles have energy or velocity roughly according to Maxwellian distribution. As they travel along the magnetic field, there is a chance of collision. A collision of particles with sufficient energy produces fusion reaction. MCF is one of the two major branches of fusion energy research along with ICF. The magnetic approach is more developed and is considered more promising for energy production in terms of steady-state operation and commercial use. There are many types of magnetic configurations being studied including tokamaks, stellarators, and mirror confinement. For this thesis, the focus is on fusion experimental machine called tokamaks [6].

1.1.3 Tokamaks

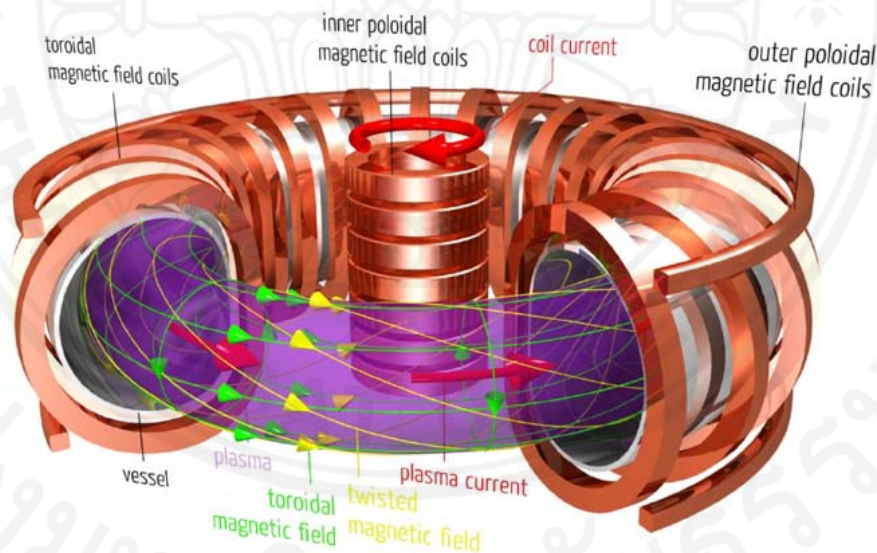


Figure 1.1: Schematic view of tokamak (figure retrieved from [10]).

Tokamak is a toroidal configuration magnetic confinement device. The word is abbreviated from Russian word *Toroidalnoya Kamera* (toroidal chamber) *Magnitnaya Katushka* (magnetic coil). It was invented in Moscow at Kruchatov Institute (in 1956) [6]. It utilizes magnetic field to confine the hot plasma. The current inside the plasma in toroidal direction is induced using an external transformer. This toroidal current generates poloidal magnetic field. The toroidal magnetic field is generated by external poloidal field coils. The resulting magnetic field forms a helical

path around the torus. Figure 1.1 shows the schematic view of typical tokamak. The important tokamak's parameters are shown as follows:

- Plasma major radius (R) is the distance from center of the torus to center of the plasma
- Plasma minor radius (a) is the distance from center to edge of the plasma
- Toroidal magnetic field (B_ϕ) is the magnetic field in toroidal direction generated by external coils. It is important for control of instability and shape of the plasma
- Poloidal magnetic field (B_θ) is the magnetic field in poloidal direction generated by plasma current in toroidal direction. It is important to generate magnetic pressure in order to balance the plasma outward pressure
- Plasma current (I_p) is the plasma current induced by external transformer.
- Total heating power (P_{TOT}) is a combination of external heating schemes, for example, Ion Cyclotron Resonance Heating (ICRH), Neutral Beam Injection (NBI), Electron Cyclotron Resonance Heating (ECRH), Radio Frequency heating (RF), and Lower Hybrid Resonance Heating (LHRH).
- Elongation (κ) and Triangularity (δ) are parameters used to define the shape of plasma's cross section [6]. The typical shape can be seen in figure 1.2.

$$\kappa = \frac{b}{a} \quad (1.7)$$

$$\delta = \frac{(d' + d'')/2}{a} \quad (1.8)$$

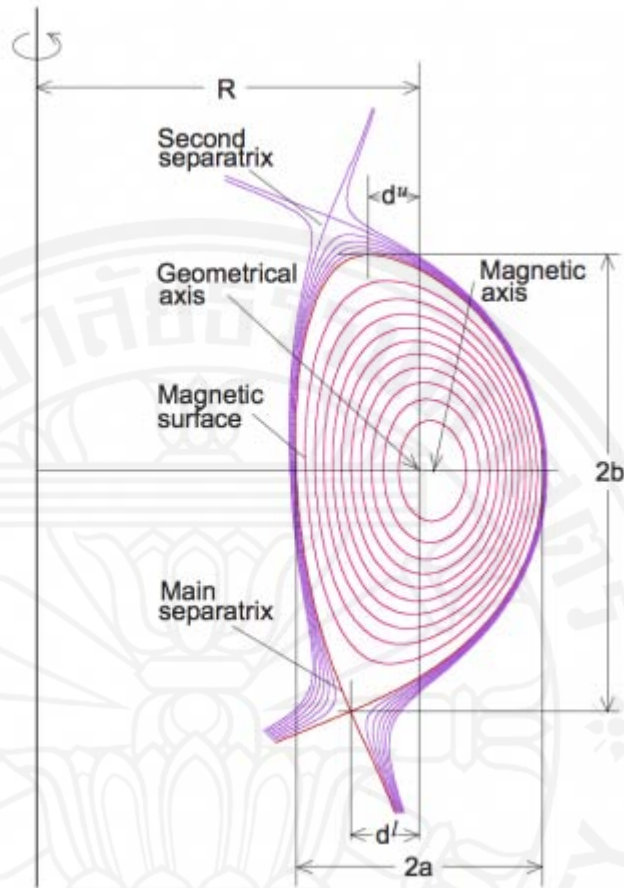


Figure 1.2: Cross-section of tokamak plasma (retrieved from [11]).

There are many tokamaks around the world, both small and large sizes. Largest tokamak ever built is JET [12] in UK ($R = 2.96 \text{ m}$ and $a = 1.25 \text{ m}$). Other examples of tokamaks are TFTR [13] in USA, JT-60U [14] in Japan, DIII-D [6] in USA, Tore Supra [6] in France, ASDEX Upgrade [15] in Germany, Aditya [16] in India, Alcator C-Mod [17] in USA, COMPASS [18] in Czech republic, EAST [19] in China, FTU [20] in Italy, HT-7 [21] in China, ISTTOK [22] in Portugal, KSTAR [23] in South Korea, STOR-M [24] in Canada, T-10 [22] in Russia, TCV [25] in Switzerland, TEXTOR [26] in Germany and TRIAM-1M [27] in Japan. Each has its own parameters value including typical pulse length.

In addition, there is a big international project called International Thermonuclear Experimental Reactor (ITER), which will illustrate the first burning plasma tokamak, i.e., alpha heating as partial heat source. ITER is a collaboration of 7 major countries including China, EU, India, Japan, Russia, South Korea and USA

[28]. Currently, it is being constructed in Caradache, France, with experimental parts shipped from all the partners. The tokamak is planned to be ready to operate around 2022. ITER will be the largest Tokamak ever built by human with major radius around 6.2 meters. It is designed to provide power output of 500 MW for 1,000 seconds operation length [29]. The objective for ITER is to demonstrate the scientific and technological feasibilities of a fusion power plant. It will produce a burning DT plasma with majority of heating comes from self-produced alpha power. Currently, there are several plans on different scenario that ITER will be run on including Full-Current, Inductive, Hybrid, and Steady-state scenarios. There will also be implementations and technological test on ITER for what will be needed on future fusion power plants such as superconducting magnetic coils and remote handling by robots. ITER's design parameters and its expected performance are shown in table 1.1.

Table 1.1: Design ITER parameters and performance capabilities [29].

<i>Parameter</i>	<i>Values</i>
R	6.2 m
a	2.0 m
I_p	15 – 17 MA
κ	1.85
δ	0.48
B_ϕ	5.3 T
Fusion power	500 – 700 MW
Fusion gain	5 – 10
Heating	73 – 110 MW
Plasma volume	830 m ³
Pulse duration	> 1000 s

Fusion gain is defined as

$$\text{Fusion gain} = \frac{5 \times P_\alpha}{P_{aux}} \quad (1.9)$$

where P_α is the alpha power and P_{aux} is the auxiliary heating (total input heating). As neutron and α -particle carry 80% and 20%, respectively, of the resulting energy from DT reaction, fusion gain equals to 1 is referred to as “breakeven” where the total output power is equal to input power. Fusion gain equals to 5 means fusion heating power is equal to external heating power. Infinite fusion gain corresponds to ignition condition where external heating is no longer required.

Ultimately, the goal of tokamak is to produce positive net power output as well as to reach ignition condition. This will provide self-sustainable fusion reactor possibility. As product particles of DT reaction, neutron is neutral so it can escape freely from the torus. Meanwhile, alpha particle is trapped inside by the magnetic field. This alpha particle contains about 20% of total output energy in the form of kinetic energy. It can transfer this energy back to electron and fuel ions by collisional process. If total alpha power is equal to input power, the plasma becomes self-sustaining and ignition condition is reached.

1.1.4 Development of fusion research

The scientific feasibility of nuclear fusion on Earth has been proved successfully by various large tokamaks, like JET, JT-60U and TFTR. The world research progress in the present is on the next phase, which is technical feasibility testing. For example, one of the tests is to examine whether tokamak’s wall and a divertor can sustain a heavy power load from the plasma, especially those from instabilities like Edge Localized Mode (ELM). This will be illustrated in the constructing ITER tokamak. The ultimate goal of tokamak research is to develop a power plant based on fusion reactions in order to supply world’s future energy. Tokamak confinement concept is to achieve magnetohydrodynamics (MHD) equilibrium using a combination of toroidal and poloidal magnetic fields in a toroidal shape plasma. The plasma particles are hence confined along the magnetic fields. In this configuration, the toroidal magnetic field is generated using external coils. Whereas, the poloidal magnetic field is a consequence of toroidal plasma current, which is induced by the flux changed in transformer coils at the center of tokamak. The important milestones of fusion research are shown in table 1.2.

Table 1.2: Milestones in Fusion Research

Year	Report	Milestones in Fusion Research
1969	Peacock <i>et al.</i> [30]	First measurement from T-3 tokamak (1 keV of electron temperature)
1982	Wagner <i>et al.</i> [31]	High confinement mode (<i>H</i> -mode) discovery
1992	JET Team [32]	First tritium used in tokamak
1994	Strachan <i>et al.</i> [33]	First experiment with the same percentage of deuterium and tritium used
1997	Keilhacker <i>et al.</i> [34] (1999)	Highest fusion power achieved (16 MW in JET)
1997	JET Team [32] Ishida <i>et al.</i> [35] Fujita <i>et al.</i> [36]	Achievement of breakeven or better outputs (JET and JT-60U)
1998	ITER Council [37]	Revised performance specifications for ITER
2004	Zushi <i>et al.</i> [27]	Longest pulse duration of 5 h 16 m in TRIAM-1A

1.2 Motivation, research concept and outline of the thesis

As shown in table 1.2, discovery of *H*-mode is considered as one of the milestone events in nuclear fusion research [31, 38]. Experimental observations in various magnetic confinement fusion devices have revealed that the formation of an edge transport barrier results in a sudden transition from low confinement mode (*L*-mode) to *H*-mode with great improvement in plasma performance [39]. The phenomenon is commonly known as *L-H* transition. Generally, *H*-mode plasma operational regime provides plasma performance enhancement including high plasma temperature and density as well as long energy confinement time [31]. However, *H*-mode with high current lasts for only a few seconds in present day tokamaks. This enhancement is crucial for future nuclear fusion projects, like ITER, that they are planned to be operated in *H*-mode [28], with new strategies to maintain *H*-mode at high current for a longer time.

The improvement of plasma density and temperature profiles is mainly caused by an ETB formation [40], generally known as the pedestal. As the name implied, ETB is located at the plasma edge. Inside ETB region, the plasma has relatively strong pressure/density gradients and the transport is greatly reduced. Plasma performance can further be improved by a formation of an internal transport barrier within the plasma core [41]. The presence of both ETB and ITB will lead to a high performance operation mode because significant bootstrap current fraction can be reached. The bootstrap current is an intrinsic neoclassical toroidal current. It is driven by the pressure gradient. The current is generated from the particles which are trapped in the banana orbits, their collisions result in a net current flow in toroidal direction. Therefore, a successful steady-state tokamak experiment in the future can be realized with the simultaneous formation of both transport barriers; the operation is called advanced scenario.

It was experimentally found that an ETB formation is possible when an injected heat, regardless of heating scheme, exceeds a threshold. Theoretically, full understanding of $L-H$ transition is still an open question because its underlying description is still not completed [42]. It is known that the reduction of transport within transport barrier region is a consequence of suppression of turbulent transport. The examples of suppression mechanism are such as magnetic shear and flow shear [43]. Within the barrier, the transport could be decreased to the neoclassical level implying that anomalous transport is fully suppressed or quenched [44]. The effects of flow shear and magnetic shear suppression on the transport barriers are subjected to study in this thesis. The first mechanism is the flow shear which was first proposed to be the main mechanism for ETB formation because it was found to be able to reduce the turbulent level by using linear stabilization [45]. A strong correlation between the flow shear strength and the turbulent fluctuations in tokamak plasma has also been observed [46]. The second mechanism is the magnetic shear which associates with magnetic topology in the plasma. It was found that tokamak confinement can be further improved with transport barrier formation near plasma center where the magnetic shear is low or negative [39]. Generally, the magnetic shear, via current control technique, can affect the formation of ITB whereas the flow shear, driven by both external and intrinsic sources, can affect formations of ETB and ITB.

Experimentally, it was found that ITB formations were achieved both in L -mode [47] and H -mode [48] plasmas. Therefore, ITB and ETB formations appear to be independent of each other. However, there might be some kind of compatibility between them as discussed by Fukuda *et. al.* [49] from the analysis in JT-60U. In spite of that, interactions between the two types of transport barrier are possible and may play significant role in confinement control.

The aim of this thesis is to utilize theoretical models based on bifurcation concept in order to study, describe and analyze formation and dynamics of ETB and ITB, as well as related properties like hysteresis. The previous one-field and two-field bifurcation models are improved here by providing more realistic anomalous transports and sources such as thermal and particle. Analytical and numerical techniques are then used to show criteria for L - H transition, which appear to be very complex and non-linear, this part can be seen in chapters 3 and 4. Furthermore, a new stability analysis method is used to analyze the bifurcation models. Important results are such as the detailed mechanisms during the transition are revealed. Moreover, this method also illustrates the dynamics of the back H - L transition and conditions in which it occurs. Those results lead to explanation of hysteresis in tokamak plasma, which are described in chapters 3 and 5. Mechanics of ETB including the width expansion are studied in chapter 4 using numerical method. The limitation in this thesis is the exclusion of instabilities effects such as ELMs, Neoclassical Tearing Mode (NTM), or sawtooth oscillation. These instabilities can drastically change the results; for example, an ELM crash can limit the growth of ETB. They are not included in the current state of the models in order to study the intrinsic properties of the plasma. The results can be realized when instabilities can be fully controlled, like ELM-free scenario plasma.

In chapter 6, a new form of transport suppression mechanism, modified by including both magnetic shear and flow shear effects, is applied to the two-field bifurcation model. This new model allows study of both ITB and ETB formation and their widths. The results interestingly show that ITB also has bifurcation properties but it is governed by the magnetic topology of the plasma as oppose to the heating power as in the case of ETB. New results also imply that there is a new class of ITB called weak ITB. Weak ITB was found in the experiments, but its detailed

characterization has never been done before. The effects of current drive location, transport strength, and sources on transport barrier formation are analyzed as well. In chapter 7, toroidal rotation models are developed and installed in an integrated predictive modeling code BALDUR[50]. This improves the predictive capability of the code. This physical quantity is one of the important ingredients used in the plasma research. In the last part, the toroidal rotation models are combined with the bifurcation models to analyze its role in the plasma behavior. The results show that, at least on some models, the toroidal rotation plays a role in transport barrier.

1.3 Objectives

1. To study $L-H$ transition and formation of an ITB in tokamak plasma
2. To improve and develop $L-H$ transition model based on bifurcation concept.
3. To develop models and numerical codes in order to explain and study both ETB and ITB formation based on bifurcation concept
4. To describe and predict formation and dynamic of transport barriers by both analytical and numerical methods
5. To develop toroidal velocity models and implement into an integrated predictive modeling code and verify with experiment data
6. To include the developed toroidal velocity models into the bifurcation picture of tokamak plasma

1.4 Scope of research

1. Developing L-H transition model based on bifurcation concept to predict formation and dynamic of transport barrier at the edge of tokamak plasma
2. Developing models and numerical codes based on bifurcation concept to explain both ETB and ITB formation in the plasma
3. Developing toroidal velocity models and implementing them into an integrated predictive modeling code BALDUR
4. Simulating profiles of existing tokamaks and predicting performance of ITER using the toroidal velocity models
5. Implementing the toroidal velocity models into bifurcation models and examining the effects on plasma behavior

1.5 Research procedure

In summary, the study and research procedure consists of the following steps:

Step 1: Study on fusion plasma, tokamak confinement system, and transport barriers in tokamak plasma.

Step 2: Study and research on *L-H* transition model based on bifurcation concept.

Step 3: Improve and develop *L-H* transition model to explain transport barrier formation.

Step 4: Develop model to explain both edge and internal transport barriers.

Step 5: Develop numerical codes to study formation and dynamics of transport barriers based on bifurcation concept

Step 6: Study on and learn how to use BALDUR integrated predictive modeling code, which is written in FORTRAN.

Step 7: Study and obtain characteristics of each JET discharge run and future ITER, parameters such as magnetic field, plasma major and minor radius, plasma current, heating scheme and power, etc. are used as input for simulation program.

Step 8: Implement existing and newly developed toroidal velocity models into BALDUR code.

Step 9: Perform simulations using BALDUR code.

Step 10: Analyze the results using MATLAB and Microsoft Excel.

Step 11: Make conclusion, write reports, publish the results, and write thesis.

Chapter 2

Literature Review

2.1 Transport barriers

A transport barrier is a local narrow region in radial direction with steep radial temperature or density gradients and transport reduction. There are two types of transport barriers, depending on barrier location; internal transport barrier and edge transport barrier. The transport barrier is very important in fusion research because its formation facilitates a self-organized mechanism of heat and particle loss prevention from plasma core to the outside region. Thus, central plasma temperature and density are increased. Consequently, tokamak performance can be improved greatly. The schematic of how transport barriers can improve central pressure is illustrated in figure 2.1. The plasma discharge without the presence of transport barrier is categorized as *L*-mode (lower line). The upper line represents the plasma with ETB, where the barrier's location is shown as shaded box near plasma edge. With ETB formation, the plasma profiles are improved and the plasma abruptly changes from *L*-mode to *H*-mode (*L-H* transition). Additionally, the plasma can be improved even further with transport barrier occurs in its core (ITB). Due to the fact that plasma total power output is increased when transport barriers are observed, it is essential to understand the physics of them.

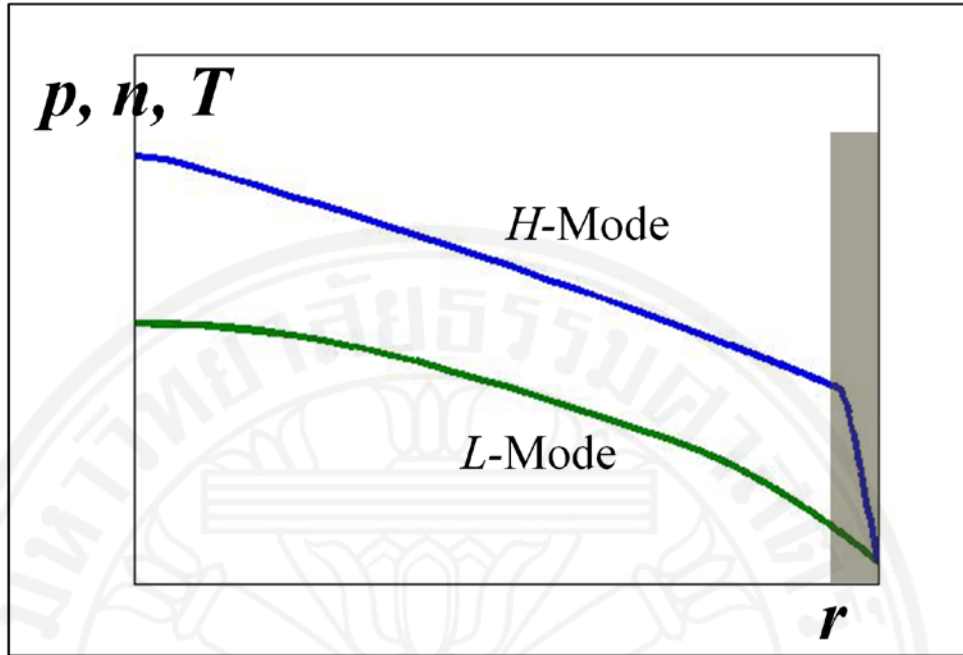


Figure 2.1: Illustration of pressure, density and temperature profiles as a function of plasma minor radius, the shaded area indicates region of ETB.

2.1.1 *L-H* transition and formation of ETB

Historically, a human attempt to harvest nuclear fusion energy as alternative fuel source started since 1969 when first electron temperature of 1 keV was successfully achieved in T-3 tokamak at Kurchatov Institute [30]. From then on, the development in tokamak research has made significant and steady progress with some obstacles met along the way. For example, scientists found a problem when plasma heating by generated current (ohmic heating) gets higher, the heating efficiency actually decreases because the plasma resistivity reduces at high temperature [6]. So, ohmic heating was insufficient to heat the plasma to a desired range. Later, an important phenomenon was discovered with the help of additional external heating schemes (via beam injection or wave). The plasma can make an abrupt transition, called *L-H* transition, when sufficient total power was applied to the plasma. The transition occurs when the plasma confinement mode changes from *L*-mode to *H*-mode. This new mode was discovered in 1982 by the ASDEX team [31], and the plasma performance was found be increased by a factor of two.

The transition to *H*-mode is always accompanied by the formation of transport

barrier at the edge which is called ETB [40]. In this region, the anomalous transport is quenched so almost only neoclassical transport exists with characteristic such as high temperature (pressure) or density gradient. Whenever a formation of transport barrier is taken place, the temperature or density at the plasma center is significantly increased, resulting in improvement of plasma performance. The plasma performance can also be further enhanced by formation of ITB [41]. Transport barriers are very important in fusion research because they improve tokamak performance which means increasing total power output, for example the highest power produced up to date by any tokamak experiment was from JET of 16 MW discharge, which was discharge with ITB existence in *H*-mode plasma [34].

Even though, at present, the underlined physics of *L-H* transition is still unclear, there are many hypotheses based on the concept of a suppression of the turbulent transport by the flow shear or/and magnetic shear [43]. It is known that the turbulent transport can be stabilized by flow shear because of the breaking of a convection cell [45]. In other word, the flow shear in perpendicular direction to that of the transport via convection cell can distort the cell and even break them apart if the shear is large enough. Experimental results support that turbulent fluxes can be reduced or quenched by a sheared flow in the transport barrier region [41, 43].

L-H transition occurs at the onset transport barrier formation at the edge of the plasma resulting in steep rising of the profiles in that region. Understanding physics behind this phenomena is very important because the performance of tokamaks is significantly enhanced if the plasma in those tokamaks can access *H*-mode operational regime [31]. Typically, the *L-H* transition occurs in short timescale [42], which suggests a bifurcation nature. Experimental results from many tokamaks indicate that this *L-H* transition can only occur when sufficient heating power is deposited into the plasma. This power threshold (P_{th}) has been empirically derived by the ASDEX team as:

$$P_{th} = 0.04n_{el}BS_a, \quad (2.1)$$

where n_{el} is the line averaged electron density (10^{20} m^{-3}), B is the plasma magnetic field (T) and S_a is the plasma surface area (m^2) [42]. However, to provide confidence for projection into a large tokamak like ITER scale one needs to develop the threshold

based on theoretical foundation. Due to the difficulties in understanding of the plasma transport, one common way fusion physicists prefer is to derive an empirical scaling using data from several tokamaks operating at various engineering parameters. For example, the power threshold scaling done by the ITER *H*-mode database working group has the relation:

$$P_{th} = (0.45 \pm 0.10) B n_{el}^{0.75} R (0.6 n_{el} R^2)^\alpha, \quad (2.2)$$

where $|\alpha| \leq 0.25$ [51]. However, the more recent results from JET which used hydrogen, deuterium and tritium as fuels illustrated that the threshold condition is also inversely dependent on isotope effect. Hence, the scaling becomes:

$$P_{th} = 2.84 M^{-1} B_\phi^{0.82} n_e^{-0.58} R^{1.00} a^{0.81}, \quad (2.3)$$

where M is hydrogenic mass in amu [52].

Since *H*-mode transition is a phenomena taking place at plasma edge, local physical quantity can be of interest. Specifically, physical evidence suggests that a critical edge electron temperature ($T_{e,crit}$) plays a role in determination of the transition threshold. It has the following scaling:

$$T_{e,crit} \sim B^\alpha n^{-\gamma}, \quad (2.4)$$

with $1/2 < \alpha < 2$ and $0 < \gamma < 2/3$ [42, 53-56]. On the other hand, in one particular work by the ITER *H*-mode threshold database working group, experimental data from six different tokamaks were combined to derive an empirical scaling for edge electron temperature $T_{e,edge}$ [55]. The derived scaling law has the form:

$$T_{e,edge} \sim 0.17 n_e^{-0.14} B^{0.98} R^{0.86} q_{95}^{-0.93}, \quad (2.5)$$

where n_e is the electron density, q_{95} is the edge safety factor q (at normalized minor radius (r/a) equal to 0.95). This empirical equation is to show that the edge electron temperature is related to magnetic field and the safety factor. Both parameters are related to transport barrier formation as will be discussed shortly.

Theoretically, many conceptual approaches and hypothesis have been proposed to study the *L-H* transition phenomena. In dimensional analysis approach, the threshold power is developed using relevant parameters and dimensionless edge parameters based on empirical approach [57]. In edge power balance approach, the power threshold is introduced relating to criterion in terms of edge parameters and the

local power balance [58]. The shear flow paradigm approach relies on the idea that the sheared radial electric fields plays role in the reduction of the turbulent transport [59]. The radial electric field approach makes use of a simple calculation of ion species force balance equation in radial direction. The bifurcation approach is chosen to be the main focus of this research. It will be described in details later.

2.1.2 Formation of ITB

ITB formation is also important in fusion research because it can further enhance tokamak performance which means increasing total power output. The highest power produced by JET of 16 MW [34] was discharge with ITB existence. In ITB region, the transport coefficients were found to be reduced to neoclassical level [60]. Usually, the radial location of ITB is found in the range between $r/a = 0.2$ to $r/a = 0.8$.

The specific ITB location can vary with time depending on the unclear mechanics of its evolution. Though, it is found that most of the time it moves outward as heating is increased and inward as heating is decreased. ITB can be observed in all transport channels, either individual or simultaneous, which are ion and electron heat transport, electron transport, and momentum (ion) transport channels. Sometimes it can only be observed in one or two channels but sometimes all channels exhibit ITB formation like on JET [61], DIII-D [62-63], and JT-60U [64]. The reason for these behaviors is not fully understood yet. Though, it appears to relate with heating schemes because each heating configuration can affect electron and ion particles differently.

Historically, a few years after 1990 an improved confinement mode, with ITB formation, over the standard H -mode were discovered in various tokamak experiments such as JET [32], TFTR [65], DIII-D [66], and JT-60U [67]. After that, ITB (including ETB) can be achieved widely in many tokamaks with various controlling methods including NBI heating, ICRH heating, ECRH heating, Lower Hybrid Current Drive (LHCD), and momentum and mass injection etc. This implies that there may be several mechanisms that affect the dynamics of transport barriers. Even though, the physics of ITB formation has not yet been clearly understood, it is believed that the suppression of anomalous transport near plasma center is governed

by magnetic shear s and flow shear ω_{ExB} [68-69]. Moreover, integer and rational values of the safety factor are also evidently found to be related to ITB formation and its sustainment.

Quantitatively, a condition for determination of ITB formation has been derived by Tresset *et al.* [70-71]. The authors assumed that the magnetic shear stabilization remains constant throughout the plasma and that the ExB shearing rate is driven by the pressure gradient. As a result, an ITB is formed if the following condition is satisfied:

$$\rho_T^* = \frac{\rho_s}{L_T} = \frac{\sqrt{m_i} \sqrt{T_e}}{ze} \frac{\partial T_i}{T_i \partial r} \geq \rho_{ITB}^*, \quad (2.6)$$

where ρ_T^* is the normalized Larmor radius, ρ_s is the Larmor radius, L_T is the gradient scale length, m_i is the ion mass, T_e is the electron temperature, T_i is the ion temperature, and ρ_{ITB}^* is an ITB normalized Larmor radius threshold determined from experimental data. This threshold is statistically computed by Tresset *et al.* from many JET experiments with ITB to be:

$$\rho_{ITB}^* = 1.4 \times 10^{-2}. \quad (2.7)$$

2.1.3 Causes of transport barriers

It is widely believed that the radial velocity shear v_E' is the main effect that causes ETB. Whereas for ITB, there are three main effects that are believed play role in its formation: flow velocity shearing rate ω_{ExB} , magnetic shear s , and safety factor q .

2.1.3.1 Radial velocity shear

Currently, the effect of velocity shear is the leading candidate of formation explanation for both ETB and ITB. When the magnetic field is perpendicular to the electric field, $\vec{E} \times \vec{B}$ drift velocity can be generated in the direction perpendicular to both fields. This velocity varies radially in tokamak's cross-section causing the shear in velocity flow. This results in de-correlation of the convective cell, hence reduction

of transport, which is the main effect for transport barrier formation. In modeling of ETB, the radial $E \times B$ velocity is in the form:

$$v_E = c \frac{E_r}{B}, \quad (2.8)$$

where E_r is radial electric field, which can be calculated according to the force balance between pressure gradient and Lorentz forces:

$$E_r = \frac{1}{Zen_i} \frac{\partial p_i}{\partial r} - v_\theta B_\phi + v_\phi B_\theta, \quad (2.9)$$

where Z is the ion charge number, e is the elementary charge, n_i is the ion density for each ion species, $\frac{\partial p_i}{\partial r}$ is the pressure gradient and v_θ and v_ϕ are the poloidal and toroidal velocities, respectively. The velocity shear is the derivative of this term in radial direction:

$$v'_E = c \frac{E'_r}{B}. \quad (2.10)$$

This term is used to suppress the turbulent or anomalous transport for ETB formation. In ITB explanation, usually the shearing rate ω_{ExB} term is used. It is calculated according to Hahm-Burrell model [72-74]:

$$\omega_{ExB} = \left| \frac{RB_\theta}{B_\phi} \frac{\partial (E_r/RB_\theta)}{\partial r} \right|. \quad (2.11)$$

The theoretical explanation is that the turbulent eddies can be stabilized by the sheared ω_{ExB} velocities [43]. The sheared flow causes a de-correlation in the dominant turbulent modes, resulting in transport reduction [45]. It was found that the turbulence level is greatly decreased when ω_{ExB} exceeds the maximum linear growth rate γ_{lin} [75]:

$$\omega_{ExB} > \gamma_{lin}^{\max}. \quad (2.12)$$

Experimentally, there exist some evidences from JET [48], DIII-D [43, 76], and TFTR [77-78] that, prior to ITB formation, the magnitude of ω_{ExB} is similar to γ_{lin}^{\max} , while during ITB formation it is noticeably larger. However, it remains to be answered whether the turbulence quenching due to shearing rate or the transport reduction due to other mechanism takes place first. It is rather complicated because

both ω_{ExB} and $\gamma_{\text{lin}}^{\text{max}}$ are proportional to the temperature gradient with ω_{ExB} increases faster. So it is quite natural that after ITB formation (high temperature gradient) the ω_{ExB} will surpass $\gamma_{\text{lin}}^{\text{max}}$.

2.1.3.2 Magnetic shear

Magnetic shear (s) is also believed to play role in turbulence stabilization at plasma edge and core, resulting in ETB and ITB formations, respectively [43]. It is found experimentally that ITB formation and its sustainment are influenced by either small or reversed (negative) magnetic shear. It can be calculated as follows:

$$s \approx \frac{r}{q} \frac{dq}{dr}, \quad (2.13)$$

which implies that the magnetic shear is related to the radial derivative of the q -profile. Usually, the q -profile in tokamak has monotonic shape (left panel of figure 2.2). However, in ITB formation discharge, it has non-monotonic shape which means the magnetic shear has reversed its sign (right panel of figure 2.2) [60]. The q -profile is defined as how many times the field line rotates in toroidal direction divided by how many times the field line rotates in poloidal direction when the total field line is back to its starting position.

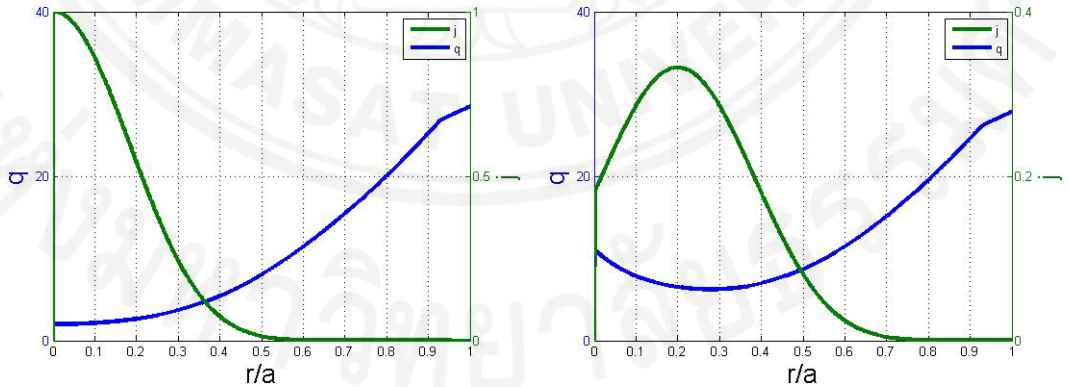


Figure 2.2: Illustration of current density and safety factor profiles for center peak (left) and off-center peak (right) currents.

This special non-monotonic q -profile is associated with the position of current profile peaking as shown in figure 2.2. This can be done experimentally by two ways. One way is by ramping down the plasma current [79-81]. Another way is by enlarging

the plasma cross section elongation [82]. Both changes must be transiently carried out in order to obtain a current profile deviation from its equilibrium distribution. In order to obtain a negative or small magnetic shear, an elaborate preparation phase must be prepared to reach appropriate target q -profile. In some tokamaks, LHCD or ICRH is used in the preheating phase together with a fast current ramp-up. In some other tokamaks, ECRH and NBI preheating are applied to achieve the desirable profile [83-85]. These external heating induce an off-center peaking of the current profile which alters the poloidal magnetic field. According to equation (2.13), the q -profile can be shaped appropriately this way. ITBs are reported only in experiments with negative, low or reversed magnetic shear [32, 35, 65-67, 86-91]. Typically, the growth rate decreases in the radial zone with reversed magnetic shear profile resulting in reduction of turbulent transport, which again may be associated with disruption of convection cells.

There are still debates of whether magnetic shear alone can trigger ITB formation or it merely facilitates other mechanism. Tala and Garbet [92] proposed a relationship between ω_{ExB} and s . They investigated experimental data from thirteen ITB discharges in H -mode and three ITB discharges in L -mode from JET tokamak. It was found empirically that ITB can be formed if the following condition is met:

$$s - 1.47 \frac{\omega_{ExB}}{\gamma_{ITG}} - 0.14 < 0, \quad (2.14)$$

where, γ_{ITG} is the ion temperature gradient (ITG) mode dominant linear growth rate. ITB is collapsed otherwise. This relationship implies that both ω_{ExB} and s play important roles in ITB formation and the ITG turbulence is the dominant instability mode.

2.1.3.3 Safety factor

The q -profile is called “safety factor” because it is related to plasma instability, the higher q value the more instability. Evidently, it is found that integer and rational surfaces of the q -profile is associated with triggering and mechanics of ITB on JET [93], JT-60U [67], and DIII-D [76]. In most of ITB JET discharges, ITB appears to form near $q = 2$ surface in the core region and to follow it outwardly. However, in recent study of 40 Tore Supra discharges [94], it was found that

formation of ITB is also strongly connected to low order rational surface of the q -profile at plasma center (q_0), mostly equal to 2 or 3/2. It also concluded that the position of q_{\min} or minimum safety factor was not related to position of ITB. Many believe that q surface is indirectly related to ITB formation while the ω_{ExB} shearing rate is the actual turbulence suppression.

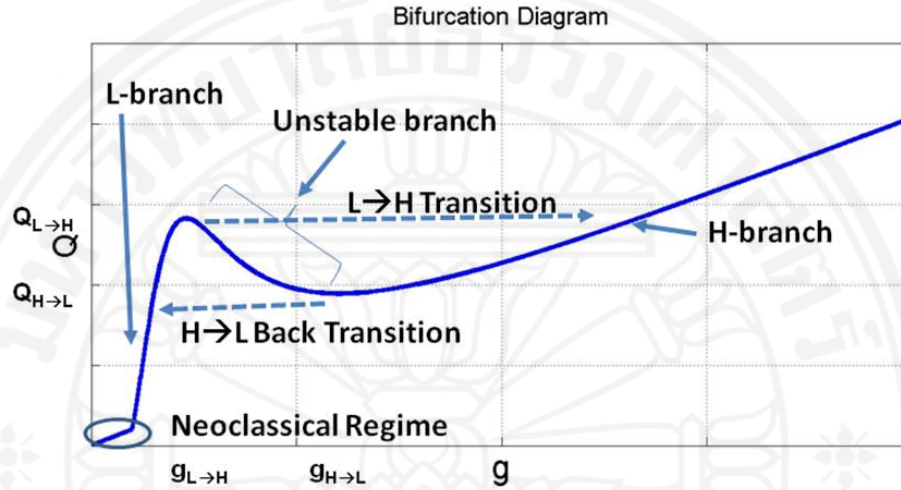


Figure 2.3: Illustration of bifurcation diagram.

2.2 Bistable s-curve bifurcation model

Bifurcation behavior in physical quantities, such as magnetization in ferromagnet and radial electric field, heat flux (Q) and particle flux (I) in fusion plasma, can exist when the governing equation yields multi-solutions with respect to independent variable (induced magnetic field or pressure and density gradients). The multiplicity of solutions indicates bifurcation nature of the system. Moreover, the bifurcation can occur at any first-order phase transition. Figure 2.3 shows sample of bifurcation diagram when there exist multi-valued solutions. In this figure, $Q_{L \rightarrow H}$ and $Q_{H \rightarrow L}$ represents heat flux at the onset of L - H transition and H - L back transition, respectively, while $g_{L \rightarrow H}$ and $g_{H \rightarrow L}$ represent their respective pressure gradients. The bifurcation nature can also be categorized as hard and soft bifurcations [95], which are classified as ‘first order phase transition’. There are other types where gradients of the solutions change while the solutions themselves are monotonic. These are called ‘second order phase transition’. Usually these bifurcation diagrams are presented as

dependent variables like density or pressure gradients versus independent variables like particle or heat fluxes, respectively.

This bifurcation concept studied in this thesis is mainly based on analytical work by Malkov and Diamond [96]. The so-called bistable s -curve bifurcation model considers each mode (L and H modes) like a phase of plasma state so L - H transition resembles to a phase transition. Additionally, variation of system state like pressure or density gradients as a function of the independent variables such as heat or particle fluxes, respectively, can be represented on a graph like in figure 2.3. The graph exhibiting bifurcation nature has an s -curve line with two stable branches corresponding to the L and H modes. The two branches are connected by an unstable branch covering transition region. Historically, the report by Hinton developed the model using thermal conductivity model approach [97]. It used general analysis by Biglari [45] that the sheared poloidal rotation suppress the turbulent transport. In this study, the model is done using one-field approach. Later in the year 1992, Hinton and Staebler studied the model using two-field approach. The velocity shear is in the form as shown in equation (2.10), by reducing the equation into one dimension or radial direction the velocity shear can be expressed using force balance equation (2.9) as:

$$v'_E = \frac{c}{B} \frac{\partial}{\partial r} \left(\frac{1}{Z e n_i} \frac{\partial p_i}{\partial r} - v_\theta B_\phi + v_\phi B_\theta \right). \quad (2.15)$$

Since the first term is dominant, the derivation becomes

$$v'_E = \frac{c}{B} \frac{\partial}{\partial r} \left(\frac{1}{e n_i} \frac{\partial p_i}{\partial r} \right). \quad (2.16)$$

Note that the value of Z is included in e from now on. In 2008, Malkov and Diamond [96] studied this model using analytical approach in one dimension using slab geometry assumption.

In their model, the particle and heat transport equations, respectively, are of the form:

$$\frac{\partial n}{\partial t} - \frac{\partial}{\partial x} \left[D_0 + \frac{D_1}{1 + \alpha v_E'^2} \right] \frac{\partial n}{\partial x} = S(x), \quad (2.17)$$

$$\frac{\partial p}{\partial t} - \frac{\partial}{\partial x} \left[\chi_0 + \frac{\chi_1}{1 + \alpha v_E'^2} \right] \frac{\partial p}{\partial x} = H(x), \quad (2.18)$$

where particle and thermal neoclassical transport coefficients (D_0 and χ_0 , respectively) and particle and thermal anomalous transport coefficients (D_1 and χ_1 , respectively) represent the total transport of the system, n represents plasma density, p represents plasma pressure, S is the particle source, H is the heat source, and α is a constant representing the strength of the suppression term. They also use

$$v'_E = \frac{c}{eB} \frac{\partial}{\partial x} \left(\frac{1}{n(x)} \right) \frac{\partial p(x)}{\partial x}. \quad (2.19)$$

The curvature of the pressure term is neglected for simplicity of their analysis. During stationary state, the time dependent terms in equations (2.17) and (2.18) vanish. The stationary condition can be shown as:

$$\left[D_0 + \frac{D_1}{1 + \alpha v'^2_E} \right] \frac{\partial n}{\partial x} = \int_0^x S(x') dx' = \Gamma_s(x), \quad (2.20)$$

$$\left[\chi_0 + \frac{\chi_1}{1 + \alpha v'^2_E} \right] \frac{\partial p}{\partial x} = \int_0^x H(x') dx' = Q_s(x), \quad (2.21)$$

where Γ_s and Q_s are the source particle and heat fluxes, respectively. The results show bistable bifurcation behavior similar to the one show in figure 2.3 when plotting heat/particle fluxes as a function of pressure/density gradients. This model is open to expanding study, especially if using numerical approach. So it allows the possibilities to include more physics such as the nature profiles of heat and particle sources, or the neglected term in equation (2.19). More importantly, the dynamic of transport barrier can be studied as well.

2.3 Integrated predictive modeling code

Many integrated predictive modeling codes have been developed to carry out simulations for predicting tokamak's performance, i.e. spatio-temporal profiles of plasma density and temperature. One of the objectives of these codes is to investigate and study the physical processes in tokamak plasma. Generally, each simulation requires input data or engineering parameters such as plasma geometry, heating power, magnetic field, plasma current, plasma density, and etc., and self-consistently computes plasma profiles. Example of these codes are such as ASTRA [98], BALDUR [50], CORSICA [99], CRONOS [100-101], JETTO [102], ONETWO

[103], TSC [104], and XPTOR [105]. In this thesis, BALDUR is chosen as a choice of modeling code because of its availability and flexibility for installation of new models.

The 1.5D BALDUR integrated predictive modeling code [50] is a time-dependent transport modeling code, used to compute many physical quantities in tokamaks. It assumes that the plasma has equilibrium on the flux surface so there are symmetries in toroidal and poloidal directions. Hence, the code solves the plasma transport only in radial direction and extends the results over the flux surface where the cross section is defined by the triangularity and elongation. That is why it is considered one and a half dimensional code. The code computes the plasma profiles such as spatio-temporal evolution of electron density, ion and electron temperatures. It can also be used to compute heat and particle sources (NBI), sinks, (impurity radiation), fusion reactions, MHD equilibrium, and physical quantities like impurity and hydrogen densities, magnetic q and other gas densities [106].

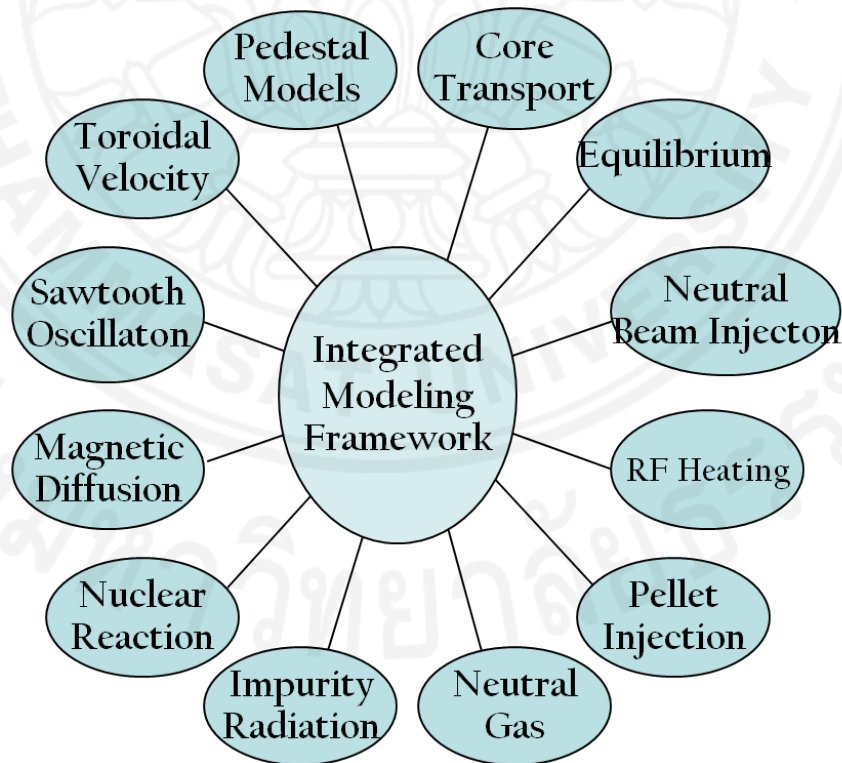


Figure 2.4: Schematic structure of integrated predictive modeling code.

BALDUR code self-consistently computes the plasma profiles using a combination of many physical processes together in form of modules. Example of

BALDUR modules are plasma transport, plasma heating, particle flux, boundary conditions, instability models, sawtooth oscillations modules, and etc. All modules are linked together by central framework as shown in figure 2.4. It is accepted widely that results from BALDUR are in agreements with experimental data to about 10% relative root mean square deviation (RMSD) [107-108].

2.3.1 Description of BALDUR

In tokamak system, plasmas can be described using diffusion processes. BALDUR essentially evolves plasma profiles according to the diffusion equations. These diffusion equations are derived based on the Fick's laws [109], in which the first and second laws can be expressed as

$$\bar{J} = -D\nabla\Phi, \quad (2.22)$$

$$\frac{\partial\Phi}{\partial t} = D\nabla^2\Phi, \quad (2.23)$$

where Φ (m^{-3}) is the concentration of interested quantity, J ($\text{m}^{-2}\text{s}^{-1}$) is the corresponding diffusion flux and D (m^2s^{-1}) is the diffusion coefficient. Combining these two equations, one obtains a simple diffusion equation as:

$$\frac{\partial\Phi}{\partial t} = -\bar{\nabla} \cdot \bar{J}. \quad (2.24)$$

In a simple fashion, one can imagine the diffusion equation as a conservative law of plasma parameter. BALDUR solves three different diffusion equations with assumption that the only dependency on space is on radial direction. This assumption is valid because the plasma appears to be symmetric in toroidal and poloidal direction over the magnetic flux surface. In addition, it allows source or sink terms to be included [50]. The first equation represents the conservation of mass for of each plasma species

$$\frac{\partial n_a}{\partial t} = -\frac{1}{r} \frac{\partial}{\partial r} (r\Gamma_a) + S_a, \quad a = 1, 2, l, h, \quad (2.25)$$

where n_a represents number density of corresponding species (1 for deuterium, 2 for tritium, l and h for impurities defined by users), Γ_a is the particle flux and S_a is the particle source. The second equation explains conservation of energy in the plasma

$$\frac{\partial E_j}{\partial t} = -\frac{1}{r} \frac{\partial}{\partial r} (r q_j) + Q_j, \quad (2.26)$$

where E_j is the energy density, q_j is energy flux and Q_j is energy sources. The subscript j represents each species in the plasma, both ions and electron. The last equation represents magnetic diffusion (in Gaussian unit):

$$\frac{\partial B_\theta}{\partial t} = \frac{c^2}{4\pi} \frac{\partial}{\partial r} \left[\frac{\eta}{r} \frac{\partial (r B_\theta)}{\partial r} \right] - c \frac{\partial}{\partial r} (\eta J_{\text{beam}}), \quad (2.27)$$

where, η is plasma parallel resistivity, J_{beam} is the net current density driven by external source which acts as the source of magnetic diffusion equation. More details of how BALDUR determine particle as well as energy fluxes and sources can be found in the work of Singer *et al.* [50].

2.3.1.1 Boundary conditions

The boundary conditions at plasma center of equations 2.25, 2.26, and 2.27 are

$$\frac{\partial n_a}{\partial r} = \frac{\partial E_j}{\partial r} = B_\theta = 0. \quad (2.28)$$

For outer boundary condition, BALDUR allows many options to be used including using density and temperature pedestal values as boundary conditions as explain later in pedestal theory section. The calculation of B_θ at the outer boundary can be done by specifying I_p , B_θ , or voltage at the surface.

2.3.1.2 Initial conditions

BALDUR allows three options for setting initial conditions for densities and temperatures. Firstly, they can be input by users in array format. Secondly, specific form built-in profiles can be used. Lastly, the densities can also be given as fraction of initial total ion density. The initial condition for B_θ can be calculated from an initial toroidal current profile or as a function of electron temperature.

2.3.1.3 Description of physics used in BALDUR

- The anomalous diffusivities represent contribution from anomalous transport which is the transport caused by turbulence. These diffusivities can be

calculated from empirical transport models, theories of turbulence transport, or semi-empirical transport models.

- Toroidal velocity model used in transport modeling, this is needed because BALDUR does not directly solve the toroidal momentum conservation.
- Toroidal field ripple, influencing only on ion thermal diffusivity, consists of three contributions; banana-drift, ripple-plateau and ripple-trapping.
- Neoclassical transport which is based on collisional transport.
- Ware pinches effect which explains inward particle transport due to toroidal electric field.
- Resistivity for calculation of ohmic heating.
- Sources and sinks of particle and energy including neutral hydrogen isotopes, NBI, fast-ion thermalization, thermonuclear fusion power (DT and catalyzed DD fusion reactions), radiative losses, scrape-off losses, auxiliary heating, ECRH, Ohmic heating, collisional energy interchange, cold helium source, pellet fueling, recombination, and neutral impurity influxes.
- Numerical values for densities and temperatures are preset in scrape off layer to avoid numerical overflows.
- Compression model for calculations of adiabatic compression.

2.3.2 BALDUR transport modules

2.3.2.1 Mixed Bohm/gyro-Bohm module

The turbulent transport, including ITB formation and its dynamics, are modeled through a semi-empirical transport model called mixed Bohm/gyro-Bohm (Mixed B/gB) [110]. Initially, the Bohm transport was developed to describe local transport based on Bohm scaling. This means the diffusivities are proportional to the multiplication of the thermal velocity and plasma gyro radius. These transport diffusivities are dependent on several plasma parameters, i.e. q and profile shapes. So in the regular simulations, all parameters are fixed while the gyro radius is varied in radial direction. The Bohm transport used in this thesis was at first derived for electron transport for the JET tokamak [111]. Then, it was modified by adding the gyro-Bohm term in order to additionally explain ion transport [112] and to simulate results for both larger and smaller size tokamaks [113]. Gyro-Bohm scaling

essentially means the diffusivities are proportional to the multiplication of the thermal velocity and the square of the gyro radius divided by the major radius [106]. Typically, the Bohm contribution dominates over the majority of most plasma scenarios. On the other hand, the gyro-Bohm contribution governs mainly near plasma center and in small tokamaks with small magnetic field and low heating power.

(a) Bohm term

The Bohm term is derived using dimensional analysis approach with the diffusivity in the plasma written as:

$$\chi = \chi_b F(x_1, x_2, x_3, \dots), \quad (2.29)$$

where χ_b is the basic transport coefficient and F represents an arbitrary function which depends on plasma dimensionless parameters (x_1, x_2, x_3, \dots). For Bohm diffusivity the χ_b is chosen as:

$$\chi_b = \frac{cT_e}{eB_T}, \quad (2.30)$$

where c is the appropriate constant. The function F is chosen according to the diffusivity criteria as:

$$F = \frac{q^2}{L_{pe}^*}, \quad (2.31)$$

$$L_{pe}^* = \frac{P_e}{R \cdot |\vec{\nabla} p_e|}. \quad (2.32)$$

So the diffusivity of Bohm term can be written as:

$$\chi_B = \alpha^B R \left| \frac{\vec{\nabla}(n_e T_e)}{n_e B_T} \right| q^2, \quad (2.33)$$

with the constant α to be determined empirically. However, evidence from JET suggest that the Bohm term in equation (2.33) should also depend on temperature gradient near plasma edge [69]. Consequently, Bohm scaling has final form as follows:

$$\chi_{B_0} = 4 \times 10^{-5} R \left| \frac{\bar{\nabla}(n_e T_e)}{n_e B_T} \right| q^2 \left(\frac{T_e \left(\frac{r}{a} = 0.8 \right) - T_e \left(\frac{r}{a} = 1 \right)}{T_e \left(\frac{r}{a} = 1 \right)} \right). \quad (2.34)$$

(b) Gyro-Bohm term

The Gyro-Bohm is developed similarly using empirical approach. In this scaling the function F is chosen as

$$F = \frac{\rho^*}{L_{pe}}, \quad (2.35)$$

$$\rho^* = \frac{c \sqrt{M_i T_e}}{R Z_i e B_T}, \quad (2.36)$$

where M_i is ion atomic mass and Z_i is ion charge. Substituting these two equations into (2.29), the Gyro-Bohm term can be written as

$$\chi_{gB} = 5 \times 10^{-6} \sqrt{T_e} \left| \frac{\bar{\nabla}(T_e)}{B_T^2} \right|, \quad (2.37)$$

(c) Mixed Bohm/Gyro-Bohm model

In this model, the ion and electron diffusivities are calculated as linear combinations of Gyro-Bohm and Bohm transport coefficients [110]:

$$\chi_i = 0.5 \chi_{gB} + 4.0 \chi_B, \quad (2.38)$$

$$\chi_e = 1.0 \chi_{gB} + 2.0 \chi_B. \quad (2.39)$$

In the simulations, the particle diffusivity (D_H) and the impurity diffusivity (D_Z) are assumed to be the same. They can be calculated as follows

$$D_H = D_Z = \left(0.3 + 0.7 \frac{r}{a} \right) \frac{\chi_e \chi_i}{\chi_e + \chi_i}. \quad (2.40)$$

Empirically, the ITB effect is included into the Bohm-term as a cut-off or step function of shearing rate and magnetic shear relation as shown in equation (2.14):

$$\chi_B = \chi_{B_0} \times \Theta \left(s - 1.47 \frac{\omega_{E \times B}}{\gamma_{ITG}} - 0.14 \right). \quad (2.41)$$

The γ_{ITG} can be calculated as

$$\gamma_{ITG} = \frac{v_{th}}{qR}, \quad (2.42)$$

where v_{th} is the electron thermal velocity. Note that, this version of mixed B/gB model does not take effect of the impurity transport. Therefore, the impurity transport is assumed to be the same as the particle transport throughout this thesis.

2.3.2.2 NCLASS module

In the simulation, the code that is used to simulate neoclassical transport is called NCLASS module, the details can be seen in Ref. [114]. In short, the module can calculate the collisional transport in the plasma, where the non-uniformity of electric and magnetic fields leads to particles drift. It allows the flexibility in calculating the results using different values of plasma collisionality, tokamak geometry and aspect ratio. It is also possible to compute for multi-species plasma within axisymmetric assumption. It is designed to be called from a transport code that provides the plasma temperature and density profiles as well as a number of flux surface averaged geometric quantities. In summary, the module can compute and yield several outputs to be used by the transport solver. For example, poloidal velocity is one of the outputs and it is needed for calculation of the radial electric field. Obviously, NCLASS computes most of neoclassical related transport like ion heat transport, main ions and impurity transport. It can also calculate other plasma characteristics such as parallel electrical resistivity and bootstrap current.

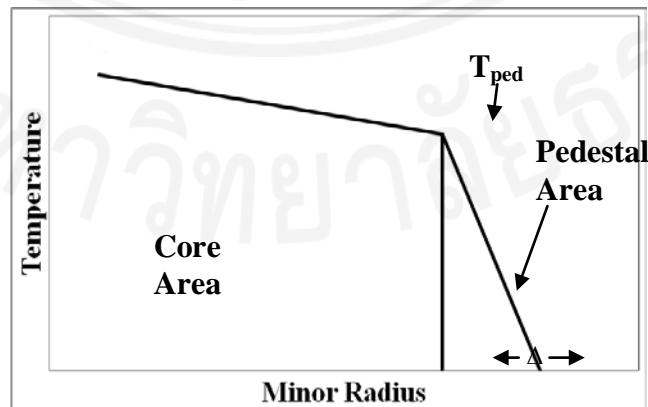


Figure 2.5: Plot of temperature profile near the edge of *H*-mode plasma.

2.3.2.3 Pedestal module

The boundary conditions needed for plasma transport solver is set to be at the pedestal top in the BALDUR code [115]. A simple sketch illustrating pedestal area can be seen in figure 2.5. In other word, pedestal area is where ETB is observed, exhibiting high gradient near plasma edge. First of all, the pressure gradient within pedestal area is more or less constant because normally the pressure profiles are similar to those of temperature, especially in the pedestal (figure 2.5). The pedestal temperature (T_{ped}) in keV unit can be calculated from the following relations [116]:

$$p_{\text{ped}} \equiv (n_{\text{ped},e} + n_{\text{ped},i}) k T_{\text{ped}}, \quad (2.43)$$

$$\frac{p_{\text{ped}}}{\Delta} = \left| \frac{\partial p}{\partial r} \right|, \quad (2.44)$$

where n_{ped} (m^{-3}) is the pedestal density which is the same for ion (subscript i) and electron (subscript e), k is the usual Boltzmann's constant and Δ represents the pedestal width. Using these two equations, the pedestal temperature is in the form:

$$T_{\text{ped}} = \frac{1}{2kn_{\text{ped}}} \Delta \left| \frac{\partial p}{\partial r} \right|. \quad (2.45)$$

So in order to calculate T_{ped} , one must first determine pedestal density, pedestal width and pedestal pressure gradient.

It is known that the pressure gradient in the plasma, especially near the edge, has a maximum limit. This limitation is caused by a ballooning mode instability [117]. Hence, there exists a critical normalized pressure gradient:

$$\alpha_c(s, \delta, \kappa) = -\frac{2\mu_0 R q^2}{B_T^2} \left(\frac{\partial p}{\partial r} \right)_c, \quad (2.46)$$

where μ_0 is permeability of free space and B_T is vacuum toroidal magnetic field. Rewriting this relation and substituting the pressure gradient back into equation (2.89), one obtains

$$T_{\text{ped}} = \frac{\Delta}{2kn_{\text{ped}}} \frac{\alpha_c B_T^2}{2\mu_0 R q^2}. \quad (2.47)$$

The pedestal width Δ is determined using the pedestal width scaling model described in references [116, 118]. It is based on an assumption that ETB is formed when the levels of turbulence growth and shearing rate are comparable. As mentioned earlier,

the shear rate acts as turbulent stabilizing mechanism. The shearing rate is of the form:

$$\omega_{E \times B} \approx \frac{\rho c_s}{\Delta^2}, \quad (2.48)$$

whereas, the maximum turbulence growth rate is proportional to

$$\gamma_{\max} \propto \frac{c_s}{\Delta s^2}, \quad (2.49)$$

where c_s is the ion sound velocity. In essence, the turbulent transport is quenched when the following relation is satisfied:

$$\omega_{E \times B} \geq \gamma_{\max}. \quad (2.50)$$

Substituting this approximation into equations (2.48) and (2.49), the pedestal width is in the form:

$$\Delta = C_1 \rho s^2 = C_1 \left(4.57 \times 10^{-3} \frac{\sqrt{A_H T_{ped}}}{B_T} \right) s^2, \quad (2.51)$$

where C_1 is the proportionality constant and A_H is the average hydrogenic mass. Combining equations (2.47) and (2.51), the final form of T_{ped} can be calculated as:

$$T_{ped} = C_1^2 \left(\left(\frac{4.57 \times 10^{-3}}{4\mu_0 (1.6022 \times 10^{-16})} \right)^2 \left(\frac{B_T^2}{q^4} \right) \left(\frac{A_H}{R^2} \right) \left(\frac{\alpha_c}{n_{ped}} \right)^2 s^4 \right). \quad (2.52)$$

This result is used in BALDUR code to calculate the pedestal temperature which is the boundary condition for transport model, and to eventually compute plasma profiles. According to Onjun *et. al.* [116], the constant C_1 was statistically calculated to be 2.42. The pedestal density (n_{ped}) is calculated using empirical approach [119]. It has the form:

$$n_{ped} = 0.71 n_{el}, \quad (2.53)$$

where n_{el} can be taken from experimental data.

2.3.2.4 Toroidal velocity module

In BALDUR, data for $\omega_{E \times B}$ used in equation (2.41) is given to the code. The code can also use the data taken from experiments. Moreover, $\omega_{E \times B}$ can be calculated from toroidal velocity which can also be taken from experiments. In many cases, these data are not available; they are also quite difficult to measure experimentally.

Most importantly, in order for BALDUR to self-consistently predict the future machine like ITER, it is important that it can calculate ω_{ExB} from fundamental physics quantities such as geometrical data of each tokamak and temperature. Since BALDUR does not directly compute the toroidal momentum equation, the toroidal velocity calculation is done through predictive module. There exists toroidal velocity models both for empirical based model [120-123] and theoretical based model [124]. The first model relates toroidal velocity to local plasma ion temperature and the latter model is based on neoclassical toroidal viscosity (NTV) physics. The details of these models can be seen later in chapter 7.

Chapter 3

Locality Effects on Bifurcation Paradigm of L - H Transition

3.1 Introduction

As mentioned in the previous chapter that L - H transition phenomenon exhibits a bifurcation nature of plasmas [96]. Other quantities can also exhibit this behavior such as plasma temperatures and densities, toroidal rotation and radial electric field [44]. The transition can be visually captured using an s -curve bifurcation diagram similar to that in the work of Malkov *et. al.* [96] where a graph of flux versus gradient has a non-monotonic behavior resulting in bifurcation regime within a certain range of heating. Figure 2.3 shows similar curve with addition of neoclassical regime, which will be explained in later section. The figure captures qualitatively possible regimes in the plasma. At low heat flux, the plasma is dominated by the neoclassical transport, named a “neoclassical regime”. As heat flux is increased, the anomalous effect gradually takes over the transport. Once the heat flux surpasses a critical threshold, the plasma makes a transition to H -mode where anomalous transport is quenched in the barrier region. In the intermediate range, there exists a bifurcation regime where three equilibria are possible, two stable and one unstable. Previous works on bistable s -curve bifurcation models discussed on various characteristics of the models, which result in better understanding of the qualitative aspects as well as gaining considerable insight into L - H transition physics [96-97, 125-129]. The bifurcation model was introduced to explain particle and energy confinement in tokamaks [125]. The work by Lebedev and Diamond used a simple one-field bifurcation model to study spatiotemporal behavior of the plasma and found hysteresis behavior [127]. Malkov and Diamond later applied this concept to analyze the coupled heat and particle transport equations simultaneously and showed that with inclusion of the hyper-diffusion effect, the transition follows Maxwell’s rule [96]. The two-field bifurcation model was then used by Chatthong *et al.* to numerically investigate pedestal width and its dynamics with [130] and without toroidal rotation effect included [131]. Recently, the model includes heat and momentum density transports to analytically study the impact of external torque on formation of the internal transport barrier (ITB)

[128]. Different approaches can also be taken, for example, in the report of Weymiens *et. al.* [129], bifurcation theory is used to explain the transition as well as the dithering H -mode.

3.2 Bifurcation concepts and transition points

Previously, authors of reference [125] used the Fourier transform method to identify the stability of each branch in bifurcation diagram. However, the mechanism during transition was not quite clearly explained. The attempt in this section takes different point of view, in which can be easily understood. In fact, not only the existence of three equilibrium branches within bifurcation regime is thoroughly illustrated, but the location of transitions and dynamics during transitions can be also explained.

This particular work focuses on a one-field transport equation, which assumes that heat and particle transport equations are completely independent from each other. This approach has showed that many important qualitative features of the L - H transition can be analyzed like those discussed in the report of Lebedev *et. al.* [127]. A version of heat transport equation, in slab geometry, representing the conservation of energy is of the form:

$$\partial_t p - \partial_x \left(\left[\chi_{neo} + \frac{\chi_{ano}}{1 + \alpha v_E'^\beta} \right] \partial_x p \right) = H(x), \quad (3.1)$$

where χ_{neo} and χ_{ano} represent the neoclassical and anomalous transports, respectively, and β is the mode of the suppression relating to how the turbulent convective cells are distorted by the flow shear v_E' , which is always positive in this work. This form of transport equation is improved from that discussed in the work of Malkov *et. al.* [96]. It was found that the confinement improvement of H -mode is a result of transport reduction in the anomalous channel, reducing transport to a neoclassical level [44]. The time variation of the pressure can be written as:

$$\partial_t p = H(x) - \partial_x \left[\chi_{neo} + \frac{\chi_{ano}}{1 + \alpha g^\beta} \right] g, \quad (3.2)$$

where $g = -\partial_x p$ (always positive) and the flow shear is assumed to be driven by the pressure gradient. Equation (3.2) can be integrated with respect to x as follows:

$$\frac{\partial}{\partial t} \int_0^x p dx' = \int_0^x H(x') dx' - \int_0^x \frac{\partial}{\partial x'} \left[\chi_{neo} + \frac{\chi_{ano}}{1 + \alpha g^\beta} \right] g dx', \quad (3.3)$$

with

$$w = \int_0^x p dx', \quad (3.4)$$

equals to the energy content per surface area. Thus, $\dot{w} = \partial_t w$ represents the energy density flow of plasma within the flux surface. As a result, equation (3.3) can be written as:

$$\dot{w}(x) = Q(x) - \left[\chi_{neo} + \frac{\chi_{ano}}{1 + \alpha g(x)^\beta} \right] g(x), \quad (3.5)$$

where $Q(x)$ is the heat flux given to the plasma. This is an integro-differential partial differential equation. Evidently, this equation shows that only the heat flux, as an independent variable, determines possibility of $L-H$ transition.

Physically, equation (3.5) can be treated as the time variation of the energy density, which is a function of both pressure gradient and heat flux. It is plotted in figure 3.1 with each panel representing a graph of \dot{w} versus g at different values of Q , which is a function of x . Note that the constants are arbitrarily chosen in this figure as well as in later figures, only the qualitative information will be of importance. Treating a local point along the graph as an initial point, as time goes on, three different scenarios can happen. If the point lies within regions where $\dot{w} > 0$, the plasma energy increases with time resulting in increase of pressure gradient (arrow to the right). On the other hand, if the point lies within regions where $\dot{w} < 0$, the pressure gradient decreases because the plasma energy decreases with time (arrow to the left). Lastly, when the point lies where $\dot{w} = 0$, the pressure gradient does not change because the point is in equilibrium; such points are called fixed points. At a low value of Q (panel a), there exists only one stable fixed point. If Q reaches the first critical value $Q_1^{st\ crit}$ (panel b), an additional half-stable fixed point is created. At higher Q (panel c), there are three fixed points: two stable and one unstable fixed points. If Q reaches the second critical value $Q_2^{nd\ crit}$ (panel d), the two fixed points on the left are combined and become a single half-stable point. If Q exceeds $Q_2^{nd\ crit}$ (panel e), the half-stable point is destroyed and there remains one stable point at a relatively high

pressure gradient.

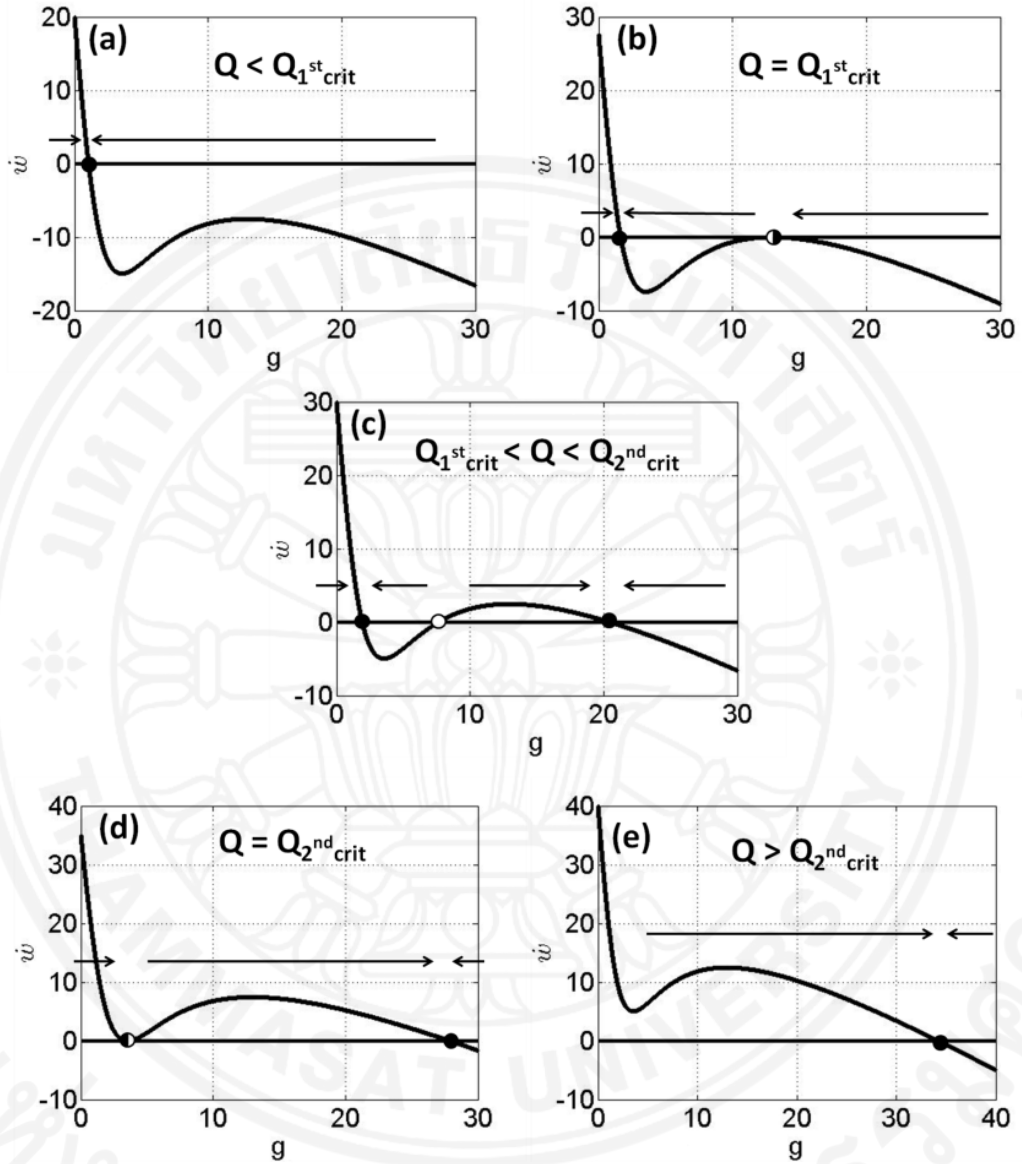


Figure 3.1: Fixed points for each value of heat flux and their stabilities: solid dot for stable, open dot for unstable and semi-open dot for half-stable fixed points.

The graphical interpretation can be used to describe the dynamics of a local pressure gradient. The foundation of *L-H* and *H-L* transitions can be understood using a stability analysis approach from time evolution of the plasma profiles. One can imagine the heat flux Q as an independent variable which can be increased or decreased. Accordingly, the qualitative structure of the plasma system can potentially be changed as Q is varied. In particular, the fixed points can be destroyed or created,

or their stability can also change. The critical assumption used is that the plasma the change of Q is slow enough for the plasma to relax. Figure 3.2 illustrates the dynamics near bifurcation regime and identifies the transition points. In this figure, the equilibrium fixed points (both stable and unstable) as a function of heat flux are showed. They form a traditional bifurcation diagram. Essentially, the pressure gradient depends non-monotonically on the heat flux. The two stable branches of the s -curve stand for low (L -branch) and high (H -branch) pressure gradients, while the other branch is physically irrelevant because it would correspond to unstable equilibrium. Based on the fixed points analysis described above, as Q is increased from zero, the plasma remains on L -branch in the bifurcation regime and jumps to H -branch when Q is greater than the second critical flux. On the other hand, when Q is decreased from high value, the plasma remains on H -branch in the bifurcation regime until Q is below the first critical flux. In fact, $Q_2^{nd\ crit} = Q_{L \rightarrow H}$ and $Q_1^{st\ crit} = Q_{H \rightarrow L}$. In addition, the heat flux at H - L transition is found to be lower than that of L - H transition, implying hysteresis phenomenon.

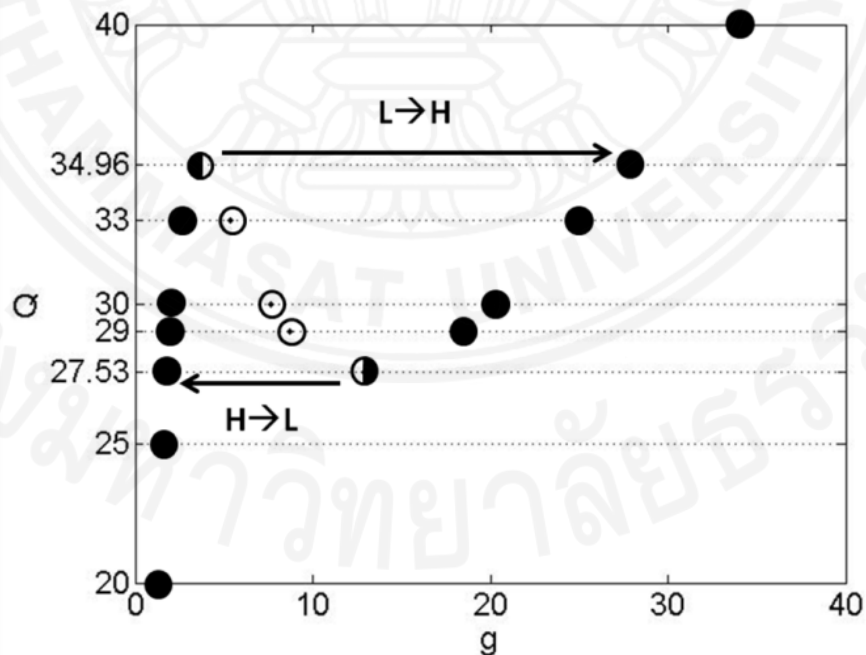


Figure 3.2: Bifurcation diagram constructed from fixed points illustrating 2 stable branches and 1 unstable branch with L - H and H - L transitions.

3.3 Locality effects on L - H transition and hysteresis

This part emphasizes on the locality effects on this bifurcation description of L - H transition. In the previous works of Malkov *et. al.* [96], the neoclassical and anomalous transports were assumed to be constant. Those assumptions made the simplification suitable for analytical study, but they are not physically preferable. In this section, localities of plasma transports are implemented into this bifurcation picture of L - H transition. The changes and improvements are discussed.

3.3.1 Transition criteria

The bifurcation diagram shown in figure 2.2 can be used to explain L - H transition only with non-monotonic behavior of the flux versus gradient curve. Namely, it is required that local maximum and minimum must exist to represent bifurcation regime. This requirement leads to a criterion that the ratio of anomalous over neoclassical transport coefficients has to be greater than a certain value. The criterion for constant transport coefficients was discussed in the work of [96] to be either 8 or 16/9 depending on the strength of shear suppression. This is a mathematical implication of the model. However it has a physical agreement where it is known that anomalous transport is one (for ion) or two (for electron) order of magnitude higher than neoclassical transport. Thus, the discussion on this work is based on the plasma that behaves accordingly. In other words, L - H transition is always possible for the plasma with relatively high anomalous transport. Therefore, if a sufficient heat flux is provided to the system, the plasma will bifurcate to H -mode. The ratio lower than the criterion implies that the stabilization is insufficient for such a transition, which means that the plasma remains in L -mode because of no discontinuity of the gradient profile. Experimentally, if this kind of low anomalous transport can be achieved then the suppression is not even necessary and the plasma can reach high performance L -mode.

This section shows that the similar but more complicated criteria for the transition retain with more realistic models of anomalous transport used. Three different models for describing anomalous transport χ_{ano} , which is the dominant term in fusion plasma as opposed to the neoclassical term χ_{neo} , are considered. Being much weaker, χ_{neo} is assumed to be just a constant. For the first model, the anomalous

transport is assumed to be just constant, which is similar to those previous works of [96, 125]:

$$\chi_{ano} = c_1, \quad (3.6)$$

For the second model, the anomalous transport is assumed to be driven by the local pressure gradient:

$$\chi_{ano} = c_2 g^m, \quad (3.7)$$

similar to what explored in the work of [97] with additional parameter m representing the mode of the drive. The third model is a critical gradient model in which there exists a critical point which turns on the anomalous transport [132-133]:

$$\chi_{ano} = c_3 (g - g_c) \theta(g - g_c), \quad (3.8)$$

where g_c is a critical gradient point, θ represents a Heaviside step function and c_i represent proportional constants. Based on these three models, the generalized form of heat transport equation at steady state, i.e., for the fixed points of equation (3.5), is as follows:

$$Q = \begin{cases} \chi_{neo} g & , g < g_c \\ \left[\chi_{neo} + \frac{c(g - g_c)^m}{1 + \alpha(g)^\beta} \right] g & , g \geq g_c \end{cases}. \quad (3.9)$$

A plot of Q versus g from this equation is illustrated in figure 2.2, the neoclassical regime represent the range where anomalous transport is minuscule. First of all, equation (3.9) implies that $\beta > m + 1$ in order for the plot to be non-monotonic. This algebraic constraint is a limitation in which this model is applicable. Physically, this means the mode of the suppression has to be greater than the mode of anomalous transport. Algebraically, for $g \geq g_c$, the locations (g^*) of the local maximum and minimum exist where $\partial_g Q = 0$, giving relation:

$$(1 + \alpha g^{*\beta})^2 + \lambda(1 + \alpha(1 - \beta)g^{*\beta})(g^* - g_c)^m + \lambda m(1 + \alpha g^{*\beta})g^*(g^* - g_c)^{m-1} = 0 \quad (3.10)$$

where $\lambda = c/\chi_{neo}$. This can be rewritten to the form:

$$\lambda = \frac{(1 + \alpha g^{*\beta})^2}{\left(\alpha((\beta - (m + 1))g^* - (\beta - 1)g_c)g^{*\beta} - (m + 1)g^* + g_c \right)(g^* - g_c)^{m-1}}. \quad (3.11)$$

This function $\lambda(g^*)$ has a notable feature in which, for $g^* > 0$, there exist a single local minimum value. This minimum value can be calculated simply from $\partial_g \lambda = 0$. For existence of non-monotonic curve in Q versus g space, it is required that λ has to be greater than this minimum value. The first model with $m=0$ and $g_c = 0$ yields that:

$$\lambda_1 > \lambda_{crit} = \frac{4\beta}{(1-\beta)^2}, \quad (3.12)$$

which agrees with what found in the work of [96] with β equals to 2 and 4. The second model with $g_c = 0$ yields that:

$$\lambda_2 > \lambda_{crit} = f\alpha^{m/\beta}, \quad (3.13)$$

where

$$f = f(m, \beta) = \frac{(f_1 + \beta f_2 + 2f_3)^2 (2f_3)^{\frac{m}{\beta}-1}}{(f_1 + \beta f_2)^{\frac{m}{\beta}} [(\beta - (m+1))(f_1 + \beta f_2) - 2f_3(m+1)]}, \quad (3.14)$$

$$f_1 = f_1(\beta, m) = \beta^2 + \beta(2m+1) - 2m(m+1), \quad (3.15)$$

$$f_2 = f_2(\beta, m) = \sqrt{\beta^2 + 2\beta(2m+1) - 4m(m+1) + 1}, \quad (3.16)$$

$$f_3 = f_3(\beta, m) = (\beta - m)(\beta - (m+1)). \quad (3.17)$$

It is analytically not possible to find the criteria for the third model ($m = 1$) because of the odd terms in equation (3.11). However, a numerical method can be applied to show that there indeed exists a critical value like the previous two models. Before showing the numerical results, it is worth noting here that equation (3.11) with $m=1$ can be rewritten as:

$$g_c = \frac{\frac{(1 + \alpha g^{*\beta})^2}{\lambda} + 2g^* - \alpha(\beta - 2)g^{*\beta+1}}{1 - \alpha(\beta - 1)g^{*\beta}}. \quad (3.18)$$

Apparently, the graph of g_c versus g^* has a local maximum within the applicable region. This limitation is shown as example in figure 3.3 where the non-monotonic behaviour of the bifurcation diagram vanishes if g_c reaches its threshold value $g_{c,th}$. Physically, g_c represents critical gradient value where the anomalous transport is turned on. Therefore, if this critical gradient is too high, then the anomalous transport will be too small relative to the neoclassical transport. Consequently, the system enters the ineffective stabilization regime or the high performance L -mode with no

possibility of L - H transition. Figure 3.4 (top panels) also shows that as the critical gradient value is higher, the heat flux required for the transition is reduced but the gradient value at the transition is increased. This makes sense because, when the anomalous transport is reduced, it should be easier to reach the heat flux requirement ($Q_{L \rightarrow H}$). Furthermore, the bottom panels of this figure shows that the threshold of critical pressure gradient $g_{c,th}$ is increased if either the anomalous transport is increased or the neoclassical transport is decreased. In summary, this analysis shows the existence of a critical ratio of anomalous to neoclassical transport coefficients above which the L - H transition becomes a bifurcation. This critical ratio is dependent on variables m , β , the suppression constant α , as well as the critical gradient g_c .

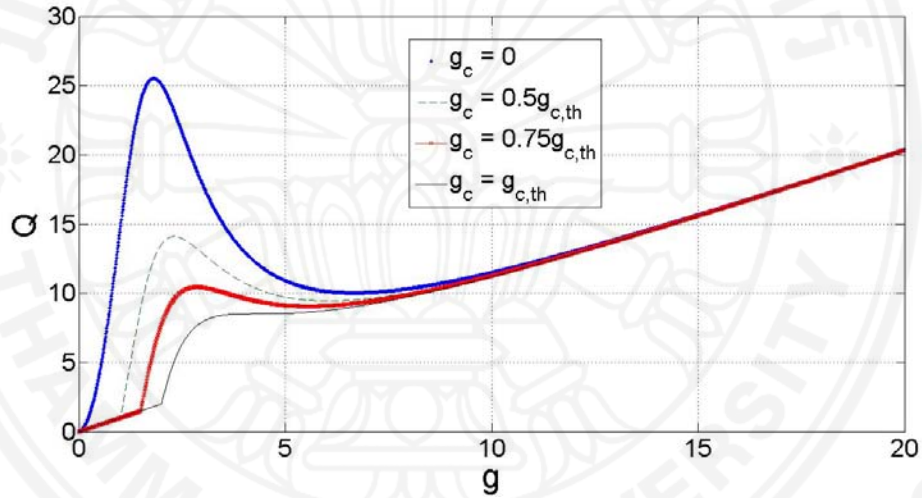


Figure 3.3: Bifurcation diagram at different values of critical gradient.

3.3.2 Backward transition and hysteresis properties

It was found that H -mode plasmas can be retained even if heating power is reduced below L - H transition threshold. This hysteresis characteristic in fusion plasma has been found in various experiments and the reduction of heating power was found to be even as high as a factor of two [44, 134]. The bifurcation diagram, figure 2.2, also captures this hysteresis loop behavior. The question of which mode the plasma resides, depends on the direction of heat ramping. If it is ramped up, the plasma makes an abrupt jump to H -mode as heat flux exceeds $Q_{L \rightarrow H}$. From H -mode plasma, if the heat flux is reduced below $Q_{H \rightarrow L}$, it transits back to L -mode. In this section, analytical study on hysteresis depth is discussed based on this bifurcation

picture. Definition is given here for hysteresis depth study which consists of the heat fluxes and pressure gradients at $L\text{-}H$ transition ($Q_{L\rightarrow H}$, $g_{L\rightarrow H}$) and back $H\text{-}L$ transition ($Q_{H\rightarrow L}$, $g_{H\rightarrow L}$) as well as their differences (ΔQ , Δg), respectively. This part analyzes the effects of neoclassical and anomalous transports and parameter m on the hysteresis depth. This study can be used to further optimize plasma performance versus heating with respect to H -mode sustainment.

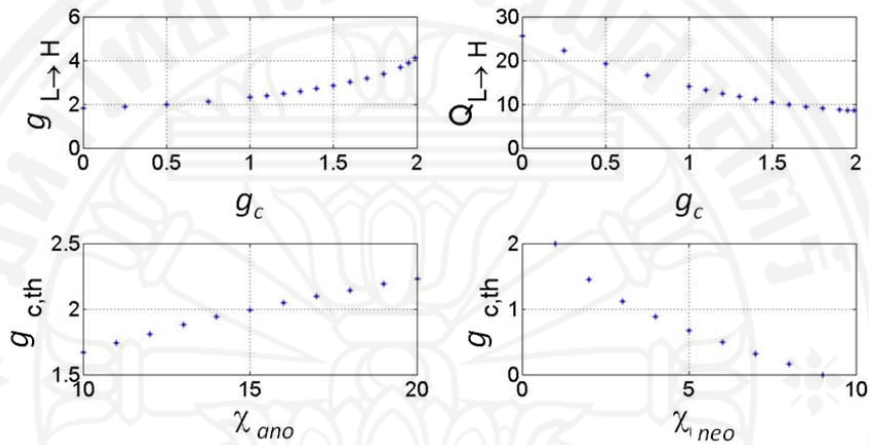


Figure 3.4: Effects of critical pressure gradient on the pressure gradient (top left) and threshold flux (top right) at $L\text{-}H$ transition and effects of anomalous (bottom left) and neoclassical (bottom right) transport coefficients on the threshold limit of the critical pressure gradient.

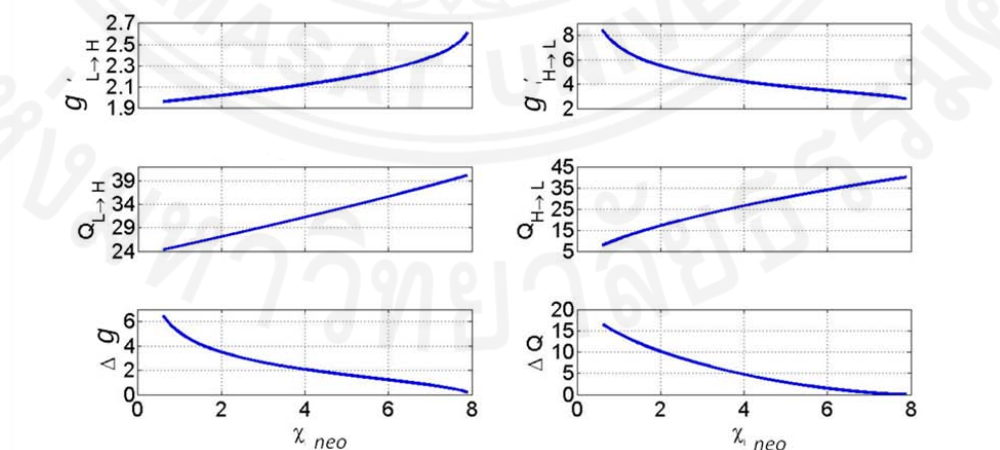


Figure 3.5: Hysteresis depth as a function of neoclassical transport.

Hysteresis depth as a function of neoclassical transport is illustrated in figure 3.5. First of all, the heat flux reduction ratio ($Q_{L\rightarrow H}/Q_{H\rightarrow L}$) is ranged from around 4 to

1 depending on the values of χ_{neo} . As χ_{neo} is increased, both heat flux thresholds are increased because more heat is needed to compensate the increment of the transport. The interesting part here is that the rate of thresholds increase is not the same. Consequently, it causes ΔQ to reduce non-linearly to zero or the reduction ratio becomes unity as neoclassical effect is higher. This is where the plasma reaches ineffective stabilization regime. Similarly, the difference in pressure gradient Δg is also reduced with higher neoclassical effect. It can be seen that $g_{L \rightarrow H}$ is increased while $g_{H \rightarrow L}$ is decreased.

Figure 3.6 shows hysteresis depth as a function of anomalous transport. The heat flux reduction ratio is ranged from around 1 to 2 as c is higher. As anomalous effect is increased, $Q_{L \rightarrow H}$ is increased almost linearly whereas $Q_{H \rightarrow L}$ is also increased but at lower rate. Both heat flux thresholds are increased because more heat is needed to compensate the increment of the transport. As a result, ΔQ is enlarged at a non-linear rate as the plasma moves away from the ineffective stabilization regime. This result tells us that at higher value of anomalous transport the hysteresis in heating becomes more prominent. Similarly, the difference in pressure gradient Δg is also increased with higher anomalous effect. It can be seen that $g_{L \rightarrow H}$ is decreased while $g_{H \rightarrow L}$ is increased.

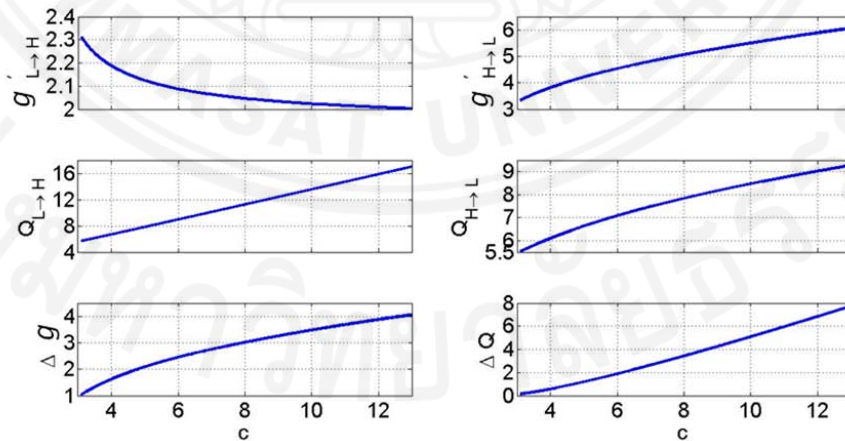


Figure 3.6: Hysteresis depth as a function of anomalous transport.

Figure 3.7 shows hysteresis depth as a function of the mode m of pressure gradient driven anomalous transport for $\beta=4$. The heat flux reduction ratio is ranged from around 2 to 1 as m is higher. As m is increased, both $Q_{L \rightarrow H}$ and $Q_{H \rightarrow L}$ are

increased, the same trend as effects of c as expected. Both heat flux thresholds are increased because more heat is needed to compensate the increment of the transport. ΔQ is initially increased but its increasing rate is reduced, as the limit $m=\beta+1$ is reached, and is eventually decreased. This is because β starts to take over at the limit. The behavior is the same in Δg and $g_{H \rightarrow L}$ while $g_{L \rightarrow H}$ keeps increasing with m .

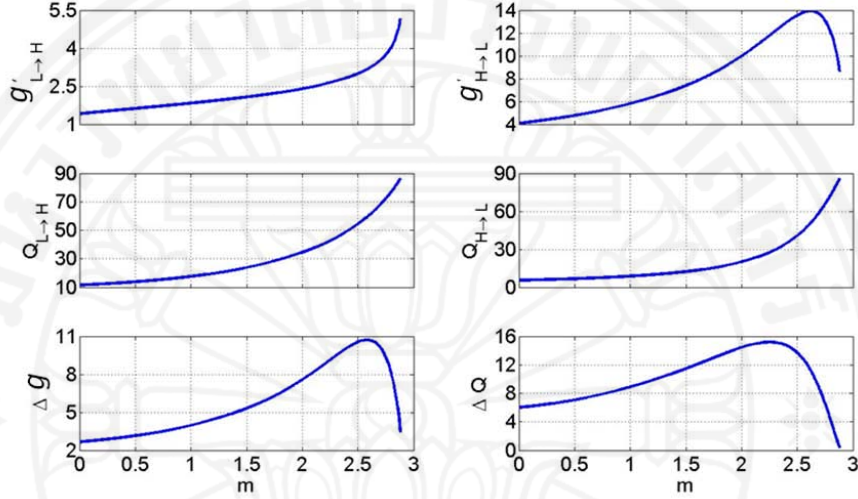


Figure 3.7: Hysteresis depth as a function of m .

3.3.3 Stability diagram

Figure 3.8 summarizes the discussions in this work with stability diagram. It shows the plot of ratio of anomalous over neoclassical effect λ with the heat flux Q representing different regimes in the plasma. When the criteria like those in equations (3.12) and (3.13) are not satisfied $L-H$ transition is not possible and the plasma remains in the ineffective stabilization regime (L -mode). Above the horizontal line in the regime where the transition is possible, the mode of the plasma is determined by the heat flux. So the plasma regimes are separated into four regions: neoclassical, L -mode, H -mode and the bifurcation regime where the plasma can either be in L -mode or H -mode. However, the plasma can only exist in one equilibrium state which is determined from the dynamics of the heat flux variation. If the heat flux is increased from lower value, then the plasma stays in L -mode in this coexistence regime. Whereas, if the heat flux is decreased from higher value, the plasma remains in H -mode until it enters the L -mode regime. At low heat flux, the anomalous transport becomes intrinsically stabilized so the plasma is in neoclassical regime. Moreover, it

can be seen that as the ratio is increased the region of bifurcation regime is also enlarged. It appears that the enlargement is nonlinear which will have significant implication on the sustainment of *H*-mode plasma in the high heating regime.

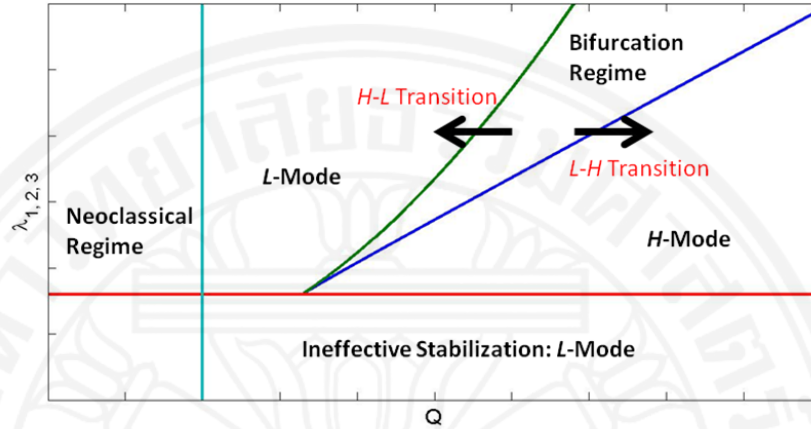


Figure 3.8: Fixed points for each value of heat flux and its stability.

3.4 Conclusion

An analytical study based on bifurcation and stability of fixed points shows that at low value of heat flux, the plasma is governed by neoclassical regime and at higher heat flux the anomalous transport dominates with a range of bifurcation regime existence. As a result, a sudden increase of local pressure gradient can be achieved, which exhibits the *L-H* transition. This transition depends on the direction of heat ramping, where a backward *H-L* transition can occur at lower heating power than that for a forward *L-H* transition during ramping down phase, implying hysteresis phenomena. An analytical study of bifurcation shows that two conditions are necessary for plasma to make an *L-H* transition. Firstly, the ratio between anomalous and neoclassical transport coefficients must reach a critical value which is found to be a function of flow suppression and anomalous forms, in which locality effects on anomalous transport appear to stringent the requirement. This criterion persists even with more realistic choices of anomalous transport models. Secondly the source heat flux injected into the system must be higher than a threshold. The hysteresis depth is found to be proportional to anomalous transports and inversely proportional to neoclassical transport and suppression strength except near marginal point.

Chapter 4

Study of L - H Transition and Pedestal Width Based on 2 Fields Bifurcation and Fixed Point Concepts

4.1 Introduction

Previously, some research works based on bistable s -curve bifurcation models [96-97, 125-129] have been developed, which result in understanding of the qualitative aspects as well as gaining considerable insight into L - H transition physics. However, the dynamics of the transport barrier with respect to intrinsic property of the plasma has not been fully understood. In this chapter, two-field bifurcation models are used to analyze formation of ETB as well as its evolution. Using numerical method to solve the coupled transport equations, the time evolution results can be illustrated.

4.2 Bifurcation model and fixed points analysis

The focus of this section is to introduce the two-field bifurcation model and conceptually and visually discuss local stability of a plasma and dynamics of L - H transition as well as its locations on bifurcation diagram [131]. Simplified version of heat and particle transport equations, in slab geometry, can be expressed respectively in the form:

$$\frac{3}{2} \frac{\partial p}{\partial t} - \frac{\partial}{\partial x} \left[\chi_{neo} + \frac{\chi_{ano}}{1 + \alpha v_E'^2} \right] \frac{\partial p}{\partial x} = H(x, t), \quad (4.1)$$

$$\frac{\partial n}{\partial t} - \frac{\partial}{\partial x} \left[D_{neo} + \frac{D_{ano}}{1 + \alpha v_E'^2} \right] \frac{\partial n}{\partial x} = S(x, t), \quad (4.2)$$

where D_{neo} represents particle neoclassical transport coefficient, D_{ano} represents particle anomalous transport coefficient, and the thermal H and particle S sources are localized at plasma center and edge, respectively. The main ingredient for the stabilization of the anomalous transport is the flow shear v_E' , which accounts for the known reduction of turbulent transport by sheared radial electric field [45]. It couples the two transport equations according to the force balance equation as showed in the work of Malkov *et.al.* [96]:

$$v'_E = c \frac{E'_r}{B} \approx -\frac{c}{eBn^2} p'n', \quad (4.3)$$

Note that the curvature, the toroidal and poloidal rotation contributions are neglected here. Equations (4.1) and (4.2) can be rewritten as time variation of the pressure and density as:

$$\frac{\partial p}{\partial t} = H - \frac{\partial}{\partial x} \left[\chi_{neo} + \frac{\chi_{ano}}{1 + \alpha v_E'^2} \right] g_p, \quad (4.4)$$

$$\frac{\partial n}{\partial t} = S - \frac{\partial}{\partial x} \left[D_{neo} + \frac{D_{ano}}{1 + \alpha v_E'^2} \right] g_n, \quad (4.5)$$

where $g_p \equiv -p'$ and $g_n \equiv -n'$. Integrations of these two equations with respect to x yield the followings:

$$\dot{w} = Q - \left[\chi_{neo} + \frac{\chi_{ano}}{1 + \alpha v_E'^2} \right] g_p, \quad (4.6)$$

$$\dot{\eta} = \Gamma - \left[D_{neo} + \frac{D_{ano}}{1 + \alpha v_E'^2} \right] g_n, \quad (4.7)$$

where $Q = \int H dx$ and $\Gamma = \int S dx$ are the heat and particle fluxes given to the plasma. These two equations represent the time variation flow of energy and particle contents through a flux surface with $\dot{w} = \partial w / \partial t$ and $\dot{\eta} = \partial \eta / \partial t$ defined as follows:

$$\int p dx = \sum_i p_i \Delta x_i = \sum_i \frac{F_i}{A_i} \Delta x_i = \sum_i \frac{W_i}{A_i} = \sum_i w_i \equiv w, \quad (4.8)$$

$$\int n dx = \sum_i n_i \Delta x_i = \sum_i \frac{N_i}{V_i} \Delta x_i = \sum_i \frac{N_i}{A_i} = \sum_i \eta_i \equiv \eta, \quad (4.9)$$

where F_i is the total force acting on a flux surface area A_i due to the plasma pressure p_i , W_i is the work done by the pressure, w is total work done per surface area or the energy density of plasma within the flux surface and η is the particle surface density of plasma. They are coupled through the shear term of equation (4.3). In a transient limit $\dot{w} = \dot{\eta} \approx 0$, a simple decoupling technique can be applied as $D_{ano} g_n \times (6) - \chi_{ano} g_p \times (7)$ resulting in:

$$g_n = \frac{\Gamma \chi_{ano} g_p}{(Q D_{ano} + D_{neo} \chi_{ano} g_p - \chi_{neo} D_{ano} g_p)}. \quad (4.10)$$

This can be substituted in equation (4.6) to decouple the two fields.

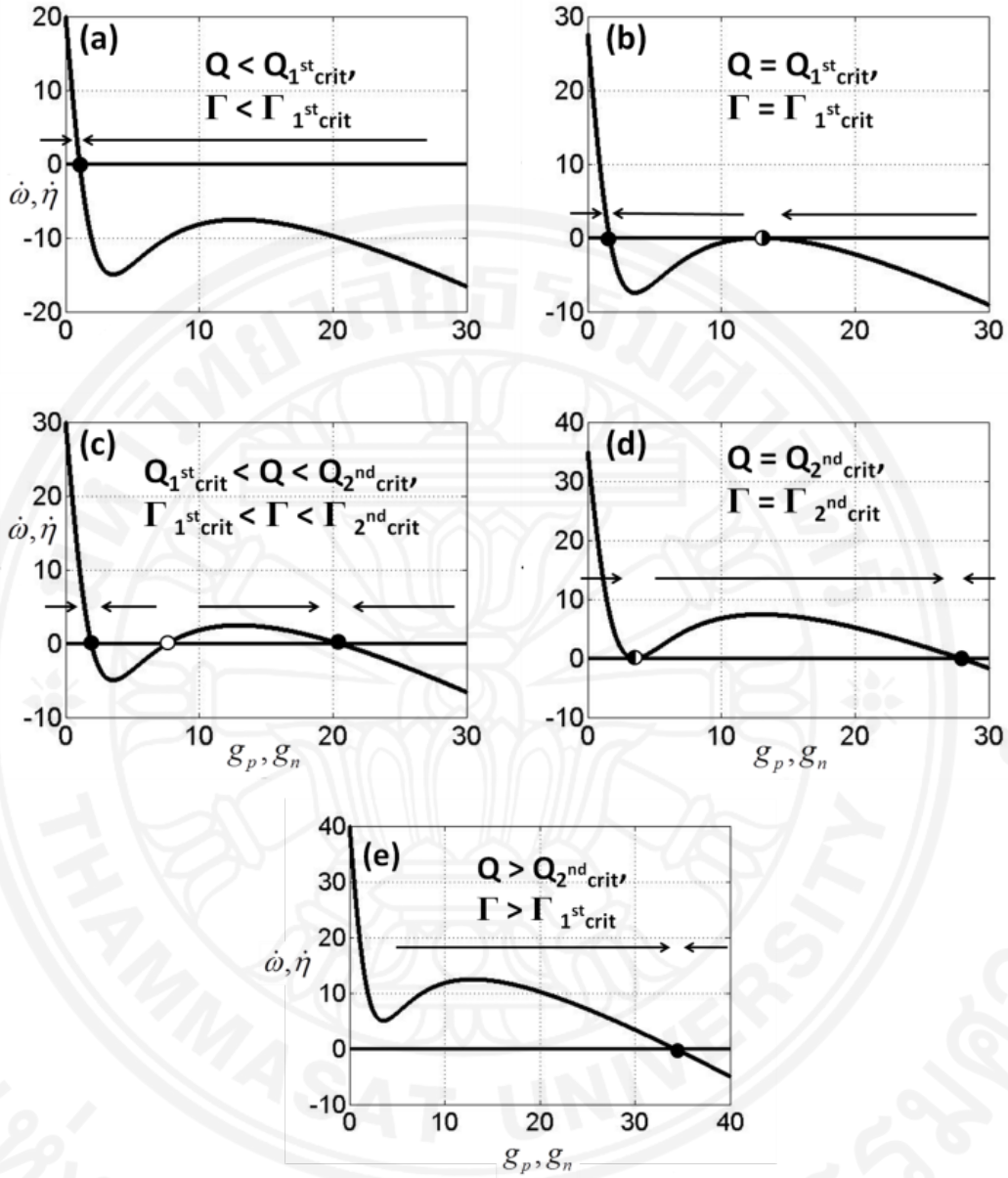


Figure 4.1: Fixed points for each value of heat/particle flux and their stabilities: solid dot for stable, open dot for unstable, and semi-open dot for half-stable fixed points.

Analysis from this point on is based on the heat transport equation for L - H transition. A similar discussion can be carried out for the particle transport equation as the ASDEX team [38] has shown that there exists both heating power and density thresholds for L - H transition. Equation (4.6) is similar to that of (3.5), so the consequences are similar. It is plotted in figure 4.1 with each panel representing a

graph of \dot{w} versus g_p (or versus $\dot{\eta}$ versus g_n for particle field) at different values of Q (or Γ).

Figure 4.2 illustrates where only fixed points are mapped onto fluxes versus gradients spaces. The fixed point stability is also showed as closed circle for stable and open circle for unstable points. This is a traditional bifurcation diagram, similar to those showed in the works of Malkov *et. al.*, Staebler *et. al.*, and Jhang *et. al.* [96, 127-128], respectively. Evidently, $Q_{L \rightarrow H} = Q_2^{nd\ crit}$, $Q_{H \rightarrow L} = Q_1^{st\ crit}$, $\Gamma_{L \rightarrow H} = \Gamma_2^{nd\ crit}$ and $\Gamma_{H \rightarrow L} = \Gamma_1^{st\ crit}$. Even though each of pressure and density fields can have bifurcation diagram with threshold fluxes for L - H transition and hysteresis loop they interact with each other. This is illustrated in figure 4.3 which shows three bifurcation curves on Q versus g_p space at different values of particle flux ($\Gamma_1 < \Gamma_2 < \Gamma_3$). As particle flux is increased the suppression strength by the flow shear is also increased. Hence it is physically relevant that the requirement $Q_{L \rightarrow H}$ for the transition is less stringent.

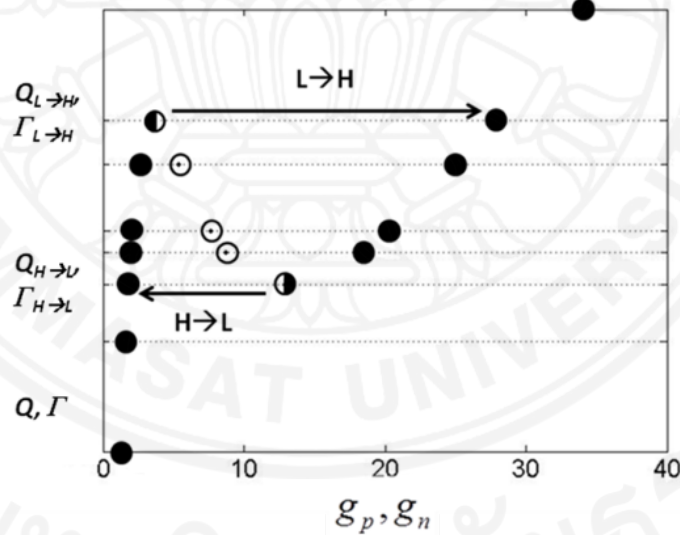


Figure 4.2: Bifurcation diagram illustrating 2 stable branches and 1 unstable branch with L - H and H - L transitions.

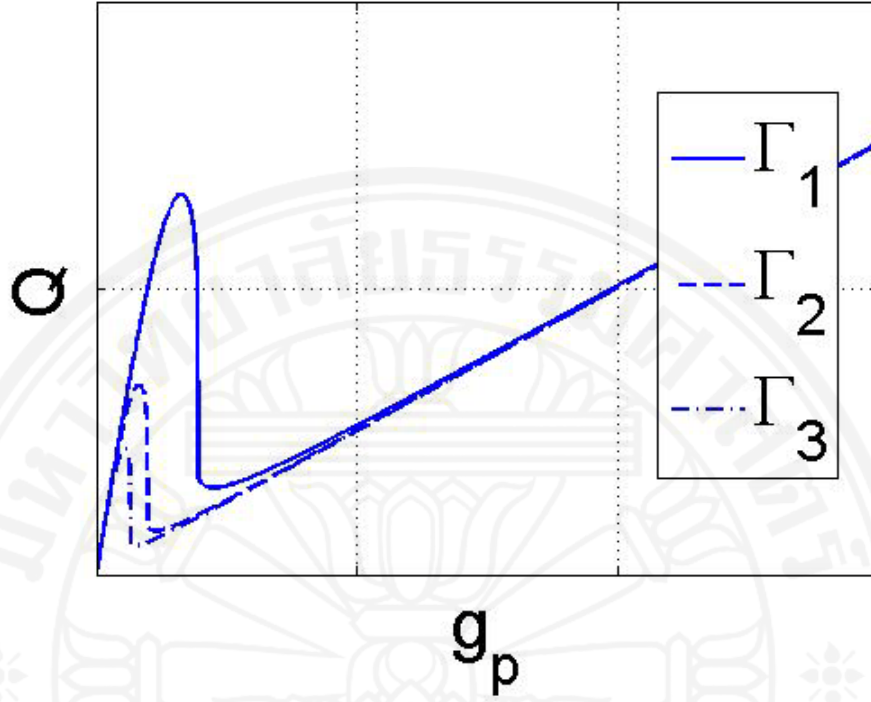


Figure 4.3: Bifurcation diagram of pressure field at different values of particle flux.

4.3 Numerical results and discussions

In this section, the two transport equations (4.1) and (4.2) are solved simultaneously using discretization method for partial differential equation. Heat and particle sources are localized at plasma center and edge, respectively, and they are constant in time. The numerical results yield time evolution of plasma profiles i.e. pressure, density, and their gradients. The neoclassical transport coefficients are simply set to be constant while the anomalous transport coefficients follows critical gradient transport model similar to that described by Garbet *et. al.* [132]:

$$\chi_{ano} = c_z (p' - p'_c) \theta(p' - p'_c), \quad (4.11)$$

$$D_{ano} = c_d (n' - n'_c) \theta(n' - n'_c), \quad (4.12)$$

where c_z and c_d are constants, p'_c and n'_c are the critical gradients for pressure and density fields, respectively, and θ represents a Heaviside step function.

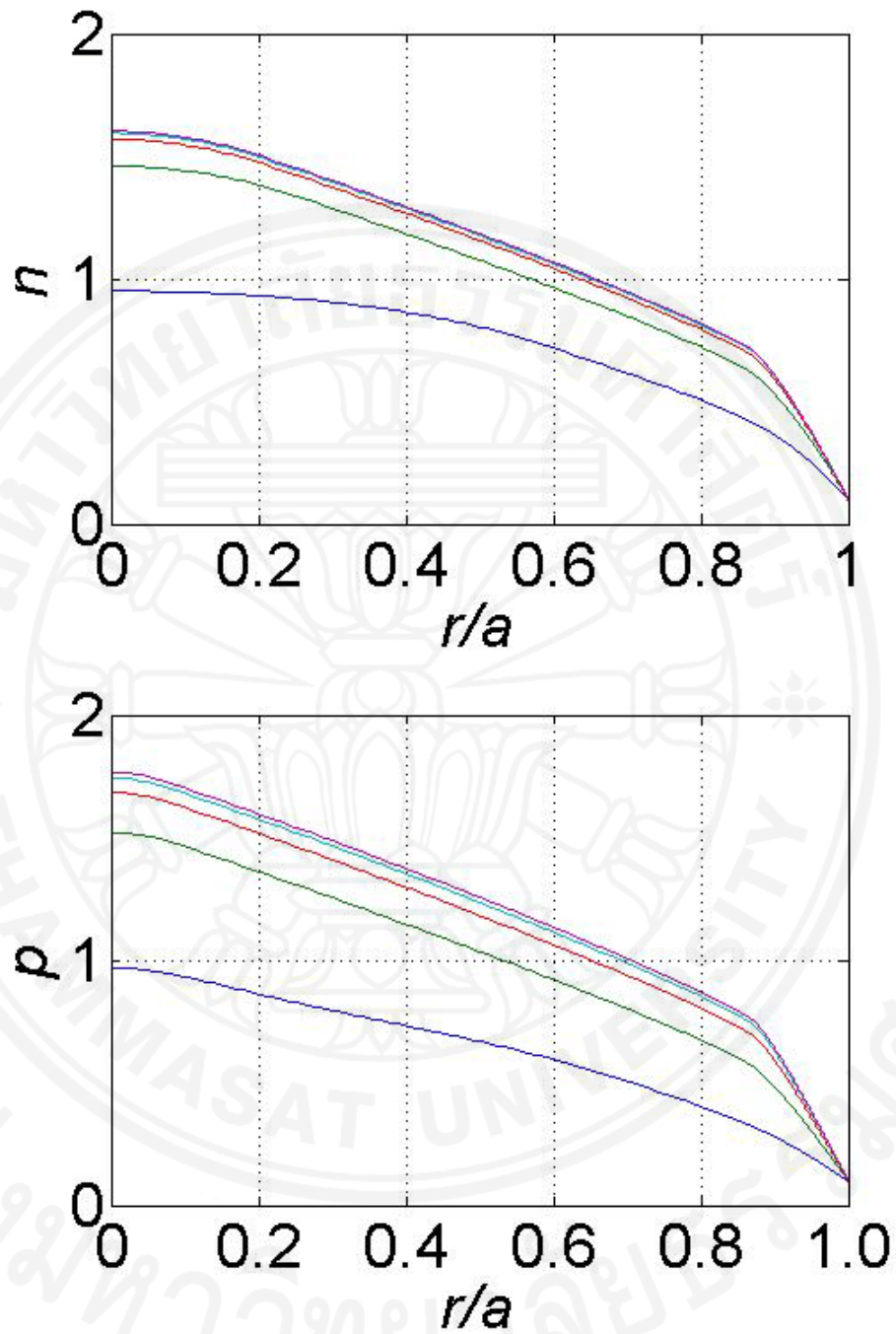


Figure 4.4: Plasma density (top) and pressure (bottom) profiles as a function of normalized minor radius at times 200 ms apart.

4.3.1 Pedestal dynamics

This section illustrates the pedestal growth in the plasma. The crucial assumption to be noted here is that the pedestal is allowed to grow without any

constraint, like MHD instability, as the aim of this work is to study the intrinsic property of this plasma system. Hence, these results presumably predict what would happen to the plasma and its pedestal if loss mechanism like ELM can be controlled. First of all, the two criteria (minimum flux and minimum diffusivities ratio) for possibility of L - H transition according to bifurcation model are satisfied [135] so the plasma is ensured to reach H -mode at steady state. Figure 4.4 demonstrates the time evolution profiles of plasma density and pressure at time approximately 200 ms apart. It shows that the plasma profiles make bigger increases early on. The change is slower as the plasma reaches steady state. It can also be seen that the central pressure is increased by almost two times from L -mode to H -mode. Similarly, the increase in central density is around 50%. One other thing to notice here is that the density profiles tend to be more flat in the plasma core. This makes sense because the density flux is generated from plasma edge while the thermal flux comes from plasma core.

It appears that when plasma instability, i.e. pressure gradient driven instability or current driven instability, is neglected, the pedestal is intrinsically able to expand inward. This growth of the pedestal is showed in figure 4.5 which illustrates pedestal width as a function of time for both pressure and density channels. The heat and particle sources are assumed to be constant in time. Evidently, the pedestal is formed first on the density channel. The growth of pedestal is initially fast, and then it slows down and eventually reaches its steady state. It appears that the pedestal growth is strongly superdiffusive ($\Delta_{ped} \propto t^b, b > 0.5$), agreeing with the turbulent nature of the plasma because in this phase the suppression effect is still low, thus turbulent transport plays a dominant role. Later, wider region of the plasma is suppressed so only the neoclassical transport takes effect in the pedestal region resulting in slower pedestal growth (subdiffusion or even lower). At some later time, the pedestal is also formed for the pressure. Two interesting points are worth mentioning here. First of all, even though the pedestals of both channels do not form at the same time, they have the same width. This is likely to be explained by symmetry between both transport equations. Secondly, the time it takes the plasma to evolve during H -mode or the pedestal expansion time is around one order of magnitude slower than the time it takes for the plasma to evolve from L to H modes. This characteristic of the model is

doubtful because, in the real tokamak plasma, instabilities at the edge cannot yet be controlled fully and efficiently. Moreover, one has to make sure that plasma loss via transport is the sole mechanism in order to observe this behavior.

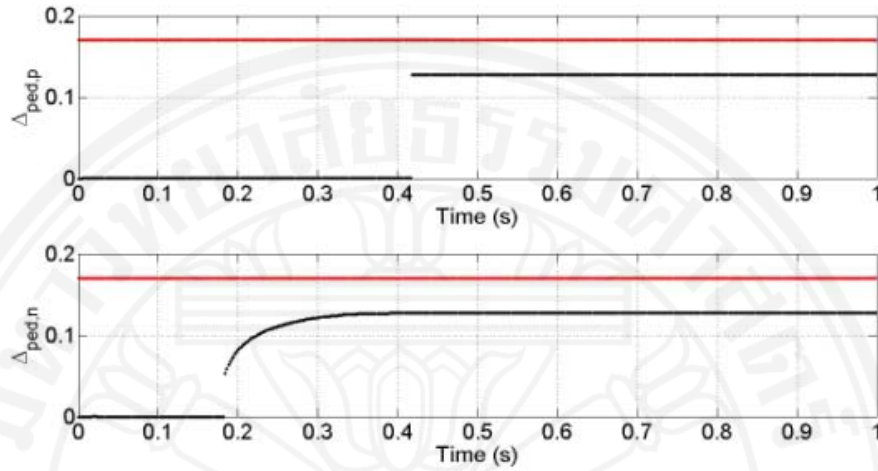


Figure 4.5: Pressure (top) and density (bottom) pedestal widths as a function of time for constant sources (horizontal line) scenario.

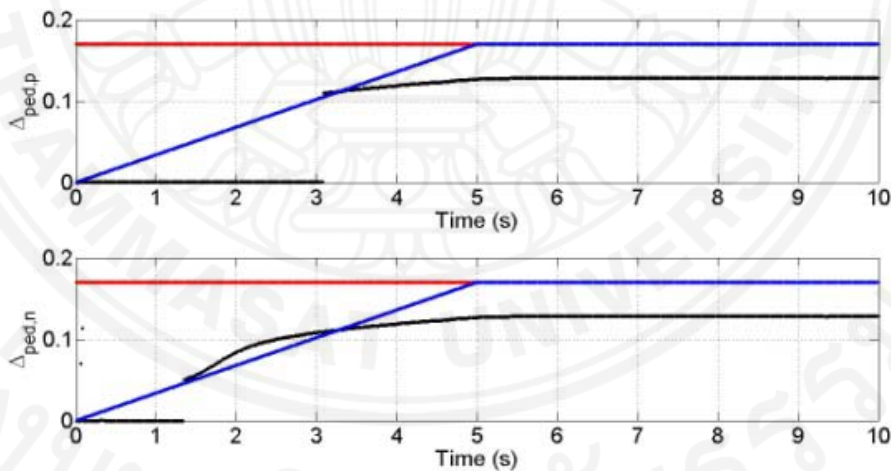


Figure 4.6: Pressure (top) and density (bottom) pedestal widths as a function of time for heat ramping scenario.

Figure 4.6 shows different scenarios by having heat source no longer constant in time. Plasma heating (blue line) is ramping up to a constant value, same as in previous scenario, while the particle source (red line) is kept at constant at all time. Once again, the pedestal is formed first in the density channel. In this case, the expansion rate of the pedestal is slower than that in the previous case. It takes longer

time for the plasma to reach steady state because the heat is being ramped up instead of keeping at constant value like in figure 4.5. But eventually, the pedestal widths become the same as in the previous scenario at steady state. This makes sense because in the end the heat and particle fluxes given to the plasma are the same.

4.3.2 Pedestal width

This section focuses on the pedestal width analysis at steady state. The relationships between the pedestal widths and various plasma parameters are shown in figures 4.7-4.12. In these figures, the square bullets represent pedestal width for both pressure and density channels. Note that the pedestal widths are the same for both channels at steady state. The triangle bullets represent central plasma pressure normalized to its value at the onset of $L-H$ transition. The cross bullets represent central plasma density normalized to its value at the onset of $L-H$ transition.

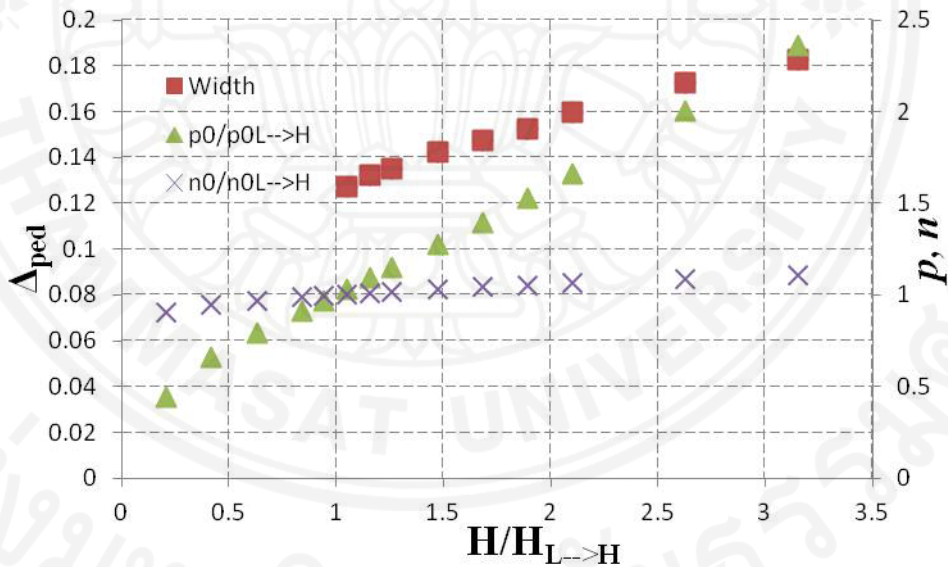


Figure 4.7: Pedestal width and central pressure and density at steady state as a function of heat source.

Figure 4.7 shows the effects of heat source giving to the plasma. It confirms that there exists an $L-H$ transition threshold for heating. Below the threshold, there is no formation of a transport barrier. As the heating is increased over the threshold, the pedestal width gets wider. However, the enlargement rate is slower as the heat is increased. Apparently, the change in heat source has higher effect on plasma pressure

than plasma density. Numerically, the central pressure is increased to 3.76 times and the central density is increased to 1.18 times as the heat source is increased by 10 times of the lowest value.

Figure 4.8 illustrates the effects of particle source giving to the plasma. Similarly, this confirms that there exists also an $L-H$ transition threshold for particle flux. Below the threshold, there is no formation of a transport barrier. This result qualitatively agrees with stability analysis of section 2. On the contrary to the previous case, as the particle source is increased over the threshold, the pedestal width is instead reduced. This can be explained by the suppression form of equation (4.3) used in the simulations. As the particle source is increased, plasma density is higher resulting in lower value of the suppression. Consequently, the plasma performance is reduced and the pedestal width as well as pressure profile are decreased. Evidently, the change in particle source has higher effect on plasma density than plasma pressure. Numerically, the central density is increased to 3.31 times and the central pressure is reduced to 0.69 times as the particle source is increased to 10 times of the lowest value.

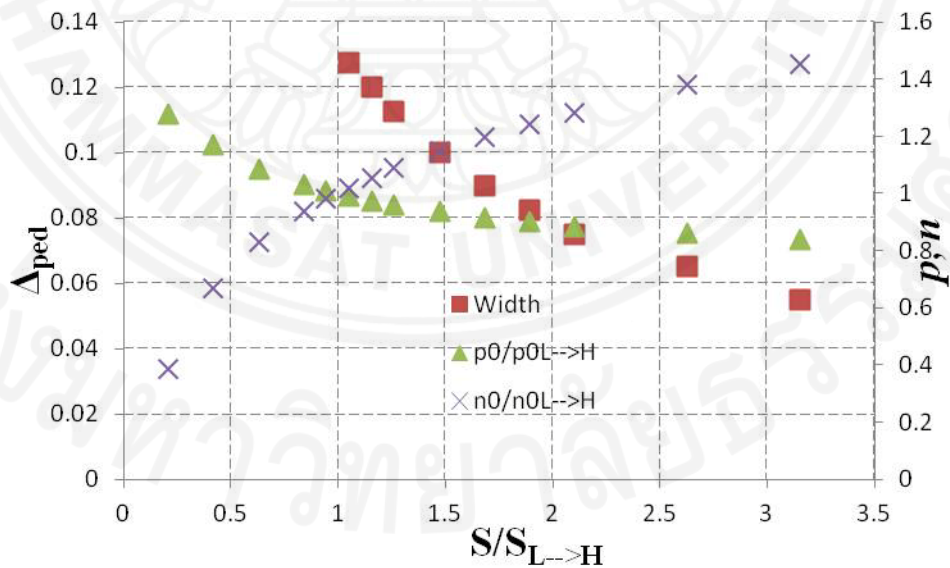


Figure 4.8: Pedestal width and central pressure and density at steady state as a function of particle source.

Effects of thermal anomalous transport are considered as showed in figure 4.9. This study is carried out as variation of the proportional constant c_χ , appeared in

equation (4.11), which controls the strength of thermal anomalous transport coefficient. First of all, previous analysis by Malkov *et. al.* and Chatthong *et. al.* [96, 135], respectively, concluded that the $L-H$ transition is possible only if a ratio of anomalous over neoclassical transport must exceeds a critical value. Generally, this value is in the order of 1 to 2. Physically, this condition always holds in the real plasma because the anomalous transport is normally about 10 times higher in the ion channel and can even reach 100 times higher in electron channel [60]. Figure 4.9 confirms the existence of this critical value for realization of an $L-H$ transition. If the anomalous transport is too low, there is no formation of a transport barrier. Furthermore, as the strength of the anomalous transport is increased, the pedestal width gets narrower, resulting in the reduction of the central plasma pressure and density. This makes sense because the plasma loss through transport is enhanced so plasma performance should reduce. The reductions of the profiles appear to be stronger in plasma pressure than density. Numerically, the central pressure is reduced to 0.71 times and the central density is reduced to 0.93 times as the proportional constant c_χ is increased to 10 times of the lowest value.

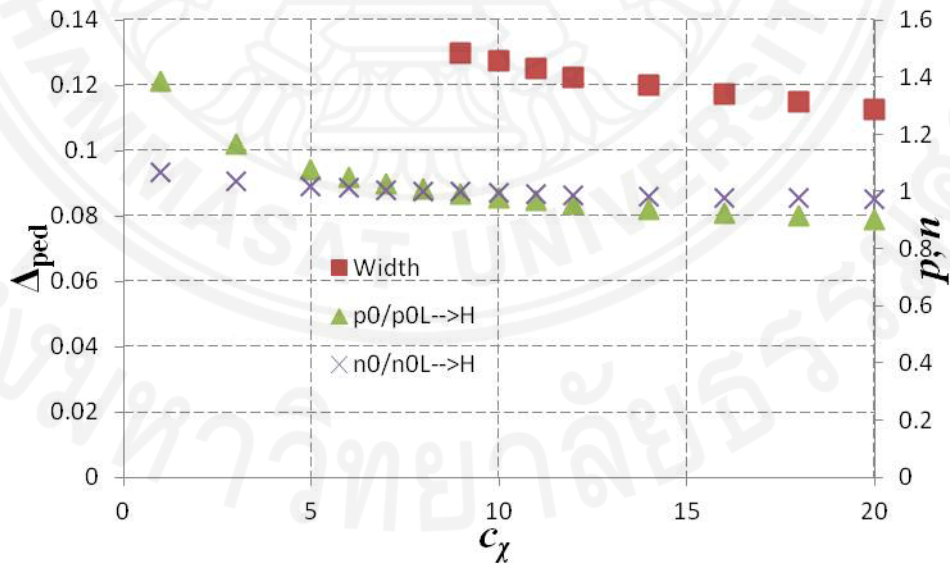


Figure 4.9: Pedestal width and central pressure and density at steady state as a function of thermal anomalous transport.

Effects of particle anomalous transport are showed in figure 4.10. This study is carried out as variation of the proportional constant c_D , appeared in equation (4.12),

which controls the strength of particle anomalous transport coefficient. Similarly, this figure also confirms the existence of the critical value for possibility of an $L-H$ transition. If the anomalous transport is too low there is no formation of a transport barrier. The results are similar to that of figure 4.9 in which as the strength of the anomalous transport is increased, the pedestal width gets narrower and the central plasma pressure and density are reduced. However, the reductions of the profiles appear to be stronger in plasma density than pressure. Numerically, the central pressure is reduced to 0.96 times and the central density is reduced to 0.78 times as the proportional constant c_D is increased to 10 times of the lowest value.

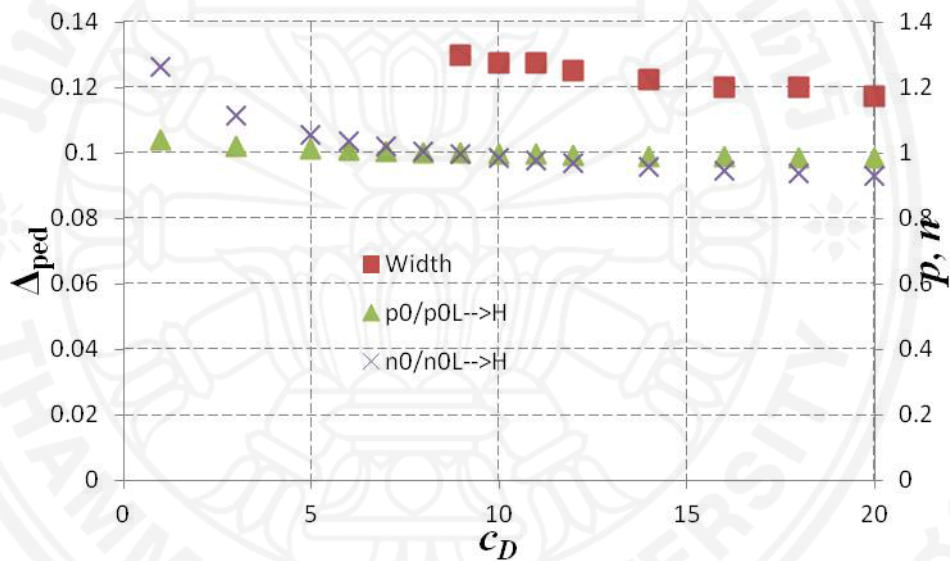


Figure 4.10: Pedestal width and central pressure and density at steady state as a function of particle anomalous transport.

Effects of thermal neoclassical transport can be seen in figure 4.11 where the transport coefficient is varied. The critical ratio for possibility to obtain $L-H$ transition is also showed here because if the strength of neoclassical transport is greatly increased, H -mode cannot be achieved. Also, as the strength of the thermal neoclassical transport is increased, the pedestal width gets narrower and the central plasma pressure and density are reduced. However, the reductions of the profiles appear to be stronger in plasma pressure. Numerically, the central pressure is reduced to 0.23 times and the central density is reduced to 0.98 times as the thermal neoclassical transport coefficient is increased to 10 times of the lowest value.

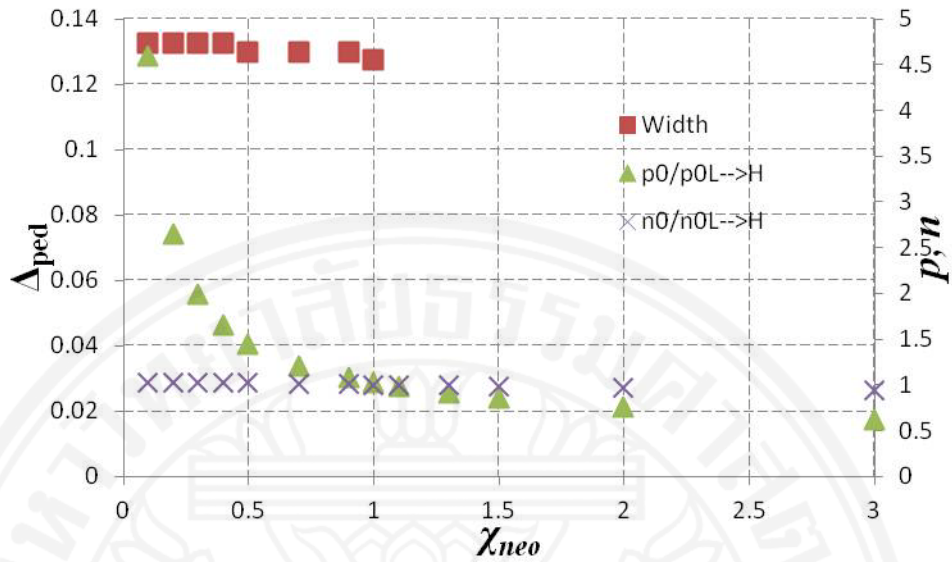


Figure 4.11: Pedestal width and central pressure and density at steady state as a function of thermal neoclassical transport.

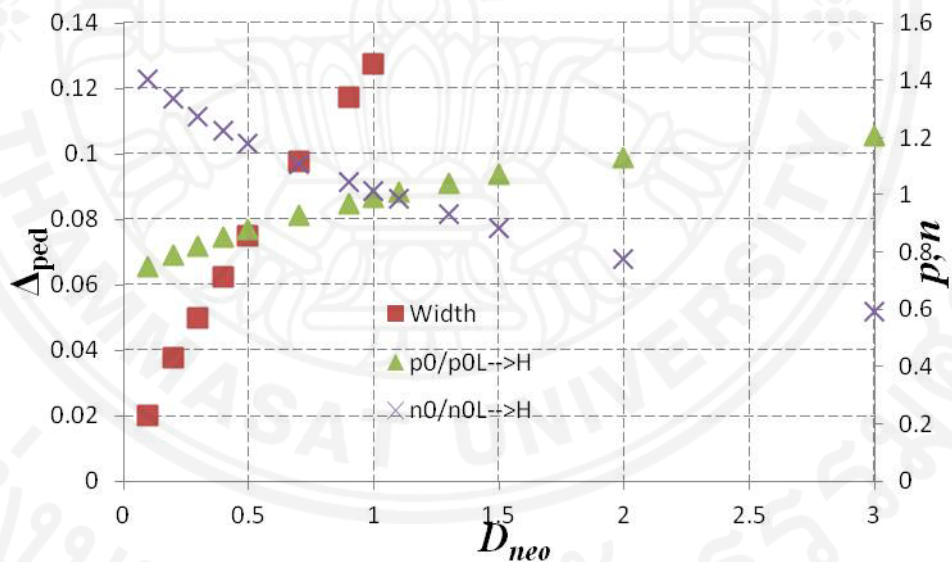


Figure 4.12: Pedestal width and central pressure and density at steady state as a function of particle neoclassical transport.

Figure 4.12 illustrates effects of particle neoclassical transport on pedestal width and central plasma values. The critical ratio for possibility to obtain *L-H* transition is also evident here. Moreover, as the strength of the particle neoclassical transport is increased, the pedestal width is enlarged, the central pressure is increased and the central density is reduced. These results seem to be strange comparing to

those of figure 4.11. The explanation is that when strength of particle neoclassical transport is increased, plasma particle loss is enhanced. Subsequently, the plasma density is reduced, which increases the flow shear suppression resulting in increase of pressure profiles as well as pedestal width. The changes of the profiles appear to be stronger in plasma density. Numerically, the central pressure is increased to 1.32 times but the central density is reduced to 0.72 times as the particle neoclassical transport coefficient is increased to 10 times of the lowest value.

4.4 Conclusion

A numerical method is used to analyze the 2 fields (heat and particle) transport equations. The transport effect considered is a combination of neoclassical transport which is assumed to be constant and anomalous transport which follows the critical gradient transport model. The suppression mechanism is the flow shear calculating from the shear of radial electric field equation. An analytical study based on bifurcation and stability of fixed points shows that an abrupt increase of local gradients occurs at the onset of $L-H$ transition. This transition is also found to depend on the direction of heat ramping, where a backward $H-L$ transition can occur at lower fluxes than that of a forward $L-H$ transition, implying hysteresis phenomena. Numerically, it is found that without gradient limiting instability, the pedestal width can expand initially superdiffusively and later subdiffusively. The time the plasma takes for pedestal expansion is about one order of magnitude longer than it takes to transit from L - to H -mode. The pedestal tends to form first in the density channel but at steady state both pedestal has the same value. Furthermore, the pedestal width at steady state and central plasma pressure appears to be proportional to heat source and particle neoclassical transport, and inversely proportional to particle source, thermal and particle anomalous transports and thermal neoclassical transport. Central plasma density appears to be proportional to heat and particle sources, and inversely proportional to all plasma transports.

Chapter 5

Analysis of Hysteresis Properties in Tokamak Plasma Based on Bifurcation Concepts

5.1 Introduction

Hysteresis phenomena for $L-H$ transition have been observed in various tokamak plasma experiments[136]. It was found that once the H -mode plasma was achieved, the heating power could be reduced below the $L-H$ transition threshold while retaining the H -mode characteristics. This hysteresis characteristic in fusion plasma has been found with the reduction of heating power to be even as large as a factor of two [44, 134]. Normally, hysteresis is associated with the controlled parameters, for example heat flux/magnetic field, and dependent quantities, for example the pressure gradient in plasma/magnetization in ferromagnetic materials. In other word, the controlled parameters can facilitate calculation of the dynamical changes of the system, which is generally interpreted using the dependent quantities. As controlled parameters are varied, the qualitative information of the dependent quantities can abruptly change, implying bifurcation behavior. Bifurcation nature of the system often relates to hysteresis phenomena because it is often found that the direction that the controlled parameters are varied affect the system differently. In tokamak plasma, the controlled parameters are the injected heating, which can be in any form of heat source, and particle source in the system, while the interested quantities can be plasma pressure, density and temperature. The hysteresis phenomena can be very important in tokamak. For example, in ITER hysteresis allows an opportunity to reach H -mode at low density because it is easier to obtain. Several $L-H$ threshold power scaling laws tend to yield linear density scaling with acceptable agreement with experimental results [44, 137-139]. Then, one can raise the density to the desirable level while keeping the heating at constant[136]. This scenario is only possible if hysteresis really exists.

In bifurcation approach of $L-H$ transition modeling, one generally studies this complex phase change behavior using flux versus gradient space graph[140]. The flux is an integration of the source in the plasma so they are closely dependent. The non-

monotonic behavior of the graph in flux versus gradient space allows possibility to analyze the hysteresis behavior in the plasma. As described in chapter 3, the direction of heat ramping can affect the plasma mode. For example, when the heat is ramped up, the plasma makes a transition to H -mode when the heating power exceeds L - H power threshold. Whereas, if the heat is ramped down from H -mode condition, the plasma remains H -mode until the heat is below H - L threshold. Typically, the H - L threshold is lower than that of the L - H threshold, allowing hysteresis existence. This chapter attempts to explain hysteresis phenomena in tokamak plasma based on bifurcation concept. Previous study analyzed weak hysteresis in the plasma using simplified one-field model [141]. The results implied that the hysteresis strength is weaker than that expected from the s -curve bifurcation model. In this chapter, thermal and particle transport equations at steady state are solved simultaneously to calculate heat flux versus pressure gradient and particle flux versus density gradient spaces. These two graphs illustrate non-monotonic relation and thus form hysteresis loops. The important quantities in hysteresis loop are analyzed as various parameters are varied.

5.2 Transport equations and bifurcation diagrams

This section introduces the transport equations used in this work and illustrates that the analytical solution implies bifurcation nature of the plasma. First of all, the study is based on simplified version of thermal and particle transport equations as showed in equations (4.1) and (4.2). In this study, the neoclassical transport coefficients are assumed to be just constant. Whereas the anomalous transport coefficients, which are the more dominant terms in the plasma, are calculated based on critical gradient models [132-133] in the forms:

$$\chi_{ano} = c_x (g_p - g_{pc}) \theta(g_p - g_{pc}), \quad (5.1)$$

$$D_{ano} = c_d (g_n - g_{nc}) \theta(g_n - g_{nc}), \quad (5.2)$$

where c_x and c_d are constants, $g_p = -\frac{\partial p}{\partial x}$, $g_n = -\frac{\partial n}{\partial x}$, $g_{pc} = \left(-\frac{\partial p}{\partial x}\right)_c$ and $g_{nc} = \left(-\frac{\partial n}{\partial x}\right)_c$ are the critical gradients for pressure and density fields, respectively, and θ represents a Heaviside step function. At steady state, the two transport equations become:

$$\begin{aligned} \chi_{neo} g_p &= Q, & g_p < g_{pc} \\ \chi_{neo} g_p + \frac{c_\chi (g_p - g_{pc})}{1 + \alpha v_E'^2} g_p &= Q, & g_p \geq g_{pc} \end{aligned} \quad (5.3)$$

$$\begin{aligned} D_{neo} g_n &= \Gamma, & g_n < g_{nc} \\ D_{neo} g_n + \frac{c_D (g_n - g_{nc})}{1 + \alpha v_E'^2} g_n &= \Gamma, & g_n \geq g_{nc} \end{aligned} \quad (5.4)$$

respectively. As in the previous chapters, the suppression mechanism on the anomalous channel is the flow shear v_E' . It can be calculated from the approximated force balance equation [96]:

$$v_E' = c \frac{E_r'}{B} \simeq -\frac{c}{eBn^2} p'n' \propto g_p g_n, \quad (5.5)$$

with the curvature, the toroidal and poloidal rotation contributions neglected because their effects are smaller. Also, all the constants are allowed to merge into α . Apparently, the flow shear term couples both transport equations in the range where the gradients exceed their critical values. In general treatment of bifurcation picture of transports, one often solves the system and express them in fluxes (thermal/particle) versus gradients (pressure/density) space. The graph exhibits *s*-curve characteristic which is used to represent the transition from *L*-mode to *H*-mode. The pressure (equation (5.3)) and density (equation (5.4)) fields above the neoclassical regime can be decoupled using a simple algebraic method. By subtraction of the multiplication of equation (5.3) with $c_D (g_n - g_{nc}) g_n$ and of equation (5.4) with $c_\chi (g_p - g_{pc}) g_p$, the following quadratic equation with g_n as variable can be obtained as follows:

$$\begin{aligned} (Q - \chi_{neo} g_p) c_D g_n^2 - [(Q - \chi_{neo} g_p) c_D g_{nc} - D_{neo} c_\chi g_p (g_p - g_{pc})] g_n \\ - c_\chi g_p (g_p - g_{pc}) \Gamma = 0 \end{aligned} \quad (5.6)$$

The solution of this equation, which identifies g_n as a function of g_p , is then substituted into equation (5.5) to decouple the two transport fields. The only problem is which of the two solutions of the quadratic solutions represents physical interpretation of the system. Note that $Q \geq \chi_{neo} g_p$ and the last term on the left hand side of equation (5.6) is always negative. Only one of the two quadratic solutions yields physical interpretation (g_n is positive). The decoupling term can be written as:

$$g_n = \frac{-b_n + \sqrt{b_n^2 - 4a_n c_n}}{2a_n}, \quad (5.7)$$

where $a_n = (Q - \chi_{neo} g_p) c_D$, $b_n = -[(Q - \chi_{neo} g_p) c_D g_{nc} - D_{neo} c_\chi g_p (g_p - g_{pc})]$ and $c_n = -c_\chi g_p (g_p - g_{pc}) \Gamma$. This yields possibility to plot Q versus g_p with obvious indication that the graph is affected by parameters from both pressure and density fields. Similarly, the bifurcation diagram in the density field can also be calculated using the substitution:

$$g_p = \frac{-b_p + \sqrt{b_p^2 - 4a_p c_p}}{2a_p}, \quad (5.8)$$

where $a_p = (\Gamma - D_{neo} g_n) c_\chi$, $b_p = -[(\Gamma - D_{neo} g_n) c_\chi g_{pc} - \chi_{neo} c_D g_n (g_n - g_{nc})]$ and $c_p = -c_D g_n (g_n - g_{nc}) Q$. Examples of bifurcation diagram resulting from this analysis are showed in figure 5.1 with top panel representing pressure field and bottom panel representing density field. All numerical results in this work are carried out using the same set of chosen constants. The alteration of those will be specified accordingly. The transport coefficients are defined such that both thermal and particle anomalous diffusivities are around one to two order of magnitude over their neoclassical counterparts. In addition, the particle diffusivities are set to be roughly a quarter of thermal diffusivities [6]. Specifically, $\chi_{neo} = 1$, $c_\chi = 10$, $D_{neo} = 0.25$, $c_D = 2.5$, $g_{pc} = g_{nc} = 1$, $Q_s = Q$ (maximum heat flux) = 20, $\Gamma_s = \Gamma$ (maximum particle flux) = 2 and $\alpha = 0.1$.

In figure 5.1, the graphs of heat flux versus pressure gradient (top panel) and particle flux versus density gradient (bottom panel) illustrate the non-monotonic behavior which characterizes the bifurcation. As explained in the previous chapter using stability analysis, this graphical interpretation can be used to identify the $L-H$ and $H-L$ back transitions. One can imagine heat and particle fluxes as an independent variable which can be increased or decreased. This figure characterizes the plasma into four different regimes. At low fluxes, the plasma is governed by neoclassical transport with low gradients. As the fluxes increase, the gradients also raise until the critical values are reached and the anomalous transports start to grow. Once the bifurcation ranges are reached, the plasma remains in L -mode according to stability

analysis. It makes a sudden transition to H -mode when the heat flux exceeds L - H transition threshold for heat flux $Q_{L \rightarrow H}$ or the particle flux exceeds L - H transition threshold for particle flux $\Gamma_{L \rightarrow H}$, with $p'_{L \rightarrow H}$ and $n'_{L \rightarrow H}$ as their respective gradients. On the other hand, if the fluxes are decreased from high value, the plasma remains in H -mode in the bifurcation range. It makes a transition back to L -mode when the heat flux is below $Q_{H \rightarrow L}$ or particle flux is below $\Gamma_{H \rightarrow L}$, with $p'_{H \rightarrow L}$ and $n'_{H \rightarrow L}$ as their respective gradients. This dynamic implies hysteresis phenomena of the plasma. Next section, the hysteresis properties are discussed in details.

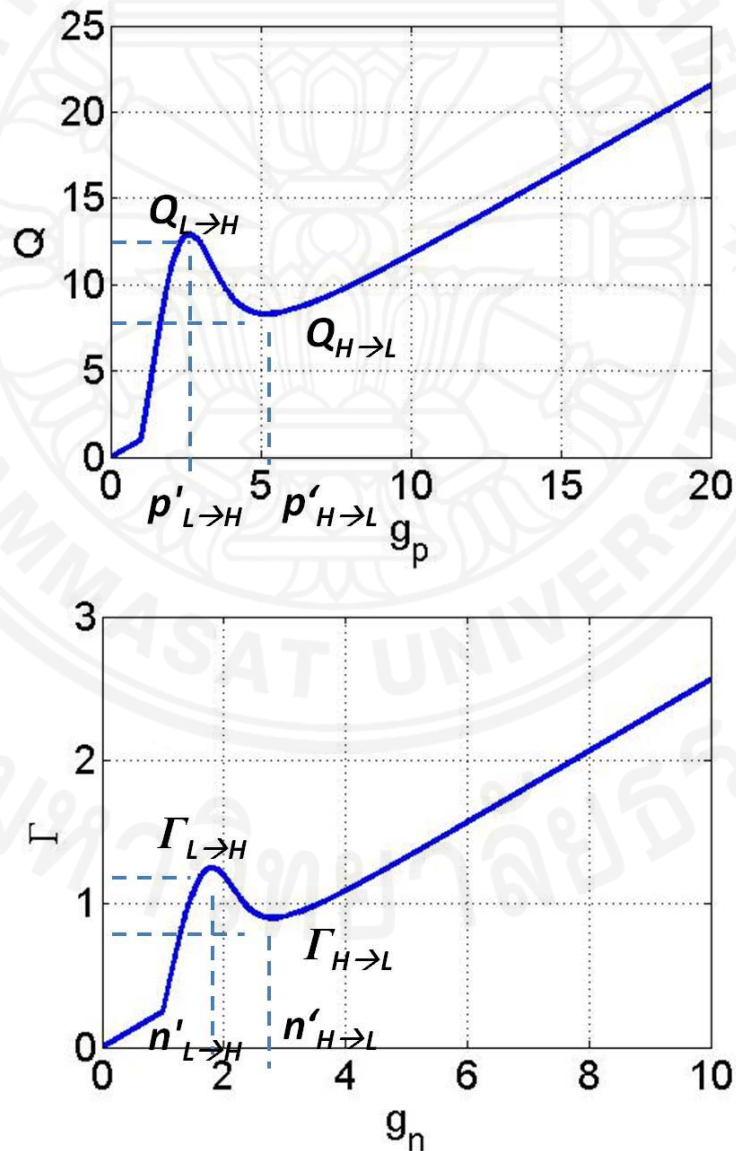


Figure 5.1: Bifurcation diagrams for pressure field (top) and density field (bottom) illustrating L - H and H - L back transitions.

5.3 Hysteresis depth analysis

Hysteresis phenomena was found in experiment [142]. In this section, the depths of hysteresis properties in the bifurcation diagram shown in figure 5.1 are explored. In particular, the study analyzes the effects on hysteresis depth from variation of various model parameters i.e. $c_\chi, c_D, \chi_{neo}, D_{neo}, g_{pc}, g_{nc}, Q_s$ and Γ_s .

5.3.1 Effects of thermal transports

Figure 5.2 illustrates the hysteresis depth of pressure field as a function of c_χ which indicates the strength of thermal anomalous transport. The top left panel shows the pressure gradient at the onset of $L \rightarrow H$ ($p'_{L \rightarrow H}$) and $H \rightarrow L$ back transitions ($p'_{H \rightarrow L}$), while the bottom left panels shows the ratio of the two quantities. Note that the gradient at the back transition is higher because the gradient is taken from pedestal region of the H -mode prior to the transition. The top right panel shows the heat flux needed to access H -mode ($Q_{L \rightarrow H}$) and the minimum heat flux needed to maintain it ($Q_{H \rightarrow L}$). The bottom right panel illustrates the ratio $Q_{L \rightarrow H}/Q_{H \rightarrow L}$. This is an important quantity because it describes how much the heating power that can be reduced while maintaining the H -mode. As the thermal anomalous transport strength increases, both heat fluxes required to obtain and maintain the H -mode also increase, but the effect on $Q_{L \rightarrow H}$ is stronger. As c_χ increases to 250% of its lowest value, the values of $Q_{L \rightarrow H}$ and $Q_{H \rightarrow L}$ increase to 205% and 140%, respectively. This is because higher heat source is needed to compensate the loss by transport. As a result, the heat flux ratio is ranged from around 1.3 to almost 1.9 as c_χ is higher. This is in the similar order as what found in the experiments and what to be expected from ITER [136]. What the analysis implies is that at higher value of anomalous transport the hysteresis loop becomes more prominent. On the other hand, the pressure gradient ratio reduces from less than 0.6 to almost 0.45 as c_χ increases because $p'_{H \rightarrow L}$ increases to 121% while $p'_{L \rightarrow H}$ slightly decreases to 96%. The pressure gradient at the onset of $H \rightarrow L$ back transition increases with c_χ because in this state the plasma is still in the H -mode where the turbulent is suppressed so the plasma is governed mostly by the neoclassical flux. As c_χ is higher,

the flux $Q_{H \rightarrow L}$ is also higher resulting in the increase of $p'_{H \rightarrow L}$ ($\chi_{neo} p' = Q$). The pressure gradient at the onset of L - H transition slightly decreases with c_χ because the plasma is in L -mode so it is governed by both neoclassical and anomalous flux. The rate of c_χ increase is a bit higher than the rate of increase in the responding $Q_{L \rightarrow H}$ resulting in the decrease of $p'_{L \rightarrow H}$.

Effects of thermal anomalous transport on hysteresis depth of density field can be seen in figure 5.3. The top left panel shows the density gradient at the onset of L - H ($n'_{L \rightarrow H}$) and H - L back transitions ($n'_{H \rightarrow L}$), while the bottom left panels shows the ratio of the two quantities. Note that the gradient at the back transition is higher because the gradient is taken from pedestal region of the H -mode prior to the transition. The top right panel shows the particle flux needed to access H -mode ($\Gamma_{L \rightarrow H}$) and the minimum particle flux needed to maintain it ($\Gamma_{H \rightarrow L}$). The bottom right panel illustrates the ratio $\Gamma_{L \rightarrow H}/\Gamma_{H \rightarrow L}$. Similarly to the previous case, as the thermal anomalous transport strength increases both particle fluxes required to obtain and maintain the H -mode also increase but the effect on $\Gamma_{L \rightarrow H}$ is stronger. As c_χ increases to 250% of its lowest value, $\Gamma_{L \rightarrow H}$ and $\Gamma_{H \rightarrow L}$ increase to 232% and 154%, respectively. This is because higher particle source is needed to compensate the loss by transport. As a result, the particle flux ratio is ranged from around 1.1 to almost 1.7 as c_χ is higher. The density gradient ratio is found to be reduced from 0.75 to a bit below 0.6 as c_χ increases because $n'_{H \rightarrow L}$ is increased to 161% while $n'_{L \rightarrow H}$ increases to 128%. Both pressure gradient at the onset of L - H transition and H - L back transition increase with c_χ because their transports are only affected through the suppression term which can be diminished in H -mode. When particle fluxes $\Gamma_{L \rightarrow H}$ and $\Gamma_{H \rightarrow L}$ increase, the corresponding density gradients enhance as well.

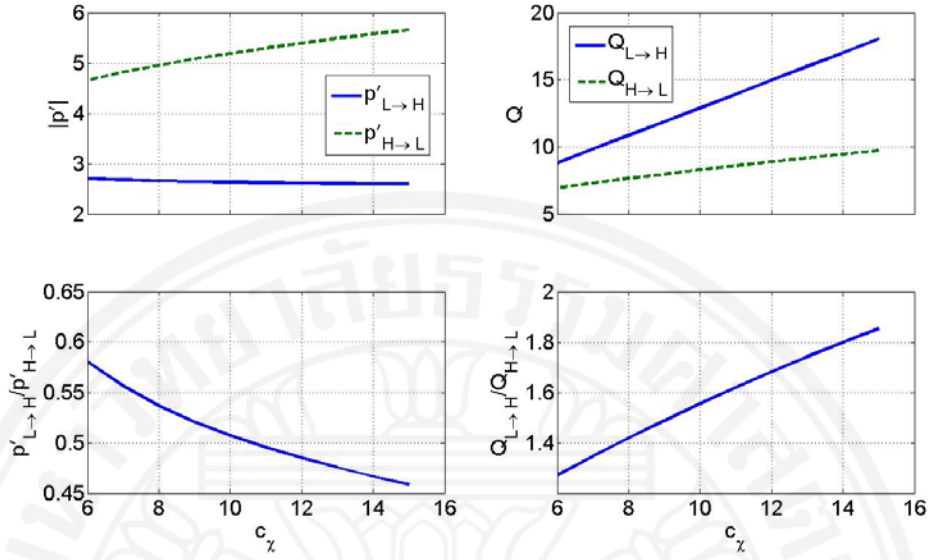


Figure 5.2: Hysteresis depth in pressure field as a function of thermal anomalous transport coefficient proportional constant.

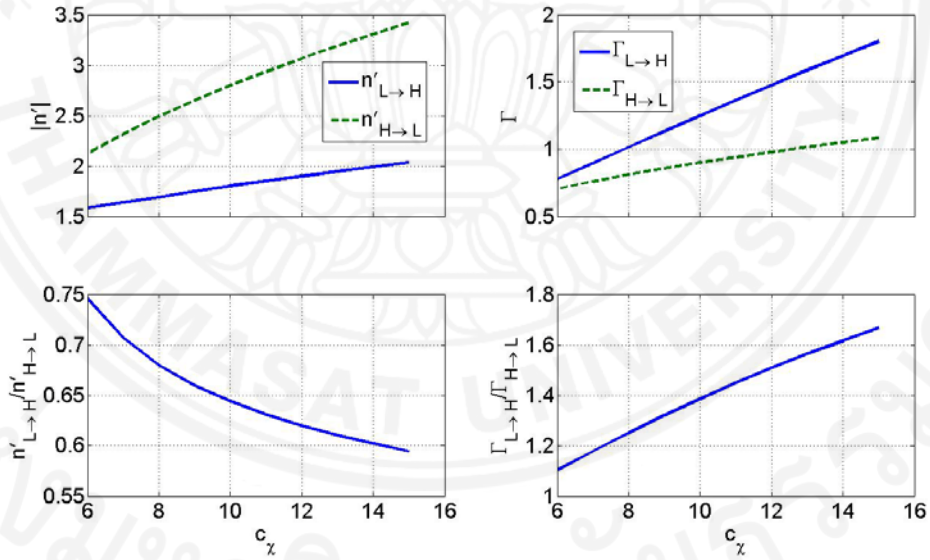


Figure 5.3: Hysteresis depth in density field as a function of thermal anomalous transport coefficient proportional constant.

Figure 5.4 illustrates the hysteresis depth of pressure field as a function of χ_{neo} which indicates the strength of thermal neoclassical transport. As the thermal neoclassical transport increases, both heat fluxes required to obtain and maintain the H -mode also increase. As χ_{neo} increases to 250% of its lowest value, the values of

$Q_{L \rightarrow H}$ and $Q_{H \rightarrow L}$ increase to 120% and 176%, respectively. This is because higher heat source is needed to compensate the loss by neoclassical transport. Consequently, the heat flux ratio is ranged from around 1.9 to almost 1.3 as χ_{neo} is higher. As oppose to the anomalous transport, increase of neoclassical transport reduces the ratio. This makes sense because the bifurcation behavior of the plasma only exists when ratio of anomalous over neoclassical transport exceeds a threshold value as described in the previous chapters and by Malkov *et. al.* and Chatthong *et. al.* [96, 135], respectively. This means that at higher value of neoclassical transport the hysteresis loop becomes less prominent. The pressure gradient ratio increases from around 0.45 to almost 0.6 as χ_{neo} increases because $p'_{H \rightarrow L}$ decreases to 82% while $p'_{L \rightarrow H}$ slightly increases to 104%. This makes sense because as χ_{neo} is higher, the flux $Q_{H \rightarrow L}$ is also higher resulting in the reduction of $p'_{H \rightarrow L}$. Whereas, $p'_{L \rightarrow H}$ is a consequence of both neoclassical and anomalous contribution. Even though, the increase rate of χ_{neo} is higher than that of the responding $Q_{L \rightarrow H}$ resulting in the decrease of $p'_{L \rightarrow H}$. But this contribution is less than the anomalous term which yields increase in $p'_{L \rightarrow H}$ because χ_{neo} indirectly reduces the suppression, see equation (5.9).

Figure 5.5 illustrates the effects of thermal neoclassical transport on hysteresis depth of density field. As χ_{neo} increases to 250% of its lowest value, $\Gamma_{L \rightarrow H}$ and $\Gamma_{H \rightarrow L}$ increase to 118% and 139%, respectively. Consequently, the particle flux ratio reduces from over 1.5 to below 1.3 as χ_{neo} increases. The density gradient ratio is found to reduce from around 0.66 to 0.63 because $n'_{H \rightarrow L}$ increases to 115% while $n'_{L \rightarrow H}$ increases to 1.09%. The reasons are because χ_{neo} only affects particle transport through the suppression term which can be diminished in *H*-mode. When particle fluxes $\Gamma_{L \rightarrow H}$ and $\Gamma_{H \rightarrow L}$ increase, the corresponding density gradients enhance as well.

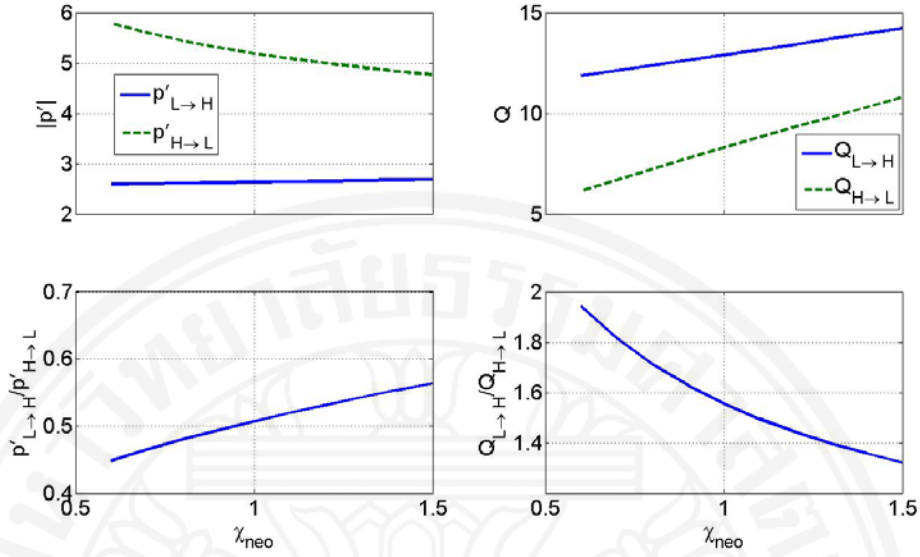


Figure 5.4: Hysteresis depth in pressure field as a function of thermal neoclassical transport coefficient.

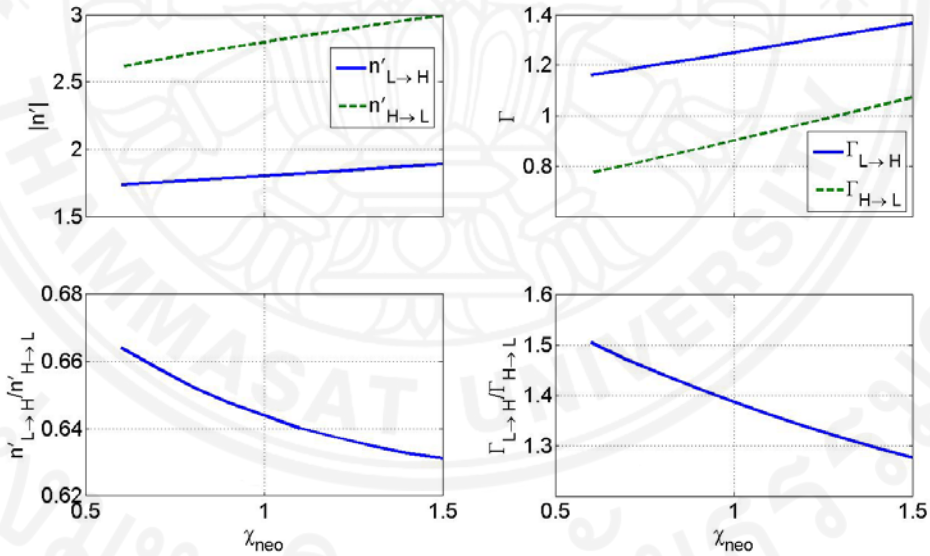


Figure 5.5: Hysteresis depth in density field as a function of thermal neoclassical transport coefficient.

5.3.2 Effects of particle transport

The model used in this work provides a lot of symmetry between pressure and density fields. The effects of particle transports are similar to that of thermal transports in the opposite fields. In this section, only numerical results are reported because there still is a factor of 4 difference in defining transport coefficients. The

explanations for the graph are similar to those in the previous section so they are omitted here.

Figure 5.6 illustrates the effects of particle anomalous transport on hysteresis depth of the pressure field. As c_D increases to 143% of its lowest value, the values of $Q_{L \rightarrow H}$ and $Q_{H \rightarrow L}$ increase to 129% and 114%, respectively. Consequently, the heat flux ratio increases from almost 1.5 to around 1.65. The pressure gradient ratio is found to reduce from around 0.52 to 0.49 because $p'_{H \rightarrow L}$ increases to 119% while $p'_{L \rightarrow H}$ increases to 1.11%.

Figure 5.7 illustrates the effects of particle anomalous transport on hysteresis depth of the density field. As c_D increased to 1.43% of its lowest value, $\Gamma_{L \rightarrow H}$ and $\Gamma_{H \rightarrow L}$ increase to 126% and 108%, respectively. Consequently, the particle flux ratio increases from 1.3 to 1.5. The density gradient ratio is found to reduce from over 0.66 to almost 0.62 because $n'_{H \rightarrow L}$ increases to 1.05% while $n'_{L \rightarrow H}$ decreases to 0.98%.

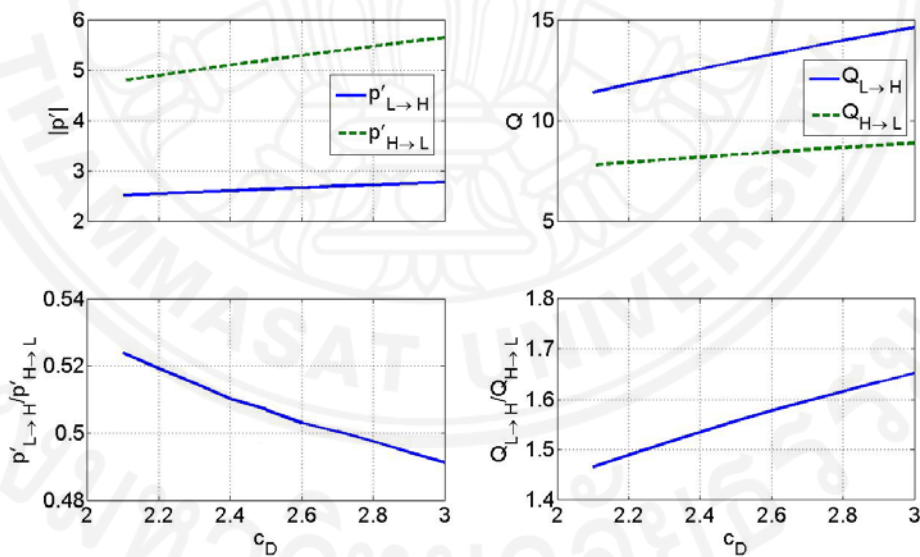


Figure 5.6: Hysteresis depth in pressure field as a function of particle anomalous transport coefficient proportional constant.

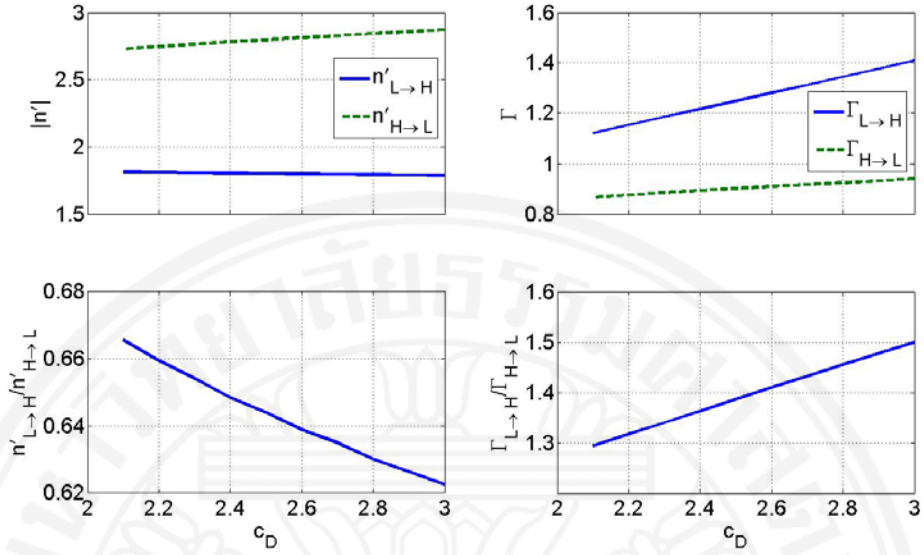


Figure 5.7: Hysteresis depth in density field as a function of particle anomalous transport coefficient proportional constant.

Figure 5.8 illustrates the effects of particle neoclassical transport on hysteresis depth of the pressure field. As D_{neo} increases to 143% of its lowest value, the values of $Q_{L \rightarrow H}$ and $Q_{H \rightarrow L}$ increase to 110% and 126%, respectively. Consequently, the heat flux ratio reduces from almost 1.7 to above 1.4. The pressure gradient ratio is found to reduce slightly around the value 0.5 because $p'_{H \rightarrow L}$ increases to 108% while $p'_{L \rightarrow H}$ increases to 106%.

Figure 5.9 illustrates the effects of particle neoclassical transport on hysteresis depth of the density field. As D_{neo} increases to 143% of its lowest value, $\Gamma_{L \rightarrow H}$ and $\Gamma_{H \rightarrow L}$ increase to 114% and 132%, respectively. Consequently, the particle flux ratio decreases from 1.5 to 1.3. The density gradient ratio is found to increase from over 0.62 to over 0.66 because $n'_{H \rightarrow L}$ reduces to 95% while $n'_{L \rightarrow H}$ increases to 102%.

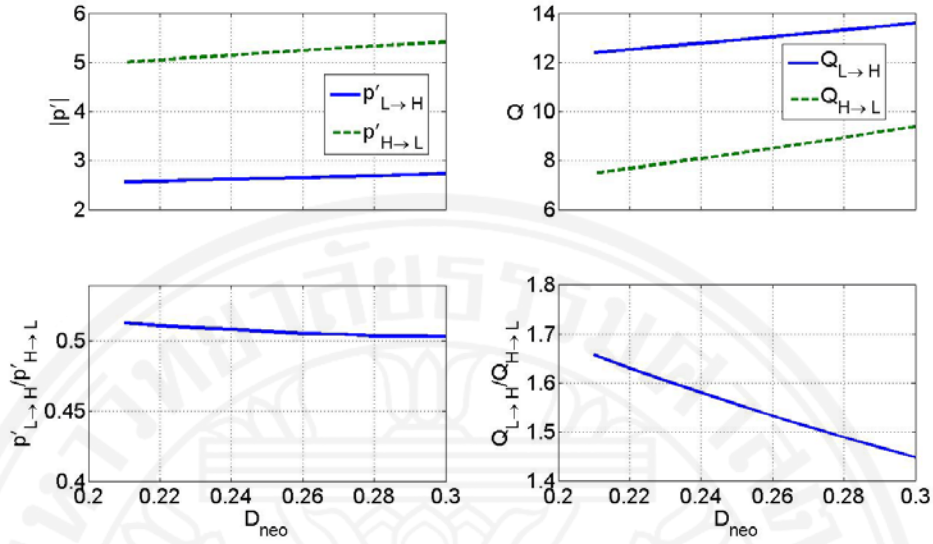


Figure 5.8: Hysteresis depth in pressure field as a function of particle neoclassical transport coefficient.

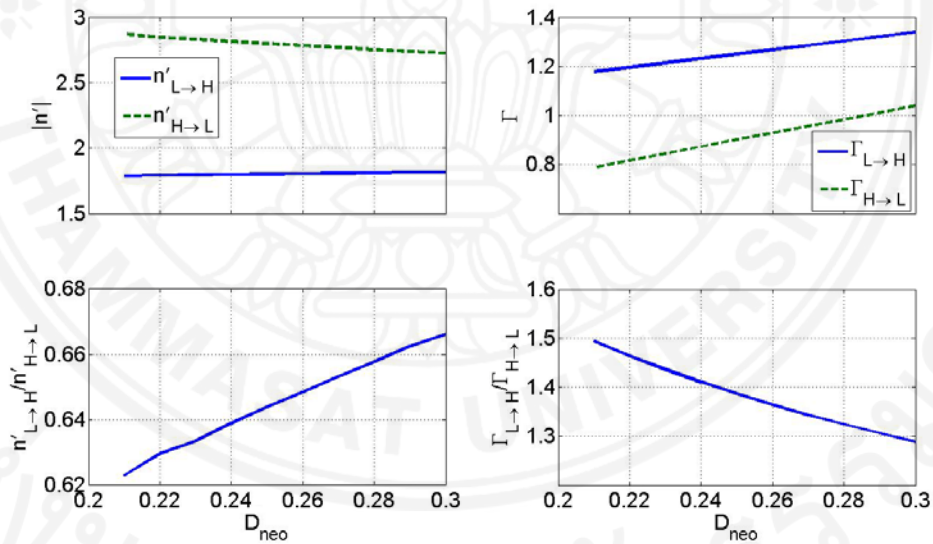


Figure 5.9: Hysteresis depth in density field as a function of particle neoclassical transport coefficient.

5.3.3 Effects of critical gradient thresholds

The critical gradient thresholds can be considered as the reduction of anomalous transport. The higher of the thresholds implies lower value of anomalous transport. Thus if it is too high, the L - H transition will not be possible. In this regime, the suppression by flow shear is ineffective in formation of a transport barrier. As a result, increase of critical gradient threshold values can lead to less projection of

hysteresis depth. In other word, the ratios of heat or particle fluxes asymptotically approach unity and eventually the hysteresis phenomena are no longer present. However, higher values of the thresholds also imply that L - H transition is easier to achieve because the total plasma loss is reduced.

Figure 5.10 illustrates the effects of critical pressure gradient on hysteresis depth of the pressure field. As g_{pc} increases to 250% of its lowest value, $Q_{L \rightarrow H}$ and $Q_{H \rightarrow L}$ decrease to 65% and 92%, respectively. The reduction rate of $Q_{H \rightarrow L}$ is lower because the plasma is in the H -mode where the anomalous contribution is much less effective. Consequently, the heat flux ratio reduces from around 1.8 to around 1.3. The pressure gradient ratio is found to increase from around 0.45 to almost 0.6 because $p'_{H \rightarrow L}$ decreases to 92% while $p'_{L \rightarrow H}$ increases to 118%. As mentioned already, if the critical gradient is higher the hysteresis depth is reduced, so the ratio of the pressure gradients approaches unity.

Figure 5.11 illustrates the effects of critical pressure gradient on hysteresis depth of the density field. First of all, as g_{pc} increases to 250% of its lowest value, $\Gamma_{L \rightarrow H}$ and $\Gamma_{H \rightarrow L}$ decrease to 70% and 95%, respectively. Consequently, the particle flux ratio reduces from 1.6 to 1.2. The density gradient ratio is found to increases from around 0.63 to over 0.67 because $n'_{H \rightarrow L}$ decreases to 92% while $n'_{L \rightarrow H}$ decreases to 98%.

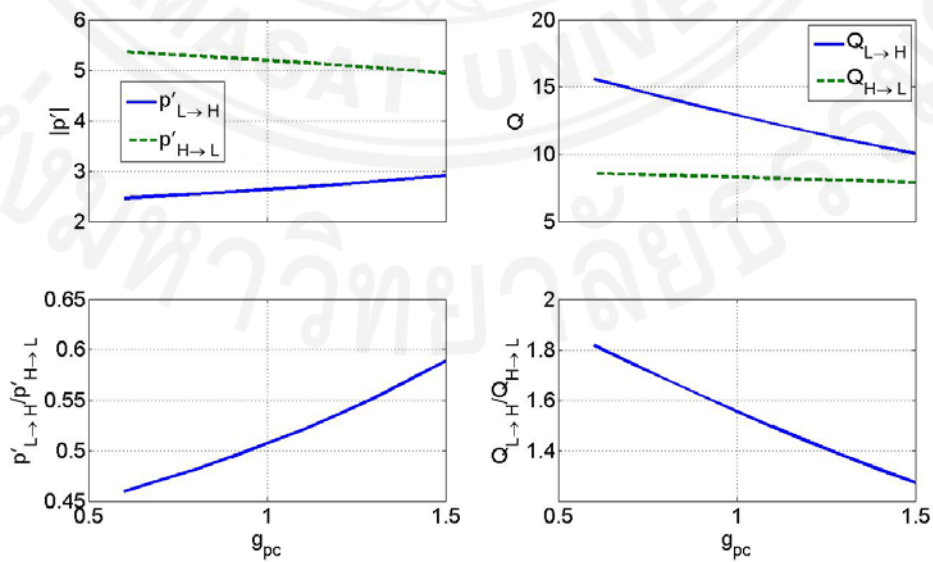


Figure 5.10: Hysteresis depth in pressure field as a function of critical pressure gradient.

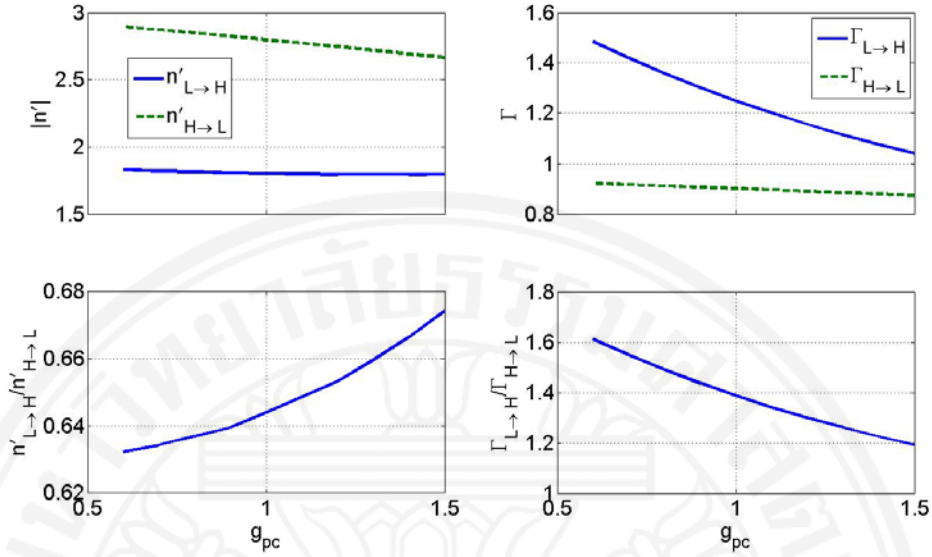


Figure 5.11: Hysteresis depth in density field as a function of critical pressure gradient.

Figure 5.12 illustrates the effects of critical density gradient on hysteresis depth of the pressure field. As g_{nc} increases to 250% of its lowest value, the values of $Q_{L \rightarrow H}$ and $Q_{H \rightarrow L}$ decrease to 58% and 92%, respectively. Consequently, the heat flux ratio reduces from almost 2 to a bit over 1.2. The pressure gradient ratio is found to increase from below 0.5 to around 0.55 because $p'_{H \rightarrow L}$ decreases to 87% while $p'_{L \rightarrow H}$ decreases to 97%.

Figure 5.13 illustrates the effects of critical density gradient on hysteresis depth of the density field. First of all, as g_{nc} increases to 250% of its lowest value, the values of $\Gamma_{L \rightarrow H}$ and $\Gamma_{H \rightarrow L}$ decrease to 51% and 88%, respectively. Consequently, the particle flux ratio reduces from over 1.7 to almost 1.0, which is where the hysteresis vanishes. The density gradient ratio is found to increase from below 0.6 to over 0.8 because $n'_{H \rightarrow L}$ decreases to 88% while $n'_{L \rightarrow H}$ increases to 130%.

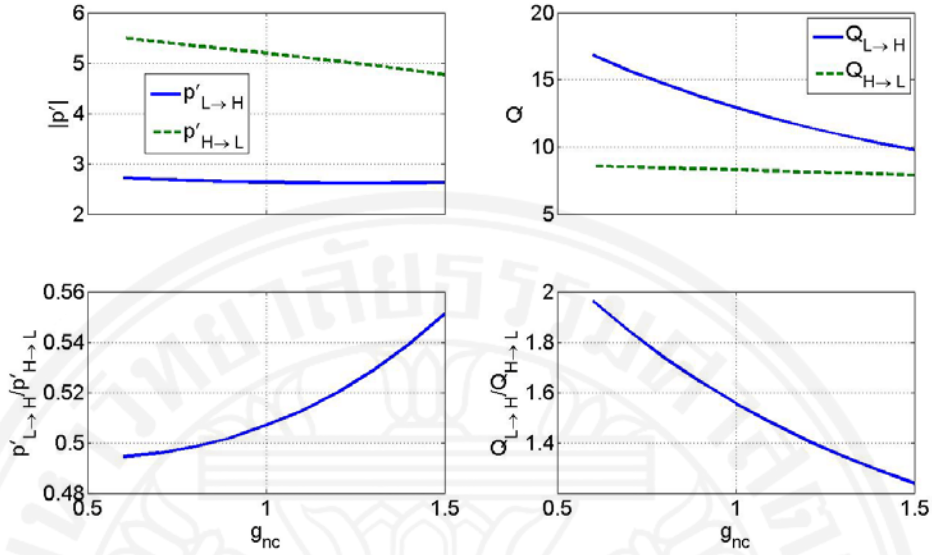


Figure 5.12: Hysteresis depth in pressure field as a function of critical density gradient.

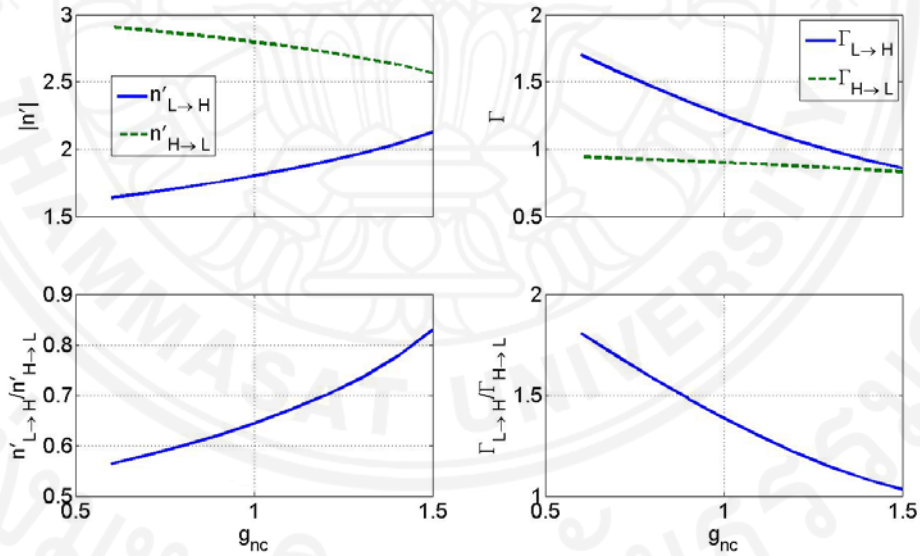


Figure 5.13: Hysteresis depth in density field as a function of critical density gradient.

5.3.4 Effects of sources

Analysis in chapter 4 shows that an increase of particle flux can reduce the heat flux required to obtain and maintain the H -mode. This is also true in the opposite case because the two fields are dependent of each other. They are coupled through the flow shear term. This section demonstrates the hysteresis depth of pressure field as a

function of particle flux and that of density field as a function of heat flux. First of all, figure 5.14 illustrates the effects of particle flux on hysteresis depth of the pressure field. As Γ_s increases to 156% of its lowest value, the values of $Q_{L \rightarrow H}$ and $Q_{H \rightarrow L}$ decrease to 65% and 64%, respectively. Consequently, the heat flux ratio remains almost constant close to 1.5. The pressure gradient ratio is found to increase from 0.48 to 0.54 because $p'_{H \rightarrow L}$ decreases to 74% while $p'_{L \rightarrow H}$ decreases to 82%.

Figure 5.15 illustrates the effects of heat flux on hysteresis depth of the density field. As Q_s increases to 156% of its lowest value, the values of $\Gamma_{L \rightarrow H}$ and $\Gamma_{H \rightarrow L}$ decrease to 61% and 69%, respectively. Consequently, the particle flux ratio reduces from below 1.5 to 1.3. The density gradient ratio is found to increase from around 0.61 to over 0.68 because $n'_{H \rightarrow L}$ decreases to 74% while $n'_{L \rightarrow H}$ decreases to 84%.

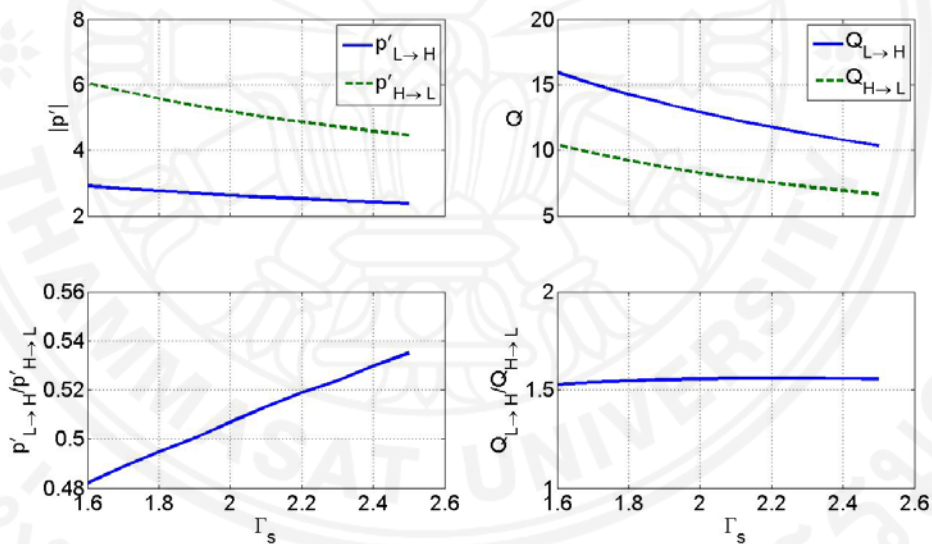


Figure 5.14: Hysteresis depth in pressure field as a function of particle flux.

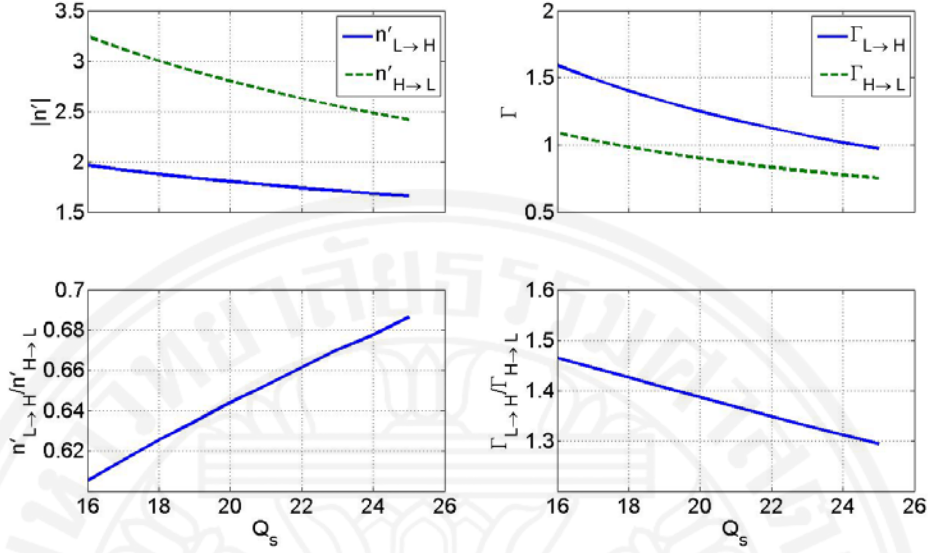


Figure 5.15: Hysteresis depth in density field as a function of heat flux.

5.4 Plasma gradients at the transitions

Other quantities of interest from the plasma regarding the hysteresis properties are the changes of plasma pressure and density gradients at the onset of L - H transition and H - L back transition. Typically, higher plasma gradients lead to higher plasma core profiles (pressure or density), hence better fusion performance. Therefore, it is also important to analyze how the variation of model parameters can affect these changes. In this study, $p'_{H(L\rightarrow H)}$ represents the pressure gradient in H -mode at the transition. Whereas, $p'_{L\rightarrow H}$ is the pressure gradient in L -mode prior to the transition. Technically, it can be assumed that both occur at the same heat flux (see figure 5.1). Similarly, $p'_{L(H\rightarrow L)}$ represents the pressure gradient in L -mode at the back transition, with $p'_{H\rightarrow L}$ as the pressure gradient in H -mode prior to the back transition. In density fields, $n'_{H(L\rightarrow H)}$ represents the density gradient in H -mode at the transition and $n'_{L(H\rightarrow L)}$ represents the density gradient in L -mode at the back transition. The effects of model parameters ($c_\chi, c_D, \chi_{neo}, D_{neo}, g_{pc}, g_{nc}, Q_s$ and Γ_s) on these quantities and their ratios (gradients of H -mode over those of L -mode) are showed in figures 5.16 - 5.29.

Evidently, the ratios of pressure and density gradients increase as both thermal and particle anomalous transport coefficient proportional constants increase. On the

other hand, the ratios decrease as both thermal and particle neoclassical transport coefficients increase. This makes sense because the graph of hysteresis depth is proportional to the ratio between anomalous over neoclassical transport. If this ratio is lower than the threshold value, hysteresis vanishes. As this ratio is higher, the hysteresis loop becomes enhanced. For this same reason, the increase of critical pressure and density gradients reduces the gradient ratios because they reduce anomalous transport effects. At last the increase of particle and thermal fluxes also reduce the gradient ratios because they tend to reduce the requirements of L - H transition which also decreases the change in pressure and density gradients across the transition. Tables 5.1 and 5.2 summarized the quantitative information of figures 5.16 - 5.29. They show the changes of pressure and density gradients and their ratios at L - H transition and H - L back transition as a function of model parameters illustrated as ratio to the lowest value of model parameters in the range. Note that value above 1 means that the ratio is increased and value below 1 means otherwise.

Table 5.1: Changes of pressure gradients and their ratios at L - H transition and H - L back transition as a function of model parameters illustrated as ratio to the lowest value.

Model parameters	ratio to the lowest value of model parameters						
	$P'_{L \rightarrow H}$	$P'_{H(L \rightarrow H)}$	$\frac{P'_{H(L \rightarrow H)}}{P'_{L \rightarrow H}}$	$P'_{L(H \rightarrow L)}$	$P'_{H \rightarrow L}$	$\frac{P'_{H \rightarrow L}}{P'_{L(H \rightarrow L)}}$	
c_χ	2.50	0.96	2.06	2.15	0.82	1.21	1.49
c_D	1.43	1.11	1.34	1.21	1.02	1.18	1.15
χ_{neo}	2.50	1.04	0.48	0.46	1.21	0.82	0.68
D_{neo}	1.43	1.06	1.00	0.94	1.11	1.08	0.98
g_{pc}	2.50	1.18	0.59	0.50	1.60	0.92	0.57
g_{nc}	2.50	0.97	0.52	0.53	1.15	0.87	0.76
Γ_s	1.56	0.82	0.70	0.85	0.86	0.74	0.86

Table 5.2: Changes of density gradients and their ratios at L - H transition and H - L back transition as a function of model parameters illustrated as ratio to the lowest value.

Model parameters	ratio to the lowest value of model parameters						
		$n'_{L \rightarrow H}$	$n'_{H(L \rightarrow H)}$	$\frac{n'_{H(L \rightarrow H)}}{n'_{L \rightarrow H}}$	$n'_{L(H \rightarrow L)}$	$n'_{H \rightarrow L}$	$\frac{n'_{H \rightarrow L}}{n'_{L(H \rightarrow L)}}$
c_χ	2.50	1.28	2.55	1.98	1.02	1.61	1.58
c_D	1.43	0.98	1.26	1.28	0.94	1.05	1.12
χ_{neo}	2.50	1.09	1.06	0.97	1.13	1.15	1.01
D_{neo}	1.43	1.02	0.79	0.78	1.06	0.95	0.89
g_{pc}	2.50	0.98	0.67	0.68	1.09	0.92	0.85
g_{nc}	2.50	1.30	0.45	0.35	1.93	0.88	0.46
Q_s	1.56	0.84	0.62	0.73	0.93	0.74	0.80

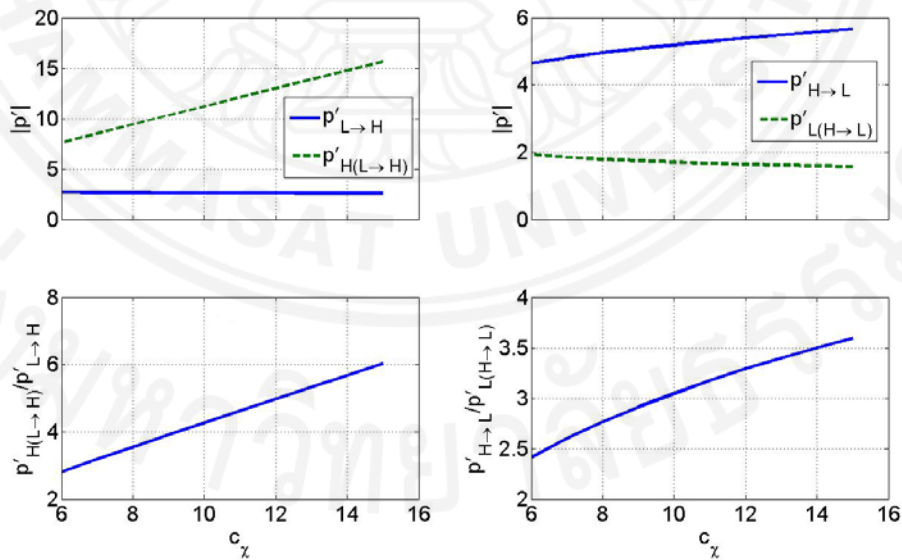


Figure 5.16: Pressure gradient changes at L - H (left) and H - L (right) transitions as a function of thermal anomalous transport coefficient proportional constant.

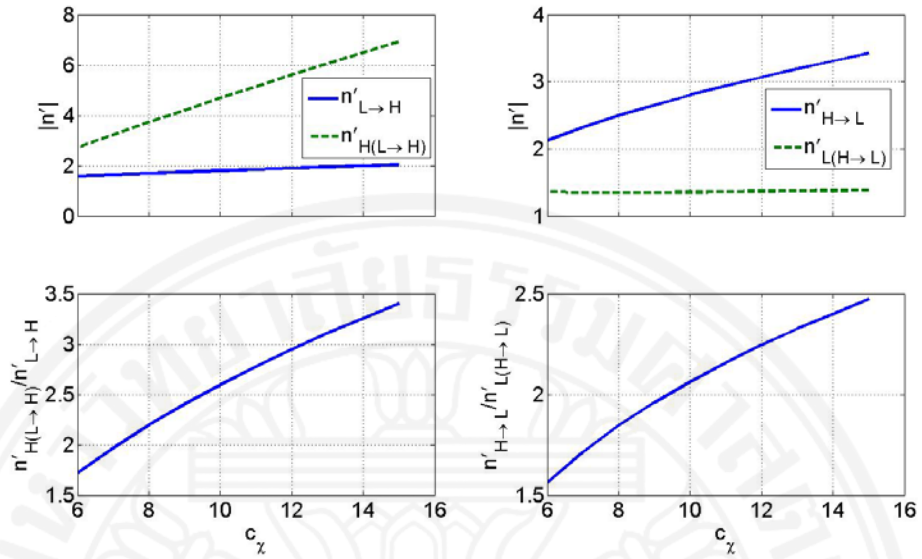


Figure 5.17: Density gradient changes at L - H (left) and H - L (right) transitions as a function of thermal anomalous transport coefficient proportional constant.

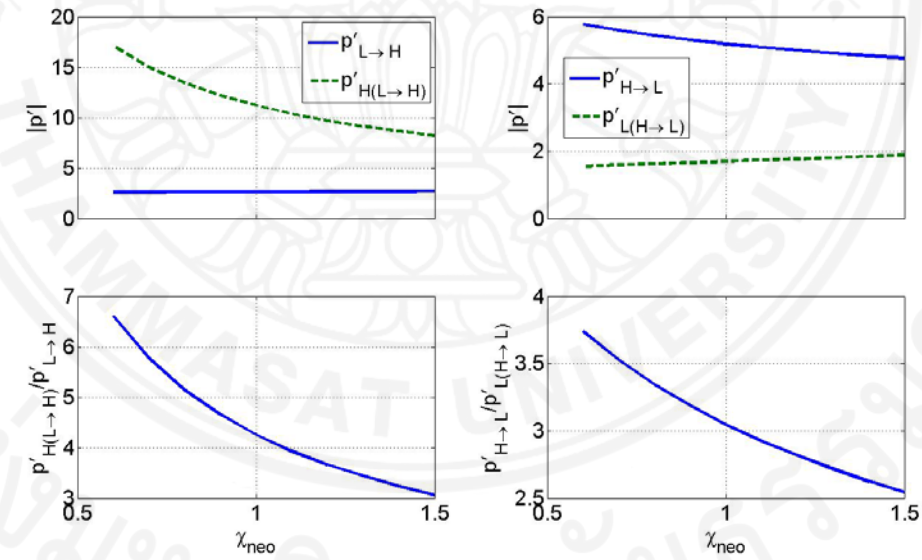


Figure 5.18: Pressure gradient changes at L - H (left) and H - L (right) transitions as a function of thermal neoclassical transport coefficient.

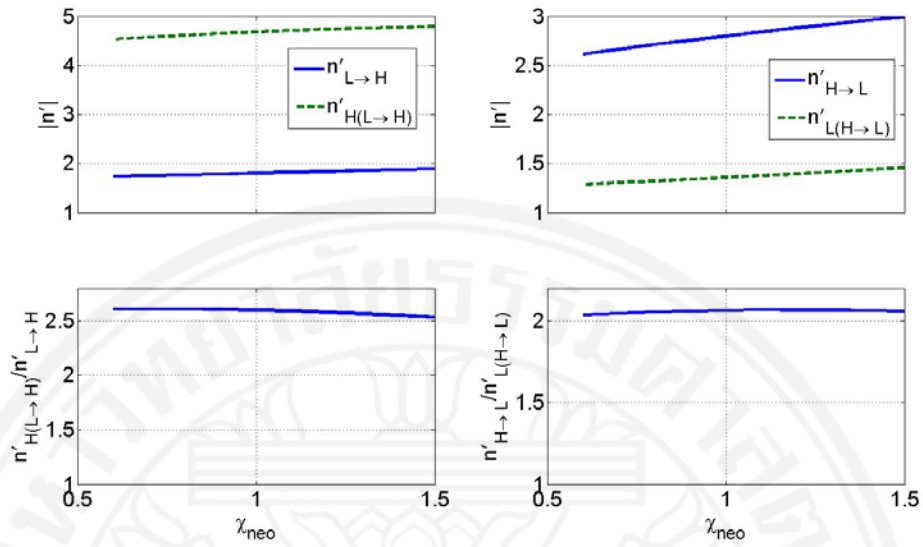


Figure 5.19: Density gradient changes at *L-H* (left) and *H-L* (right) transitions as a function of thermal neoclassical transport coefficient.

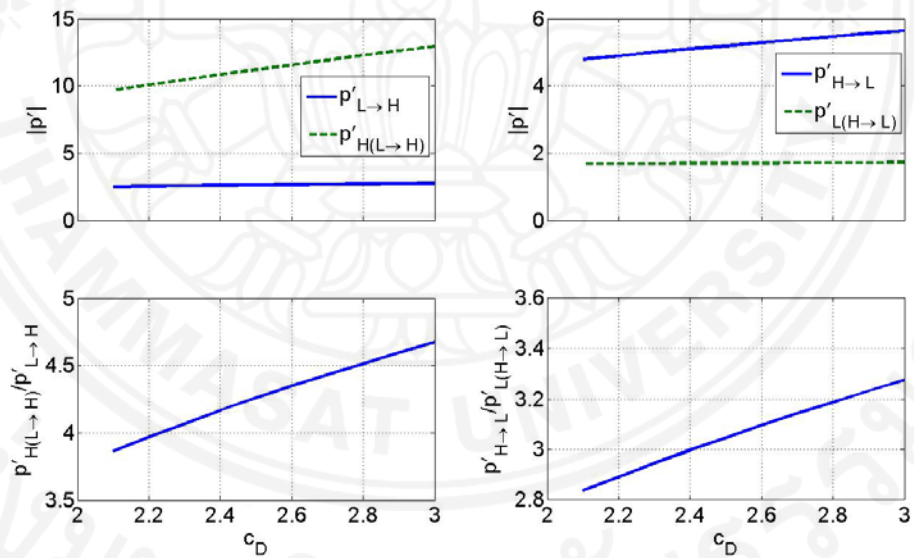


Figure 5.20: Pressure gradient changes at *L-H* (left) and *H-L* (right) transitions as a function of particle anomalous transport coefficient proportional constant.

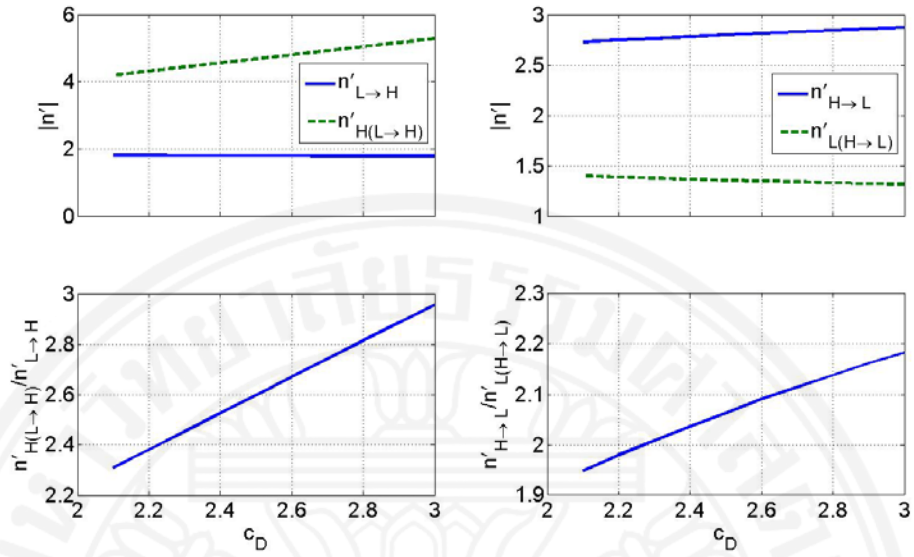


Figure 5.21: Density gradient changes at *L-H* (left) and *H-L* (right) transitions as a function of particle anomalous transport coefficient proportional constant.

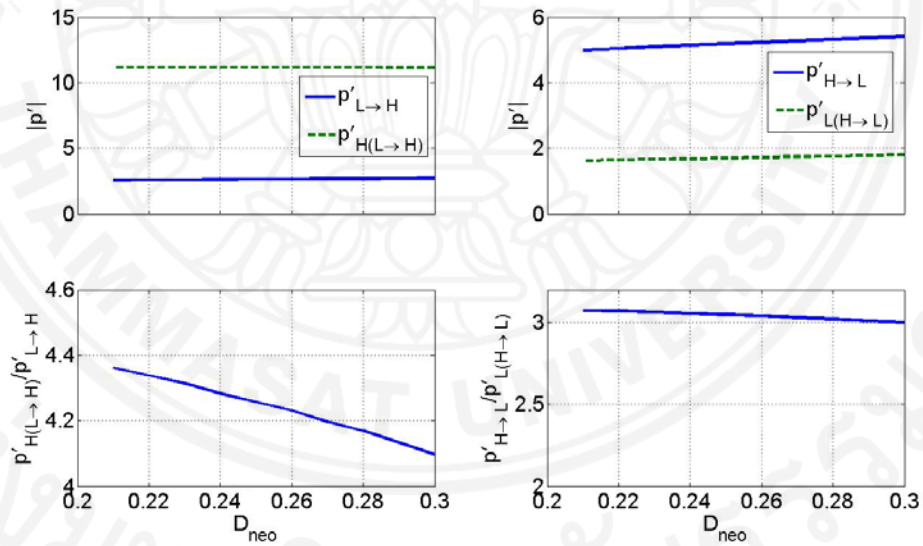


Figure 5.22: Pressure gradient changes at *L-H* (left) and *H-L* (right) transitions as a function of particle neoclassical transport coefficient.

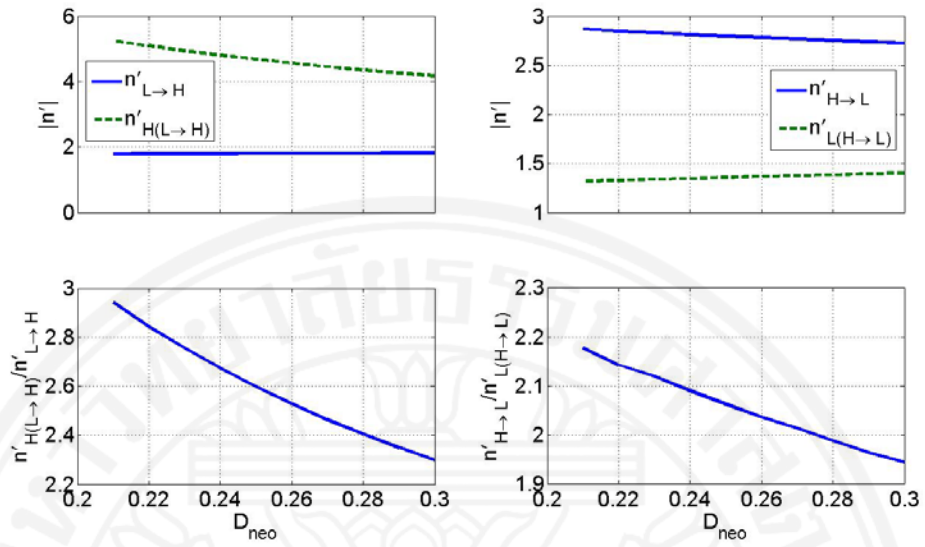


Figure 5.23: Density gradient changes at L - H (left) and H - L (right) transitions as a function of particle neoclassical transport coefficient.

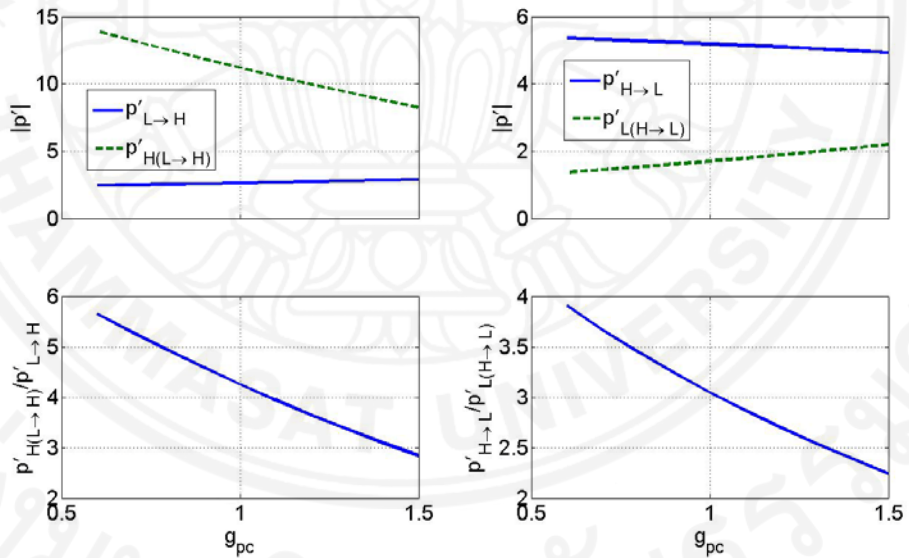


Figure 5.24: Pressure gradient changes at L - H (left) and H - L (right) transitions as a function of critical pressure gradient.

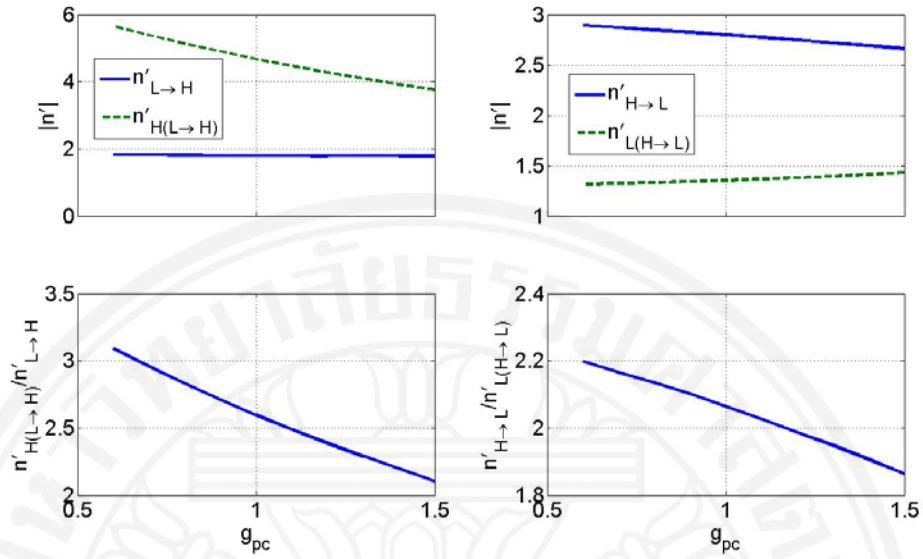


Figure 5.25: Density gradient changes at L - H (left) and H - L (right) transitions as a function of critical pressure gradient.

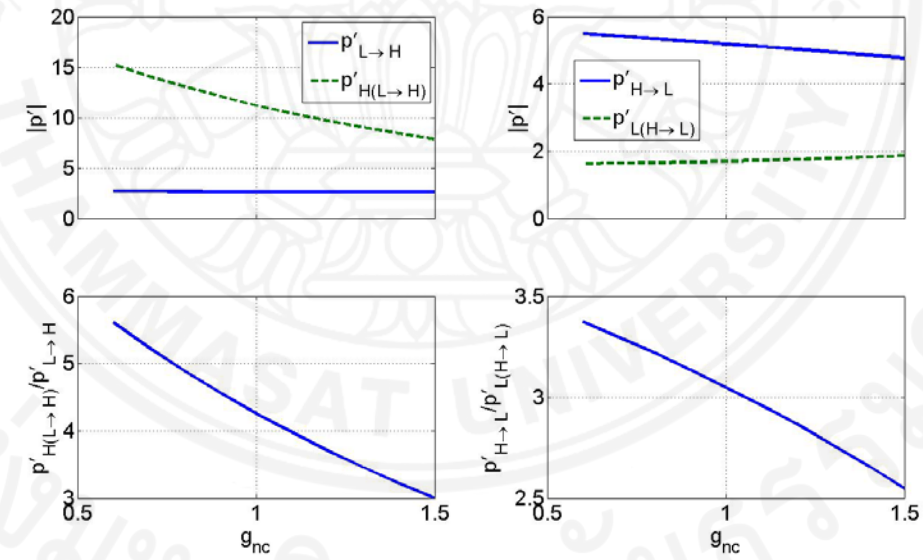


Figure 5.26: Pressure gradient changes at L - H (left) and H - L (right) transitions as a function of critical density gradient.

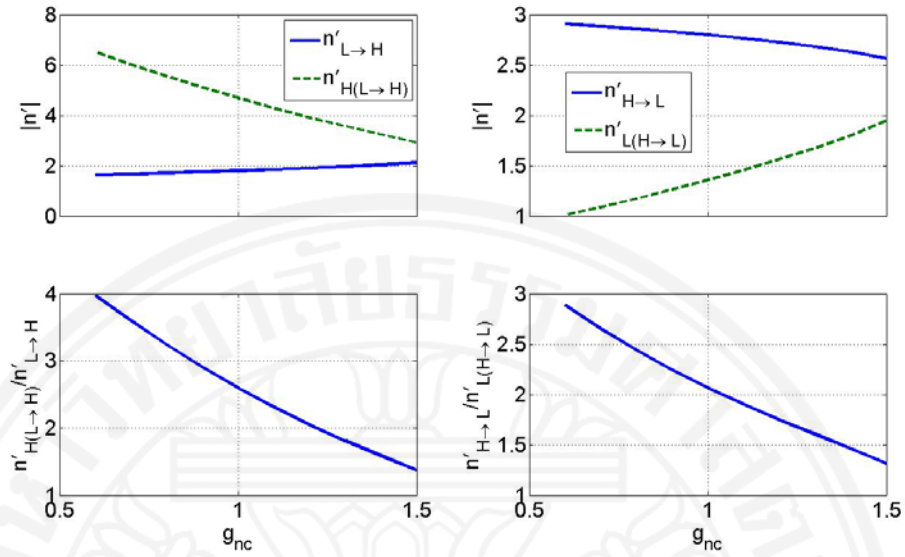


Figure 5.27: Density gradient changes at $L-H$ (left) and $H-L$ (right) transitions as a function of critical density gradient.

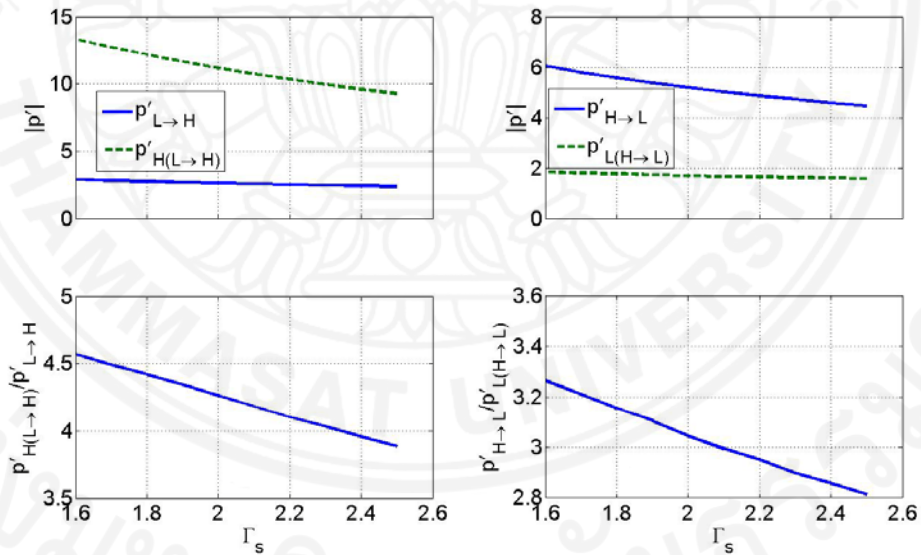


Figure 5.28: Pressure gradient changes at $L-H$ (left) and $H-L$ (right) transitions as a function of particle flux.

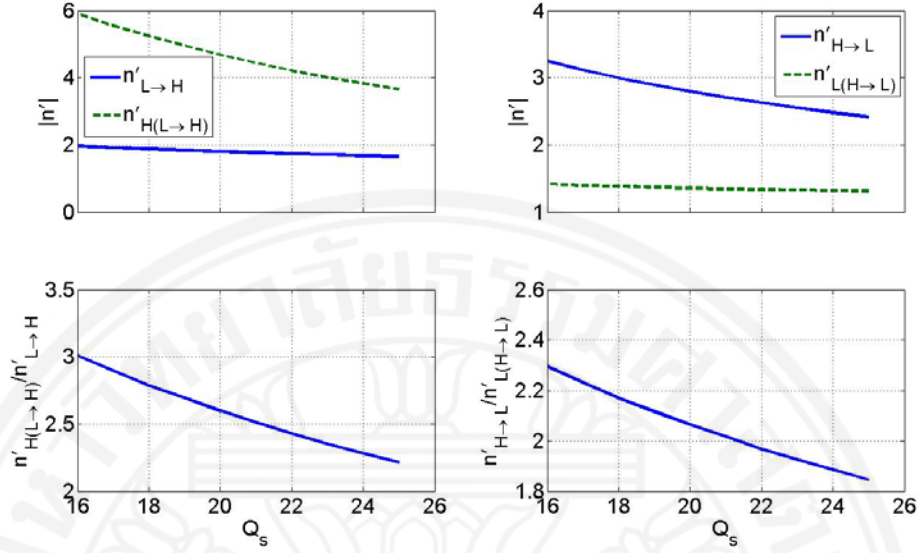


Figure 5.29: Density gradient changes at L - H (left) and H - L (right) transitions as a function of heat flux.

5.5 Conclusion

In this chapter, a coupled 2-fields transport equations (pressure and density) are analytically solved to study hysteresis properties of the tokamak plasma. In this model, the neoclassical transport coefficients are assumed to be constant while the anomalous transport coefficients assume the form of critical gradients relation. It is assumed that only the anomalous channels are suppressed in the transport barrier region by the flow shear, which is calculated from the force balance equation. Analytical results show that with simple form of flow shear suppression, the two fields can be decoupled to illustrate bifurcation diagram of each field. It is found that the heat and particle flux ratios are increased with anomalous transports, but decreased with neoclassical transports and critical gradients thresholds. On the other hand, the heat flux ratio is increased with particle flux while the particle flux ratio is decreased with heat flux. The heat and particle fluxes required to reach and to maintain H -mode are increased with transport strength but reduced with the increase of critical gradient thresholds. It also appears that the changes of both pressure and density gradients at the onset of L - H transition are increased with anomalous transports, while decreased with neoclassical transports, critical gradient thresholds and magnitude of the sources.

Chapter 6

Analysis of Transport Barriers Formation and Properties in Tokamak Plasma Using Bifurcation Concept

6.1 Introduction

The work in this chapter aims to investigate formations of transport barriers, including their locations and properties for both ITB and ETB and interactions between them, using bifurcation concept. In this work, the suppression part of the transport is modified to include the magnetic shear effect. The new transport suppression function results in possibility of both ITB and ETB formation, simultaneously or individually. In addition, the effect of bootstrap current is also included. Various effects such as thermal and particle sources, and transport strengths are analyzed on their effects toward the transition as well as barrier widths.

6.2 Modeling of plasma transport based on bifurcation concept

ETB and ITB in tokamak plasma are studied based on a coupled 2-fields bifurcation model. In this work, simplified heat and particle transport equations can be written, in slab geometry, as:

$$\frac{3}{2} \frac{\partial p}{\partial t} - \frac{\partial}{\partial x} [\chi_{neo} + \chi_{ano} f_s(v'_E, s)] \frac{\partial p}{\partial x} = H(x) \quad (6.1)$$

$$\frac{\partial n}{\partial t} - \frac{\partial}{\partial x} [D_{neo} + D_{ano} f_s(v'_E, s)] \frac{\partial n}{\partial x} = S(x) \quad (6.2)$$

where f_s is a suppression function which is assumed to depend on the flow shear v'_E and the magnetic shear s . Both thermal and particle sources are assumed to have Gaussian shape, with their distributions are defined such that over 90% of the total source is located within ± 0.1 of normalized minor radius unit (r/a) from the peak of the shape, which is localized near plasma center for thermal source and plasma edge for particle source. Furthermore, it is assumed that only the anomalous channel is suppressed by the two mechanisms with the suppression function of the form:

$$f_s(v'_E, s) = \frac{\beta |s|}{1 + \alpha v'^2_E} \frac{1}{1 + \gamma s^2}, \quad (6.3)$$

where α , β , and γ are arbitrarily chosen constants representing strengths of the

suppression. This function is based on assumptions that the transports can be quenched or reduced by the flow shear and magnetic shear. Furthermore, the flow shear strength is also affected by the magnetic shear that is the magnetic topology also influences the flow in the plasma. This form of magnetic shear suppression is inspired by those used in the previous works [143-144]. The novel form of magnetic shear suppression effect used in this work is based on experimental evidences that the transport barriers can form in the region of large (ETB) and low (ITB) magnetic shear [43, 145]. In particular, the numerator term governs the core transport suppression, while the denominator term governs the edge transport suppression. The flow shear couples the two transport equations according to the force balance equation showed in equation (4.3). The magnetic shear s is calculated from the q -profile as follows:

$$s = \frac{x}{q} \frac{\partial q}{\partial x}, \quad (6.4)$$

$$q = \frac{x}{R} \frac{B_\phi}{B_\theta}. \quad (6.5)$$

A large aspect ratio tokamak of circular cross section approximation is assumed throughout the work. The toroidal magnetic field is assumed to be constant; while the poloidal magnetic field is calculated from the current using Ampere's law with current density of the form:

$$j(x) = j_0 \left(1 - (x - x_0)^2 / a^2\right)^v + j_b, \quad (6.6)$$

where x_0 is the location of current density peak, a is the plasma minor radius and j_b is the bootstrap current which is locally proportional to pressure gradient ($j_b \propto -\nabla p$) [146]. At steady state, the two transport equations can be rewritten into the forms:

$$-\left[\chi_{neo} + \chi_{ano} f_s(v'_E, s)\right] \frac{\partial p}{\partial x} = Q(x) \quad (6.7)$$

$$-\left[D_{neo} + D_{ano} f_s(v'_E, s)\right] \frac{\partial n}{\partial x} = \Gamma(x). \quad (6.8)$$

This condition is valid both at steady state and at transient state providing that the plasma evolves slowly. The flow shear term is calculated as in equation (5.5). These two equations can be decoupled using the method similar to that used by Malkov *et al.* [96]. Then using the given current density and sources profiles the plasma

pressure/density and their respectively gradients can be numerically solved. Note that this phenomenological approach of study ITB and ETB may have disadvantages comparing to theoretical based models like GLF23 [105], Multi-Mode [107] or TGLF [147], which use integrated predictive modeling code to simulate tokamak plasma profiles. This approach allows possibility to investigate and understand better the bifurcation nature of the plasma with respect to both ETB and ITB. As will be shown in sections 6.3 and 6.4, some interesting phenomena arise and are worthwhile for discussion.

6.3 Plasma profiles and bifurcation behavior

This section shows numerical results from consistently solving the two transport equations (6.1) and (6.2) with suppression function as explained in the previous section. It is worth mentioning again that the effects of instabilities, like edge localized mode, neoclassical tearing mode, or sawtooth oscillation, are not included, in which these instabilities can influence the results. Accordingly, the results obtained can be treated as an optimistic scenario with no instabilities. All numerical results obtained are carried out using the same set of chosen constants; otherwise it is specified promptly. The transport coefficients are defined such that both thermal and particle anomalous diffusivities are around one order of magnitude over their neoclassical counterparts. The assumption is valid for ions, while for electrons the order of magnitude can be as high as two. In addition, the particle diffusivities are set to be roughly a quarter of thermal diffusivities [6]. Specifically, $\chi_{neo} = 1$, $\chi_{ano} = 10$, $D_{neo} = 0.25$, $D_{ano} = 2.5$, $\alpha = 0.1$, $\beta = 1$, and $\gamma = 0.1$. These values of transport coefficients are in a typical range of transport predicted by simulations using integrated predictive modeling codes using predictive core transport models [107-108]. Additionally, the model parameter α is theoretically proportional to square root of the turbulence correlation time, which has the value in the order of tens to hundreds of milliseconds [96, 148]. The other model parameters (β , and γ) are selected for the suppression to be reasonable for these range of transport coefficients. Sensitively, if their values are changed by 10%, the simulation results of central plasma pressure and density as well as the pedestal width can change around 50% for β and 5% for γ .

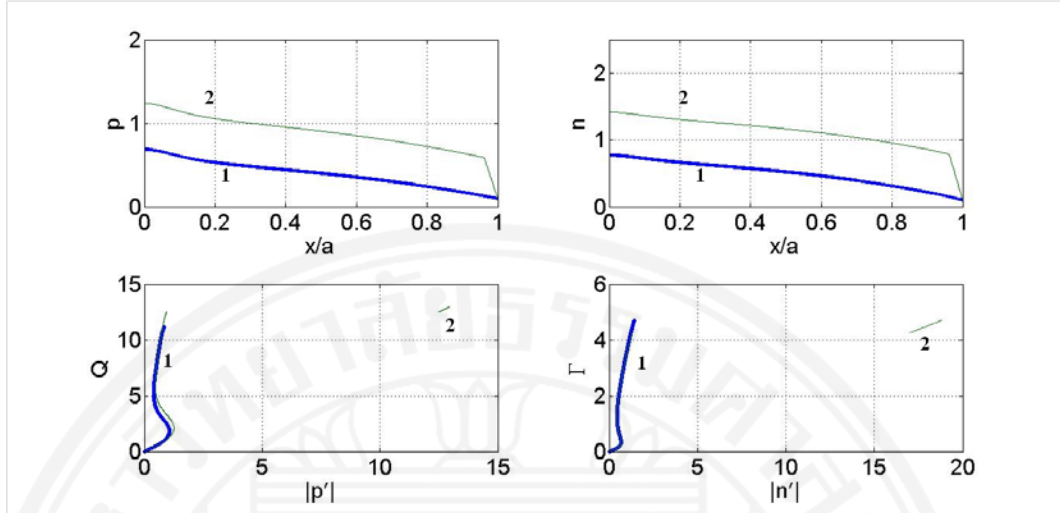


Figure 6.1: Plasma pressure (top left) and density (top right) as a function of normalized minor radius x/a for setup scenarios 1 (thick line) and 2 (thin line), and the results mapped onto heat flux versus pressure gradient (bottom left) and particle flux versus density gradient (bottom right).

Figures 6.1, 6.2 and 6.3 illustrate profiles of plasma pressure and density as a function of normalized minor radius x/a (top panels) for 6 different setup scenarios. Scenarios 1, 3 and 5 are setup with the same heating which is less than the critical value required for L - H transition ($Q_L = 0.92Q_{L \rightarrow H}$), but with different location of current density peaking; at $x_0 = 0$ (plasma center), $x_0 = 0.2$ and $x_0 = 0.1$, respectively. On the other hand, scenarios 2, 4 and 6 are setup with the same heating which is more than the critical value required for L - H transition ($Q_H = 1.06Q_{L \rightarrow H}$), but with different location of current density peaking at; $x_0=0$ (plasma center), $x_0 = 0.2$ and $x_0 = 0.1$, respectively. It can be seen that each scenario yields the plasma with different performance. Firstly, there exists a heating threshold $Q_{L \rightarrow H}$ in which the plasma makes a transition from L -mode to H -mode with formation of an edge transport barrier near plasma edge. In scenario 1, the plasma is set up with low heat source and no reverse shear profile (current profile peak at plasma center). This plasma remains in L -mode with central pressure and density equal to 0.69 and 0.77, respectively. Scenario 2 is setup with heat source greater than the critical value required for L - H transition ($Q_H > Q_{L \rightarrow H}$) and no reverse shear profile. In this scenario, the plasma makes a transition to H -mode with a pedestal width of 0.038 and central pressure and density of 1.24 and

1.42, respectively. Numerically, the heating in scenario 2 increases from that of scenario 1 by 15% but the central plasma pressure and density are almost doubled. The increase of plasma performance by around a factor of two as a result of *H*-mode transition has been observed in tokamak experiments [31, 44]. This is a very significant enhancement which is why the *H*-mode is preferred for tokamak operation. The bottom panels illustrate bifurcation diagram which mapped numerical results of each scenario into heat flux Q versus pressure gradient p' and particle flux Γ versus density gradient n' spaces. So, each location on the curves is a different location in the plasma. Theoretically, an example of a tradition *s*-curve bifurcation diagram can be found in Ref. [96] which shows a non-monotonic behavior. In figure 6.1, there appear discontinuities in pressure and density gradient profiles for scenario 2. They identify the locations of top of ETB.

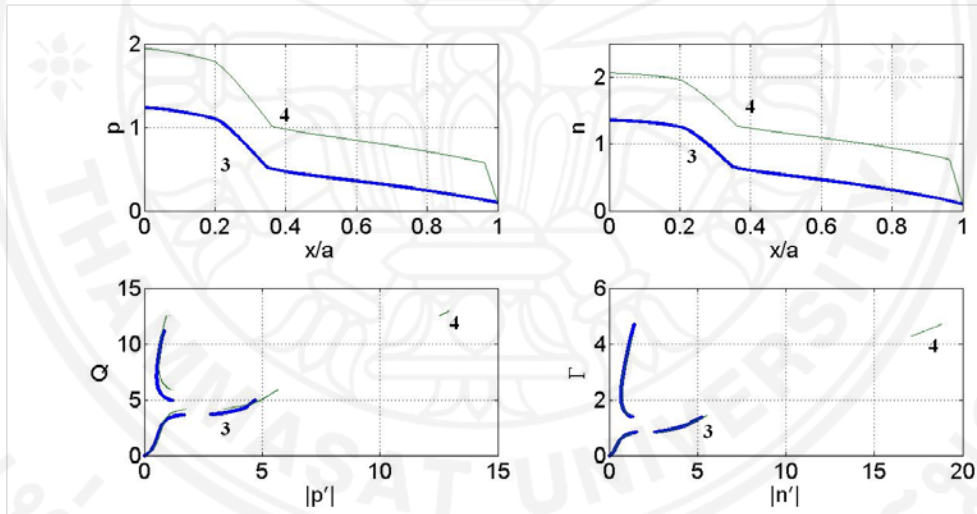


Figure 6.2: Plasma pressure (top left) and density (top right) as a function of normalized minor radius x/a for setup scenarios 3 (thick line) and 4 (thin line), and the results mapped onto heat flux versus pressure gradient (bottom left) and particle flux versus density gradient (bottom right).

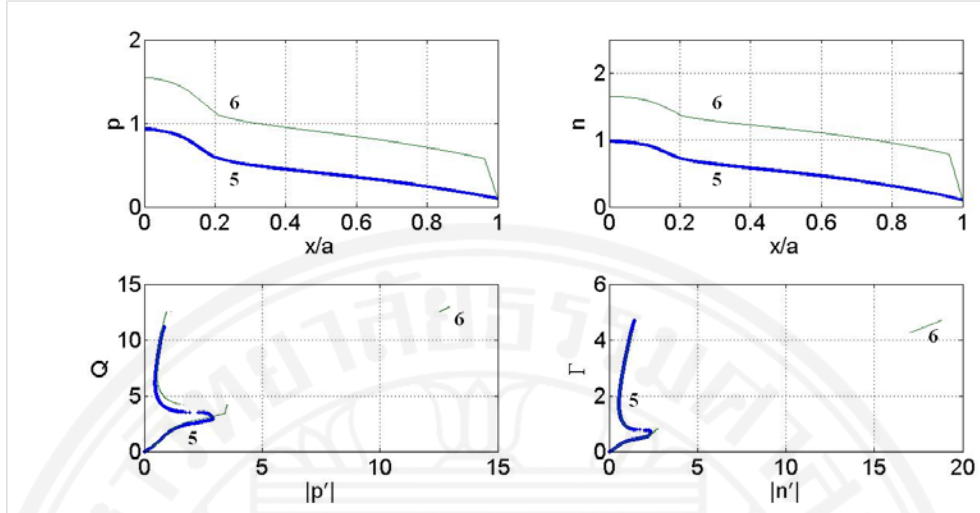


Figure 6.3: Plasma pressure (top left) and density (top right) as a function of normalized minor radius x/a for setup scenarios 5 (thick line) and 6 (thin line), and the results mapped onto heat flux versus pressure gradient (bottom left) and particle flux versus density gradient (bottom right).

Scenario 3 is setup with low heat source ($Q_L < Q_{L \rightarrow H}$) and current profile peaking at $x/a = 0.2$ ($x_0 = 0.2$) representing reversed shear profile. In this case, the plasma is still in L -mode but there is a formation of ITB near plasma core (see figure 6.2). The central pressure and density are around 1.23 and 1.36, which are increased from L -mode plasma without ITB by 78% and 77%, respectively. This implies that appropriate control of current profile in the plasma can lead to enhancement of plasma performance as well. In various tokamak experiments, the desired reverse shear profiles can be obtained using different schemes of current control, such as off-axis lower hybrid current drive, which can result in off-axis current density peaking [149-151]. The simulations in this work assume a form of current density distribution [6] with possibility to change the current peak location and with addition of bootstrap current effect (equation (6.6)). Scenario 4 is setup with high heat source ($Q_H > Q_{L \rightarrow H}$) and current profile peaking at $x/a = 0.2$. As expected based on the previous results, ETB and ITB formations can occur simultaneously. Note that the top of ITB appears to be closed to the location of current drive peak, detailed results on this will be showed in a later section. The central pressure and density are increased to 1.94 and 2.06 which are 181% and 168% enhancement over L -mode performance, respectively.

In this particular scenario, the jump in the gradients at lowest value of Q corresponds to the top of ITB, next jump corresponds to the foot of ITB and the jump at highest value of Q corresponds to the top of ETB. The magnetic shear and suppression function profiles for all scenarios are showed in figure 6.4. It can be seen that the suppression function reduced to zero or almost zero within the barrier regions. Also, the magnetic shear has a very small negative value within the region of ITB.

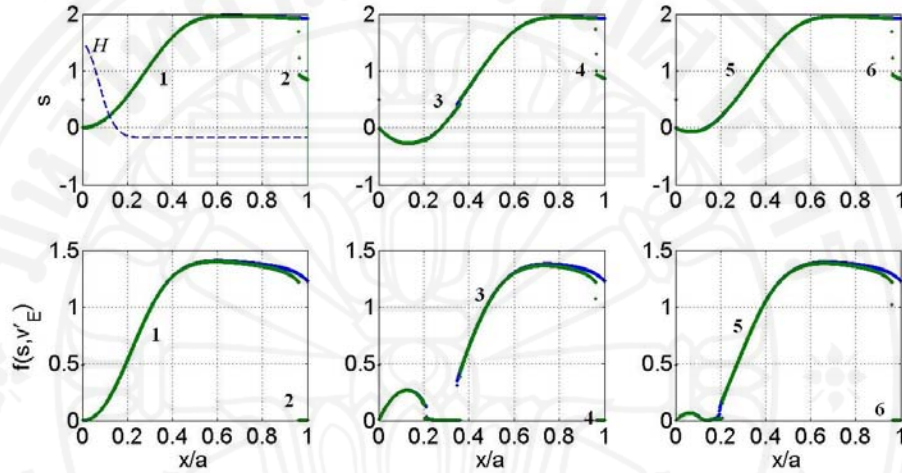


Figure 6.4: Profiles of magnetic shear (top) and suppression function (bottom) as a function of normalized minor radius x/a for setup scenarios 1 to 6; the heat source profile is also shown as dashed line.

The results of scenarios 5 and 6 illustrate another type of ITB called “weak ITB” as shown in figure 6.3. They are corresponding to the setup where the current density peak is given near plasma center ($x_0 = 0.1$). It is called weak ITB because the top of ITB is not so clearly identified as opposed to the foot of ITB. This can be seen more clearly in figure 6.5 which illustrates the pressure gradient profiles of all scenarios. First of all, in this work the formation of transport barriers is identified as a drastic change in gradient profiles. The locations of ETB_{top} , ITB_{top} , and ITB_{foot} are defined as location in which the change in gradient of the vicinity plasma local points is more than 10%. This number is arbitrarily chosen but it serves as a threshold for transport barriers formation in this work. As this work only solves simple forms of transport equations, the change in gradient is considerable and obvious that this criterion can be used effectively. Based on this criterion, it can be seen, for example, in the bottom left and right panels of figure 6.5 that only the change in pressure

gradient at the foot of ITB is clearly visible (near $x/a = 0.2$). In this weak ITB regime, the suppression by magnetic shear is not sufficient at the top of ITB because the region is close to plasma core where the profiles tend to flat out resulting in parabolic plasma profiles. In scenario 5, the central pressure and density is increased to 0.93 and 0.98, respectively. On the other hand, in scenario 6 (with ETB), the central pressure and density is increased to 1.55 and 1.65, respectively. The increases are less than those from the scenarios with full ITB. Figure 6.5 also shows that the jumps in gradients are higher in ETB than ITB for both pressure and density channels. Moreover, the jump in the gradients is around one order of magnitude higher. This weak ITB behavior was also found in experiments. For example, in the work of Neudatchin *et. al.*, the heat diffusivities associated with weak ITB are 5 to 10 times higher than that of the stronger or regular ITB counterpart [152]. Figure 6.4 also confirms that the area of negative magnetic shear for weak ITB plasma is smaller than that of regular ITB plasma resulting in smaller suppression strength.

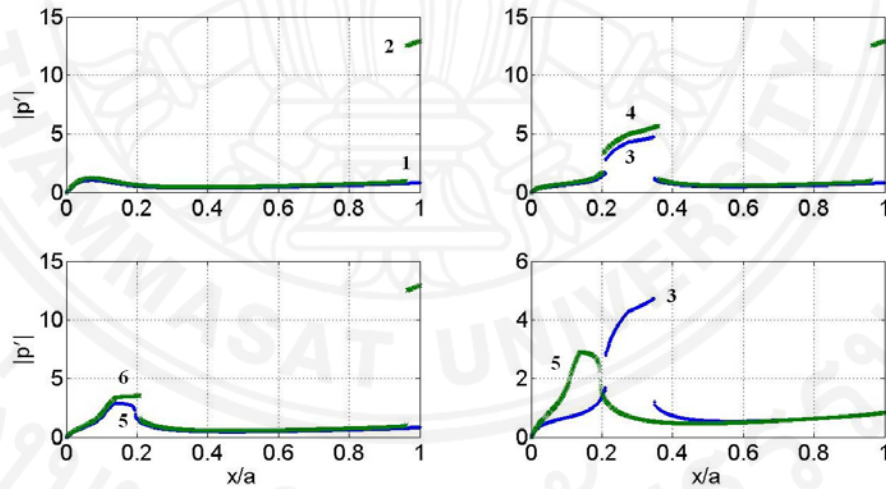


Figure 6.5: Comparison of plasma pressure gradient as a function of normalized minor radius x/a for setup scenarios 1 and 2 (top left), 3 and 4 (top right), 5 and 6 (bottom left) and 3 and 5 (bottom right).

6.4 Sensitivity analysis

6.4.1 Effects of heat and particle sources

The effects of both heat and particle sources are investigated in this section. First of all, the heat and particle fluxes are varied across the critical points $Q_{L \rightarrow H}$ and

$\Gamma_{L \rightarrow H}$, in combination with the variation of current density peaking. The location of current density peak is also varied, so that the cases with no-ITB, weak-ITB and ITB formation, altogether with and without ETB formation are present. The summary of results is showed in figure 6.6 as pressure (top panel) and density (bottom panel) contour plots. The x-axis represents location of the off-axis current peak and the y-axis represents the ratio over transition fluxes. Different regimes are categorized in these plots. The horizontal line separates *L*-mode and *H*-mode regimes. The two dashed lines separate the graph into 3 regimes; no ITB (left), weak ITB (middle) and ITB (right). Previously, the authors of reference [152] used somewhat ambiguous definition to categorize ITB type. In this work, weak ITB are differentiated from regular ITB when the top ITB is not clearly identified as already discussed in section 6.3. This graph qualitatively and quantitatively captures plasma performance and operation mode. For example, one can imagine that there are three possible scenarios to achieve the same central plasma pressure (contour line 1.5124); *L*-mode with ITB, *H*-mode with weak ITB or *H*-mode without ITB but with higher heating required. The latter case comes with more operational cost. The figure also shows us that the location of off-axis heating can affect the plasma pressure and density less in *L*-mode than in *H*-mode, illustrated with a bigger gap between contour lines. This makes sense because in the previous section, the results showed that the gradients in ETB region are stronger than that of ITB. As a summary, this figure implies that accessing the regime with simultaneous ETB and ITB formation is the most desirable with respect to plasma performance.

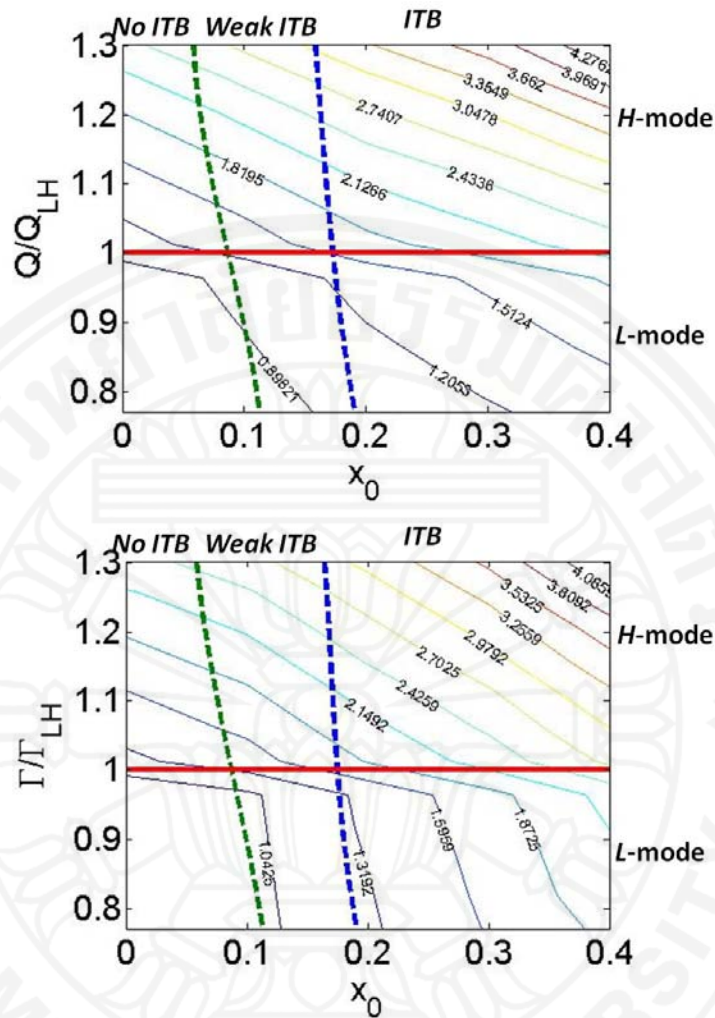


Figure 6.6: Central pressure (top) and density (bottom) contour field plots with x-axis as location of current density peaking and y-axis as heat/particle flux over critical threshold ratios.

Table 6.1 illustrates the effects of plasma heating. Clearly, it shows that the heating increases both plasma central pressure and density, which is known in many experiments [38]. From *L*-mode to *H*-mode, the central values are increased by around a factor of two, while the heating power is increased only by 26%. So, the *H*-mode plasma performs significantly better than *L*-mode plasma with not much increase in the heating. It also confirms here that if the heat flux is below the threshold value, ETB formation does not exist. Further increase of heating power results in increases of ETB and ITB widths. It is worth noting that ETB is more sensitive to an increase of heating power than ITB. For example, the results show that

when the heating is increased by almost 15% (from $1.01 Q_{L-H}$ to $1.16Q_{L-H}$), ETB width is increased by 107% and ITB width is increased by 15%. It is also found that the ITB_{foot} moves outward, whereas the ITB_{top} moves slightly inward but still within the vicinity of current drive location which is equal to 0.2. This is because the region of low magnetic shear is close to the plasma center where the plasma profiles tend to be flat, thus preventing ITB_{top} to expand as much as its foot. Even though there is no threshold heat flux for ITB formation, the reduction of heat flux lessens the jump in discontinuity of the pressure gradient. This can be observed in the top right panel of figure 6.5, which compares the pressure gradient between scenarios 3 and 4.

Table 6.1: Heating effects on plasma pressure and transport barriers

Heating (x/a)	p_0	n_0	Δ_{ETB}	ITB_{top} (x/a)	ITB_{foot} (x/a)	Δ_{ITB}
$0.92Q_{L-H}$	1.233	1.357	-	0.211	0.347	0.136
$0.96Q_{L-H}$	1.318	1.384	-	0.209	0.351	0.142
$1.01Q_{L-H}$	1.727	1.888	0.028	0.206	0.355	0.149
$1.06Q_{L-H}$	1.941	2.062	0.037	0.204	0.36	0.156
$1.11Q_{L-H}$	2.17	2.243	0.047	0.196	0.363	0.167
$1.16Q_{L-H}$	2.422	2.444	0.058	0.194	0.366	0.172

The variations both ETB and ITB widths as a function of heating are shown in figure 6.7. In this figure, the diamond, square, triangular, cross and circular bullets represent the numerical results from current peak location at $x/a = 0, 0.1, 0.2, 0.3$ and 0.4 , respectively. It can be clearly seen that as heating surpassed the $L-H$ threshold, the pedestal is formed and gets wider as the heating is further increased. Note that throughout this work, the investigation focuses on intrinsic properties of the plasma so instabilities are neglected. This can result in the pedestal width be wider than what measured in H -mode experiments. This operation regime is called VH -mode where it was found that combination of ELM avoidance and extensive suppression by radial electric field could lead to a factor of two improvement over that of H -mode confinement [153]. Also, the location of current drive does not affect ETB width. Whereas, both heating and current drive location appears to increase the width of ITB. The bottom panel of this figure illustrates the effects. Figure 6.8 shows the bootstrap current fraction (I_b) per total current. It can be seen that as the heating increases the

bootstrap fraction is also increased because the transport barrier width is wider. Also, ITB formation appears to further enhance bootstrap fraction. For example, at $1.3Q_{L \rightarrow H}$ the bootstrap current fraction is increased from 15% to almost 25% with ITB forms near $x/a = 0.4$. The pressure and density profiles at various heating, shown in the bottom panels of figure 6.8, exemplifies the fact that the heating affects the plasma stronger in *H*-mode than in *L*-mode, similar to the early results from ASDEX study of *H*-mode [38].

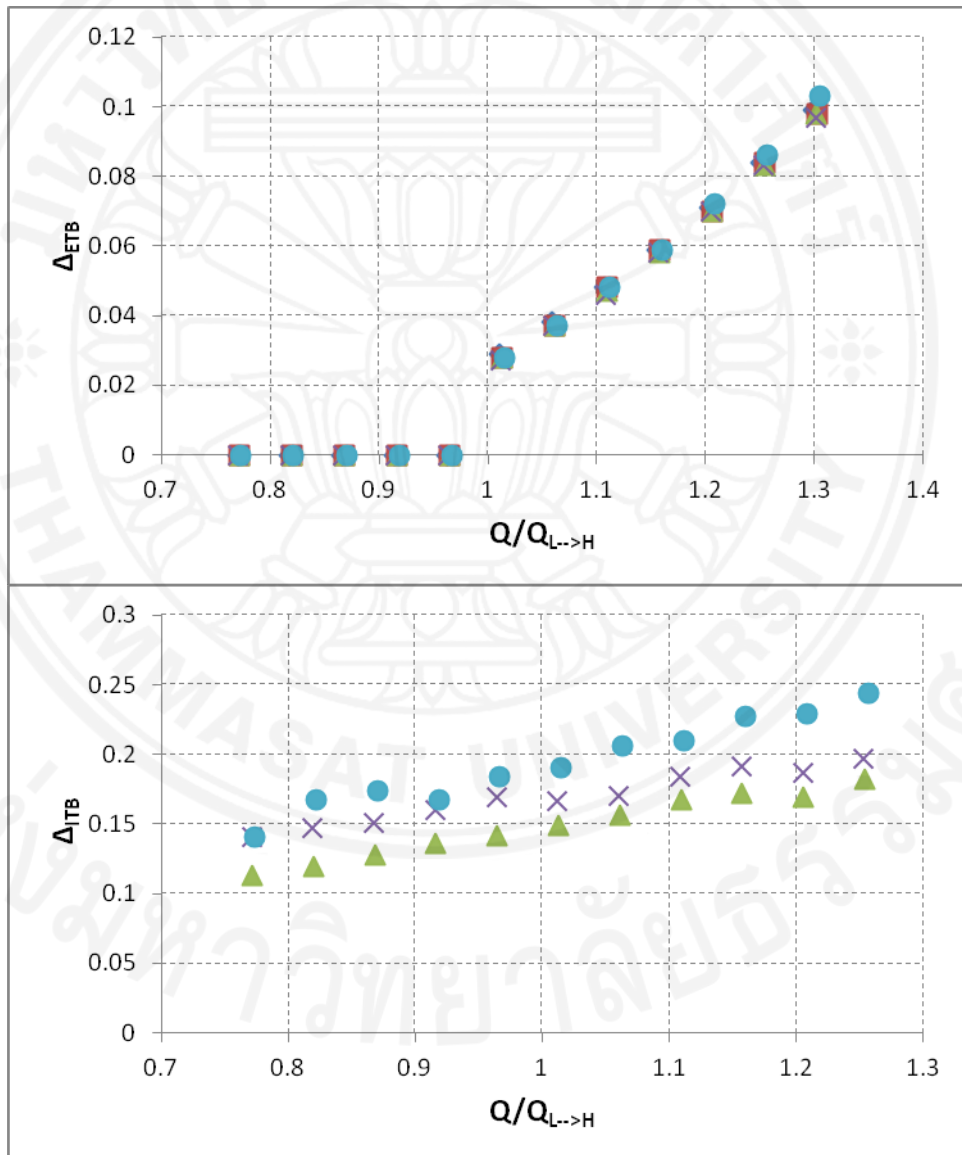


Figure 6.7: Pedestal width (top) and ITB width (bottom) as a function of heat flux.

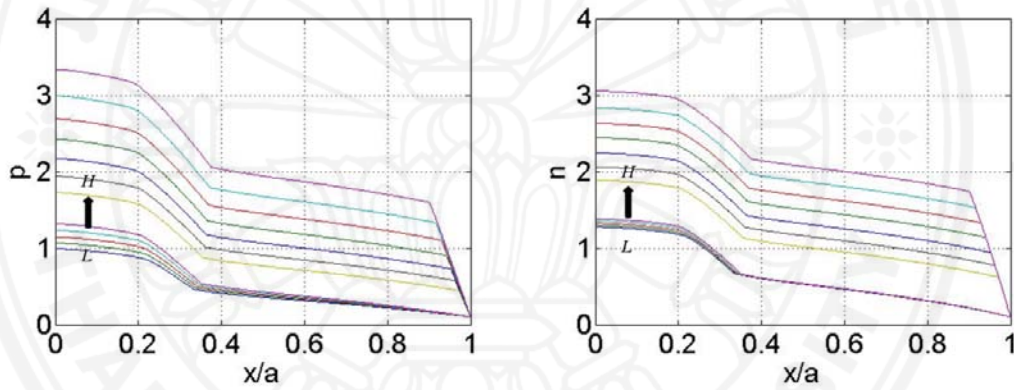
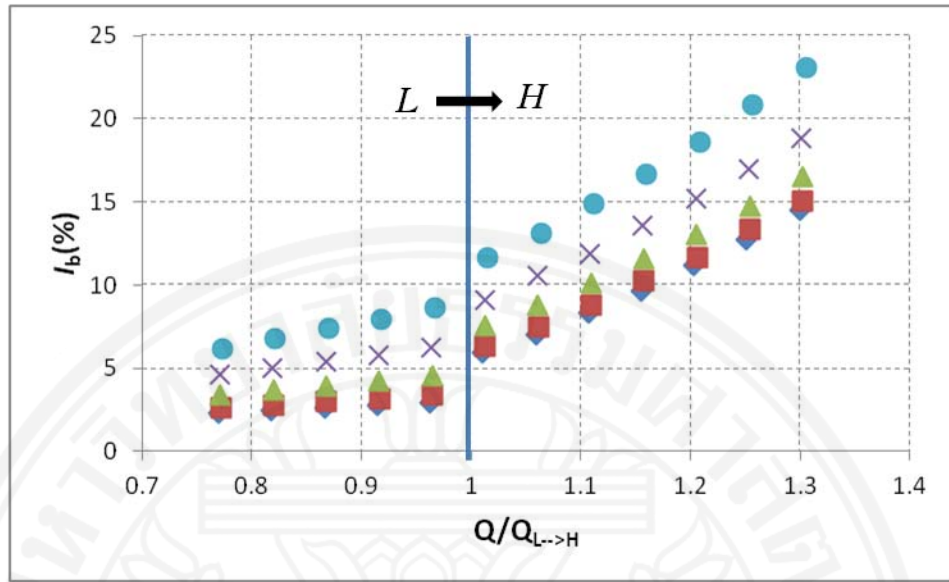


Figure 6.8: Bootstrap current fraction of total current as a function of heating at various location of driving current peaking (top) and pressure (bottom left) and density (bottom right) profiles as a function of normalized radius at different heating and driving current peaking at $x_0 = 0.2$.

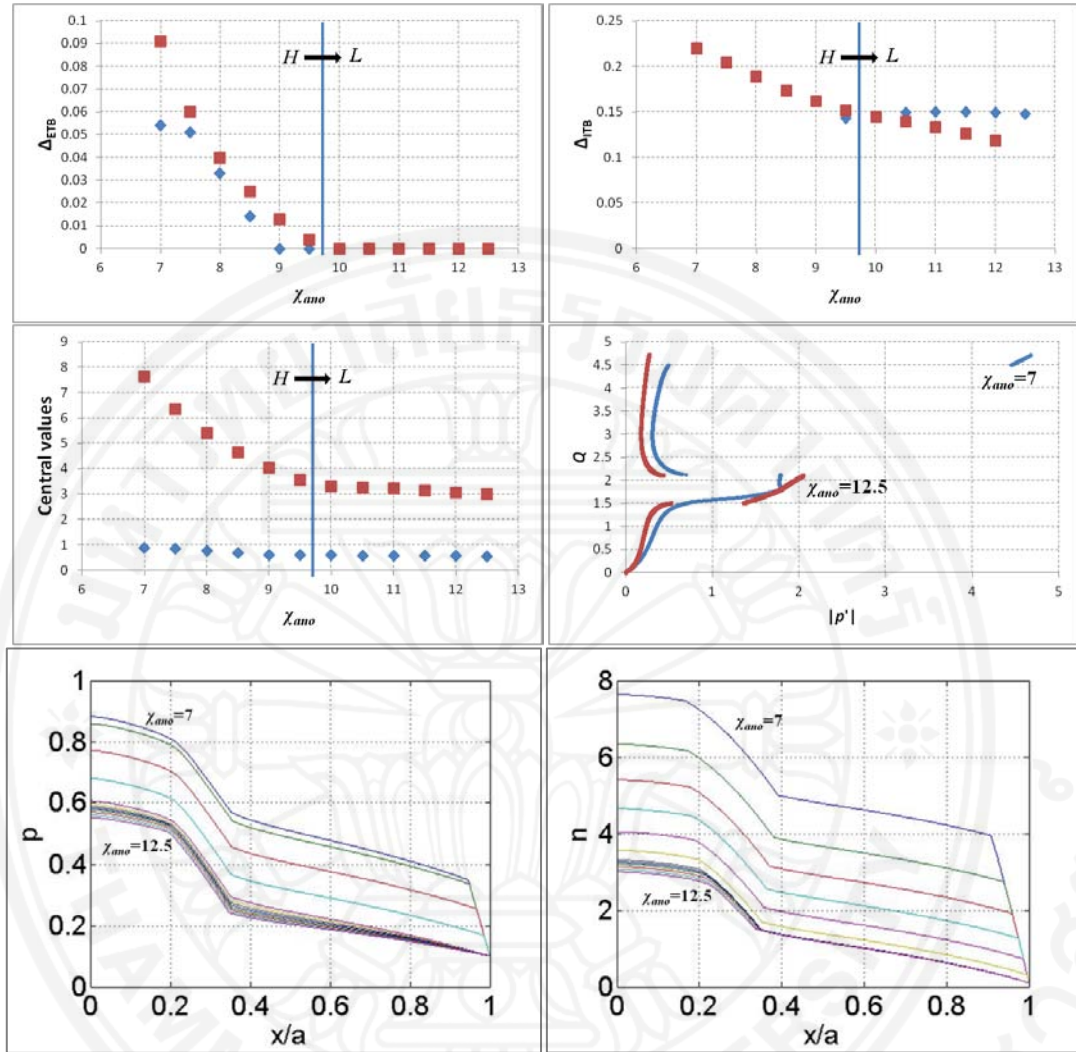


Figure 6.9: Pedestal width (top left), ITB width (top right) and central plasma values (middle left) as a function of thermal anomalous transport strength (diamond is for pressure and square is for density), heat flux versus pressure gradient (middle right) and radial profiles of pressure (bottom left) and density (bottom right) at different values of thermal anomalous transport.

6.4.2 Effects of transport strength

This section investigates impacts of transport strength on the plasma, including the central plasma pressure and density, plasma profiles and the widths of both ITB and ETB. The transport strength is assumed in the form of thermal and particle neoclassical and anomalous transport diffusivities, χ_{ano} , D_{ano} , χ_{neo} and D_{neo} , respectively. Figure 6.9 illustrates the effects of thermal anomalous transport diffusivity. In this figure, diamond bullets represent results of pressure field and

square bullets represent results of density fields. As the transport strength increases, the central pressure and density (middle left panel) are reduced as expected because of higher loss. The reduction rate appears to be stronger in *H*-mode than that in *L*-mode. Note that the changes in pressure are not so clear in this panel because the values are small relative to that of density. Nevertheless, the evolution of pressure (bottom left panel) and density (bottom right panel) profiles piloted by the variation of thermal anomalous transport parameter are also shown, which illustrates the different reactions to the transport in *L*-mode and *H*-mode. Evidently, there exists a critical value of thermal anomalous transport diffusivity where the plasma no longer remains in *H*-mode. This is illustrated as the reduction of pedestal width as the transport is stronger and eventually the pedestal collapses. This behavior agrees with earlier works of bifurcation concept in which there exists a threshold ratio of anomalous over neoclassical transport where *L-H* transition is possible [96, 135]. In other word, if the ratio is lower than this threshold value, the plasma cannot bifurcate to *H*-mode. It is also found that the pedestal widths for both pressure and density are almost the same. The transport effect on ITB formation is rather interesting. First of all, as thermal anomalous transport is increased, the ITB width in the density channel is reduced with different rate in *H*-mode and *L*-mode. At low transport, there exists weak ITB in the energy channel with parabolic pressure profile near the plasma center (bottom left panel). As the transport is increased over certain value, the weak ITB turns into a regular ITB. The mapping on bifurcation diagram is shown in middle right panel where at low value of thermal anomalous transport ($\chi_{ano}=7$) there is no discontinuity in the pressure gradient at top of ITB. Whereas, at high transport ($\chi_{ano}=12.5$), identification of ITB is more clear. The interesting point here is that once χ_{ano} reduces to comparable value to χ_{neo} (same order of magnitude), the suppression by magnetic shear to the energy channel is reduced, especially near plasma center. Meanwhile, the magnetic shear suppression strength is more effective in the particle channel, resulting in larger ITB. The reason for this behavior is not clear, but it is possible to be a result of correlation between transport diffusivities. As discussed in details by Malkov and Diamond, the ratio of $\chi_{ano}D_{ano}/\chi_{neo}D_{neo}$ plays significant role in determination of the transition and the suppression [96].

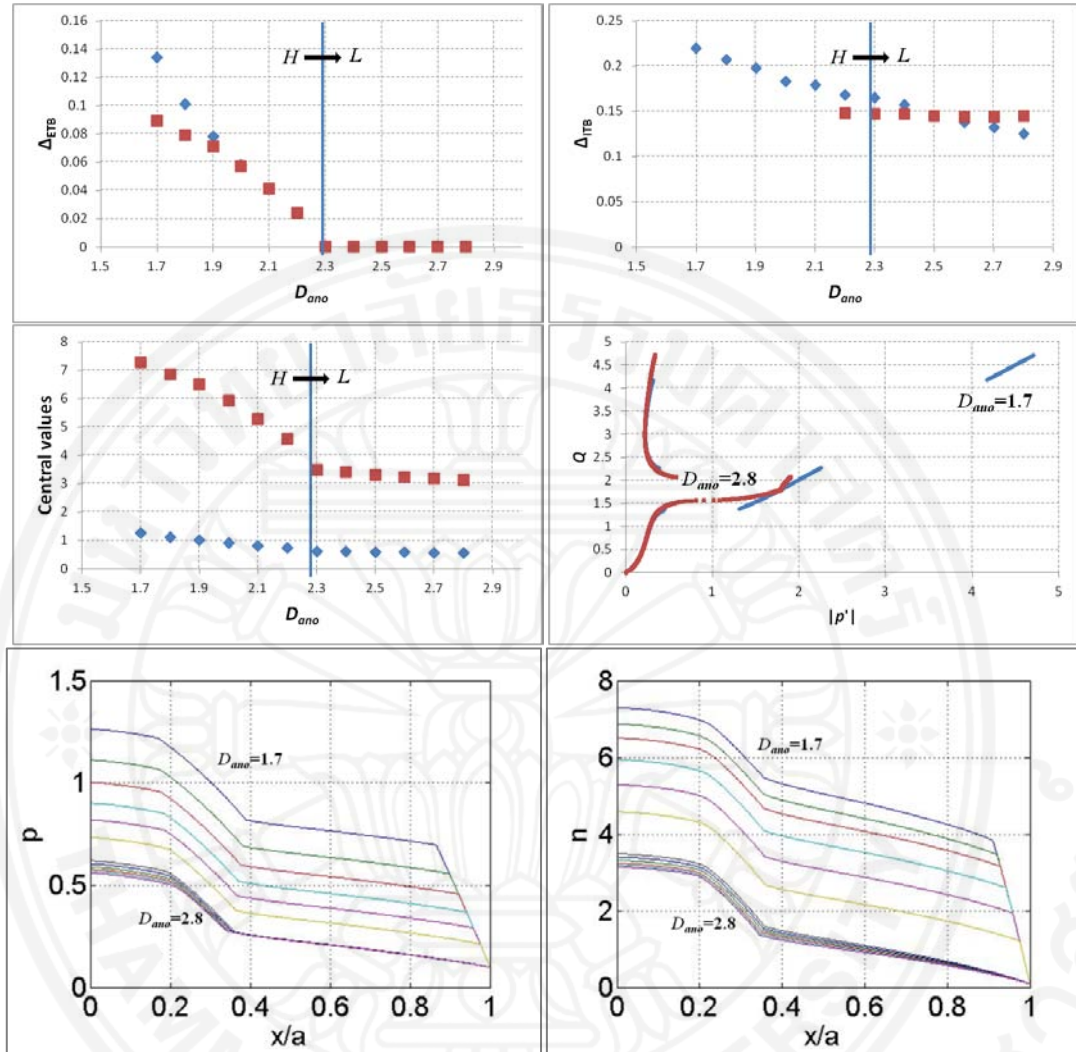


Figure 6.10: Pedestal width (top left), ITB width (top right) and central plasma values (middle left) as a function of particle anomalous transport strength (diamond is for pressure and square is for density), heat flux versus pressure gradient (middle right) and radial profiles of pressure (bottom left) and density (bottom right) at different values of particle anomalous transport.

Effects of particle anomalous transport diffusivity is showed in figure 6.10. First of all, the central pressure and density is decreased as the transport gets stronger. Again, the reduction is stronger in *H*-mode than in *L*-mode because the change in pedestal width. There also exists a critical transport value where the plasma no longer stays in *H*-mode. The pedestal width appears to be wider in the pressure channel in this case, though its central value is much lower. As the transport is stronger, ITB width of the pressure profile is also reduced. Similarly, it can be observed that if the

transport is too low, the magnetic shear suppression is too weak to form regular ITB in the particle channel, resulting in weak ITB. Effects of both thermal and particle neoclassical transports are showed in figures 6.11 and 6.12, respectively. Similar to anomalous transport case, the central pressure and density are reduced as the transports get stronger. The reduction appears to be strongly nonlinear in the cases of particle neoclassical transport, which also shows that ETB only forms in particle channel, shown in figure 6.12. Furthermore, if thermal neoclassical transport increases, the pressure ITB is reduced while the particle ITB is increased. The result is opposite in the variation of particle neoclassical transport strength. This shows that the increase of neoclassical transports cause the suppression to be less effective in its own channel but enhances the suppression in the other channel. This is because the assumption of the flow shear as shown in equation (5.5). First of all, it makes sense that the increase of neoclassical transport (thermal/particle) causes ITB in its own channel to be reduced because the loss is enhanced. In the opposite channel, it is clear the profiles, especially near plasma core, quantitatively decrease (see bottom panels of figures 6.11 and 6.12). The ITB appears to slightly expand even though the gradient in the ITB region reduces, resulting in reduction of central density/pressure value.

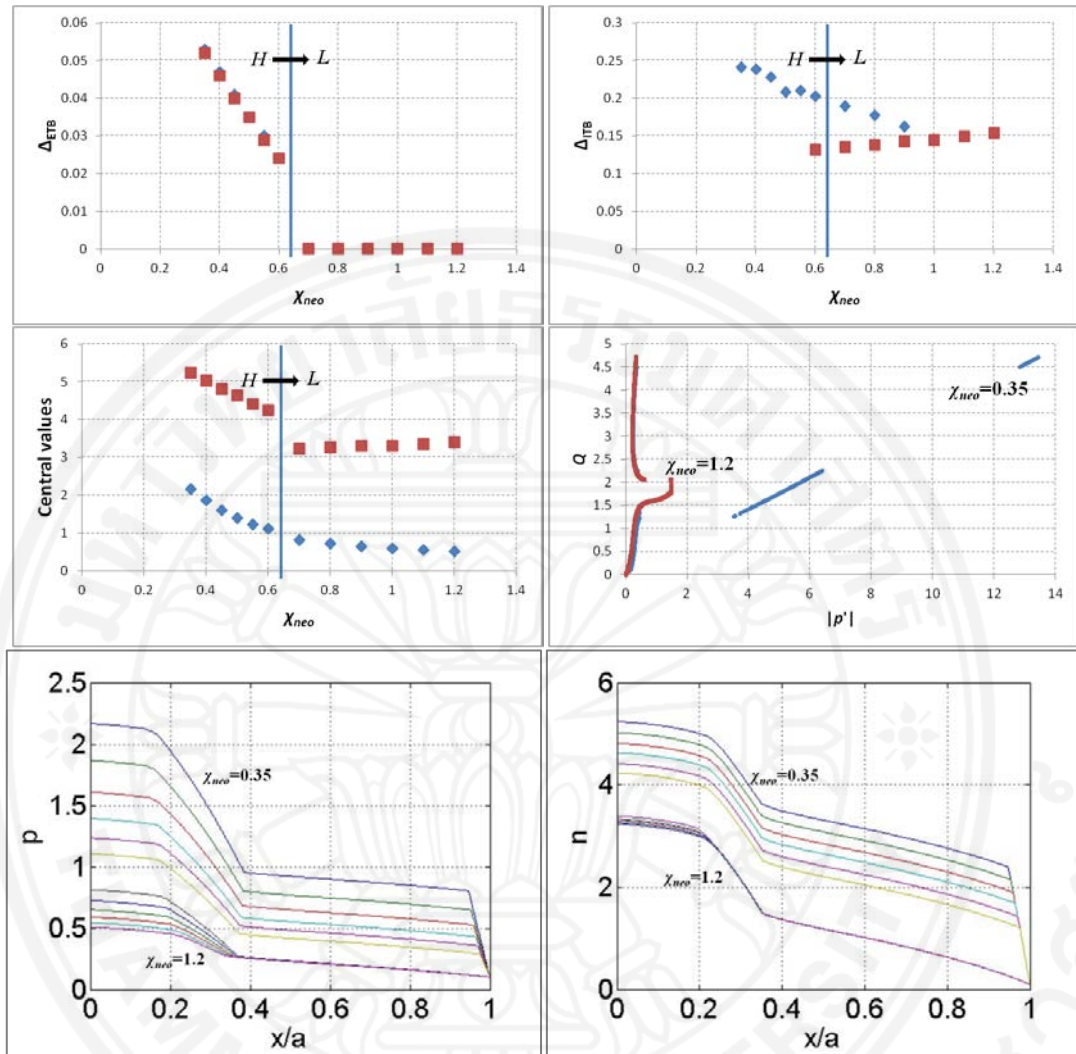


Figure 6.11: Pedestal width (top left), ITB width (top right) and central plasma values (middle left) as a function of thermal neoclassical transport strength (diamond is for pressure and square is for density), heat flux versus pressure gradient (middle right) and radial profiles of pressure (bottom left) and density (bottom right) at different values of thermal neoclassical transport.

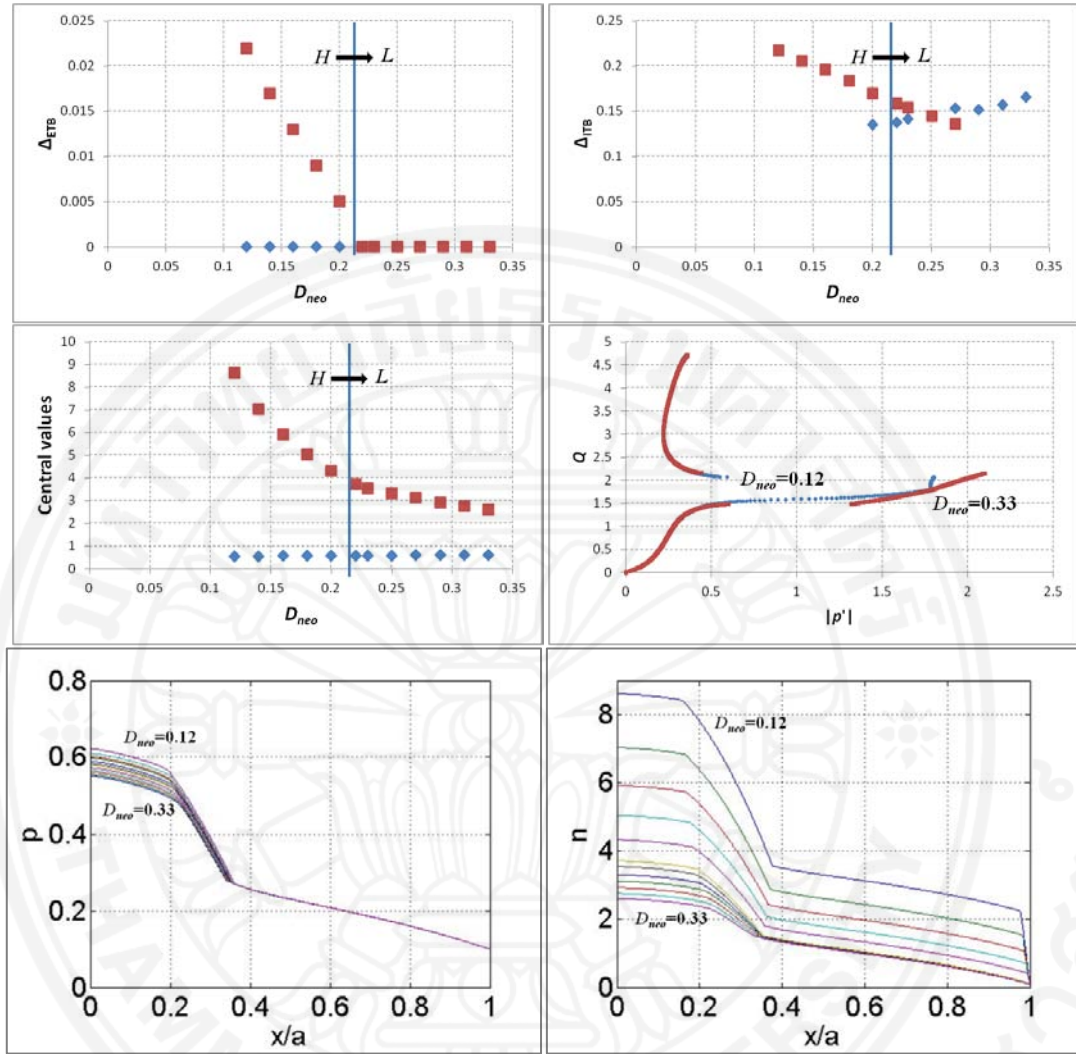


Figure 6.12: Pedestal width (top left), ITB width (top right) and central plasma values (middle left) as a function of particle neoclassical transport strength (diamond is for pressure and square is for density), heat flux versus pressure gradient (middle right) and radial profiles of pressure (bottom left) and density (bottom right) at different values of particle neoclassical transport.

6.4.3 Effects of current drive location

This section investigates the effects of current density peak location. The summary of this study is showed in table 6.2 where the peaking location x_0 is varied within the inner half of the plasma core from 0 to 0.1, 0.2, 0.3 and 0.4. The heat source given to this study is equal to Q_H to ensure that the plasma reaches H -mode. The reason for this setup is to study the interaction between both transport barriers and the effects of current peak location on them. First of all, it is found that the central

pressure p_0 and density n_0 are increased as the peak location moves outward. This is not a surprising result because moving peak location away from plasma center or magnetic axis can widen the zone with low magnetic shear, resulting in formation of ITB and performance improvement. The increase is more than double when the current peak is moved from plasma center to $x/a = 0.4$. Similarly, peak location appears to only affect ITB formation. As showed in the table, ETB width (Δ_{ETB}) remains almost the same value, while ITB width (Δ_{ITB}) is increased from 0.156 ($x/a = 0.2$) to 0.206. Note that on-axis current drive does not produce ITB formation and $x_0 = 0.1$ produces weak ITB as already discussed in the previous section. The interesting point to notice here is that the location of top of ITB (ITB_{top}) appears to be in the vicinity of the peaking location. The location of foot of ITB (ITB_{foot}) also expands outward as the current density peaking location moves outward.

Table 6.2: Effects of current density peaking location on plasma pressure and transport barriers

Peak location (x/a)	p_0	n_0	Δ_{ETB}	ITB_{top} (x/a)	ITB_{foot} (x/a)	Δ_{ITB}
0	1.241	1.417	0.038	-	-	-
0.1	1.546	1.653	0.037	-	0.207	-
0.2	1.941	2.062	0.037	0.204	0.36	0.156
0.3	2.233	2.473	0.037	0.329	0.499	0.17
0.4	2.569	2.976	0.037	0.437	0.643	0.206

6.5 Conclusion

In this chapter, a coupled 2-fields bifurcation model is used to analyze the formation and properties of ETB and ITB in tokamak plasmas. The transport equations for temperature and particle are self-consistently solved for the relation between local plasma gradients and corresponding fluxes in order to examine the ETB and ITB formations. It is found that the results can exhibit bifurcation nature when mapped onto fluxes versus gradients space in which abrupt changes in the gradients can be observed at plasma edge for ETB and plasma core for ITB. ETB formation depends sensitively on the heat flux. On the other hand, ITB formation is possible only with a presence of reverse magnetic shear profile with its width depends weakly

on the heat flux. Weak ITB formation is also found when the reverse shear profile happens close to plasma magnetic axis. ITB location and width are also found to be correlated to the nature of current peaking. In particular, the top of ITB is in the vicinity of where current density profile is maximum. Both ITB and ETB widths appears to be proportional to heat source and off-center distance of current peaking. Thermal and particle neoclassical and anomalous transport appears to affect plasma profiles, ETB and ITB widths.

Chapter 7

Toroidal Rotation Effects on L - H Transition Based on Bifurcation Concept

7.1 Introduction

Recently, there have been many reports on the prediction of ITER performance in the standard type I ELMy H -mode using different integrated predictive modeling codes [119, 154-158]. The core transport models used in those simulations were Mixed B/gB [110], MMM95 [107], and GLF23 [105] running under different predictive modeling codes such as BALDUR [50], JETTO [102], and ASTRA [98] code. The performance of ITER was normally evaluated in terms of central temperature, alpha power or total fusion power output. Those simulations yielded a wide range of predictions depending on initial conditions like heating power, plasma density, impurity condition, or even cross-section shape of the plasma. Additionally, the differences were also dependent on the choice of transport model and the code implemented in the simulations. Furthermore, in the recent work by Onjun *et al* [106], the simulations of ITER with combined effects of ITB and ETB were carried out by BALDUR code to predict performance of ITB H -mode plasma. At later years, simulation works were carried out to study the impact of pellet injection on ITB in ITER H -mode plasma [159] and on ITER plasma without ITB [160-161]. Moreover, behaviors of impurity in ITER plasma was studied and explored by Pianroj *et. al.* [162]. The similar set of code was most recently extended to cover core-edge simulations of H -mode plasma [163-164] as well as bootstrap current projection in ITER [165]. The L - H transition investigation was also carried out using MMM95 transport model, which illustrates the threshold criteria in heating power [166].

The reduction of anomalous transport is associated with the shear effects, including both velocity shear and magnetic shear [43]. Even though another mechanism like zonal flow [167] can also intrinsically generate the electric field shear, its role is omitted in this thesis. Theoretically, the calculation of ω_{ExB} flow shear requires the information of pressure gradient, poloidal rotation, and toroidal

rotation. There have been studies of momentum and velocity transport in poloidal direction [168-171] but not much has been done on toroidal direction. Toroidal rotation is found to play a significant role in the enhancement of plasma performance because the rotation could generate the flow shear which results in transport reduction and, consequently, formation of transport barriers [172]. It was found in the unbalanced injection scenario that the toroidal rotation can be the main contributor to the radial electric field and, consequently, the ω_{ExB} flow shear [172]. It is expected that external torque from NBI injection may not be enough to produce sufficient toroidal rotation in ITER. However, the toroidal momentum can be potentially generated from an intrinsic property of the plasma. As a result, it is interesting to investigate the intrinsic rotation in ITER. Simulations of ITER by Onjun *et. al.* [106] were carried out using the experimental data of toroidal velocity from some JET optimized shear discharges, which demonstrated the importance of toroidal velocity over the ITER performance. A simple empirical model for predicting toroidal velocity was developed by Chatthong *et. al.* [120] based on 10 optimized shear discharges from JET tokamak, which then was extended to predict ITER performance by Chatthong *et. al.* [123]. However, there was a concern over the validity of these works, especially when it is extended for ITER, due to a lack of sufficient theoretical foundations of those models. M. Kikuchi developed a theoretical toroidal rotation model based on Neoclassical Toroidal Viscosity (NTV) concept [124]. This NTV model is based on the idea the symmetry breaking in the plasma can result in plasma rotation in the toroidal direction. This breaking can be generated by an introduction of a non axisymmetric field. Recently, the effect of NTV toroidal rotation has been investigated in ITB ITER-like plasma using BALDUR code [173]. Even though there is a concern over the validity of this application for ITER, it is still interesting explore the results and the implication of this model for ITER.

In this chapter, a 1.5D BALDUR integrated predictive modeling code is used to simulate the time evolution profiles of density and temperature of electrons and ions. The ETB model used in this work is based on the report of Onjun *et. al.* [116]; in this model the ETB is expressed in terms of a pedestal model. The pedestal temperature is explained using the theory based pedestal width model combining with pressure gradient limits by ballooning mode instability. The model for ITB used in

this work is based on literature review of ITB (both theoretical work and experimental work). It is called semi-empirical Mixed Bohm/gyroBohm (Mixed B/gB) core transport model which proposes that formation of ITB is caused by the suppression in anomalous transport due to ω_{ExB} flow shear and magnetic shear [110]. In BALDUR, data for ω_{ExB} is either given to the code or calculated. The code can also use the data taken from experiments. The first part focuses on the use of the NTV toroidal rotation model. The second part focuses on the toroidal velocity based on toroidal current density. The BALDUR simulations use toroidal velocity models to combine with ITB and ETB models to simulate JET discharges and to predict ITER performance in standard type I ELMy H-mode scenario. In the last part, the impact of toroidal velocity model in the bifurcation picture of L - H transition is analyzed.

7.1.1 Simulation procedure

In this section, the simulation procedure follows closely to that described by Chatthong, *et. al.* [120]. Namely, the integrated predictive modeling code used throughout the work is a time-dependent 1.5D transport code called BALDUR [50]. The code simultaneously solves three sets of diffusion equations for number density, energy density and poloidal magnetic field. Consequently, different plasma profiles, including temperatures, densities, plasma current, can be self-consistently obtained. The core transport is computed by BALDUR using a version of semi-empirical mixed Bohm/gyro-Bohm (Mixed B/gB) transport model, which includes ITB formation through the assumption that ITB is formed by the suppression of anomalous transport due to the ω_{ExB} flow shear and magnetic shear [110]. Mixed B/gB calculates both heat and particle transports as a function of both Bohm and gyro-Bohm terms. The Bohm term, which dominates the transport in plasma core, is suppressed by a Heaviside function of the ω_{ExB} flow shear, magnetic shear, and the instability growth rate as shown in the reports of Tala *et. al.* [110] and Chatthong *et. al.* [120]. The main hydrogen species considered in this work are deuterium and tritium; while the main impurity species are beryllium and helium, in which their transport coefficients are assumed in this work to be equal.

In this work, the boundary condition of the plasma simulations is taken to be at the top of pedestal. In general, the pedestal width is taken around 5% of the plasma

radius which is considered to be somewhat significant volume due to large value of the radius. However, the temperature in that region is very small, so small fusion reaction can take place. That means only small fusion energy can be produced from that region. Nevertheless, it should be noted that the large bootstrap current can be generated in the pedestal region due to a strong gradient and it could strongly influence the pedestal formation. This effect is already considered in the boundary predictions separately from the rest of the code. More details on the development of the pedestal model can be found in the report of Onjun *et. al.* [116]. The pedestal temperature is calculated using the pedestal model based on the magnetic and flow shear stabilization width model combining with the ballooning mode instability used to set the pressure gradient limits [116]. On the other hand, the pedestal density is estimated empirically to be a fraction of line average density [119].

The focus of this part will be on applying the developed toroidal rotation model to BALDUR in order to simulate ITER plasma and study its behavior including ITB formation and its dynamics. The reason is that the toroidal rotation appears to be one of the ingredients for calculation of the ω_{ExB} flow shear. The radial electric field E_r is derived from the force balance equation as shown in equation (2.9). This radial electric field is then used to calculate the ω_{ExB} shearing rate according to Hahn-Burrell model [43, 72]:

$$\omega_{\text{ExB}} = \frac{(RB_0)^2}{B} \frac{\partial(E_r / RB_0)}{\partial\psi} \quad (7.1)$$

where Ψ is the poloidal flux. Note that this form of ω_{ExB} shearing rate is slightly different from that described in the reports of Onjun *et. al.*, Chatthong *et. al.* and Chatthong *et. al.* [106, 120, 123], respectively, and thus the absolute value of ω_{ExB} is used in the mixed B/gB transport model. It is also noted that the poloidal flow is determined based on neoclassical theory using NCLASS [174]. Descriptions of BALDUR code, mixed B/gB model and pedestal model are described in chapter 2.

7.2 Simulations of ITER with the presence of ITB using NTV intrinsic toroidal rotation model

7.2.1 NTV toroidal rotation model

This model is based largely on the derivation by M. Kikuchi [124], in which the offset toroidal rotation can be produced by neoclassical toroidal viscosity (NTV) dissipation caused by symmetry breaking via application of a non-axisymmetric field [175]. Kikuchi has further refined the formula for offset toroidal rotation by including parallel flow effect on residual poloidal flow and impurity effect. It has the form:

$$v_\phi = \frac{1}{eZB_\theta} \left(3.54 - \frac{r}{R} K_1 \right) \frac{dT_i}{dr}, \quad (7.2)$$

where $K_1 = \frac{\gamma \hat{\mu}_{i2}}{D}$, $D = \hat{\mu}_{i1} (\hat{\mu}_{i3} + \gamma) - \hat{\mu}_{i2}^2$, $\gamma = \sqrt{2} + \alpha$, and $\alpha = \frac{n_I Z_I^2}{n_i Z_i^2}$, where the

subscripts I and i represents impurity and ion species, respectively. In short, the model implies that the toroidal rotation is driven by the temperature gradient. This calculated toroidal velocity is then used by BALDUR to determine the flow shear by directly substituting v_ϕ profile into the force balance equation (2.9) to find E_r . Then E_r is used to find ω_{EXB} , which can affect the suppression of anomalous stransport. In the banana regime, the elements of parallel viscosity matrix are estimated as follows [176]:

$$\hat{\mu}_{i1} = g \left(\alpha + \sqrt{2} - \ln(1 + \sqrt{2}) \right), \quad (7.3)$$

$$\hat{\mu}_{i2} = g \left(\frac{3\alpha}{2} + \frac{4}{\sqrt{2}} - \frac{5 \ln(1 + \sqrt{2})}{2} \right), \quad (7.4)$$

$$\hat{\mu}_{i3} = g \left(\frac{13\alpha}{4} + \frac{39}{4\sqrt{2}} - \frac{25 \ln(1 + \sqrt{2})}{4} \right), \quad (7.5)$$

where g is defined as

$$g \equiv \frac{f_t}{f_c} = \frac{1 - f_c}{f_c}, \quad (7.6)$$

here f_t and f_c are the average fractions of trapped and circulating particles, respectively. The value of f_c is approximated numerically to be [177]

$$f_c \cong 1 - 1.46\sqrt{\varepsilon} + 0.46\varepsilon\sqrt{\varepsilon}, \quad (7.7)$$

where ε is the plasma inverse aspect-ratio. It is worth to note one compatibility issue of this model with BALDUR code. Since BALDUR is an axisymmetric transport code whereas this NTV model is developed from non-axisymmetric field basis, it is natural to question the validation of applying this model in this work. However, the problem is omitted at present. This issue is left for future work.

Table 7.1: Standard type I ELMy H-Mode ITER design engineering parameters

<i>Parameters</i>	<i>Simulation Values</i>	<i>Unit</i>
<i>R</i>	6.2	m
<i>a</i>	2.0	m
<i>I_p</i>	15.0	MA
<i>B_φ</i>	5.3	T
<i>κ</i>	1.7	-
<i>δ</i>	0.33	-
RF	7.0	MW
NBI	33.0	MW
<i>n_{el}</i>	1.0x10 ²⁰	m ⁻³

7.2.2 Results and discussion

All simulations in this work are carried out based on standard type I ELMy H-mode scenario of ITER design using BALDUR integrated predictive modeling code. Some design engineering parameters used in this work can be seen in table 7.1, where RF represents radio frequency heating scheme and NBI represents neutral beam injection heating scheme. These values are kept the same throughout the work unless otherwise stated. In addition, the duration of each ITER simulation running time is set at 3,000 seconds, of which the plasma current and density are slowly ramped up to the designated values within the first 100 seconds. This is similar to other previous BALDUR works for ITER [106, 123, 159-162]. It is observed in all simulations that the plasma reaches stationary state quickly after the plasma current reaches the maximum value. In the stationary state, the plasma still varies with some degrees of

fluctuations due to plasma instability, i.e., sawtooth oscillation.

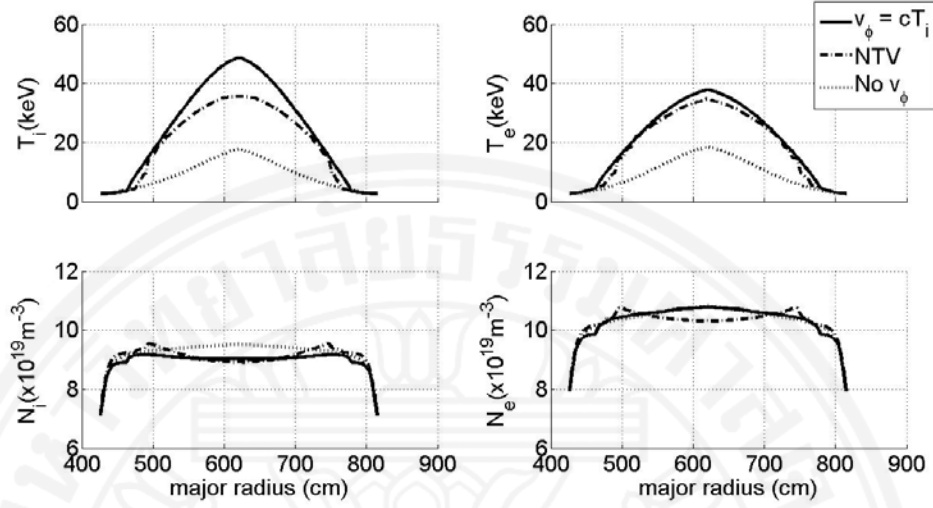


Figure 7.1: Profiles of ion (top left) and electron temperatures (top right), and ion (bottom left) and electron densities (bottom right) at stationary state ($t = 2,600$ s). Each line represents simulation results using empirical model (solid), model based on NTV (dash-dot), and no-value (dot) for toroidal rotation calculation.

7.2.2.1 Plasma profiles and ITER performance

First of all, it is interesting to investigate how toroidal rotation affects ITER plasma, focusing during stationary state. This can be seen in figure 7.1 which illustrates simulation results for ion temperature (T_i), electron temperature (T_e), ion density (N_i), and electron density (N_e) as a function of major radius at the time 2,600 seconds. This specific time is randomly chosen from after the plasma has already reached stationary state condition. In this part, three different options of toroidal rotation calculation are employed in the BALDUR code to simulate the ITER plasma: the first option using the empirical model developed by Chatthong *et. al.* [120], the second option using the model based on NTV in proposed by Kikuchi [124], and the third option using zero toroidal velocity. The purpose of this task is to compare how the difference in the toroidal rotation predictions for ITER can impact on the ITER plasma. It is worth to emphasize that the first model was empirically developed based on 10 JET optimized shear discharges. It has the form $v_\phi = cT_i$, where the constant c equal to 1.43×10^4 is used in this work, which was obtained from the optimization

with those 10 JET discharges. The details development can be obtained in the report of Chatthong *et. al.* [120]. It is found in the simulation using the empirical toroidal velocity model in the report of Chatthong *et. al.* [120] that optimistic plasma profiles are obtained for both temperatures and densities, which was reported by Chatthong *et. al.* [123]. It is also observed in the simulations using NTV model that there is a strong temperature gradient in the vicinity of position $r/a = 0.6$, which demonstrates the formation of ITB. The analysis on ITB's location and dynamics will be discussed later in more details. For the case without the presence of toroidal velocity, pessimistic plasma profiles were obtained. To compare the plasma temperature between each simulation in detail, the central values are evaluated. The simulation using the empirical model yields extremely optimistic values about 49 keV for ion temperature and 38 keV for electron temperature; whereas the simulation using the NTV model yields modest optimistic results for ion and electron temperature about 36 and 35 keV, respectively. It is worth mentioning that the fluctuation in the simulation using the NTV model is higher than that using the empirical model. It is also apparent that without the presence of toroidal rotation, the plasma central temperatures significantly drop to 18 keV. This strong reduction in temperature profiles is not surprising because of the absence of ITB. The possible cause of the fluctuation in NTV model simulations could be the Heaviside function built in Mixed B/gB model as ITB formation criteria. The function has the form:

$$H\left(-0.14 + s - \frac{1.47|\phi_{E \times B}|}{\gamma_{ITG}}\right), \quad (7.8)$$

where s is magnetic shear and γ_{ITG} is the linear growth rate. Figure 7.2 illustrates the plot of Heaviside values and toroidal velocity profiles as a function of normalized minor radius. It seems to be that the fluctuation takes place where the function switches its value. However, it is not always the case as the fluctuation also appears when the Heaviside profile is flat. Thus, it is not certain if the marginal points in the step function causes the fluctuation in the toroidal rotation profile.

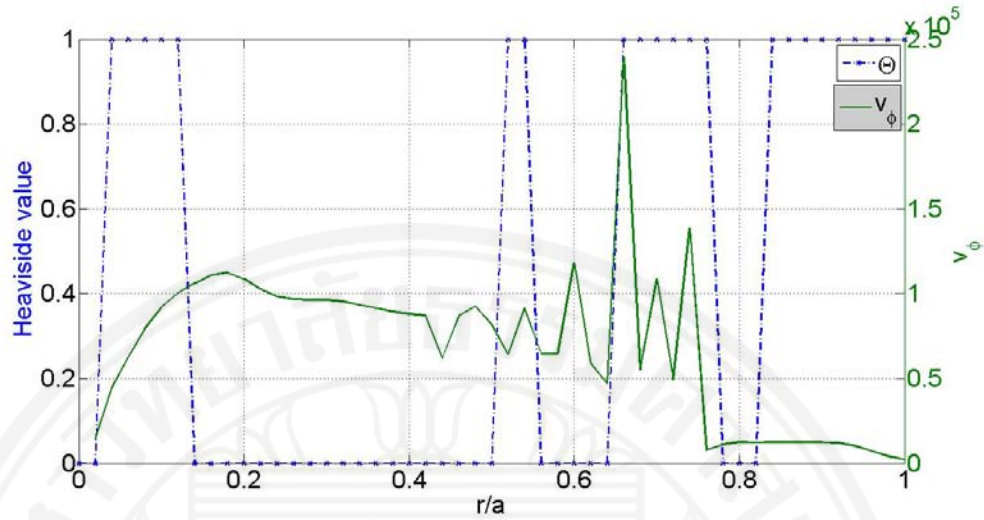


Figure 7.2: Toroidal velocity (solid) and the value of Heaviside step function (dash) profiles at 2600 s obtained from the simulation using NTV toroidal velocity model.

Note that the temperatures at the boundary remain roughly the same for all three simulations, so with regard to different toroidal rotation profiles the plasma performance is independent of boundary values. This also illustrates that the gradient of toroidal rotation can enhance plasma confinement. In the bottom panels of this figure, ion and electron density profiles are shown. The central electron densities from three simulations differ by less than 5% while the central ion densities differ by less than 6%. It is worth mentioning that the line average electron density is kept at the same value. Also, the ion density is set to be the combination of deuterium and tritium densities i.e. $N_i = N_D + N_T$. Profiles from simulations based on the empirical toroidal velocity model and based on zero toroidal rotation show that the densities are high at the center and decrease outward. On the other hand, different profiles can be observed in the case of simulation with the NTV model. There is an off center peak near the location of the high temperature gradient. This characteristic can sometimes be observed from BALDUR simulations like those from the report of Onjun *et. al.* [106].

The strong temperature gradient can be related to the large toroidal velocity ($\sim 10^5$ m/s) and the flow shear profiles (figure 7.3). The characteristic of toroidal velocity profile in the NTV model shows that there is a profile peaking near position $r/a = 0.6-0.8$. This peak results in the peak of flow shear profile as well which

evidently coincides with the location of strong gradient in the plasma. So, the shear profile of toroidal velocity can lead to the flow shear and hence ITB formation.

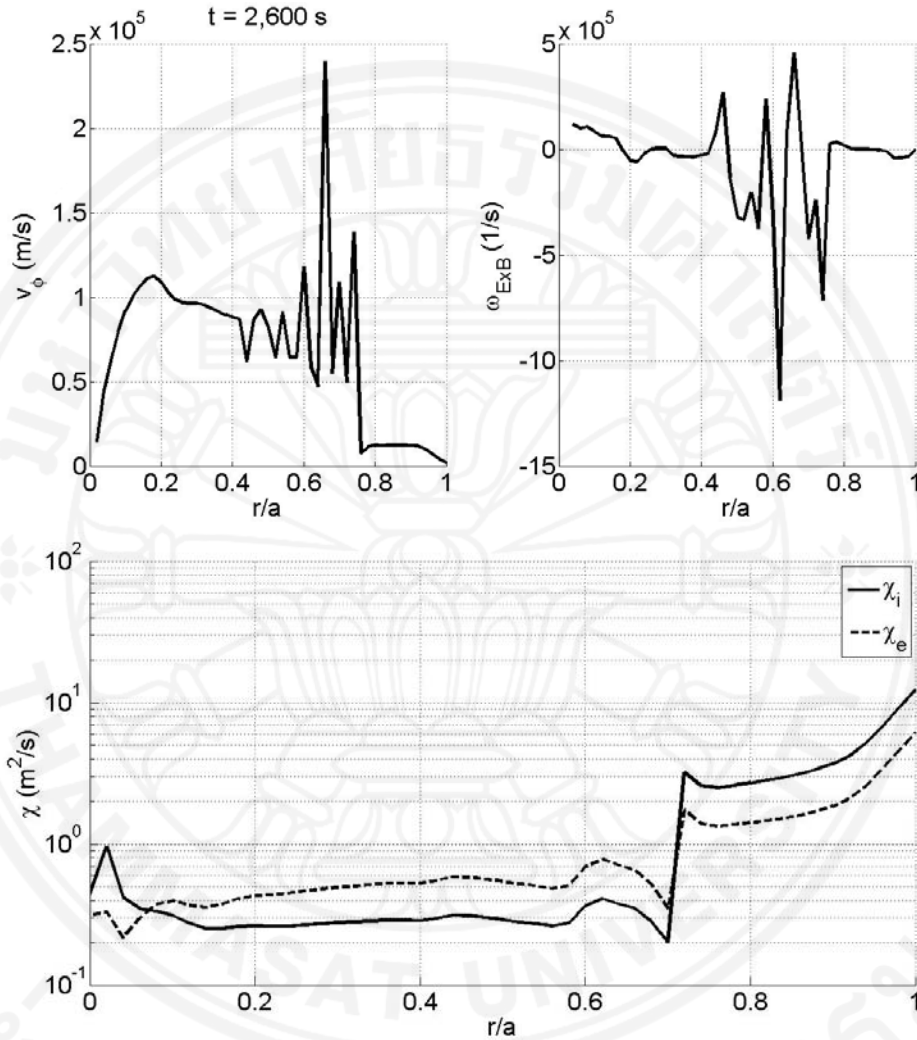


Figure 7.3: Toroidal velocity (top left), flow shear (top right), and ion and electron thermal diffusivities (bottom) profiles at stationary state ($t = 2,600$ s) obtained from the simulation using NTV toroidal velocity model.

It is also found in these simulations that the average alpha power during the stationary state are 194.4 MW, 166.7 MW, and 35.3 MW for the simulations using empirical model, NTV model, and zero toroidal rotation, respectively. The alpha power in the both cases with the presence of toroidal velocity is much higher than that without the toroidal velocity. In this work, the total auxiliary power is set to be equal to 40 MW (7 MW RF and 33 MW NBI). Without toroidal rotation, the predicted

alpha power is less than the auxiliary power. The large alpha power production in the simulation with the presence of toroidal velocity is quite importance for the success of ITER. However, it remains to be evaluated in the future whether the intrinsic toroidal rotation based on NTV can be generated in ITER (as well as strong toroidal velocity based on the empirical toroidal velocity model). It is not clear whether the torque caused by NBI heating, as implied by the empirical model, would be enough to rotate the plasma in ITER, in the same way that it apparently did at JET [120]. It is worth noting that the fluctuations in the alpha power production using the NTV model (10.2 MW) is relatively high compared to that using the empirical toroidal velocity model (3.3 MW) and zero toroidal rotation (0.4 MW).

7.2.2.2 ITB analysis

It was found in the previous section that the presence of toroidal velocity in ITER is expected to result in ITB formation. It is observed that the ITB location seems to be correlated to the plasma toroidal velocity profile. This is demonstrated in figure 7.4. In the top panel (at 2,600 sec), there exists a strong peak of toroidal velocity near $r/a = 0.6$ which is also at the same location of a strong temperature gradient. While in the bottom panel (at 2,900 sec), the strong peak observed is much weaker in magnitude resulting in a smaller temperature gradient. Figure 7.5 illustrates the time evolution profiles of ion temperature gradient demonstrating that the strong gradient starts to develop after the plasma has reached stationary state ($t > 100$ s) and fluctuates near the vicinity of position $r/a = 0.6$. It is worth mentioning that in these simulations, the temperature scale lengths in these simulations are found to be close to or larger than the length of the simulation mesh scale. This assures that the physics of ITB is adequately and correctly captured in these simulations. In addition, the size of spatial grids used is found to be sufficient for the results to be grid independence. The sizes of spatial grids as well as time-steps used by BALDUR are enough for the simulations to be reliable as showed in previous ITB simulation work by Chatthong *et. al.* [120].

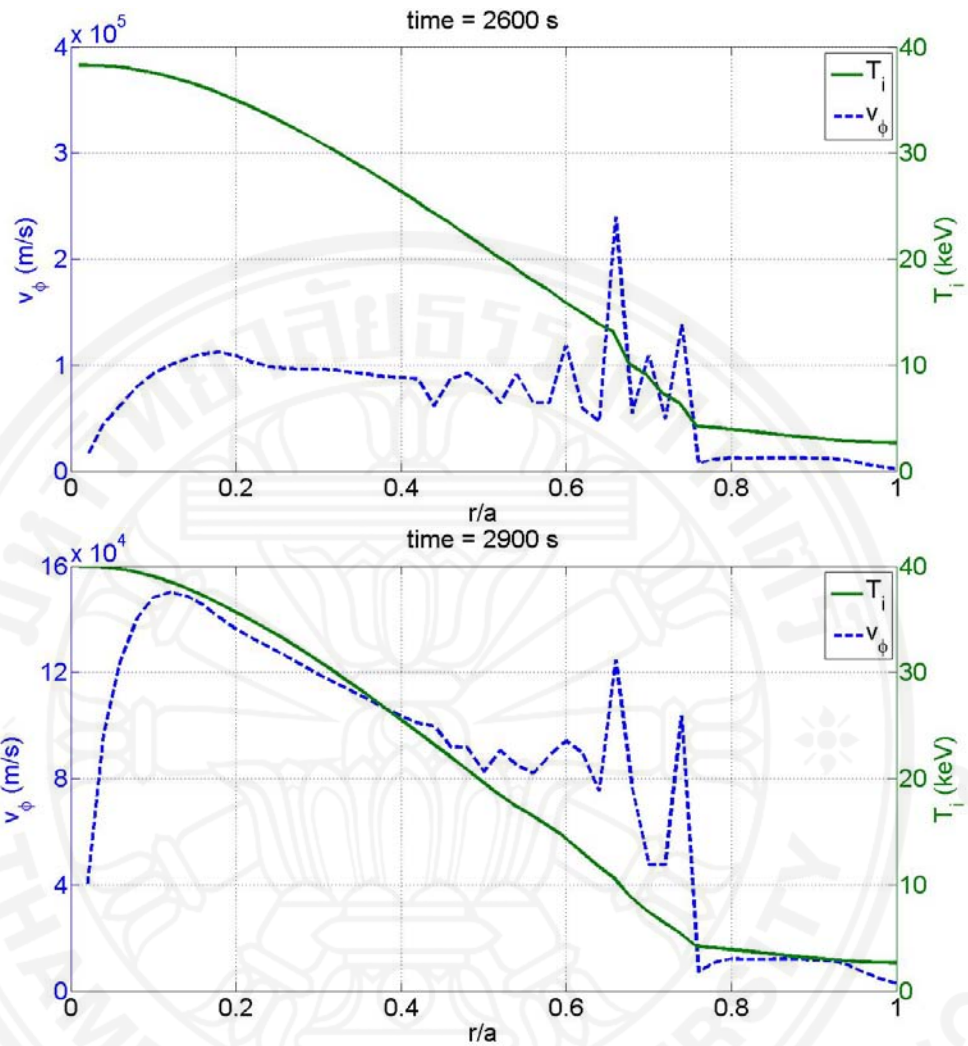


Figure 7.4: Toroidal velocity (dash) and ion temperature (solid) profiles at stationary state; 2600 s (top) and 2,900 s (bottom) obtained from the simulation using NTV toroidal velocity model.

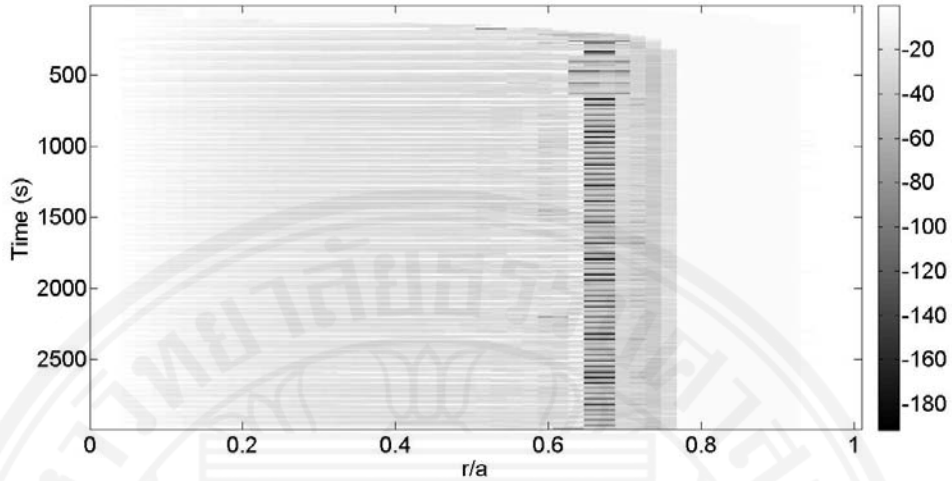


Figure 7.5: Ion temperature gradient image plot, darker region implying higher gradient obtained from the simulation using NTV toroidal velocity model.

It is known that strong temperature gradient (similar to the ITB formation) results in large bootstrap current formation. This intrinsic current is crucial for steady state tokamak operation in the future fusion machine. Figure 7.6 shows the profile of bootstrap current density which illustrates the spike of the current at the point of ITB formation. The peak is around 1.01 MA/m^2 with average value of 0.21 MA/m^2 . The total generated current density has average value of 1.41 MA/m^2 . The generated bootstrap current are about 4.98 MA in the simulation using the empirical toroidal velocity model, 4.35 MA in the simulation using the NTV model, and 0.09 MA in the simulation without toroidal rotation which account for 33%, 29%, and 1% of the total plasma current, respectively. Also in the same figure, safety factor q and magnetic shear s profiles are shown. The q -profiles exhibit non-monotonic behavior in the simulation with both empirical and NTV models suggesting the improvement of plasma confinement. Through the simulation with the NTV model, it can be observed that the ITB forms where the magnetic shear has small negative value. This is similar to the weak negative magnetic shear experiments with the presence of ITB [60, 86, 151]. In addition, the value of q , at the time, at the top of ITB is around 1.14 and that at the foot of ITB is around 1.42 which is close to the rational q -surface ($3/2$). This agrees with the report in by Wolf *et. al.* [60].

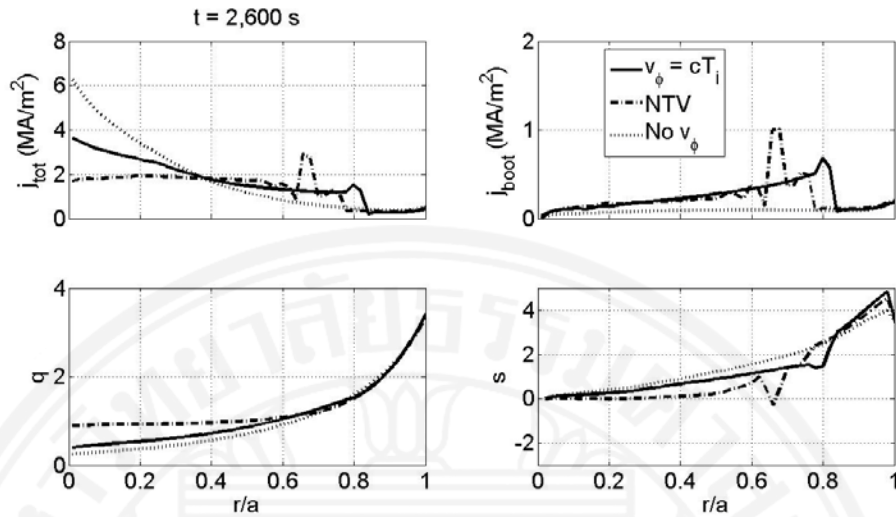


Figure 7.6: Total current density (top left), bootstrap current density (top right), safety factor (bottom left) and magnetic shear (bottom right) profiles at stationary state ($t = 2,600$ s). Each line represents simulation results with empirical model (solid), model based on NTV (dash-dot), and no-value (dot) for toroidal rotation calculation.

To investigate the dynamic of ITB, the plots of ion temperature profiles at various times from the simulation with NTV model are shown in figure 7.7. The lines $t = 10$ seconds represents earlier time where the plasma is not fully heated yet so the plasma is still in L -mode. After 100 seconds, the heating is full and the plasma reaches stationary state. At this stage, the plasma makes a transition to H -mode with central ion temperature close to the simulation result with zero toroidal rotation. At later times the plasma temperature is increased even further with the formation of ITB. As mentioned earlier, the central temperature is fluctuating considerably. Here it is shown that the ITB location also fluctuates around adjacent position. Nevertheless, at some times it can also be transiently collapsed and then later it is formed again. This observation implies that once the plasma has reached full heating state, the ITB is not so stable. It does move in and out and its gradient varies up and down. Further investigation has shown that the ITB circulation period (collapse and recovery) does not appear to be regular or predictable in these simulation results. The mechanism of this ITB dynamics is very complicated. There is no clear conclusion on the circulation period of ITB because its collapse and recovery are irregular. This particular issue is

interesting for future study which requires more details investigation. However, it appears that this ITB tends to forms near the point where the flow shear component of the radial electric field is maximum which mostly happens in the vicinity of $r/a = 0.6$. Also, the strong gradient is reduced (collapsed) when the shear is also reduced. The radial electric field is related to the toroidal and poloidal rotations as shown in equation (2.9). Since both rotations are dependent on the temperature gradient, the radial electric field must relate to the gradient as well. Figure 7.8 shows the time-correlation between the toroidal velocity and temperature gradient near the position $r/a = 0.62$. The times of each profile peaking appear to be highly correlated as implied by the model. Since the pressure gradient, the toroidal and poloidal rotations are components for a radial electric field according to the force balance equation, it is interesting to investigate how each term contributes to the flow shear profile. This is illustrated briefly in figure 7.9 where it evidently shows that the toroidal rotation term dominates significantly. It can be observed that the pressure gradient and the poloidal rotation terms tend to cancel out each other because they are comparable in magnitude with opposite sign. As a result, the radial electric field is determined mainly by the toroidal rotation term. Based on this simulation, the toroidal flow appears to be dominant for the flow shear in the plasma

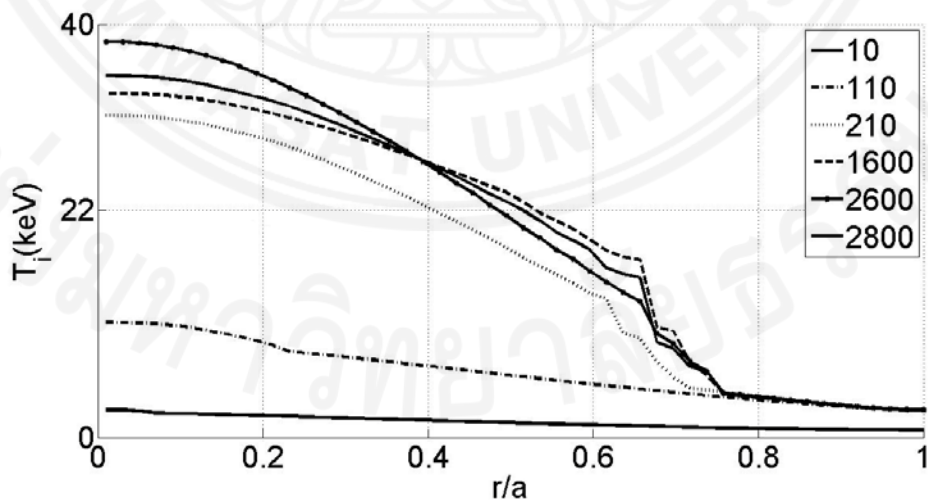


Figure 7.7: Ion temperature profiles as a function of normalized minor radius at various times illustrating the dynamic of ITB obtained from the simulation using NTV toroidal velocity model.

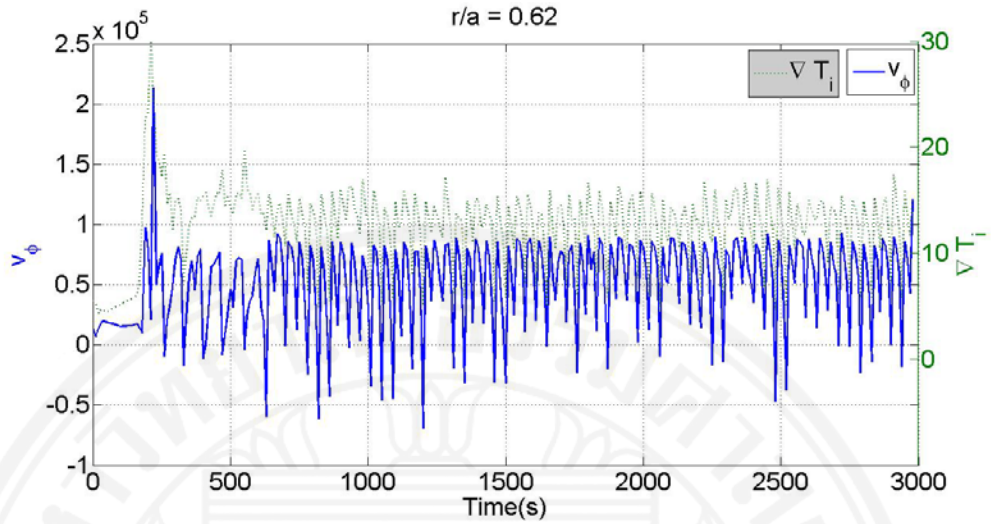


Figure 7.8: Toroidal velocity and temperature gradients evolution profiles near location of ITB obtained from the simulation using NTV toroidal velocity model.

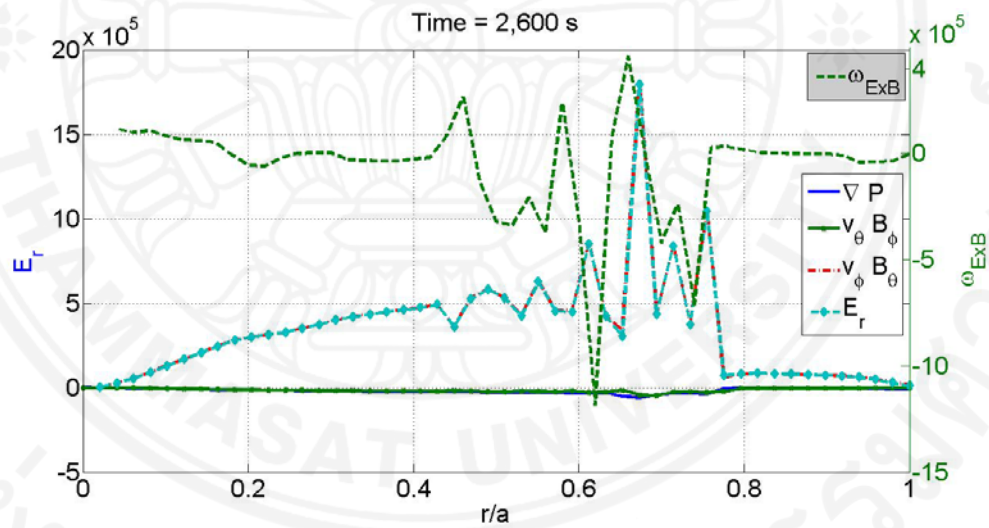


Figure 7.9: Radial electric field, its components, and flow shear profile as a function of normalized minor radius from the simulation using NTV toroidal velocity model.

The other indicator for an ITB formation is the reduction of transport diffusion. At the bottom panel of figure 7.3, the radial profiles of both ion and electron thermal diffusivities are shown for the time that the plasma reaches its steady state. It can be seen that the transport reduction is occurred in the region close to the center up to $r/a=0.7$. This region is also the region where the flow shear is strong.

Thus, it can be concluded that the transport reduction strongly correlates with the presence of toroidal velocity, which is in agreement with the explanation in the previous paragraph. Note that according to the Mixed B/gB model, the transport diffusion coefficients (both thermal and particle) are functions of Bohm and gyro-Bohm terms as described by Gryaznevich *et. al.* [22]. Thus, their profiles should be somewhat similar.

7.2.2.3 Sensitivity study

In this part the plasma simulations using the NTV model are studied in further detail. The sensitivity of plasma profiles and performance is analyzed by varying the three plasma engineering parameters: line average density (n_1), auxiliary power (P_{aux}), effective charge number (Z_{eff}), and the magnitude of the rotation.

(a) Line average density

Line average density controls the total electron density inside the plasma. Three different values of n_1 are considered for ITER simulations: 0.8, 1.0, and 1.2 x 10²⁰ m⁻³. Figure 7.10 shows the plasma profiles at time 2,600 seconds. The average values of central ion temperature and central electron density are shown in table 7.2. Note that the density values yield to those which are roughly similar to their respective engineering values. The average values of central ion temperature are found to be increased with line average density. The alternate indication of plasma performance is to monitor the alpha power production, in which its average values are shown in table 7.2. Here, it can be concluded that the plasma fusion power is increased with line average density.

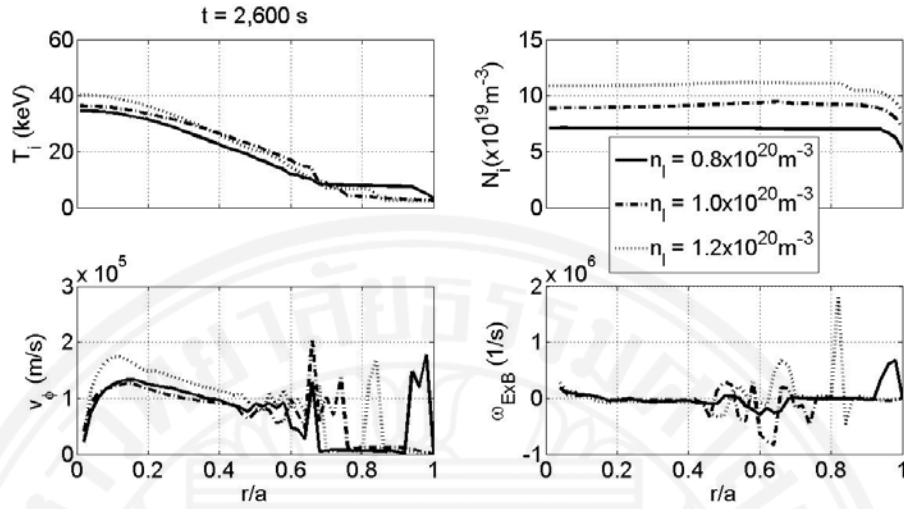


Figure 7.10: Ion temperature (top left), ion density (top right), toroidal velocity (bottom left), and flow shear (bottom right) profiles at stationary state ($t = 2,600$ s) obtained from the simulation using NTV toroidal velocity model. Each line represents simulation results with different values of line average density.

Table 7.2: Average values of central ion temperature, central electron density and alpha power for each simulation during stationary state.

<i>Simulations</i>	$T_{i,0}$ (keV)	$N_{e,0}$ ($\times 10^{19} \text{ m}^{-3}$)	P_α (MW)
$n_l = 0.8 \times 10^{20} \text{ m}^{-3}$	32.72	8.34	87.44
$n_l = 1.0 \times 10^{20} \text{ m}^{-3}$	34.92	10.27	166.70
$n_l = 1.2 \times 10^{20} \text{ m}^{-3}$	37.34	12.39	242.27
$P_{\text{aux}} = 30 \text{ MW}$	32.61	10.26	156.97
$P_{\text{aux}} = 40 \text{ MW}$	34.92	10.27	166.70
$P_{\text{aux}} = 50 \text{ MW}$	36.82	10.36	176.10
$Z_{\text{eff}} = 1.4$	34.92	10.27	166.70
$Z_{\text{eff}} = 1.8$	30.66	10.59	120.89
$Z_{\text{eff}} = 2.2$	22.76	10.89	64.57
$Z_{\text{eff}} = 2.6$	14.40	11.44	18.46
$0.1V_{\text{NTV}}$	14.80	10.56	28.97
$0.5V_{\text{NTV}}$	28.85	10.32	123.06
$1.0V_{\text{NTV}}$	34.92	10.27	166.70

It can also be observed in this work that in all three simulations the positions of strong temperature gradient coincide with the highest peak of toroidal velocity profile. In the case of $n_1 = 0.8 \times 10^{20} \text{ m}^{-3}$, there is a second high peak near plasma edge which causes another strong temperature gradient there. Near the center of each profiles, there is also another toroidal velocity peaking. A degree of curvature can be observed there but the strong gradient, though it exists, is not visibly clear in the profile plot. The possible explanation is that there is a large neoclassical diffusivity near the plasma center which reduces the ion temperature gradient and hence the flow shear. Furthermore, the values at the toroidal velocity peaking appear to be correlated with the level of line average density. This is because higher line average density results in higher alpha power and thus temperature. Consequently, greater gradient is obtained and eventually leading to high toroidal velocity peaking. In summary, higher line average density results in higher toroidal velocity peaking and alpha power, and hence higher plasma performance.

(b) Auxiliary power

It is interesting to analyze how the plasma performance can be changed at various auxiliary heating powers since it is not realistic to keep increasing the heating power forever in order to improve the plasma performance. In fact this is unnecessary because once the supplied heating is too high, the plasma performance is actually diminished. In this study, three heating powers are used: $P_{\text{aux}} = 30, 40, \text{ and } 50 \text{ MW}$ (only NBI heating is varied, RF heating is kept at 7 MW). Figure 7.11 shows the plasma profiles. Also, the average values of central ion temperature and central electron density are shown in table 7.2, along with average alpha power. The values show that as the heating power is increased, the alpha power is also enhanced but the plasma performance is decreased since the fusion gain appears to be reduced.

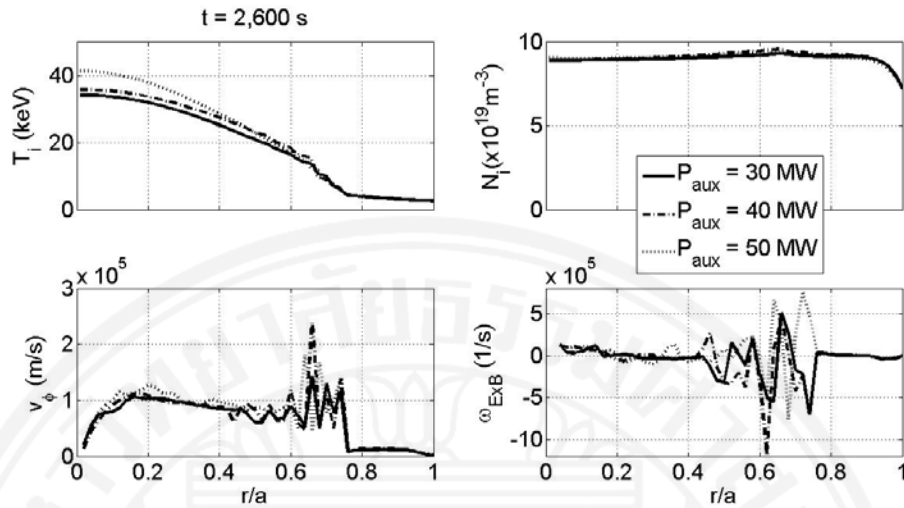


Figure 7.11: Ion temperature (top left), ion density (top right), toroidal velocity (bottom left), and flow shear (bottom right) profiles at stationary state ($t = 2,600$ s) obtained from the simulation using NTV toroidal velocity model. Each line represents simulation results with different values of auxiliary power.

The toroidal velocity profiles in figure 7.11 are consistent with the earlier conclusion that their highest peak locations are coincident with their respective positions of strong temperature gradients. The peaking of toroidal velocity are also located near the center which results in the high curvature at those respective positions but the strong temperature gradients are not clear as well as the results from the previous case.

(c) Effective charge number

In this part, the effect of effective charge number is studied. It is an average charge of the plasma over all ion species. This effect simply increases the impurities density inside the plasma. Four Z_{eff} values are used: 1.4, 1.8, 2.2, and 2.6. Figure 7.12 shows the plasma profiles. The average values of central ion temperature, central electron density and alpha power are also shown in table 7.2. The results are as expected that as Z_{eff} is increased the plasma performance is reduced because higher charge means higher plasma loss through radiation. The drop is rather significant compared to the previous two variational studies. The radiation model used in this work is based on the coronal equilibrium radiation model [178]. In ITER-like

temperature regime, the main radiation is a bremsstrahlung process.

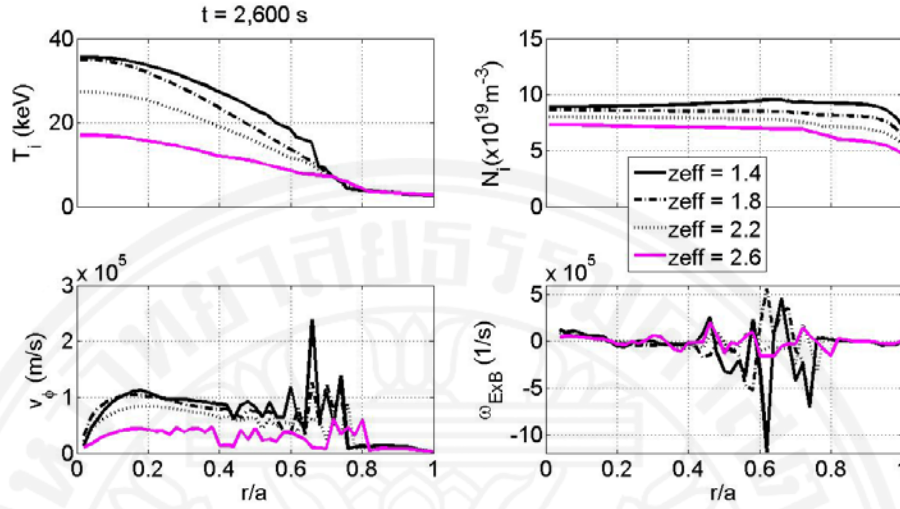


Figure 7.12: Ion temperature (top left), ion density (top right), toroidal velocity (bottom left), and flow shear (bottom right) profiles at stationary state ($t = 2,600$ s) obtained from the simulation using NTV toroidal velocity model. Each line represents simulation results with different values of effective charge number.

The toroidal velocity profiles can be seen in the same figure, bottom panel. The results are also consistent with earlier remarks with regard to location of ITB. Some strong temperature gradients may not be visibly clear in this plot but they form at the same position as their respective toroidal velocity peaking. Note that in this case the magnitude of the peaking is highest in the simulation of Z_{eff} equal to 1.4 then 2.2 and 1.8, not in the same order as plasma performance. So the correlation is uncertain in this case. The possible explanation is because in the simulation of $Z_{\text{eff}} = 1.8$, the ITB appears to be transiently collapsed during this certain time along with the lower value of toroidal velocity peaking. However, the transient collapse does not notably contribute to the plasma loss so the plasma energy still remains higher.

(d) Strength of the toroidal rotation

It is still a question whether the NTV model is applicable for ITER since ITER is an axisymmetric system. So, the strength of toroidal rotation might not be as much as that predicted using the NTV model. Therefore, in this part, the strength of the NTV toroidal rotation is investigated. This is done by comparing the previous result

with new results when toroidal velocity calculated from equation (7.2) is multiplied by 0.1 and 0.5. The results are shown in table 7.2. In summary, the magnitude of the NTV toroidal rotation is found to significantly affect the plasma profiles and, consequently, the plasma performance. When the rotation is reduced to 10% of those predicted using NTV model, the plasma central temperature is decreased to around 40% and the alpha power is decreased to around 17%. When the rotation is reduced to 50% of its value in the original model, the plasma central temperature is decreased to 82% and the alpha power is decreased to around three-quarters. Thus, the strength of the toroidal rotation is quite crucial. Further investigation is needed.

7.2.3 Conclusion

Simulations of standard ITER ELMy *H*-mode are carried out using BALDUR integrated predictive modeling code. These simulations are computed with the presence of both ITB and ETB together with the prediction of toroidal rotation. The core transport is predicted with Mixed B/gB model, while the boundary condition is computed using a pedestal model based on magnetic and flow shear stabilization width scaling and an infinite-*n* ballooning pressure gradient model. The toroidal rotation is calculated using a theoretical model based on NTV concept. It is found that the intrinsic toroidal velocity predicted by the NTV model is sufficient for a formation of an ITB. In term of plasma performance, if the plasma can be toroidally rotated, its performance can be significantly improved. The simulations obtained here shows that the ITB forms in the vicinity of position $r/a \sim 0.6-0.8$, which is not clear why such a particular position is favored by the plasma. The model yields very strong fluctuations in space and time. Additionally, once the barrier is formed, its position and magnitude appears to vary only slightly. The dynamics of the barrier cannot clearly be clarified, except that the barrier has a strong relationship with the temperature gradient, the shear of toroidal velocity and radial electric field profiles. Furthermore, the sensitivity study concludes that the plasma performance is increased with line average density and is decreased with auxiliary power and effective charge number. The location of toroidal velocity peaking is coincident to that of the strong temperature gradient and the magnitude of the peak is correlated to plasma performance.

7.3 Comparison of *H*-mode plasma simulations using toroidal velocity models depending on plasma current density and ion temperature in presence of an ITB

7.3.1 Models for predictive toroidal velocity

7.3.1.1 Current density dependent approach

This model is based on the current density flow of charge, in which, for simplicity, it is assumed to be in term of drift velocity of plasma flow.

$$v_{\phi} = \frac{J_{\phi}}{en_{i,e}Z_{eff}}, \quad (7.9)$$

where J_{ϕ} represents the current density flow in toroidal direction which can be calculated in BALDUR via Ampere's law and $n_{i,e}$ is ion and electron density. Figure 7.13 shows normalized minor radius (r/a) comparison profile of experimental v_{ϕ} of JET discharge 40847 with current density in toroidal direction from the diagnostic simulation (simulation using toroidal velocity from experiment to construct the current profile) at the diagnostic time. It can be seen that the profiles are similar in which the values are high near the centre and low near the edge with relatively flat profiles at the regions close to both boundaries.

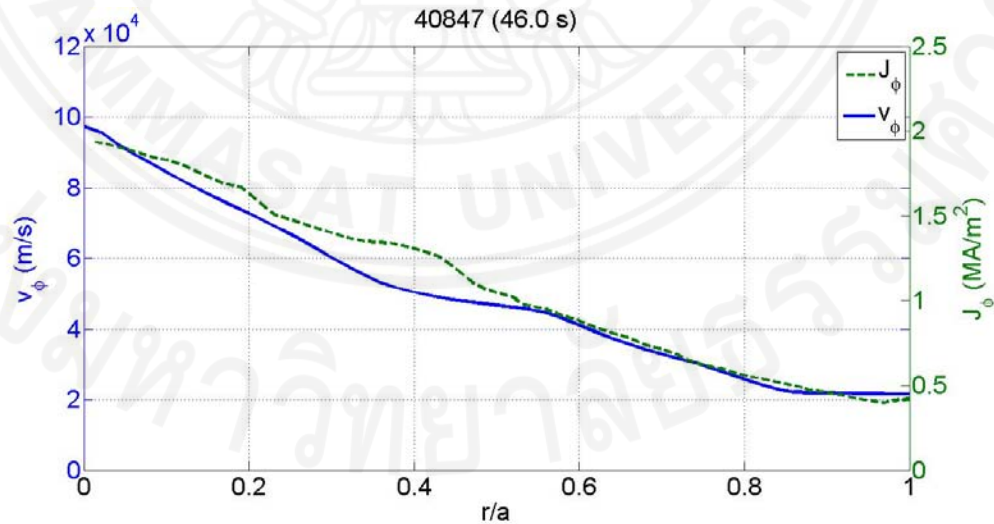


Figure 7.13: Profile plot of toroidal velocity v_{ϕ} (solid) together with toroidal current density J_{ϕ} (dashed) as a function of r/a for JET 40847 discharge at the diagnostic time.

7.3.1.2 Ion temperature dependent approach

This model describes that the toroidal velocity is linearly proportional to the local ion temperature (T_i), the exact form is as follows:

$$v_\phi [m/s] = 1.43 \times 10^4 T_i [keV]. \quad (7.10)$$

It was developed and used to simulate JET data [120]. Then later it was used to predict ITER performance [123], which illustrated that during plasma quasi-steady state the anomalous transport was suppressed over a wide region. The problem is that this model is empirically built based solely from data from JET tokamak. So the projection problem is rather questionable. Moreover, the set of experimental data used in the model development is mainly NBI (neutral beam injection)-heated plasma. In other words, the plasma is rotated toroidally by the external torque caused by NBI heating. This raises an important issue because ITER will be much larger (840 m³ plasma volume compared to 100 m³ of JET) so that the torque from NBI should not be enough to rotate it toroidally.

7.3.2 Results and discussion

7.3.2.1 JET simulations

In this work, 10 JET optimized shear *H*-mode discharges with ITB formation (40542, 40847, 46123, 46664, 51599, 51976, 52009, 53521, 53532, and 53537) are chosen from the International Profile Database [179]. Table 7.3 shows the summary of parameters from all 10 discharges used for the simulations.

Table 7.3: Summary of plasma parameters for 10 JET optimized shear discharges during their diagnostic time.

JET	Time (s)	R (m)	a (m)	I_p (MA)	B_ϕ (T)	κ	δ	$n_1 (10^{19} \text{ m}^{-3})$
40542	47	2.93	0.94	3.22	3.49	1.64	0.35	2.41
40847	46	2.92	0.96	2.85	3.50	1.56	0.20	2.33
46123	46.5	2.89	0.98	2.50	2.54	1.52	0.17	2.24
46664	45.7	2.92	0.94	2.95	3.50	1.71	0.20	2.27
51599	46	2.89	0.96	2.21	2.64	1.66	0.23	1.90
51976	46.3	2.92	0.95	2.40	3.49	1.69	0.26	2.45
52009	21.6	3.01	0.88	2.49	2.70	1.72	0.47	7.30
53521	49	2.89	0.97	2.00	3.54	1.63	0.21	2.99
53532	46.5	2.89	0.96	2.22	2.64	1.67	0.23	2.52
53537	46.5	2.90	0.96	2.22	2.64	1.67	0.23	2.15

(a) Comparison

In this part, the predicted toroidal velocities v_ϕ from two models are compared. Examples of v_ϕ profile are shown in figure 7.14. Each demonstrates v_ϕ as a function of r/a , the closed circles represent experimental data, the solid line with triangle markers represents simulation result of ion temperature dependent model, and the solid line represents simulation result of current density dependent model. Note that diagnostic time for each discharge is selected based on ITB and H -mode considerations. From this figure, it can be observed that the simulation results tend to over-predict the experiments. This is almost always the case for all 10 JET discharges. Furthermore, the general profile shape of the current density dependent model is rather unsmooth near the edge of the plasma where the v_ϕ values abruptly spike up and then decrease to zero right at the edge. This strange behaviour is a result of numerical procedure according to how BALDUR computes the current density. BALDUR assumes that the current is zero at the edge, the value at the next grid is high to conserve overall current flow.

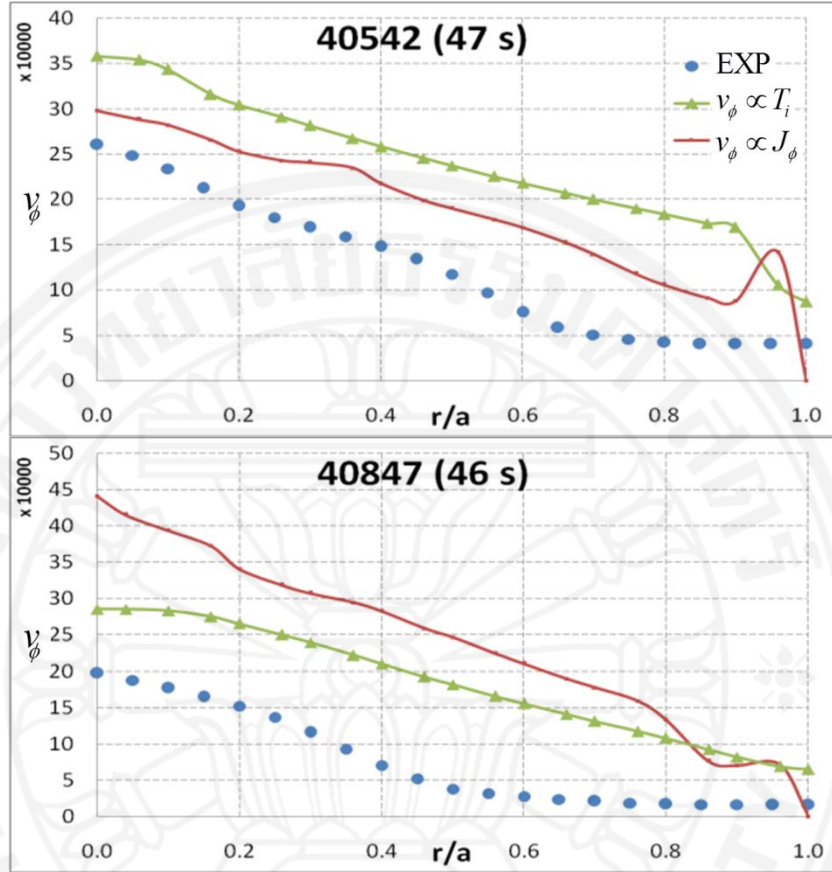


Figure 7.14: Comparison of toroidal velocity v_ϕ between experimental values (dots) and simulation results using ion temperature T_i dependent (solid-triangle) and current density J_ϕ dependent (solid) models for JET discharges 40542 (top) and 40847 (bottom) during their diagnostic time.

Quantitatively, the root mean square error (RMSE) values between simulation results and experimental data are computed for comparison according to:

$$\text{RMSE}(\%) = \sqrt{\frac{\sum_{i=1}^N (\ln(v_{\phi_exp_i}) - \ln(v_{\phi_mod_i}))^2}{N-1}} \times 100, \quad (7.11)$$

where v_{ϕ_exp} is the experimental value, v_{ϕ_mod} is the value calculated from the models, and N is total number of data points. The summary results are shown in figure 7.15. The RMSE ranges from 16.99% to 200.5% for the current density dependent model, whereas it ranges from 18.58% to 55.50% for the ion temperature dependent model.

The best agreement is found in the current density dependent prediction of discharge 51976, while the worst agreement is ironically found in the prediction using the same model of discharge 46664. The average RMSE of all 10 discharges is found to be 73.02% with the standard deviation of 60.81% for the current density dependent model, and found to be 37.09% with the standard deviation of 13.04% for the ion temperature dependent model. The average values imply that the prediction by ion temperature dependent model is better. However, if one observes discharge by discharge and also from the high standard deviation, one can see that it is possible that this current density dependent model can only capture a limited regime of the plasma. So for the applicable discharges, it can predict the profile rather adequately. While in some other discharges additional physics or models are needed.

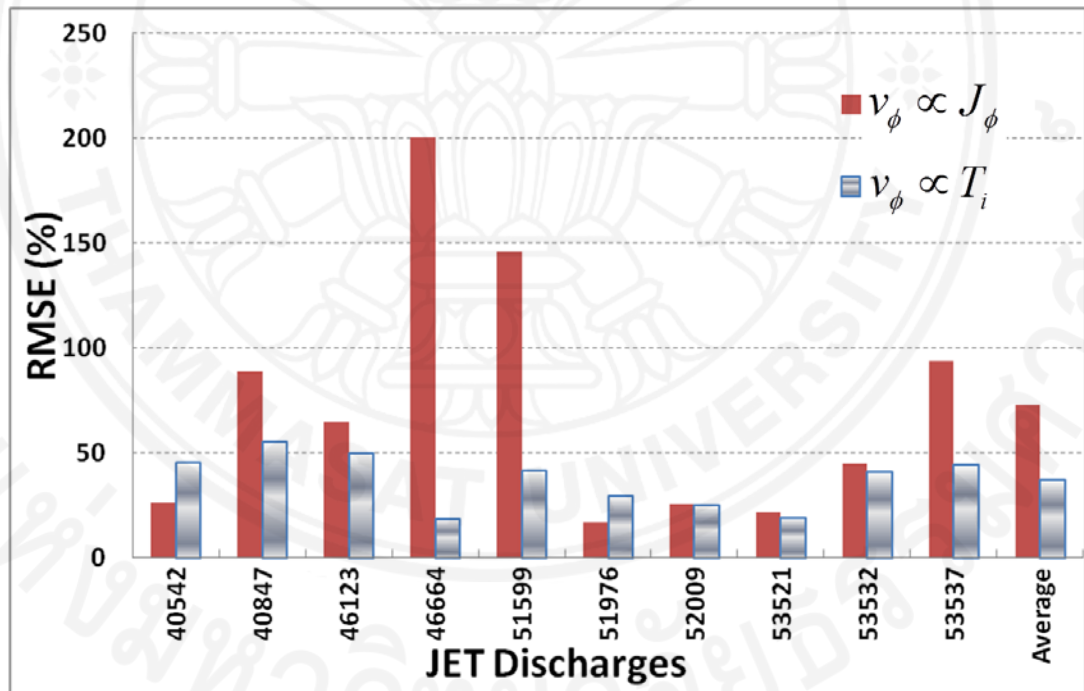


Figure 7.15: RMSE deviations of 10 JET discharges and their average for toroidal velocity v_ϕ using current density J_ϕ dependent (solid bars) and ion temperature T_i dependent (striped bars) models.

(b) Simulation profiles

For simulations of each JET discharge, the time-evolution profiles of ion temperature (T_i), electron temperature (T_e), and electron density (n_e) are calculated

and predicted by BALDUR. Figure 7.16 illustrates example profiles of JET discharges 40847 and 52009; note that the dots represent experimental data, the dashed line represents simulation results using current density dependent model, and the solid line represents simulation results using ion temperature dependent model. First of all, the figure shows that the simulation results over-predict both the temperatures and the density at the edge while they tend to under-predict the values at plasma center. In other words, the pedestal model yields higher predicted values and the Mixed B/gB model yields lower predicted values than the experimental data. Furthermore, it can be observed that when comparing to experimental data the general features of this discharge profiles are retained. However, when observing the general features of the profile plots for all 10 JET discharges the brief summary can be discussed as follows. Firstly, the simulation results of T_i , T_e , and n_e are in agreement within one order of magnitude with experimental measurements. Secondly, the general trend of the profile such as the inclination is similar in some results and different in others. This can be due to the limited availability of some experimental parameters and incompleteness of the v_ϕ model. And lastly, n_e profiles are usually in better agreement with experimental data than the others. This is because in BALDUR, the boundary condition for density equation is empirically determined from line average density (n_l) according to equation (2.53). On the contrary, the pedestal temperature (T_{ped}) is theoretically calculated according to equation (2.52) so the prediction accuracy should be less than that of empirical approach. This also can be seen in figure 7.16, in which the temperatures for both ion and electron at the edge are predicted much higher than that of the experiment, while the densities are predicted roughly closer to the experimental values.

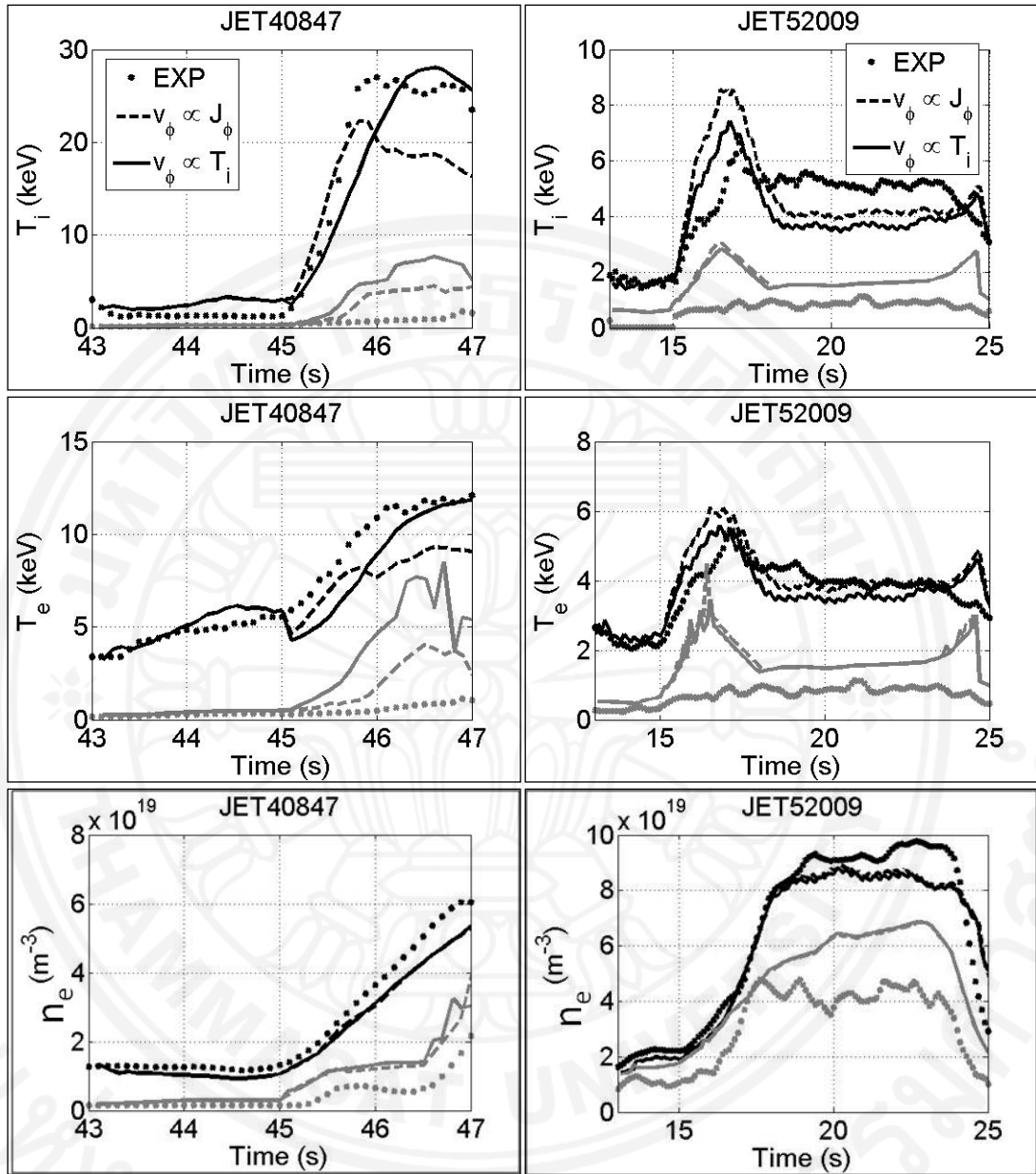


Figure 7.16: JET 40847 (left) and 52009 (right) time-evolution profiles of ion temperature T_i (top), electron temperature T_e (middle), and electron density n_e (bottom): experimental data (dots) simulation results using current density J_ϕ dependent (dashed) and ion temperature dependent (solid) models at the center (dark) and edge (gray) of the plasma.

Quantitatively, the three physical quantities profiles are compared with experimental data using the following normalized RMS comparison:

$$\text{RMS}(\%) = \sqrt{\frac{1}{N} \sum_{i=1}^N \left(\frac{x_{\text{exp}_i} - x_{\text{mod}_i}}{x_{\text{exp}_0}} \right)^2} \times 100, \quad (7.12)$$

where x represents interested physical quantities (T_e , T_i , and n_e) and x_0 represents experimental data at the centre of the plasma. Note that in these comparisons, data of all grid positions in the plasma are included and of the entire duration that the discharge remains in H -mode. These results are shown as bar plots in figure 7.17. For T_i comparison, the maximum of 41.48% is found in discharge 53532 of current density dependent model and the minimum of 18.14% is found in discharge 53521 of ion temperature dependent model. The averages of all discharges are $28.13 \pm 7.71\%$ standard deviation for the current density dependent model, and $25.47 \pm 7.10\%$ standard deviation for the ion temperature dependent model. For T_e comparison, the maximum of 63.74% is found in discharge 53532 of current density dependent model and the minimum of 14.88% is found in discharge 40847 of the same model. The averages of all discharges are $31.78 \pm 14.51\%$ standard deviation for the current density dependent model, and $30.19 \pm 13.64\%$ standard deviation for the ion temperature dependent model. For n_e comparison, the maximum of 21.54% is found in discharge 52009 of ion temperature dependent model and the minimum of 9.66% is found in discharge 46664 of the same model. The averages of all discharges are $15.00 \pm 3.23\%$ standard deviation for the current density dependent model, and $15.15 \pm 3.50\%$ standard deviation for the ion temperature dependent model. On average, it cannot be concluded which model is better because they are within the standard deviation of each other. This conclusion is different from the toroidal velocity prediction where it can be clearly seen that the ion temperature dependent model predicts better. This shows that the simulations profiles are not so much sensitive to the toroidal velocity profile. Nevertheless, if one observes the performance of each discharge simulation individually, one can find that on some discharge like 46664 the difference is significant in which the empirical model performs better.

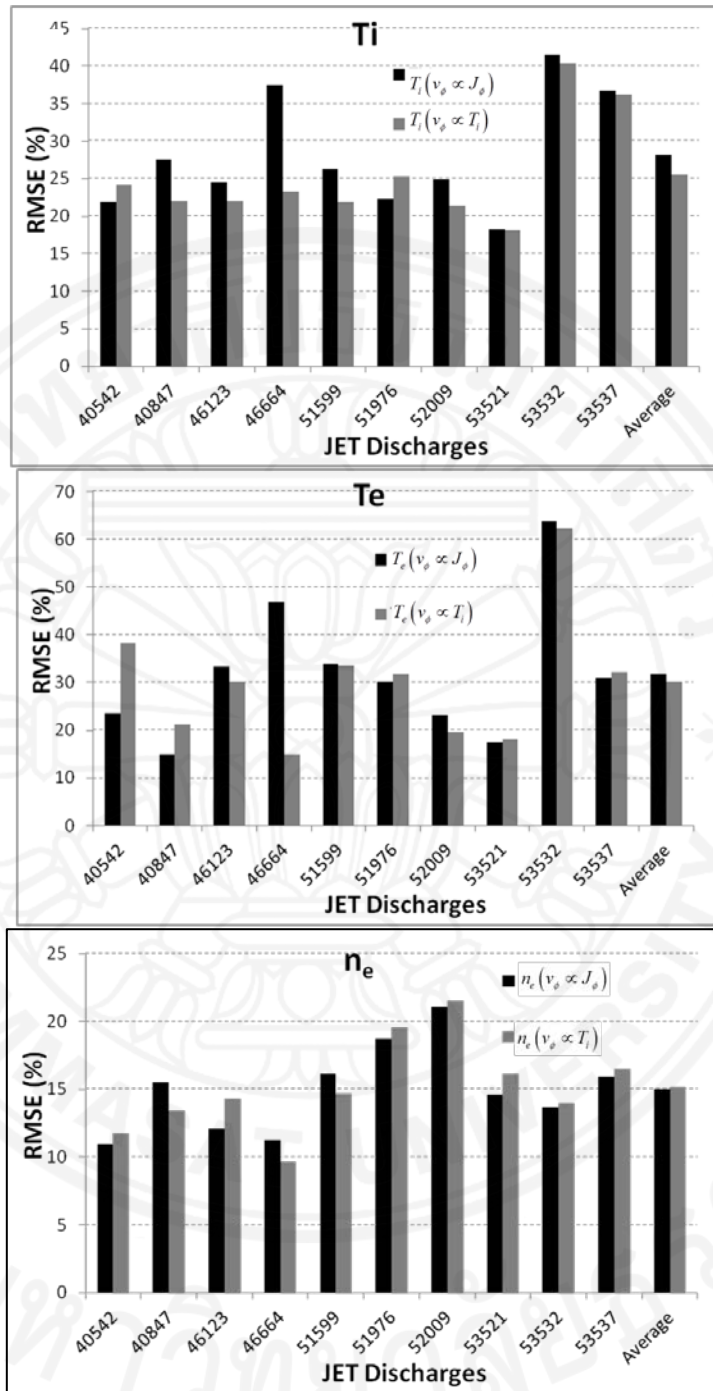


Figure 7.17: RMS deviations of 10 JET discharges and their averages for ion temperature T_i , electron temperature T_e , and electron density n_e simulation results using current density J_ϕ dependent (dark) and ion temperature T_i dependent (gray) models.

(c) ITB formation

One physical phenomenon that is important to explore in this work is the ability of this suite of code to simulate ITB formation. This v_ϕ model is developed to explain the velocity in toroidal direction which is used to calculate the shearing rate ω_{ExB} , the cause of ITB formation. ITB formation can be found in either ion or electron channel, or both channels at the same time depending on heating method. Since the main heating in JET is either NBI (neutral beam injection) or ICRF (ion cyclotron resonance frequency) or both, ITB formations are found mainly in ion temperature profile so the work on ITB identification will be in T_i profile plots. ITB is defined as a local region of steep temperature gradient. So, the gradient will be used in order to identify ITB location and time of its occurrence.

Figure 7.18 illustrates the contour plot of ion temperature gradient spatiotemporal profiles with darker area representing relative higher temperature gradient area, showing examples for JET discharges 46664 and 53532. Only ion temperature profiles are shown here because BALDUR simulations yield similar qualitative behaviour for ion and electron profiles. Moreover, there is no ITB formation in the particle channels from these experiments. In this sense, the figure can be used to trace the location and the time evolution of the ITB. The top panels are experimental data, the middle panels are the simulation results from current density dependent model and the bottom panels are simulation results from ion temperature dependent model. In discharge 46664, ITB forms around the time of 45.5 seconds near the position $r/a=0.4$. It appears that the empirical model predicts almost the exact time of formation with a location slightly shifted toward $r/a=0.5$. On the contrary, the current density dependent model predicts a wider ITB from $r/a=0.4$ to 0.8 with formation time as early as 45 seconds. In discharge 53532, ITB forms around the time of 46 seconds near the position $r/a=0.4$. Similar to the previous discharge, the empirical model predicts ITB formation better for both its time and location. Current density dependent model predicts softer ITB but for wider region. As a summary, from this qualitative observation, the empirical model predicts formation of ITB better. These results are as expected because, as mentioned earlier, the empirical model was derived from these discharges so they should fit the experimental results

better. However, it is more interesting to see how it projects into a larger machine like ITER.

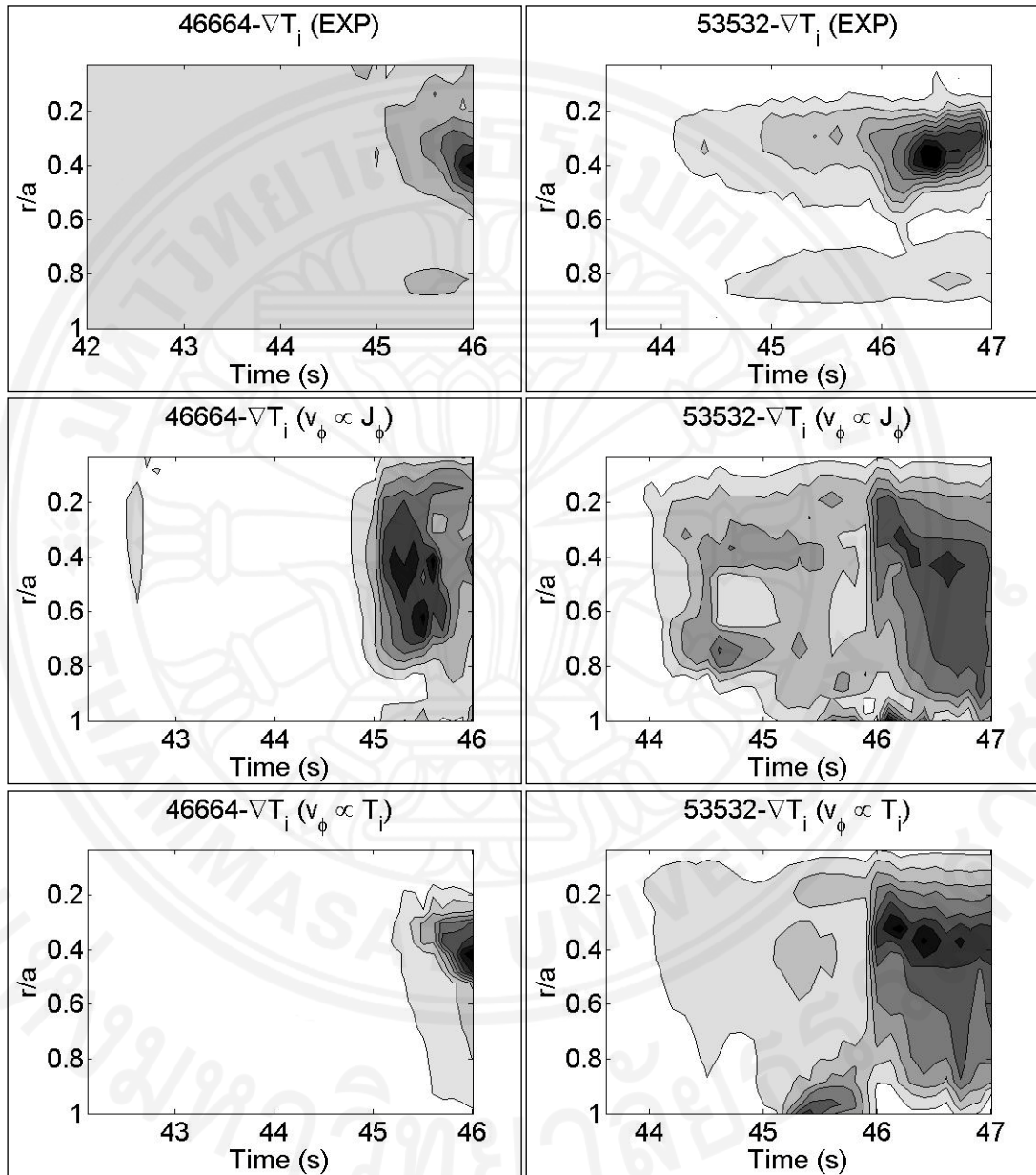


Figure 7.18: Contour plots of ion temperature gradient ∇T_i profile of JET discharges 4664 (left) and 53532 (right): experimental results (top) and simulation results using current density J_ϕ dependent (middle) and ion temperature T_i dependent (bottom) models.

7.3.2.2 ITER predictions

ITER is an international collaboration with the main goal of demonstrating scientific and engineering feasibility of nuclear fusion machine [28]. In this work, a standard type I ELMy *H*-mode ITER is chosen. Its design parameters are shown in table 7.1, the details of the operation scenario can be found in Onjun et al. (2009).

(a) ITER performance and ITB effect

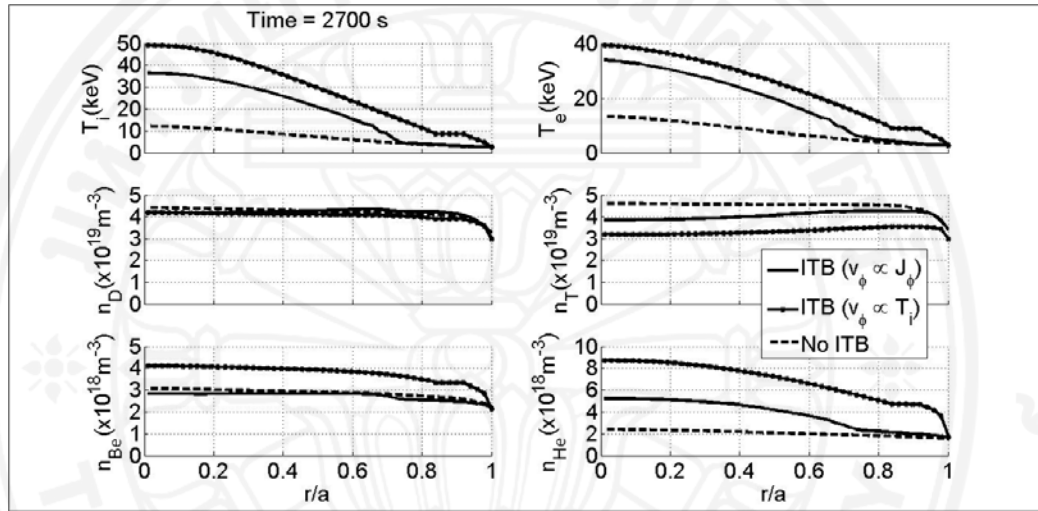


Figure 7.19: Comparison of ITER performance (for ion temperature T_i , electron temperature T_e , deuterium density n_D , tritium density n_T , beryllium density n_{Be} , and helium density n_{He}) between simulations with ITB (both current density and ion temperature dependent models) and without ITB effect during steady state ($t = 2700$ s).

Figure 7.19 illustrates simulations of ITER for ion temperature (T_i), electron temperature (T_e), deuterium density (n_D), tritium density (n_T), beryllium density (n_{Be}), and helium density (n_{He}) as a function of normalized minor radius r/a at the time of 2,700 seconds. Note that at this time, the plasma has reached quasi-steady state condition as observed from figure 7.20 that the plasma becomes relatively steady after 200 seconds. In both figures, the solid line is for simulation using current density dependent model, the solid line with bullet is for simulation using ion temperature dependent model, and the dashed line is for simulation without ITB. It can be seen in figure 7.19 that both temperatures are high near the center and lower toward the edge (from 3 to 10 times reduction), while the densities of all species remain roughly the

same throughout the plasma (around 2 times or less reduction) except helium density in ITB simulation which accumulates more toward the plasma center (at most 4 times reduction). The beryllium is an impurity that comes from the wall of the tokamak. It is found to accumulate in the plasma.

The temperature profiles indicate the existence of ITB formations which is shown by significant improvements of plasma temperature over those results without ITB. It can be seen that when ITB effects are included in the simulation, the central temperature for both ion and electron increase significantly, from 12 keV to 38 keV (current density dependent) and 49 keV (ion temperature dependent), and from 13 keV to 33 keV (current density dependent) and 39 keV (ion temperature dependent), respectively. Yet, the temperatures near the edge of plasma remain approximately the same. This implies that ITB formations indeed result in better plasma confinement for the plasma temperature, hence energy. This also shows that the empirical model predicts higher values for ITER by around 20% for ion and 15% for electron temperatures at plasma center.

The bottom right panel shows that helium impurity accumulates more in the plasma core for simulations with ITB included, also in the ion temperature dependent model more than in the current density dependent model. This agrees with the trend in central temperatures which results in higher fusion reaction. Additionally, it means that ITB formations also prevent transport of impurity species especially helium. Beryllium is an impurity from the first wall outside of the plasma, the concentration is slightly higher in plasma with the ion temperature dependent model run as expected because there are more beryllium trapped in the core. However, the current density dependent model appears to show similar beryllium accumulation to that of simulation without ITB. The situation is similar for helium species, except that the concentration in the run with ITB effect is much higher than the run without ITB effect. As stated earlier, transport barriers improve plasma energy confinement and power production, which mean the fusion reaction rate is enhanced as well. This is confirmed by figure 7.20 in the bottom panel which shows the time-evolution profile of alpha power. During quasi-steady state, the alpha powers of ITB simulations are almost 10 times higher than that without ITB formation. These alpha particles are not neutral so they are trapped by the magnetic field inside the tokamak. The energy is

used to reheat the plasma, transferred back to deuterium and tritium by way of collision. More alpha power means more alpha particles produced from fusion reaction so higher helium density is observed. This result is further confirmed by deuterium and tritium density plots in figure 7.19. Since both species are starting particles of the fusion reaction, a higher reaction rate implies more fuel burnt and hence less density accumulated for both. As observed from the figure, ITB simulation shows lower tritium and slightly lower deuterium concentrations.

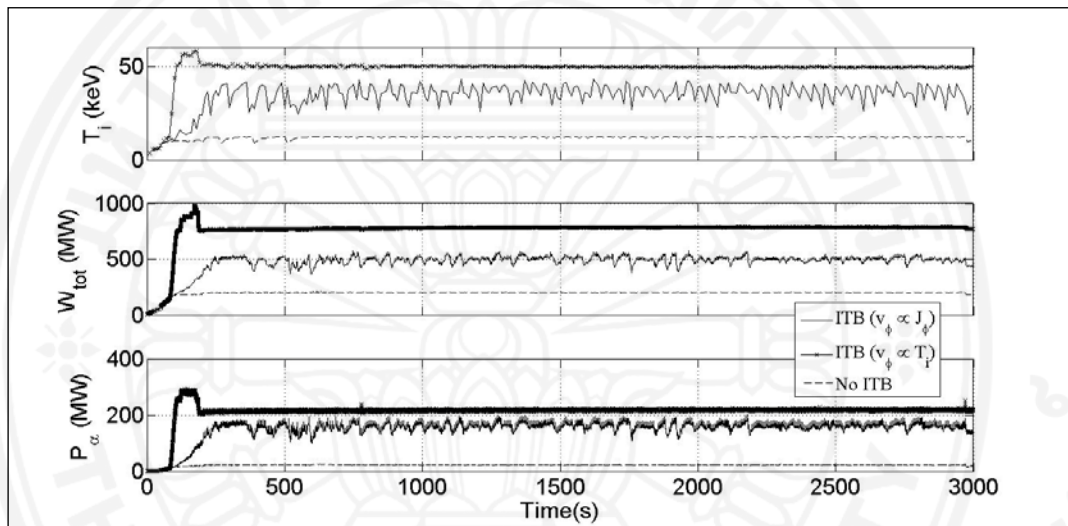


Figure 7.20: Time-evolution plots of central ion temperature T_i (top), total fusion power output W_{tot} (middle), and alpha power P_α (bottom) for simulations with ITB (both current density J_ϕ and ion temperature T_i dependent models) and without ITB effect during steady state ($t = 2700$ s).

In summary, to see what is happening at the center of the plasma, the central ion temperature is plotted as functions of time (Figure 7.20) along with total fusion power output and alpha power of the plasma. As expected, they are higher in simulations with ITB formation. Initially, during current ramp-up phase the profiles increase steeply and reach maximum around 100 seconds before dropping down because of the high radiation power to reach quasi-steady state. During this latter state, the average values of central ion temperature are 36 and 49 keV, of the total power outputs of the plasma are 492 and 800 MW, and of the alpha powers are 159 and 218 MW for the current density dependent and ion temperature dependent models, respectively. Note that the ion temperature dependent model provides more

steady plasma profiles while the results from current density dependent model are much rather fluctuated.

It is interesting to observe how ITB forms in ITER using the two toroidal rotation models. Figure 7.21 illustrates the contour plots of the ion temperature gradient profiles. The top panel shows that the current density dependent model predicts ITB to be locally located around $r/a = 0.7$ with some slight fluctuations. Once formed, its location is moving in and out around the position. It also appears to collapse and reform. However, the period of collapsing and reformation is not regular or deterministic; future investigation is required. On the contrary, the ITB region from empirical model appears to be much wider, from $r/a = 0.5$ to 0.8 . This agrees with what could be observed in the top panels of figure 7.19, in which the strong gradient from the current density dependent model can be easily identified at $r/a = 0.7$ but not so for the ion temperature dependent model because it covers a wider region. This also explains why the empirical model yields higher temperature profiles, as it has a wider region of ITB, the transport reduction is much stronger. The toroidal velocity and the flow shear profiles are shown in figure 7.22. It can be observed that in the simulation using current density dependent model, there exists a spike feature representing strong shear of the profiles at the vicinity of the ITB location. So there is a correlation between the location of the strong shear of toroidal velocity and ω_{ExB} flow shear profiles with that of temperature gradient or ITB. Moreover, the plasma appears to be rotated much faster, toroidally, in the simulation using empirical model. This will be physically quite challenging in ITER since NBI, as implied by the empirical model, should not be able to rotate the bigger machine that fast.

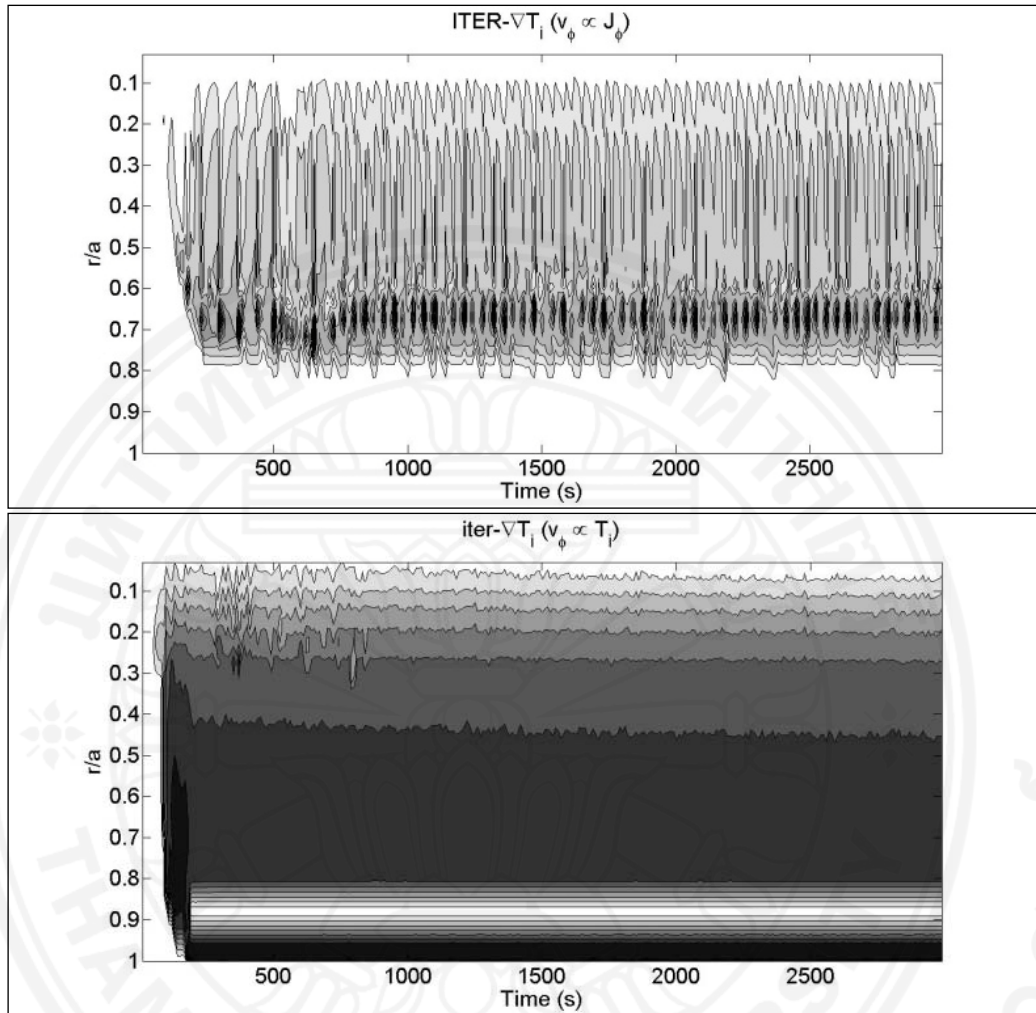


Figure 7.21: Contour plots of ion temperature gradient ∇T_i profile of ITER simulations: simulation results using current density J_ϕ dependent (top) and ion temperature T_i dependent (bottom) models.

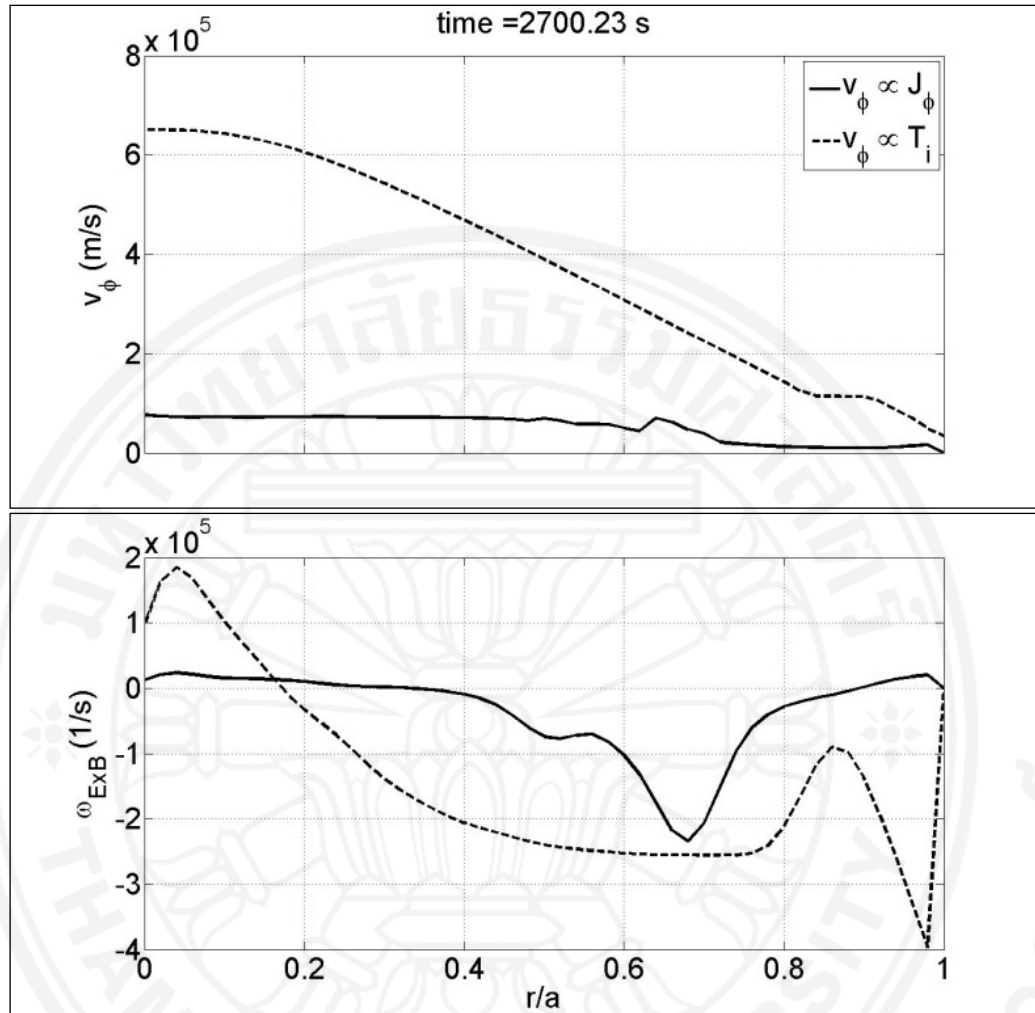


Figure 7.22: Toroidal velocity v_ϕ and flow shear ω_{ExB} profiles of simulations results for current density J_ϕ dependent (solid) and ion temperature T_i dependent (dashed) models during steady state ($t = 2700$ s).

(b) Test for plasma ignition

Plasma reaches an ignition condition if the auxiliary heating (NBI plus RF heating) is shut down but the plasma is still able to self-sustain. It is very important to study this issue for ITER because self-heating leads to possibility of long duration operation for fusion reactor. In this study, BALDUR code is used to simulate the similar ITER performance as before but the auxiliary heating is turned off after 2000 s, at which point the plasma has reached a quasi-steady state. After that, the plasma is solely heated by ohmic heating and alpha heating.

It is found in figure 7.23 that ion temperatures, total powers and alpha powers drop as soon as the external heating is shutdown. Nevertheless, the plasma adjusts to a new quasi-steady state shortly after with lower temperatures and powers. In simulation without ITB effects included, the operation continues for about 400 seconds longer before reaching disruption because alpha heating diminishes as soon as auxiliary heating is off and then ohmic heating carries on the operation until the operation stops. Note that ohmic heating is small compared to other heating modes. With ITB effects included, the plasma achieves a new quasi-steady state at central ion temperatures of around 30 and 40 keV, total powers of 400 and 650 MW and alpha powers of 110 and 180 MW, for current density dependent and ion temperature dependent models, respectively. Note that ITB formations are still maintained even after auxiliary heating is turned off as shown in figure 7.24 but the values of temperatures are slightly lower.

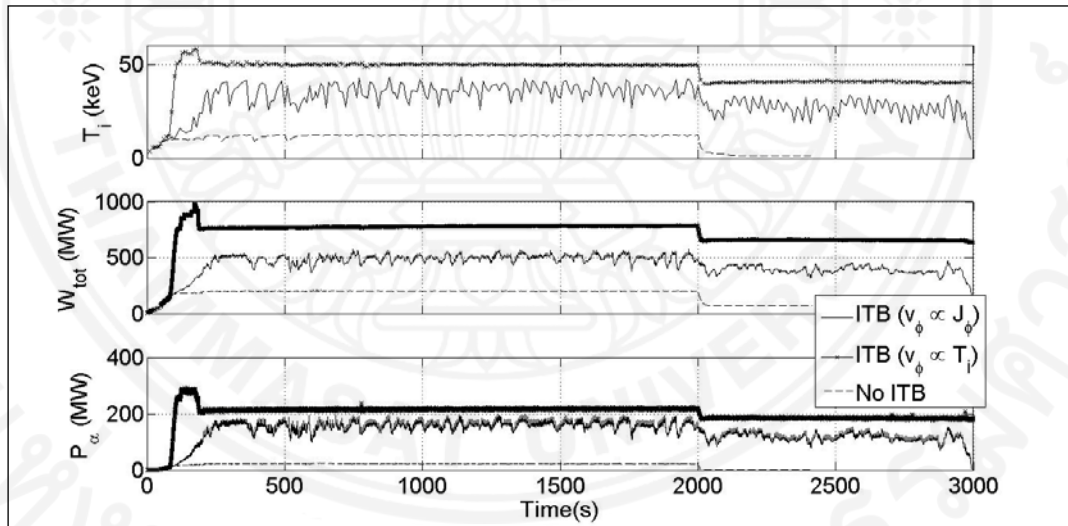


Figure 7.23: Time-evolution plots of central ion temperature T_i (top), total fusion power output W_{tot} (middle), and alpha power P_α (bottom) for simulations with ITB (both current density J_ϕ and ion temperature T_i dependent models) and without ITB effect during steady state ($t = 2700$ s), auxiliary heating is turned off after 2000 s.

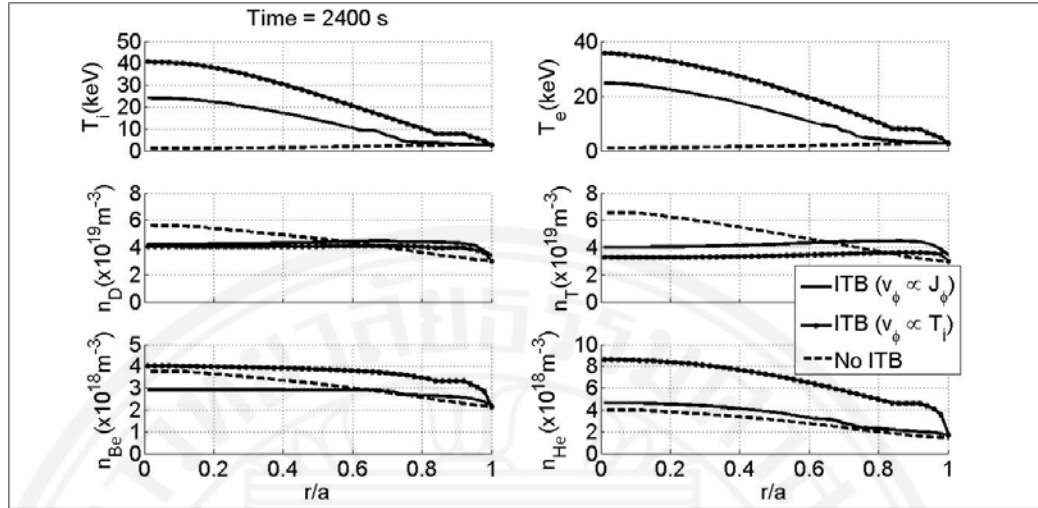


Figure 7.24: ITER performance simulations (for ion temperature T_i , electron temperature T_e , deuterium density n_D , tritium density n_T , beryllium density n_{Be} , and helium density n_{He}) with ITB (both current density and ion temperature dependent models) and without ITB effect at time after auxiliary heating is turned off ($t = 2400$ s).

7.3.3 Conclusion

Self-consistent simulations of ITER with the presence of both ITB and ETB are carried out using the BALDUR code. The combination of Mixed B/gB transport model together with pedestal model based on magnetic and flow shear stabilization pedestal width scaling and an infinite- n ballooning pressure gradient model, and with two toroidal velocity models based on ion temperature and current density of the plasma, is used to simulate the time-evolution profiles of plasma temperature, density, and current for JET optimized shear discharges and ITER standard type I ELMy H -mode operation. It is found that the simulations with the ion temperature dependent toroidal velocity model yield better agreement with JET experimental data. For ITER prediction, the ion temperature dependent model yields more optimistic predictions but the current density dependent model predicts a rather narrow region of ITB. The presence of ITB is very crucial for ITER because it results in greater plasma energy confinement over standard run without ITB effects. The presence of ITB causes both ion and electron temperatures to be higher, especially at the center. However, it only slightly affects the densities of deuterium, tritium, and beryllium. Helium concentration is higher in ITB simulation because of larger fusion reaction rate.

Therefore, this is a critical issue for ITER. In addition, when the auxiliary heating is turned off, it is found that the core temperature, total power and alpha power are decreased slightly. However, significant fusion energy still retains. The ignition condition cannot be achieved without the formations of ITB.

7.4 Investigation of toroidal flow effects on $L-H$ transition in tokamak plasma based on bifurcation model

The setback of the original bifurcation model was the assumption that both neoclassical and anomalous diffusivities to be constant. Also, in calculation of radial electric field the toroidal and poloidal rotation terms are neglected. In this section, the anomalous diffusivities are calculated based on profiles stiffness model, which means that in the low gradients regimes, the plasma transport is governed solely by neoclassical effect, while in the high gradients regimes, the dominating anomalous transport is driven by the gradients [132]. Moreover, it was found that in some regimes of the plasma, toroidal rotation can significantly dominates the calculation of radial electric field as can be seen in the report of Chatthong *et. al.* [173]. In addition, it is known that the toroidal flow can play significant role in plasma performance improvement[120]. So in this part, effects of toroidal rotation are included for investigation [130].

The pressure and density transport equations are numerically solved simultaneously for spatiotemporal profiles of plasma pressure and density, $L-H$ transition, pedestal width and its dynamics. Each equation is composed of neoclassical and anomalous transports, source term and the flow shear as suppression mechanism. The suppression only affects on the anomalous channel for the reason mentioned previously. Three calculations of toroidal velocity are used; the first one is based on empirical observation in which toroidal velocity is proportional to plasma temperature [120], the second one is based on neoclassical toroidal viscosity (NTV) physics [173], and the last one is based on empirical approximation [180]. The three models are based on different physical regimes in the plasma which are not necessary mutually exclusive so they can partially coexist. The effects of each model toward this bifurcation picture of $L-H$ transition are studied and results are compared.

7.4.1 Bifurcation concept and toroidal velocity models

This section introduces the models used in the work which include bifurcation and toroidal velocity models. The main transports equations are solved numerically using discretization method. The code is developed in MATLAB environment based on the built-in “*pdepe*” function which is appropriate for solving initial-boundary problems for parabolic-elliptic partial differential equations in one dimension.

7.4.1.1 Two-field bifurcation model

The model used in this work is based on the framework of bifurcation concept introduced by Malkov *et. al.* [96]. It conceptually explains that the *L-H* transition is an intrinsic property of the plasma where its confinement mode can abruptly change providing that some criteria are satisfied, i.e. ratio of anomalous over neoclassical diffusivities and heat or particle fluxes must exceed threshold values [135]. Graphically, the model is depicted as bifurcation diagram illustrating an *s*-curve shape graph of pressure/density gradients against heat/particle fluxes, respectively. A jump of pressure and density gradients in the graph indicates that the plasma has entered *H*-mode. The model consists of coupled pressure and density transport equations which are expressed in slab geometry as shown in equations (4.1) and (4.2), respectively. Essentially, these two equations represent conservation of energy and mass, respectively. Note that throughout this work, the thermal and particle sources are estimated to be localized at plasma center and edge, respectively, using Gaussian distribution. The stabilizing mechanic for anomalous transport is the flow shear v'_E , which accounts for the known reduction of turbulent transport by sheared radial electric field [45]. It couples the two transport equations based on force balance calculation:

$$v'_E \propto E'_r = \left(\frac{P'}{n} - v_\theta B_\phi + v_\phi B_\theta \right)'. \quad (7.13)$$

The poloidal rotation term, which is a result from neoclassical calculation, is neglected in this work. Whereas, the toroidal rotation term was found to be dominating in some plasma regime as illustrated by Chatthong *et. al.* [173] so its effect will be studied in this work because it was ignored in previous bifurcation related works. Models for toroidal velocity prediction are discussed in the next

section. The neoclassical transport coefficients are simply set to be constant while the anomalous transport coefficients follows critical gradient transport model similar to that described by Garbet *et. al.* [132], shown in equations (4.11) and (4.12). This local anomalous transport model realizes the physical plasma transport in which at low gradient, near plasma center, the neoclassical effect dominates the transport, while at high gradient, near plasma edge or transport barrier location, the anomalous transport is driven by the gradient itself.

7.4.1.2 Toroidal velocity models

This section discusses the toroidal velocity models used in this work. Four different toroidal velocity models are employed, each governs different physics in tokamak plasma. These models provide explicit calculations of toroidal velocity which means the toroidal momentum equation is not included. This requires extensive modelling and analysis, and is left for future work. Model a) is based on an empirical observation which assumes that the toroidal flow is proportional to local plasma temperature T [120]:

$$v_{\phi,a} \propto T. \quad (7.14)$$

This model is applicable in tokamak which is directly driven by on-axis neutral beam injection (NBI) heating, for example JET. Model b) is based on neoclassical toroidal viscosity (NTV) physics which applies to plasma with symmetry breaking via the application of a non-axisymmetric field [173]. It has the form:

$$v_{\phi,b} \propto \frac{\partial T}{\partial r}. \quad (7.15)$$

So, the toroidal velocity in this model is proportional to the gradient of local plasma temperature gradient. Model c) is an empirical estimation discussed by Chatthong *et. al.* [180], where the toroidal velocity is assumed to be proportional to plasma toroidal current density:

$$v_{\phi,c} \propto j_{\phi} = j_0 \left(1 - \frac{r^2}{a^2} \right)^{\nu}, \quad (7.16)$$

where j_{ϕ} and j_0 are toroidal current density and its value at plasma center, r/a is normalized minor radius and ν is a constant to control current shaping. This form of plasma current is a typical estimation for on-axis current drive system [6]. Model d) is

similar to model c) except the extra bootstrap current j_b term. This bootstrap current is an intrinsic current generated in the plasma it has the form [6]:

$$j_b = -T \frac{\partial n}{\partial r}. \quad (7.17)$$

So, the last model has the form:

$$v_{\phi,d} \propto j_\phi + j_b, \quad (7.18)$$

7.4.2 Numerical results and discussions

The numerical simulations in this work are results of solving transport equations (4.1) and (4.2) simultaneously and self-consistently. In accordance with physical observations, the anomalous transports are assumed to be one order of magnitude over the neoclassical transports, while particle diffusivities are assumed to be one third of the thermal diffusivities. The heat and particle sources are assumed to be large enough so the plasmas can access the H -mode.

7.4.2.1 Plasma response on profile and pedestal width

Effects of toroidal rotation on plasma profiles are investigated in this section. This can be seen in figure 7.25, which shows the simulation results for plasma pressure and density at plasma core and edge as a function of normalized minor radius (r/a) at steady state. The four toroidal velocity models are used for simulations in order to compare with results without toroidal flow included ($v_{\phi,0}$). In general, inclusion of toroidal flow tends to increase plasma pressure and density except at its edge where transport barrier is formed. This is not surprising because the plasma in the edge region is governed solely by neoclassical effect, which remains unaffected by the toroidal term. Moreover, the toroidal term facilitates the enhancement of transport reduction, thus higher plasma profiles. The top panels show plasma profiles near its center, it can be estimated that the increases are approximately 0.04%, 1.72%, 3.09% and 3.96% of center pressure, and 0.03%, 1.58%, 2.60% and 3.39% of center density for simulations using model a), b), c) and d), respectively.

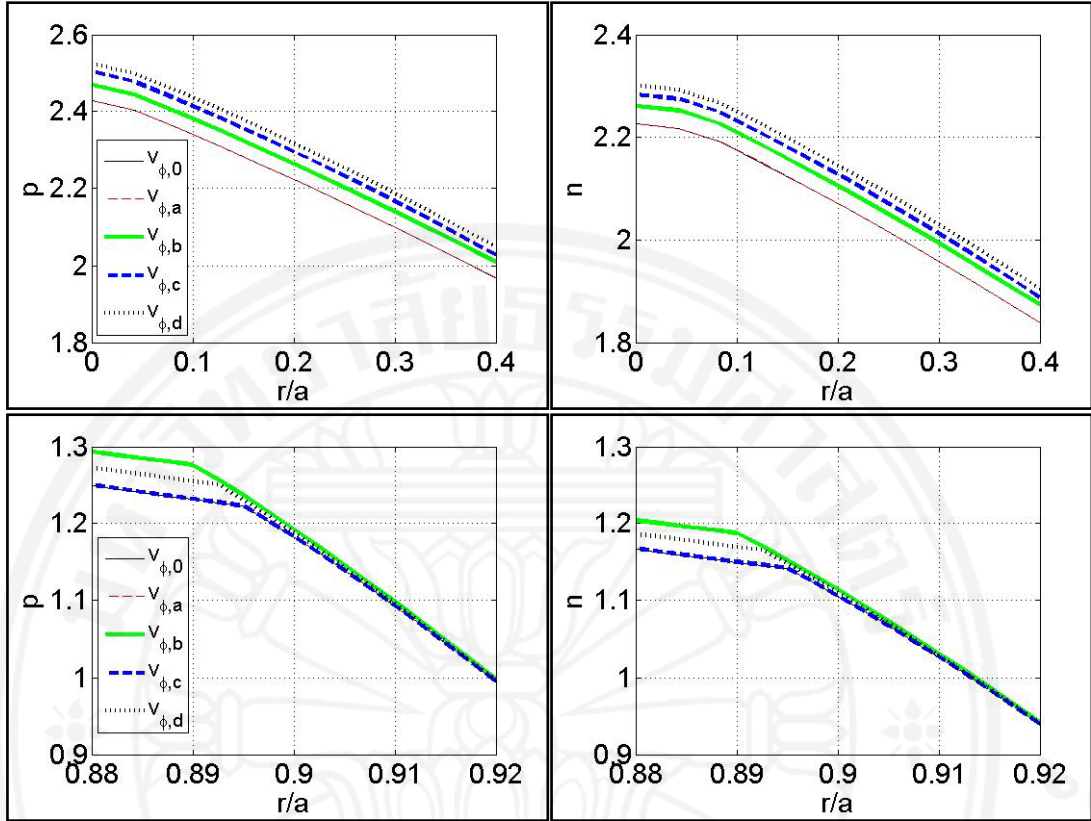


Figure 7.25. Plasma core profiles for pressure (top left) and density (top right), and plasma edge profiles for pressure (bottom left) and density (bottom right) at steady state. Each line represents simulation results without toroidal flow (thin solid), using model a (thin dashed), model b (thick solid), model c (thick dashed) and model d (dotted).

The toroidal effects yield somewhat different results at pedestal area (area with high gradients) as seen in the bottom panels of figure 7.25. First of all, the results show that the pedestal width remains unchanged from simulation without toroidal effect when using model a) and c) with pedestal width of 0.105. On the other hand, the simulations using model b) and d) yield pedestal widths of 0.110 and 0.108, respectively. Note that the pedestal width appears to be the same for pressure and density channels regardless of the model used. The values at the top of pedestal (p_{ped} , n_{ped}) are also increased by inclusion of toroidal flow. The increases are approximately 0.09%, 4.40%, 0.04% and 2.29% of p_{ped} , and 0.08%, 4.07%, 0.04% and 2.12% of n_{ped} for simulations using model a), b), c) and d), respectively. The reasons for the increase being difference from model to model at plasma center and edge can be seen

in figure 7.26 which shows radial electric field, pressure gradient and toroidal flow contributions as a function of normalized minor radius. First of all, equation (7.13) implies that the shear or gradient of toroidal velocity profile is an essential ingredient for transport reduction calculation. It can be seen that in model a), the profile is relatively flat throughout the whole plasma so it does not affect the flow shear much. In model b), the profile appears to have slight gradient at plasma center and strong gradient at plasma edge. Model c) has somewhat high gradient near plasma center and becomes flat near plasma edge. And model d) has both high gradients at plasma center and plasma edge. These results agree with the increase of plasma values at its center and pedestal.

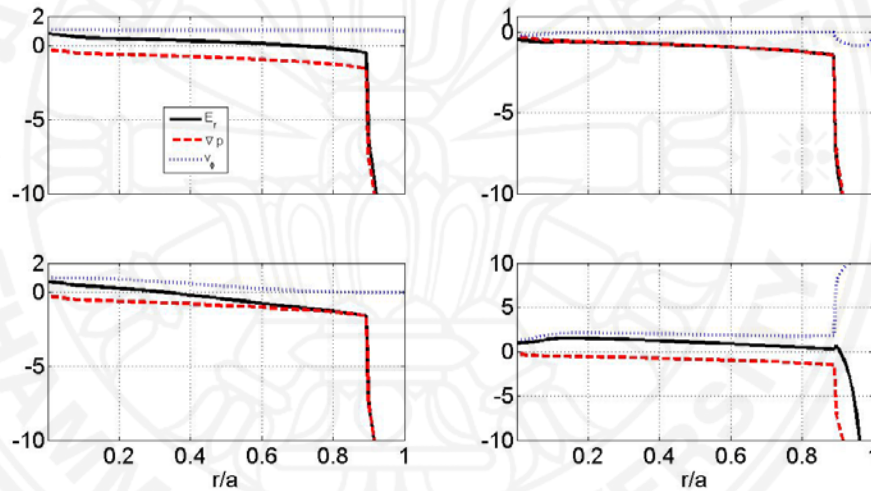


Figure 7.26. Profiles of radial electric field (solid), pressure gradient term (dashed) and toroidal rotation term (dotted) at steady state for simulations using model a(top left), b (top right), c (bottom left) and d (bottom right).

7.4.2.2 Pedestal dynamics

This section illustrates the pedestal dynamics once *L-H* transition occurs. Figure 7.27 demonstrates the change of pedestal width after it is formed. Initially, the transport barrier only forms at pressure channel. After forming, it starts to expand. It appears that the pedestal growth is categorized as superdiffusive behaviour ($\Delta_{ped} \propto t^b, b > 0.5$), agreeing with the turbulent nature of the plasma because in this phase the suppression effect is still not too high, especially at the particle channel suppression, thus turbulent transport still plays a considerable role. The speed of

pedestal width expansion appears to be related to the gradient of toroidal velocity profile near pedestal area. Left panel of figure 7.27 shows that the barrier expands fastest for simulations using model b) with expansion rate of 2.9 s^{-1} , then model d) with rate of 1.4 s^{-1} , their toroidal velocity gradients near the pedestal are 3.2 and 2.4, respectively. The correlation is not clear in model a) and c) which yield very small negative value of toroidal velocity gradients while the expansion rate is slightly less than that of model d). At some time later, the transport reduction effect becomes large enough to suppress the density channel so the transport barrier in density channel starts to form. Note that the pedestal width of both pressure and density channels are about the same regardless of the model used. The onset of transport barrier formation in density channel also improves density profiles significantly. This actually reduces the first contribution in the radial electric field calculation of equation (7.13) resulting in the flow shear being less effective. As a result, both barrier widths slowly decrease or collapse until the plasma reaches steady state. The decrease is slower than the width expansion because now the plasma is governed solely by the neoclassical transport which is a slower process than turbulent transport. In this process the width dynamics becomes subdiffusive or even slower. There is an interesting point worth mentioning here, which is the time it takes the plasma to evolve during H-mode is around one order of magnitude slower than the time it takes for the plasma to evolve from L to H mode.

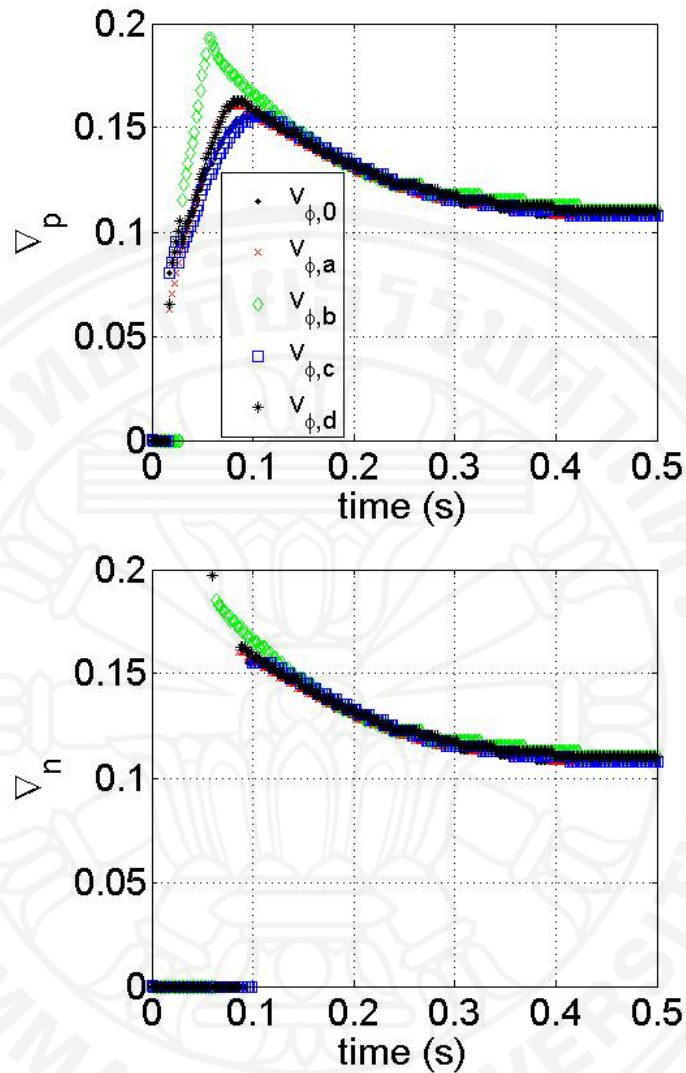


Figure 7.27. Time evolution of pedestal width of pressure (top) and density (bottom) channels.

7.4.3 Conclusion

Numerical method is used to solve the coupled pressure and density transport equations based on bifurcation concept. The transport effects included are neoclassical transport which is assumed to be constant and anomalous transport which is inspired by the critical gradient transport model. The suppression mechanism is the flow shear calculating from the force balance equation which includes toroidal flow effect. Four simple toroidal velocity models are considered in the calculation of radial electric field based on the force balance equation. It is found that inclusion of toroidal velocity can substantially increase the plasma pressure and density, mainly due to an

increase of the pedestal width. It is also found that the pedestal for pressure tends to form first. After the pedestal forms, it expands inwards with the characteristic of super-diffusive nature in initial state and become sub-diffusive nature in final state before reaching steady state. The expansion speed depends sensitively on the strength of flow shear effect. It is also found that the time required plasma to reach steady state after the *L-H* transition is much longer than that for *L-H* transition.

CHAPTER 8

SUMMARY AND RECOMMENDATIONS

8.1 Summary

In this thesis, formation and dynamics of an ETB and ITB in tokamak plasma are studied based on bifurcation concept. There are two main types of bifurcation model used in this thesis; one-field and two-field bifurcation models. Analytical study and stability analysis on both models shows that the bifurcation behavior in the plasma is intrinsic and hysteresis nature can be found in this plasma system. Certain criteria are required in order for the plasma to exhibit bifurcation resulting in an abrupt change in pressure and density gradients. The formations of ETB and ITB are characterized by the discontinuous in the gradients and the reduction of the transport. Numerical method is used to solve for the time evolution of the plasma profiles. In the two-field bifurcation model, it is found that the ETB width can expand initially superdiffusively and later subdiffusively. Eventually, it stops expanding. Also, the time the plasma takes for pedestal expansion is about one order of magnitude longer than it takes to transit from L - to H -mode. ETB appears to form only if the critical flux (heat/particle) is reached regardless of the magnetic shear profile; while ITB formation is possible only with a reversed magnetic shear profile. Weak ITB formation is found when the reverse profile happens close to plasma magnetic axis. In addition, with a suitable magnetic shear profile, the minimum flux criterion is not needed for ITB formation, though the abrupt jumps in the gradients become smoother at lower flux. ITB location and width are also found to be correlated to the nature of current peaking. In particular, the top of ITB is in the vicinity of where current density profile is maximum. Both ITB and ETB widths appears to be proportional to heat source and off-center distance of current peaking. Thermal and particle neoclassical and anomalous transport appears to affect plasma profiles, ETB and ITB widths. In addition, it is found that inclusion of toroidal velocity in the calculation of the flow shear can substantially increase the predicted plasma pressure and density, mainly due to an increase of the pedestal width. Ultimately, simultaneous formation of ETB and

ITB can lead to significant improvement of central pressure and density, and hence enhancement of fusion energy production.

8.2 Recommendations for future work

Further improvements for the models used in this thesis can be carried out in different ways. First of all, one can include the third transport equation which solves the momentum conservation in toroidal direction. This third field will yield information of toroidal velocity which can be used in the calculation of the radial electric field and the flow shear. Previous work suggested that the toroidal momentum transport equation is also coupled with the pressure and density transport equations [128]. Thus, all three equations must be solved simultaneously. Another recommendation is to apply the bifurcation concept in this thesis to use with an integrated predictive modeling code, for example BALDUR code. The code can be used to solve for the local neoclassical and anomalous transport coefficients, which then is assumed to be suppressed by the suppression function based on flow shear and magnetic shear. With more realistic thermal and particle sources and sinks calculated by the code, the transport equations can be self-consistently solved for the plasma profiles. This way, the investigation of the formations of ITB and ETB and their dynamics can be related and compared to the real tokamak experiment. Recently, an intermediate confinement mode (*I*-mode) occurring during the transition was discovered and it has been extensively investigated [181]. The mechanism of this intermediate mode is still not clear and subjected to future investigation.

REFERENCES

1. World Population Prospects: The 2006 Revision, Retrieved May 15th, 2015 from
http://www.un.org/esa/population/publications/wpp2006/WPP2006_Highlights_rev.pdf
2. Statistical Review of World Energy June 2009, Retrieved April 4th, 2010 from
<http://www.bp.com/productlanding.do?categoryId=6929&contentId=7044622>
3. Weisz, P. B. (2004). Basic Choices and Constraints on Long-Term Energy Supplies. *Physics Today*, 57 (7), 47-52.
4. Qian, H., Joseph, R., and Zeng, N. (2010). Enhanced terrestrial carbon uptake in the Northern High Latitudes in the 21st century from the Coupled Carbon Cycle Climate Model Intercomparison Project model projections. *Global Change Biology*, 16 (2), 641-656.
5. McCracken, G. M., and Stott, P. E. (2005). *Fusion : the energy of the universe*. Burlington, MA: Elsevier Academic Press.
6. Wesson, J. (2004). *Tokamaks*. New York, USA: Clarendon Press.
7. Moses, E. I., and Collaborators, t. N. (2013). The National Ignition Campaign: status and progress. *Nucl. Fusion*, 53 (10), 104020.
8. Hinkel, D. E. (2013). Scientific and technological advancements in inertial fusion energy. *Nucl. Fusion*, 53 (10), 104027.
9. Azechi, H., Mima, K., Shiraga, S., Fujioka, S., Nagatomo, H., Johzaki, T. *et al.* (2013). Present status of fast ignition realization experiment and inertial fusion energy development. *Nucl. Fusion*, 53 (10), 104021.
10. File: Tokamak (scheme).jpg, Retrieved May 15th, 2015 from
[http://commons.wikimedia.org/wiki/File:Tokamak_\(scheme\).jpg](http://commons.wikimedia.org/wiki/File:Tokamak_(scheme).jpg)
11. Triangularity, Retrieved May 15th, 2015 from
<http://fusionwiki.ciemat.es/wiki/Triangularity>
12. Romanelli, F., and Kamendje, R. on behalf of JET-EFDA Contributors (2009). Overview of JET results. *Nucl. Fusion*, 49 (10), 104006.
13. Princeton Plasma Physics Laboratory, Retrieved April 7th, 2010 from
<http://www.pppl.gov/projects/pages/tftr.html>

14. Oyama, N., and the JT-60 Team. (2009). Overview of JT-60U results towards the establishment of advanced tokamak operation. *Nucl. Fusion*, 49 (10), 104007.
15. Zohm, H., Adamek, J., Angioni, C., Antar, G., Atanasiu, C. V., Balden, M. *et al.* (2009). Overview of ASDEX Upgrade results. *Nucl. Fusion*, 49 (10), 104009.
16. Bandyopadhyay, I., Ahmed, S. M., Atrey, P. K., Bhatt, S. B., Bhattacharya, R., Chaudhury, M. B. *et al.* (2004). Modelling of Ohmic discharges in ADITYA tokamak using the Tokamak Simulation Code. *Plasma Phys. Control. Fusion*, 46 (9), 1443.
17. Hutchinson, I. H., Boivin, R., Bonoli, P. T., Boswell, C., Bravenec, R., Bretz, N. L. *et al.* (2001). Overview of recent Alcator C-Mod results. *Nucl. Fusion*, 41 (10), 1391.
18. Urban, J., and *et al.* (2010). Self-consistent transport simulations of COMPASS operation with optimized NBI. *Plasma Phys. Control. Fusion*, 52 (4), 045008.
19. Wan, Y., Li, J., Weng, P., and East, GA, PPPL team. (2006). *Overview Progress and Future Plan of EAST project*. Paper presented at the Proceedings of the 21st Fusion Energy Conference, Chengdu, China, Paper OV/1-1,
20. Tuccillo, A. A., Alekseyev, A., Angelini, B., Annibaldi, S. V., Apicella, M. L., Apruzzese, G. *et al.* (2009). Overview of the FTU results. *Nucl. Fusion*, 49 (10), 104013.
21. HT-7 Team, and Wan, B. (2002). Experiments in the HT-7 Superconducting Tokamak. *Fusion Sci. Tech.*, 42 116-123.
22. Gryaznevich, M., Oost, G. V., Peleman, P., Brotankova, J., Dejarnac, R., Dufkova, E. *et al.* (2009). Results of Joint Experiments and other IAEA activities on research using small tokamaks. *Nucl. Fusion*, 49 (10), 104026.
23. Lee, G. S., Kim, J., Hwang, S. M., Chang, C. S., Chang, H. Y., Cho, M. H. *et al.* (2000). The KSTAR project: An advanced steady state superconducting tokamak experiment. *Nucl. Fusion*, 40 (3Y), 575.

24. Plasma Physics Laboratory University of Saskatchewan, Retrieved April 7, 2010 from <http://plasma.usask.ca/storm/index.php>
25. Centre de Recherches en Physique des Plasmas, TCV Configuration Variable, Retrieved April 4th, 2010 from http://crppwww.epfl.ch/crpp_tcv.html#params
26. Institute for Energy Research (IEF), Retrieved April 7th, 2010 from http://www.fz-juelich.de/ief/ief-4/textor_en/
27. Zushi, H., Nakamura, K., Hanada, K., Sato, K. N., Sakamoto, M., Idei, H. *et al.* (2005). Steady-state tokamak operation, ITB transition and sustainment and ECCD experiments in TRIAM-1M. *Nucl. Fusion*, 45 (10), S142.
28. Aymar, R., Barabaschi, P., and Shimomura, Y. (2002). The ITER design. *Plasma Phys. Control. Fusion*, 44 (5), 519.
29. Shimada, M., Campbell, D. J., Mukhovatov, V., Fujiwara, M., Kirneva, N., Lackner, K. *et al.* (2007). Chapter 1: Overview and summary. *Nucl. Fusion*, 47 (6), S1.
30. Peacock, N. J., Robinson, D. C., Forrest, M. J., Wilcock, P. D., and Sannikov, V. V. (1969). Measurement of the Electron Temperature by Thomson Scattering in Tokamak T3. *Nature*, 224 (5218), 488-490.
31. Wagner, F., Becker, G., Behringer, K., Campbell, D., Eberhagen, A., Engelhardt, W. *et al.* (1982). Regime of Improved Confinement and High Beta in Neutral-Beam-Heated Divertor Discharges of the ASDEX Tokamak. *Phys. Rev. Lett.*, 49 1408.
32. JET Team (presented by Gormezano C.), (1997). *Optimization of JET Plasmas with Current Profile Control*. Paper presented at the Proceedings of the 16th IAEA Fusion Energy Conference, Montreal, Canada, Paper 487,
33. Strachan, J. D., Adler, H., Barnes, C. W., Batha, S., Bell, M. G., Bell, R. *et al.* (1994). Deuterium and tritium experiments on TFTR. *Plasma Phys. Control. Fusion*, 36 (12B), B3.
34. Keilhacker, M., Gibson, A., Gormezano, C., Lomas, P. J., Thomas, P. R., Watkins, M. L. *et al.* (1999). High fusion performance from deuterium-tritium plasmas in JET. *Nucl. Fusion*, 39 (2), 209.
35. Ishida, S., Fujita, T., Akasaka, H., Akino, N., Annou, K., Aoyagi, T. *et al.* (1997). Achievement of High Fusion Performance in JT-60U Reversed Shear

- Discharges. *Phys. Rev. Lett.*, 79 (Copyright (C) 2010 The American Physical Society), 3917.
36. Fujita, T., Kamada, Y., Ishida, S., Neyatani, Y., Oikawa, T., Ide, S. *et al.* (1999). High performance experiments in JT-60U reversed shear discharges. *Nucl. Fusion*, 39 (11Y), 1627.
 37. 1998 ITER Council Proceeding. (*ITER Documentation Series No 15*). Paper presented at the Proceedings of the Vienna: IAEA, Paper 148,
 38. ASDEX Team. (1989). The H-Mode of ASDEX. *Nucl. Fusion*, 29 (11), 1959.
 39. Burrell, K. H. (1994). Summary of experimental progress and suggestions for future work (H mode confinement). *Plasma Phys. Control. Fusion*, 36 (7A), A291.
 40. Hubbard, A. E. (2000). Physics and scaling of the H-mode pedestal. *Plasma Phys. Control. Fusion*, 42 (5A), A15.
 41. Connor, J. W., Fukuda, T., Garbet, X., Gormezano, C., Mukhovatov, V., Wakatani, M. *et al.* (2004). A review of internal transport barrier physics for steady-state operation of tokamaks. *Nucl. Fusion*, 44 (4), R1.
 42. Connor, J. W., and Wilson, H. R. (2000). A review of theories of the L-H transition. *Plasma Phys. Control. Fusion*, 42 (1), R1.
 43. Burrell, K. H. (1997). Effects of $E \times B$ velocity shear and magnetic shear on turbulence and transport in magnetic confinement devices. *Phys. Plasmas*, 4 (5), 1499-1518.
 44. Wagner, F. (2007). A quarter-century of H-mode studies. *Plasma Phys. Control. Fusion*, 49 (12B), B1.
 45. Biglari, H., Diamond, P. H., and Terry, P. W. (1990). Influence of sheared poloidal rotation on edge turbulence. *Physics of Fluids B: Plasma Physics*, 2 (1), 1-4.
 46. Haye, R. J. L., Osborne, T. H., Rettig, C. L., Greenfield, C. M., Hyatt, A. W., and Scoville, J. T. (1995). Core flow shear as the cause of very high confinement in the DIII-D tokamak. *Nucl. Fusion*, 35 (8), 988.
 47. Bourdelle, C., Garbet, X., Hoang, G. T., Ongena, J., and Budny, R. V. (2002). Stability analysis of improved confinement discharges: internal transport

- barriers in Tore Supra and radiative improved mode in TEXTOR. *Nucl. Fusion*, 42 (7), 892.
48. Crisanti, F., Esposito, B., Gormezano, C., Tuccillo, A., Bertalot, L., Giroud, C. *et al.* (2001). Analysis of the $E \times B$ flow shearing rate in JET ITB discharges. *Nucl. Fusion*, 41 (7), 883.
 49. Fukuda, T., Takizuka, T., Fujita, T., Sakamoto, Y., Kamada, Y., Ide, S. *et al.* (2002). Compatibility conditions of the edge and internal transport barrier formation in JT-60U. *Plasma Phys. Control. Fusion*, 44 (5A), A341.
 50. Singer, C. E., Post, D. E., Mikkelsen, D. R., Redi, M. H., McKenney, A., Silverman, A. *et al.* (1988). Baldur: A one-dimensional plasma transport code. *Comput. Phys. Commun.*, 49 (2), 275-398.
 51. ITER Confinement Database and Modelling Expert Group (presented by Takizuka T.). (1997). *Reduction of L-H transition threshold power under the W-shaped pumped divertor geometry in JT-60U*. Paper presented at the Proceedings of the 16th IAEA Fusion Energy Conference, Montreal, Canada, Paper 795,
 52. Shimomura, Y., Aymar, R., Chuyanov, V., Huguet, M., Matsumoto, H., Mizoguchi, T. *et al.* (2000). *ITER-FEAT Operation*. Paper presented at the Proceedings of the 18th Fusion Energy Conference, Paper ITER/1,
 53. Ryter, F., and *et al.* (1998). H-mode power threshold and transition in ASDEX Upgrade. *Plasma Phys. Control. Fusion*, 40 (5), 725.
 54. Hubbard, A. E., and *et al.* (1998). Local variables affecting H-mode threshold on Alcator C-Mod. *Plasma Phys. Control. Fusion*, 40 (5), 689.
 55. The ITER H-mode Threshold Database Working Group (presented by Righi E). (1998). Scaling of the H-mode power threshold for ITER. *Plasma Phys. Control. Fusion*, 40 (5), 857.
 56. Groebner, R. J., and Carlstrom, T. N. (1998). Critical edge parameters for H-mode transition in DIII-D. *Plasma Phys. Control. Fusion*, 40 (5), 673.
 57. Connor, J. W., and Taylor, J. B. (1977). Scaling laws for plasma confinement. *Nucl. Fusion*, 17 (5), 1047.
 58. Connor, J. W., Counsell, G. F., Erents, S. K., Fielding, S. J., LaBombarda, B., and Morel, K. (1999). Comparison of theoretical models for scrape-off layer

- widths with data from COMPASS-D, JET and Alcator C-Mod. *Nucl. Fusion*, 39 (2), 169.
59. Lehnert, B. (1966). Short-Circuit of Flute Disturbances at a Plasma Boundary. *Physics of Fluids*, 9 (7), 1367-1372.
 60. Wolf, R. C. (2003). Internal transport barriers in tokamak plasmas. *Plasma Phys. Control. Fusion*, 45 (1), R1.
 61. Sips, A. C. C., Baranov, Y., Challis, C. D., Cottrell, G. A., Eriksson, L.-G., Gormezano, C. *et al.* (1998). Operation at high performance in optimized shear plasmas in JET. *Plasma Phys. Control. Fusion*, 40 (6), 1171.
 62. Burrell, K. H., Austin, M. E., Greenfield, C. M., Lao, L. L., Rice, B. W., Staebler, G. M. *et al.* (1998). Effects of W_{ExB} velocity shear and magnetic shear in the formation of core transport barriers in the DIII-D tokamak. *Plasma Phys. Control. Fusion*, 40 (9), 1585.
 63. Doyle, E. J., Staebler, G. M., Zeng, L., Rhodes, T. L., Burrell, K. H., Greenfield, C. M. *et al.* (2000). Observation of simultaneous internal transport barriers in all four transport channels and correlation with turbulence behaviour in NCS discharges on DIII-D. *Plasma Phys. Control. Fusion*, 42 (5A), A237.
 64. Shirai, H., and JT-60 Team. (1998). Recent experimental and analytic progress in the Japan Atomic Energy Research Institute Tokamak-60 Upgrade with W-shaped divertor configuration. *Phys. Plasmas*, 5 (5), 1712-1720.
 65. Levinton, F. M., Zarnstorff, M. C., Batha, S. H., Bell, M., Bell, R. E., Budny, R. V. *et al.* (1995). Improved Confinement with Reversed Magnetic Shear in TFTR. *Phys. Rev. Lett.*, 75 (Copyright (C) 2010 The American Physical Society), 4417.
 66. Strait, E. J., Lao, L. L., Mauel, M. E., Rice, B. W., Taylor, T. S., Burrell, K. H. *et al.* (1995). Enhanced Confinement and Stability in DIII-D Discharges with Reversed Magnetic Shear. *Phys. Rev. Lett.*, 75 (Copyright (C) 2010 The American Physical Society), 4421.
 67. Koide, Y., Kikuchi, M., Mori, M., Tsuji, S., Ishida, S., Asakura, N. *et al.* (1994). Internal transport barrier on $q=3$ surface and poloidal plasma spin up

- in JT-60U high- beta p discharges. *Phys. Rev. Lett.*, 72 (Copyright (C) 2010 The American Physical Society), 3662.
68. Tala, T. J. J., Heikkinen, J. A., Parail, V. V., Baranov, Y. F., and Karttunen, S. J. (2001). ITB formation in terms of $\omega E \times B$ flow shear and magnetic shear s on JET. *Plasma Phys. Control. Fusion*, 43 (4), 507.
 69. Erba, M., Cherubini, A., Parail, V. V., Springmann, E., and Taroni, A. (1997). Development of a non-local model for tokamak heat transport in L-mode, H-mode and transient regimes. *Plasma Phys. Control. Fusion*, 39 (2), 261.
 70. Tresset, G., Moreau, D., Litaudon, X., Challis, C. D., Garbet, X., Joffrin, E. *et al.* (2001). *Characterisation of Internal Transport Barriers in JET and Simulations of Control Algorithms*. Paper presented at the Proceedings of the 28th EPS Conference on Controlled Fusion and Plasma Physics, Madeira, Paper 533,
 71. Tresset, G., Litaudon, X., Moreau, D., Garbet, X., and Contributor to the EFDA-JET Work Programme. (2002). A dimensionless criterion for characterizing internal transport barriers in JET. *Nucl. Fusion*, 42 (5), 520.
 72. Hahm, T. S., and Burrell, K. H. (1995). Flow shear induced fluctuation suppression in finite aspect ratio shaped tokamak plasma. *Phys. Plasmas*, 2 (5), 1648-1651.
 73. Pankin, A. Y., Voitsekhovitch, I., Bateman, G., Dnestrovski, A., Janeschitz, G., Murakami, M. *et al.* (2005). Combined model for the H-mode pedestal and ELMs. *Plasma Phys. Control. Fusion*, 47 (3), 483.
 74. Zhu, P., Bateman, G., Kritiz, A. H., and Horton, W. (2000). Predictive transport simulations of internal transport barriers using the Multi-Mode model. *Phys. Plasmas*, 7 (7), 2898-2908.
 75. Waltz, R. E., Kerbel, G. D., Milovich, J., and Hammett, G. W. (1995). Advances in the simulation of toroidal gyro-Landau fluid model turbulence. *Phys. Plasmas*, 2 (6), 2408-2416.
 76. Greenfield, C. M., Rettig, C. L., Staebler, G. M., Stallard, B. W., Austin, M. E., Burrell, K. H. *et al.* (1999). Behaviour of electron and ion transport in discharges with an internal transport barrier in the DIII-D tokamak. *Nucl. Fusion*, 39 (11Y), 1723.

77. Beer, M. A., Hammett, G. W., Rewoldt, G., Synakowski, E. J., Zarnstorff, M. C., and Dorland, W. (1997). Gyrofluid simulations of turbulence suppression in reversed-shear experiments on the Tokamak Fusion Test Reactor. *Phys. Plasmas*, 4 (5), 1792-1799.
78. Synakowski, E. J., Batha, S. H., Beer, M. A., Bell, M. G., Bell, R. E., Budny, R. V. *et al.* (1997). Roles of Electric Field Shear and Shafranov Shift in Sustaining High Confinement in Enhanced Reversed Shear Plasmas on the TFTR Tokamak. *Phys. Rev. Lett.*, 78 (15), 2972.
79. Challis, C. D., Christiansen, J. P., Cordey, J. G., Gormezano, C., Gowers, C. W., Kramer, G. J. *et al.* (1992). Current ramp experiments on the scaling of energy confinement. *Nucl. Fusion*, 32 (12), 2217.
80. Zarnstorff, M. C., and *et al.* (1992). Paper presented at the Proceedings of the 14th IAEA Conference on Plasma Physics and Controlled Nuclear Fusion Research, Wurzburg, Paper 111,
81. Kamada, Y., Ushigusa, K., Naito, O., Neyatani, Y., Ozeki, T., Tobita, K. *et al.* (1994). Non-inductively current driven H mode with high beta N and high beta p values in JT-60U. *Nucl. Fusion*, 34 (12), 1605.
82. Lao, L. L., Ferron, J. R., Taylor, T. S., Burrell, K. H., Chan, V. S., Chu, M. S. *et al.* (1993). High internal inductance improved confinement H-mode discharges obtained with an elongation ramp technique in the DIII-D tokamak. *Phys. Rev. Lett.*, 70 (Copyright (C) 2010 The American Physical Society), 3435.
83. Koide, Y., Mori, M., Fujita, T., Shirai, H., Hatae, T., Takizuka, T. *et al.* (1998). Study of internal transport barriers by comparison of reversed shear and high-beta discharges in JT-60U. *Plasma Phys. Control. Fusion*, 40 (5), 641.
84. Greenfield, C. M., DeBoo, J. C., Luce, T. C., Stallard, B. W., Synakowski, E. J., Baylor, L. R. *et al.* (2000). Understanding and control of transport in Advanced Tokamak regimes in DIII-D. *Phys. Plasmas*, 7 (5), 1959-1967.
85. Wolf, R. C., Gunter, S., Leuterer, F., Peeters, A., Pereverzev, G., Gruber, O. *et al.* (2000). Response of internal transport barriers to central electron heating and current drive on ASDEX Upgrade. *Phys. Plasmas*, 7 (5), 1839-1844.

86. Equipe Tore Supra (presented by Litaudon, X.). (1996). Stationary regimes of improved confinement in Tore Supra. *Plasma Phys. Control. Fusion*, 38 (12A), A251.
87. de Baar, M. R., Hogeweij, G. M. D., Lopes Cardozo, N. J., Oomens, A. A. M., and Schüller, F. C. (1997). Electron Thermal Transport Barrier and Magnetohydrodynamic Activity Observed in Tokamak Plasmas with Negative Central Shear. *Phys. Rev. Lett.*, 78 (Copyright (C) 2010 The American Physical Society), 4573.
88. Buratti, P., Barbato, E., Bracco, G., Cirant, S., Crisanti, F., Granucci, G. *et al.* (1999). High Core Electron Confinement Regimes in FTU Plasmas with Low- or Reversed-Magnetic Shear and High Power Density Electron-Cyclotron-Resonance Heating. *Phys. Rev. Lett.*, 82 (Copyright (C) 2010 The American Physical Society), 560.
89. Gruber, O., Bosch, H.-S., Günter, S., Herrmann, A., Kallenbach, A., Kaufmann, M. *et al.* (1999). Overview of ASDEX Upgrade results. *Nucl. Fusion*, 39 (9Y), 1321.
90. Pietrzyk, Z. A., Angioni, C., Behn, R., Coda, S., Goodman, T. P., Henderson, M. A. *et al.* (2001). Long-Pulse Improved Central Electron Confinement in the TCV Tokamak with Electron Cyclotron Heating and Current Drive. *Phys. Rev. Lett.*, 86 (Copyright (C) 2010 The American Physical Society), 1530.
91. Wolf, R. C., Hobirk, J., Conway, G. D., Gruber, O., Gude, A., Günter, S. *et al.* (2001). Performance, heating and current drive scenarios of ASDEX Upgrade advanced tokamak discharges. *Nucl. Fusion*, 41 (9), 1259.
92. Tala, T., and Garbet, X. (2006). Physics of Internal Transport Barriers. *C. R. Physique*, 7 (6), 622-633.
93. Joffrin, E., Challis, C. D., Hender, T. C., Howell, D. F., and Huysmans, G. T. A. (2002). MHD internal transport barrier triggering in low positive magnetic shear scenarios in JET. *Nucl. Fusion*, 42 (3), 235.
94. Turco, F., Giruzzi, G., Artaud, J. F., and Mazon, D. (2009). Internal transport barrier formation in the Tore Supra tokamak. *Plasma Phys. Control. Fusion*, 51 (6), 065021.

95. Itoh, K., and Itoh, S.-I. (1996). The role of the electric field in confinement. *Plasma Phys. Control. Fusion*, 38 (1), 1.
96. Malkov, M. A., and Diamond, P. H. (2008). Analytic theory of L --> H transition, barrier structure, and hysteresis for a simple model of coupled particle and heat fluxes. *Phys. Plasmas*, 15 (12), 122301.
97. Hinton, F. L. (1991). Thermal confinement bifurcation and the L- to H-mode transition in tokamaks. *Physics of Fluids B: Plasma Physics*, 3 (3), 696-704.
98. Pereverzev, G., and Yushmanov, P. N. (2002). ASTRA Automated System for Transport Analysis in a Tokamak. *Max-Planck Institut fur Plasmaphysik*, IPP 5/98.
99. Pearlstein, L. D., Bulmer, R. H., Casper, T. A., Hooper, E. B., Jong, R. A., Kaiser, T. B. *et al.* (2001). Predictive Modelling of Axisymmetric Toroidal Configurations. *ECA*, 25A 1901-1904.
100. Artaud, J. F., Basiuk, V., Imbeaux, F., Schneider, M., Garcia, J., Giruzzi, G. *et al.* (2010). The CRONOS suite of codes for integrated tokamak modelling. *Nucl. Fusion*, 50 (4), 043001.
101. Basiuk, V., Artaud, J. F., Imbeaux, F., Litaudon, X., Bécoulet, A., Eriksson, L.-G. *et al.* (2003). Simulations of steady-state scenarios for Tore Supra using the CRONOS code. *Nucl. Fusion*, 43 (9), 822.
102. Cenacchi, G., and Taroni, A. (1988). JETTO: a free boundary plasma transport code. *ENEA Report RT/TIB*, 88 5.
103. Deng, Z., John, H. S., Yemin, H., Guoqiang, L., Qilong, R., and Jin, O. (2009). Transport Modelling for EAST with LHRF and NBI. *Plasma Science and Technology*, 11 (4), 417.
104. Jardin, S. C., Pomphrey, N., and DeLucia, J. (1986). Dynamic modeling of transport and positional control of tokamaks. *J. Comput. Phys.*, 66 (2), 481.
105. Kinsey, J. E., Staebler, G. M., and Waltz, R. E. (2002). Simulations of internal transport barrier formation in tokamak discharges using the GLF23 transport model. *Phys. Plasmas*, 9 (5), 1676-1691.
106. Onjun, T., and Pianroj, Y. (2009). Simulations of ITER with combined effects of internal and edge transport barriers. *Nucl. Fusion*, 49 (7), 075003.

107. Hannum, D., Bateman, G., Kinsey, J., Kritz, A. H., Onjun, T., and Pankin, A. (2001). Comparison of high-mode predictive simulations using Mixed Bohm/gyro-Bohm and Multi-Mode (MMM95) transport models. *Phys. Plasmas*, 8 (3), 964-974.
108. Onjun, T., Bateman, G., Kritz, A. H., and Hannum, D. (2001). Comparison of low confinement mode transport simulations using the mixed Bohm/gyro-Bohm and the Multi-Mode-95 transport model. *Phys. Plasmas*, 8 (3), 975-985.
109. Fick, A. (1855). *Poggendorff's Annel. Physik.*, 94 59.
110. Tala, T. J. J., Parail, V. V., Becoulet, A., Corrigan, G., Heading, D. J., Mantsinen, M. J. *et al.* (2002). Comparison of theory-based and semi-empirical transport modelling in JET plasmas with ITBs. *Plasma Phys. Control. Fusion*, 44 (5A), A495.
111. Taroni, A., Erba, M., Springmann, E., and Tibone, F. (1994). Global and local energy confinement properties of simple transport coefficients of the Bohm type. *Plasma Phys. Control. Fusion*, 36 (10), 1629.
112. Erba, M., Parail, V., Springmann, E., and Taroni, A. (1995). Extension of a Bohm model for L-mode electron heat transport to ion heat transport and to the ohmic regime. *Plasma Phys. Control. Fusion*, 37 (11), 1249.
113. Erba, M., Aniel, T., Basiuk, V., Becoulet, A., and Litaudon, X. (1998). Validation of a new mixed Bohm/gyro-Bohm model for electron and ion heat transport against the ITER, Tore Supra and START database discharges. *Nucl. Fusion*, 38 (7), 1013.
114. Houlberg, W. A., Shaing, K. C., Shaing, S. P., and Xarnstorff, M. C. (1997). Bootstrap current and neoclassical transport in tokamaks of arbitrary collisionality and aspect ratio. *Phys. Plasmas*, 4 3230-3242.
115. Kritz, A. H., Bateman, G., Kinsey, J., Pankin, A., Onjun, T., Redd, A. *et al.* (2004). The National Transport Code Collaboration Module Library. *Comput. Phys. Commun.*, 164 (1-3), 108-113.
116. Onjun, T., Bateman, G., Kritz, A. H., and Hammett, G. (2002). Models for the pedestal temperature at the edge of H-mode tokamak plasmas. *Phys. Plasmas*, 9 (12), 5018-5030.

117. Connor, J. W. (1998). A review of models for ELMs. *Plasma Phys. Control. Fusion*, 40 (2), 191.
118. Sugihara, M., Igitkhanov, Y., Janeschitz, G., Hubbard, A. E., Kamada, Y., Lingertat, J. *et al.* (2000). A model for H mode pedestal width scaling using the International Pedestal Database. *Nucl. Fusion*, 40 (10), 1743.
119. Bateman, G., Onjun, T., and Kritz, A. H. (2003). Integrated predictive modelling simulations of burning plasma experiment designs. *Plasma Phys. Control. Fusion*, 45 (11), 1939.
120. Chatthong, B., Onjun, T., and Singhsomroje, W. (2010). Model for toroidal velocity in H-mode plasmas in the presence of internal transport barriers. *Nucl. Fusion*, 50 (6), 064009.
121. Chatthong, B., Onjun, T., Suwanna, S., Poolyarat, N., and Picha, R. (2010). JET Simulations with Edge and Internal Transport Barriers Included. *Thai Journal of Physics*, Series 5 79-83.
122. Kessel, C. E., Giruzzi, G., Sips, A. C. C., Budny, R. V., Artaud, J. F., Basiuk, V. *et al.* (2006). *Simulation of the Hybrid and Steady State Advanced Operating Modes in ITER*. Paper presented at the Proceedings of the 21st Fusion Energy Conference, Chengdu, China, Paper IT/P1-7,
123. Chatthong, B., and Onjun, T. (2011). Self-Consistent Simulation of Standard H-Mode ITER with the Presence of an Internal Transport Barrier. *Thammasat Int. J. Sc. Tech.*, 16 (1), 42-53.
124. Kikuchi, M. (2011). *On offset toroidal rotation in NTV*. Paper presented at the Proceedings of the 38th EPS Conference on Plasma Physics, Strasbourg, Paper P4.115, <http://ocs.ciemat.es/EPS2011PAP/pdf/P4.115.pdf>.
125. Hinton, F. L., and Staebler, G. M. (1993). Particle and energy confinement bifurcation in tokamaks. *Physics of Fluids B: Plasma Physics*, 5 (4), 1281-1288.
126. Staebler, G. M., Hinton, F. L., and Wiley, J. C. (1996). Designing a VH-mode core/L-mode edge discharge. *Plasma Phys. Control. Fusion*, 38 (8), 1461.
127. Lebedev, V. B., and Diamond, P. H. (1997). Theory of the spatiotemporal dynamics of transport bifurcations. *Phys. Plasmas*, 4 (4), 1087-1096.

128. Jhang, H., Kim, S. S., and Diamond, P. H. (2012). Role of external torque in the formation of ion thermal internal transport barriers. *Phys. Plasmas*, 19 (4), 042302.
129. Weymiens, W., Blank, H. J. d., Hogeweij, G. M. D., and Valenca, J. C. d. (2012). Bifurcation theory for the L-H transition in magnetically confined fusion plasmas. *Phys. Plasmas*, 19 (7), 072309.
130. Chatthong, B., and Onjun, T. (2015). Investigation of toroidal flow effects on L-H transition in tokamak plasma based on bifurcation model. *Journal of Physics: Conference Series*, 611 (1), 012003.
131. Chatthong, B., Wihakhaphirom, K., Picha, R., Poolyarat, N., Promping, J., and Onjun, T. (2014). *Investigation of ETB Formation, Pedestal Width and Dynamics Based on Bifurcation Concept*. Paper presented at the Proceedings of the 41st EPS Conference on Plasma Physics, Berlin, Paper P4.065, [http://http://ocs.ciemat.es/EPS2014PAP/pdf/P4.065.pdf](http://ocs.ciemat.es/EPS2014PAP/pdf/P4.065.pdf).
132. Garbet, X., Mantica, P., Ryter, F., Cordey, G., Imbeaux, F., Sozzi, C. *et al.* (2004). Profile stiffness and global confinement. *Plasma Phys. Control. Fusion*, 46 (9), 1351.
133. Dimits, A. M., Bateman, G., Beer, M. A., Cohen, B. I., Dorland, W., Hammett, G. W. *et al.* (2000). Comparisons and physics basis of tokamak transport models and turbulence simulations. 7 (3), 969-983.
134. Snipes, J. A., and the International H-mode Threshold Database Working Group. (2000). Latest results on the H-mode threshold using the international H-mode threshold database. *Plasma Phys. Control. Fusion*, 42 (5A), A299.
135. Chatthong, B., Sarazin, Y., Onjun, T., Wongsrisujarit, N., Imbeaux, F., Strugarek, A. *et al.* (2011). *Analytical and Numerical Modelling of Transport Barrier Formation Using Bifurcation Concept*. Paper presented at the Proceedings of the 38th EPS Conference on Plasma Physics, Strasbourg, France, Paper P4.097,
136. Thomas, D. M., Groebner, R. J., Burrell, K. H., Osborne, T. H., and Carlstrom, T. N. (1998). The back transition and hysteresis effects in DIII-D. *Plasma Phys. Control. Fusion*, 40 (5), 707.

137. Carlstrom, T. N., Campbell, D. J., Cordey, J. G., DeBoo, J. C., Groebner, R. J., Righi, E. *et al.* (1996). JET/DIII-D size scaling of the H-mode power threshold. *Plasma Phys. Control. Fusion*, 38 (8), 1231.
138. Ryter, F., Buchl, K., Fuchs, C., Gehre, O., Gruber, O., Herrmann, A. *et al.* (1994). H-mode results in ASDEX Upgrade. *Plasma Phys. Control. Fusion*, 36 (7A), A99.
139. Thomsen, K., Campbell, D. J., Cordey, J. G., Kardaun, O. J. W. F., Ryter, F., Stroth, U. *et al.* (1994). ITER H mode confinement database update. *Nucl. Fusion*, 34 (1), 131.
140. Toda, S., Itoh, S.-I., Yagi, M., Fukuyama, A., and Itoh, K. (1996). Double hysteresis in L/H transition and compound dithers. *Plasma Phys. Control. Fusion*, 38 (8), 1337.
141. Malkov, M. A., and Diamond, P. H. (2009). Weak hysteresis in a simplified model of the L-H transition. *Physics of Plasmas (1994-present)*, 16 (1), 012504.
142. Carlstrom, T. N., Shimada, M., Burrell, K. H., DeBoo, J. C., Gohil, P., Groebner, R. J. *et al.* (1989). Paper presented at the Proceedings of the The 16th European Conference on Controlled Fusion and Plasma Physics, Venice, Paper 241,
143. Pacher, G. W., Pacher, H. D., Janeschitz, G., Kukushkin, A. S., and Pereverzev, G. (2004). Operating window of ITER from consistent core–pedestal–SOL modelling with modified MMM transport and carbon. *Plasma Phys. Control. Fusion*, 46 (5A), A257.
144. Janeschitz, G., Pacher, G. W., Zolotukhin, O., Pereverzev, G., Pacher, H. D., Igitkhanov, Y. *et al.* (2002). A 1-D predictive model for energy and particle transport in H-mode. *Plasma Phys. Control. Fusion*, 44 (5A), A459.
145. Toi, K., Ohdachi, S., Watanabe, F., Narihara, K., Morisaki, T., Xiang, G. *et al.* (2006). Formation of Edge Transport Barriers by L-H Transition and Large Reversed Plasma Current on LHD. *Plasma Science and Technology*, 8 (1), 5.
146. Bickerton, R. J., Connor, J. W., and Taylor, J. B. (1971). Diffusion driven plasma currents and bootstrap tokamak. *Nature physical science*, 229 110-112.

147. Staebler, G. M., Kinsey, J. E., Belli, E. A., Candy, J., Waltz, R. E., Greenfield, C. M. *et al.* (2014). Resolving the mystery of transport within internal transport barriers. *Physics of Plasmas (1994-present)*, 21 (5), 055902.
148. Itoh, K., Itoh, S.-I., and Fukuyama, A. (1999). *Transport and Structural Formation in Plasmas*. IOP Publishing.
149. Litaudon, X. (1998). Profile control for steady-state operation. *Plasma Phys. Control. Fusion*, 40 (8A), A251.
150. Litaudon, X., Peysson, Y., Aniel, T., Huysmans, G., Imbeaux, F., Joffrin, E. *et al.* (2001). q -profile evolution and improved core electron confinement in the full current drive operation on Tore Supra. *Plasma Phys. Control. Fusion*, 43 (5), 677.
151. The JET Team (presented by Söldner, F. X.). (1997). Shear optimization experiments with current profile control on JET. *Plasma Phys. Control. Fusion*, 39 (12B), B353.
152. Neudatchin, S. V., Takizuka, T., Hayashi, N., Isayama, A., Shirai, H., Fujita, T. *et al.* (2004). Role of low order rational q -values in the ITB events in JT-60U reverse shear plasmas. *Nucl. Fusion*, 44 (9), 945.
153. Greenfield, C. M., Balet, B., Burrell, K. H., Chu, M. S., Cordey, J. G., DeBoo, J. C. *et al.* (1993). Investigations of VH-mode in DIII-D and JET. *Plasma Phys. Control. Fusion*, 35 (SB), B263.
154. Onjun, T., Kritz, A. H., Bateman, G., and Parail, V. (2005). Magnetohydrodynamic-calibrated edge-localized mode model in simulations of International Thermonuclear Experimental Reactor. *Phys. Plasmas*, 12 (8), 082513.
155. Halpern, F. D., Kritz, A. H., Bateman, G., Pankin, A. Y., Budny, R. V., and McCune, D. C. (2008). Predictive simulations of ITER including neutral beam driven toroidal rotation. *Phys. Plasmas*, 15 (6), 062505.
156. Budny, R. V., Andre, R., Bateman, G., Halpern, F., Kessel, C. E., Kritz, A. *et al.* (2008). Predictions of H-mode performance in ITER. *Nucl. Fusion*, 48 (7), 075005.

157. Roach, C. M., Walters, M., Budny, R. V., Imbeaux, F., Fredian, T. W., Greenwald, M. *et al.* (2008). The 2008 Public Release of the International Multi-tokamak Confinement Profile Database. *Nucl. Fusion*, 48 (12), 125001.
158. Pianroj, Y., Techakunchaiyanunt, J., and Onjun, T. (2012). Model for Pedestal Transport Based on Suppression of Anomalous Transport Using ω ExB Flow Shear and Magnetic Shear. *J. Phys. Soc. Jpn.*, 81 (4), 044502.
159. Leekhaphan, P., and Onjun, T. (2011). Pellet Injection into H-mode ITER Plasma with the Presence of Internal Transport Barriers. *Plasma Phys. Rep.*, 37 321-327.
160. Wisitsorasak, A., and Onjun, T. (2011). Impacts of Pellets Injected from the Low Field Side on Plasma in ITER. *Plasma Phys. Rep.*, 37 (1), 1-18.
161. Klaywitthaphat, P., and Onjun, T. (2012). Simulations of plasma behavior during pellet injection in ITER. *Plasma Phys. Rep.*, 38 (6), 496-502.
162. Pianroj, Y., Chuchinda, C., Leekhaphan, P., and Onjun, T. (2010). Behaviors of Impurity in ITER Plasma with Standard Type I ELMy H-mode and Steady State Scenarios. *Plasma Phys. Rep.*, 36 (10), 827.
163. Pianroj, Y., and Onjun, T. (2012). Simulations of H-Mode Plasmas in Tokamak Using a Complete Core-Edge Modeling in the BALDUR Code. *Plasma Science and Technology*, 14 (9), 778.
164. Pianroj, Y., Jumrat, S., Chatthong, B., and Onjun, T. (2014). A Full Radial Electric Field Calculation for Predicting Pedestal Formation in H-mode Tokamak Plasma by using BALDUR code. *Thammasat Int. J. Sc. Tech.*, 19 (2), 63-70.
165. Pianroj, Y., and Onjun, T. (2012). Projection of bootstrap current in the ITER with standard type I ELMy H-mode and steady state scenarios. *Songklanakarin J. Sci. Technol.*, 34 (1), 77-91.
166. Intharat, P., Chatthong, B., Onjun, T., Poolyarat, N., and Picha, R. (2015). The simulation of L-H transition in tokamak plasma using MMM95 transport model. *Journal of Physics: Conference Series*, 611 (1), 012005.
167. Diamond, P. H., Itoh, S.-I., Itoh, K., and Hahm, T. S. (2005). Zonal flows in plasma—a review. *Plasma Phys. Control. Fusion*, 47 (5), R35.

168. Tala, T., Crombé, K., Vries, P. C. d., Ferreira, J., Mantica, P., Peeters, A. G. *et al.* (2007). Toroidal and poloidal momentum transport studies in tokamaks. *Plasma Phys. Control. Fusion*, 49 (12B), B291.
169. Rozhansky, V., Kaveeva, E., Voskoboynikov, S., Coster, D., Bonnin, X., and Schneider, R. (2002). Modelling of electric fields in tokamak edge plasma and L-H transition. *Nucl. Fusion*, 42 (9), 1110.
170. Rogister, A. L., Rice, J. E., Nicolai, A., Ince-Cushman, A., Gangadhara, S., and Group, A. C.-M. (2002). Theoretical interpretation of the toroidal rotation velocity observed in Alcator C-Mod Ohmic H-mode discharges. *Nucl. Fusion*, 42 (9), 1144.
171. Eriksson, A., Nordman, H., Strand, P., Weiland, J., Tala, T., Asp, E. *et al.* (2007). Predictive simulations of toroidal momentum transport at JET. *Plasma Phys. Control. Fusion*, 49 (11), 1931.
172. Staebler, G. M., Waltz, R. E., and Wiley, J. C. (1997). The role of rotation in tokamak internal transport barriers. *Nucl. Fusion*, 37 (3), 287.
173. Chatthong, B., and Onjun, T. (2013). Simulations of ITER in the presence of ITB using the NTV intrinsic toroidal rotation model. *Nucl. Fusion*, 53 (1), 013007.
174. Houlberg, W. A., Shaing, K. C., Hirshman, S. P., and Zarnstorff, M. C. (1997). Bootstrap current and neoclassical transport in tokamaks of arbitrary collisionality and aspect ratio. *Phys. Plasmas*, 4 (9), 3230-3242.
175. Zhu, W., Sabbagh, S. A., Bell, R. E., Bialek, J. M., Bell, M. G., LeBlanc, B. P. *et al.* (2006). Observation of Plasma Toroidal-Momentum Dissipation by Neoclassical Toroidal Viscosity. *Phys. Rev. Lett.*, 96 (22), 225002.
176. Hirshman, S. P., and Sigmar, D. J. (1981). Neoclassical transport of impurities in tokamak plasmas. *Nucl. Fusion*, 21 1079.
177. Kim, Y. B., Diamond, P. H., and Groebner, R. J. (1991). Neoclassical poloidal and toroidal rotation in tokamaks. *Phys. Fluids B*, 3 (8), 2050-2060.
178. Tarter, C. B., and Spectros, J. (1977). *Radia. Trans*, 10 531.
179. Boucher, D., Connor, J. W., Houlberg, W. A., Turner, M. F., Bracco, G., Chudnovskiy, A. *et al.* (2000). The International Multi-Tokamak Profile Database. *Nucl. Fusion*, 40 (12), 1955.

180. Chatthong, B., and Onjun, T. (2014). Comparison of H-mode plasma simulations using toroidal velocity models depending on plasma current density and ion temperature in presence of an ITB. *Songklanakarin J. Sci. Technol.*, 36 (3), 375-387.
181. Xu, Y., Cheng, J., Dong, J. Q., Dong, Y. B., Jiang, M., Zhong, W. L. *et al.* (2015). Dynamics of low–intermediate–high-confinement transitions in the HL-2A tokamak. *Plasma Phys. Control. Fusion*, 57 (1), 014028.



Appendix A

Abbreviations and Notations

Symbols	Units	Descriptions
a	m	Plasma minor radius
B	T	Plasma magnetic field
B_θ	T	Poloidal magnetic field
B_ϕ	T	Toroidal magnetic field
c	m s^{-1}	Speed of light
D_0, D_{neo}	-	Particle neoclassical transport coefficient
D_I, D_{ano}	-	Particle anomalous transport coefficient
DD	-	Deuterium-deuterium fusion reaction
DT	-	Deuterium-tritium fusion reaction
ECRH	MW	Electron cyclotron resonance heating
ELM	-	Edge localized mode
E_r	V m^{-1}	Radial electric field
ETB	-	Edge transport barrier
g, g_p	-	Pressure gradient
g_c, g_{pc}	-	Critical pressure gradient
$g_{H \rightarrow L}$	-	Pressure gradient at the onset of H - L back transition
$g_{L \rightarrow H}$	-	Pressure gradient at the onset of L - H transition
g_n	-	Density gradient
g_{nc}	-	Critical density gradient
H	-	Heat Source
H -mode	-	High confinement mode
I_b	-	Bootstrap current fraction
ICF	-	Inertial confinement fusion
ICRH	MW	Ion cyclotron resonance heating
I_p	MA	Plasma current
ITB	-	Internal transport barrier

Symbols	Units	Descriptions
ITG	-	Ion temperature gradient
ITER	-	International Thermonuclear Experimental Reactor
j	-	Current density
j_b	-	Bootstrap current
J_ϕ	A m ⁻²	Current density flow in toroidal direction
<i>L</i> -mode	-	Low confinement mode
LHCD	-	Lower Hybrid Current Drive
LHRH	MW	Lower hybrid resonance heating
L_T	-	Gradient scale length
M	amu	Hydrogenic mass
MCF	-	Magnetic confinement fusion
MHD	-	Magnetohydrodynamics
m_i	kg	Ion mass
NBI	MW	Neutral beam injection heating
n	-	Plasma density
n_0	-	Central density
n_e, N_e	m ⁻³	Electron density
n_{el}, n_l	m ⁻³	Plasma line average electron density
n_i, N_i	m ⁻³	Ion density
n_{ped}	m ⁻³	Pedestal density
NIF	-	National Ignition Facility
NTM	-	Neoclassical tearing mode
NTV	-	Neoclassical toroidal viscosity
p	-	Plasma pressure
p_0	-	Central pressure
p_{ped}	-	Pedestal pressure
P_{aux}	MW	Auxiliary heating power
P_{th}	MW	Power threshold
P_{TOT}	MW	Total heating power

Symbols	Units	Descriptions
P_α	MW	Alpha power
q	-	Plasma safety factor
Q	-	Heat flux
$Q_{H \rightarrow L}$	-	Heat flux at the onset of H - L back transition
$Q_{L \rightarrow H}$	-	Heat flux at the onset of L - H transition
Q_s	-	Source heat flux
q_{95}	-	Edge safety factor
q_{\min}	-	Minimum safety factor
R	m	Plasma major radius
RF	MW	Radio frequency heating
RMSD	-	Root mean square deviation
RMSE	-	Root mean square error
r/a	-	Normalized minor radius
s	-	Magnetic shear
S	-	Particle source
S_a	m ²	Plasma surface area
T_e	keV	Electron temperature
$T_{e,crit}$	keV	Critical edge electron temperature
$T_{e,edge}$	keV	Edge electron temperature
T_i	keV	Ion temperature
T_{ped}	keV	Pedestal temperature
v_θ	m s ⁻¹	Poloidal velocity
v_ϕ	m s ⁻¹	Toroidal velocity
v'_E	s ⁻¹	Radial velocity shear
w	-	Energy content per surface area
x/a	-	Normalized minor radius
Z	-	Ion charge number
Z_{eff}	-	Effective charge number
α	-	Suppression term proportionality constant

Γ	-	Particle flux
Symbols	Units	Descriptions
Γ_s	-	Source particle flux
γ_{ITG}	s^{-1}	ITG mode dominant linear growth rate
γ_{lin}	s^{-1}	Linear growth rate
γ_{lin}^{max}	s^{-1}	Maximum linear growth rate
δ	-	Plasma Triangularity
Δ	-	Pedestal width
ΔE	J	Energy generated in a reaction
Δm	kg	Mass difference in a reaction
ε	-	Plasma inverse aspect-ratio
η	-	Particle surface density
κ	-	Plasma Elongation
ρ_{ITB}^*	-	ITB normalized Larmor radius threshold
ρ_s	m	Larmor radius
ρ_T^*	-	Normalized Larmor radius
χ_0, χ_{neo}	-	Thermal neoclassical transport coefficient
χ_1, χ_{ano}	-	Thermal anomalous transport coefficient
Ψ	-	Poloidal flux
ω_{ExB}	s^{-1}	Flow shear

BIOGRAPHY

Name	Mr. Boonyarit Chatthong
Date of Birth	November 15 th , 1981
Educational Attainment	2005: BS in Physics/Mathematics with distinction, University of Virginia 2010: MS in Physics, Mahidol University
Scholarship	2000-2015: Royal Thai Scholarship

Publications

Chatthong, B., and Onjun, T. (2015). Study of L-H Transition and Pedestal Width Based on 2 Fields Bifurcation and Fixed Point Concept. Accepted for publication in *Acta Polytechnica*.

Chatthong, B., and Onjun, T. (2015). Locality Effects on Bifurcation Paradigm of L-H Transition. Accepted for publication in *Songklanakarinn J. Sci. Technol.*

Chatthong, B., and Onjun, T. (2015). Investigation of toroidal flow effects on L-H transition in tokamak plasma based on bifurcation model. *Journal of Physics: Conference Series*, 611 (1), 012003.

Intharat, P., Chatthong, B., Onjun, T., Poolyarat, N., and Picha, R. (2015). The simulation of L-H transition in tokamak plasma using MMM95 transport model. *Journal of Physics: Conference Series*, 611 (1), 012005.

Chatthong, B., and Onjun, T. (2014). Comparison of H-mode plasma simulations using toroidal velocity models depending on plasma current density and ion temperature in presence of an ITB. *Songklanakarinn J. Sci. Technol.*, 36 (3), 375-387.

Pianroj, Y., Jumrat, S., Chatthong, B., and Onjun, T. (2014). A Full Radial Electric Field Calculation for Predicting Pedestal Formation in H-mode Tokamak Plasma by using BALDUR code. *Thammasat Int. J. Sc. Tech.*, 19 (2), 63-70.

Chatthong, B., and Onjun, T. (2013). Simulations of ITER in the presence of ITB using the NTV intrinsic toroidal rotation model. *Nucl. Fusion*, 53 (1),

013007.

Chatthong, B., and Onjun, T. (2011). Self-Consistent Simulation of Standard *H*-Mode ITER with the Presence of an Internal Transport Barrier. *Thammasat Int. J. Sc. Tech.*, 16 (1), 42-53.

Chatthong, B., Onjun, T., and Singhsomroje, W. (2010). Model for toroidal velocity in H-mode plasmas in the presence of internal transport barriers. *Nucl. Fusion*, 50 (6), 064009.

Chatthong, B., Onjun, T., Suwanna, S., Poolyarat, N., and Picha, R. (2010). JET Simulations with Edge and Internal Transport Barriers Included. *Thai Journal of Physics*, Series 5 79-83.

Work Experiences

2005-2006: Research assistant, Teaching assistant

Carnegie Mellon University

2004-2005: Research assistant

University of Virginia

2003-2005: Teaching assistant

University of Virginia